X-ray Diagnostics of Relativistic Reflection Around Supermassive Black Holes.

Shyam Bhayani
Astrophysics Group

Department of Physics
Imperial College London

—

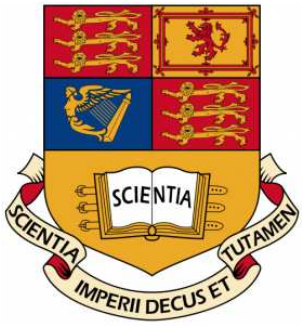

Thesis submitted for the Degree of Doctor of Philosophy to
Imperial College London

· 2011 ·

Abstract

This thesis presents an investigation into the X-ray energy and variability spectra of Seyfert galaxies. Reflection of the X-ray continuum by the accretion disc in these Active Galactic Nuclei (AGN) is expected to produce an iron line and an associated reflection continuum. The iron line should be relativistically broadened as it is subject to the strong gravitational field of the central black hole. Often, such a line is never found either because it appears not to be present or if it is, the magnitude of the broadening is less than expected. These cases pose a problem for the current understanding of accretion onto the black hole in AGN. We analyse the *XMM-Newton* observations of such objects to determine if the relativistically broadened iron line only appears to be "missing" because the accretion disc is ionised and/or there is a strong concentration of the line emission in the central disc regions. In the latter scenario, it is possible for the iron line to be smeared to such an extent that it blends into the continuum and is therefore difficult to disentangle. A combination of both effects leads to the identification of a relativistically broadened iron line in the majority of the observations where it could not be detected previously. In some of these objects, blurred disc reflection can also be detected if there is an additional source of iron line emission that arises further from the black hole such as in the Broad Line Region. We find that the strength of the blurred iron line and associated reflection continuum in these objects is consistent with the sources that exhibit a "classical" relativistically broadened iron line.

Following this, we investigate the variability of the iron line in our sample of Seyferts. In models of accretion disc reflection, a simple prediction is that variations in the reflection component should follow variations in the X-ray continuum that illuminates the disc. Using unnormalised rms variance-spectra, we investigate if this scenario is typical in our sample of observations and find that it is not generally confirmed. Instead, there is a large amount of diversity in the behaviour of the iron line variability. For example, some observations possess an iron line that is more variable than the continuum, while other iron lines exhibit variability only bluewards of the line core. Most interestingly, a large group of observations possess a broad iron line that is invariant to the continuum and there are changes in the variability of the iron line between multiple observations of the same object. In some cases, the rms spectra can distinguish between models that explain the broad red wing of the iron line.

Finally, we expand the variability analysis to between 0.3 – 10 keV and focus on the broadband X-ray variability on short time-scales ($\sim$ 40 ks). After normalising the variance spectra by the X-ray flux, a diverse range of amplitudes and shapes are

found in the variance-spectra of both different objects and the same object. Part of the scatter in the amplitudes is due to the anti-correlation between the black hole mass of an AGN and its variance, while the various classes of profile shapes suggest that there are intrinsic differences in the spectral variability throughout the sample, as found with the iron line. We model variance-spectra that are based on relativistic disc reflection and velocity-smeared models of the broadband X-ray spectra of AGN and find that a range of profile shapes are possible. The mean variance-spectrum of those that are humped in the sample can be explained solely by a small increase in the slope of the continuum as the X-ray flux increases in a reflection-based model. Interestingly, there is no requirement for either the disc reflection or absorbers local to the AGN to respond to the changing illuminating intensity.

To my family

Contents

Abstract **1**

List of Tables **10**

List of Figures **13**

Declaration and Copyright **14**

Acknowledgements **15**

Publications **16**

1 Introduction **17**

1.1 Taxonomy 18
1.2 Radio-quiet unification 20
1.3 Accretion 22
1.4 Accretion disc coronae 24
1.5 Disc reflection 25
1.5.1 Elemental abundance 27
1.5.2 Inclination angle 28
1.5.3 Ionisation of the disc surface 28
1.6 The profile of the broad iron line 30
1.7 Alternatives to relativistic blurring 31
1.8 Observations of the broad iron line 33
1.8.1 *XMM-Newton* 35
1.9 *XMM-Newton* survey of Seyfert galaxies 36
1.9.1 Weak or non-existent broad emission 38
1.10 Variability 40
1.10.1 Light bending 41
1.10.2 Narrow line variability 43

1.11 Soft excess . . . 44
1.12 Aims . . . 46

2 XMM-Newton 48
2.1 Overview . . . 48
2.2 Key features . . . 48
2.3 Telescopes . . . 50
2.3.1 EPIC detectors . . . 51
2.3.2 X-ray point-spread function . . . 52
2.4 Data reduction . . . 54
2.4.1 Preparation . . . 54
2.4.2 Event and region filtering . . . 55
2.4.3 Pile-up . . . 56
2.4.4 Low background . . . 58
2.4.5 Spectral extraction . . . 60
2.5 Summary . . . 61

3 On the apparent absence of relativistically broadened iron lines in Seyfert galaxies 62
3.1 Overview . . . 62
3.2 Introduction . . . 63
3.3 The sample and data reduction . . . 64
3.4 Model NBR . . . 65
3.4.1 The continuum and ionised absorption . . . 70
3.4.2 Compton reflection . . . 71
3.4.3 Significance of a blurred reflection detection . . . 73
3.5 Model N07 . . . 74
3.5.1 Ionised disc – Model ION . . . 75
3.6 Fit of Model ION to the data . . . 76
3.6.1 Strong relativistic effects – Model SRC . . . 78
3.6.2 Strong relativistic effects and ionisation of the accretion disc – Model SRI . . . 81
3.7 Non-relativistic iron lines . . . 83
3.7.1 Model SRC . . . 87
3.7.2 Model SRI . . . 89
3.7.3 The N07 relativistic-line observations . . . 95
3.7.4 Objects with no detected blurred reflection . . . 95
3.8 Discussion . . . 97

3.8.1 Comparison with *Suzaku* data . . . 99
3.8.2 Steep emissivity profiles . . . 100
3.8.3 Comparison with optical lines . . . 101
3.9 Conclusions . . . 101

4 Root mean square variability of iron lines in Seyferts 104
4.1 Overview . . . 104
4.2 Introduction . . . 105
4.3 The $\sigma_{\rm rms}$-spectrum . . . 108
4.3.1 Error on $\sigma_{\rm rms}$ due to measurement errors . . . 108
4.4 Results . . . 109
4.4.1 Significance of a variability excess . . . 110
4.5 Analysis of the iron line variability . . . 117
4.5.1 6.4 keV iron line core . . . 119
4.5.2 Red wing variability . . . 119
4.5.3 Blue excesses . . . 121
4.5.4 Constant iron lines . . . 121
4.5.5 Objects with multiple observations . . . 122
4.5.6 The continuum . . . 124
4.6 Discussion . . . 125
4.7 Non-variable distant reflection . . . 125
4.8 Red wing variability . . . 125
4.8.1 Artificial broadening of the red wing by warm absorption . . . 126
4.8.2 Decoupling between the continuum and iron line . . . 127
4.8.3 Narrow variability excesses . . . 128
4.9 Variability of the heavily blurred disc reflection . . . 130
4.10 Conclusions . . . 130

5 On the origin of the X-ray spectral variability in Seyfert galaxies 133
5.1 Overview . . . 133
5.2 Introduction . . . 134
5.3 Normalised excess variance-spectrum . . . 136
5.3.1 Estimation of the normalised excess variance-spectrum . . . 137
5.4 Profile shapes of the model variance-spectra. . . . 152
5.4.1 The time-averaged spectrum at hard X-rays . . . 152
5.4.2 The time-averaged spectrum at soft X-rays . . . 154
5.4.3 Model 1 variance-spectra . . . 157
5.4.4 Model 2 variance-spectra . . . 158

5.4.5 Shapes of the model variance-spectra . . . 158
5.5 Fit to the mean humped variance-spectrum . . . 162
5.5.1 Results . . . 166
5.6 Discussion . . . 170
5.6.1 The warm absorbing material . . . 171
5.6.2 Blurred disc reflection . . . 172
5.6.3 A PL continuum with variable flux *and* spectral slope . . . 173
5.6.4 Smeared absorption . . . 174
5.6.5 Comparison with past results . . . 174
5.6.6 Practical implications of our results . . . 175
5.7 Conclusions . . . 175

6 Summary **178**
6.1 Summary . . . 178
6.2 Further work . . . 181

A Blurred ionised disc reflection **184**

Bibliography **192**

List of Tables

2.1 The XMM-Newton FLAG attributes. 56
2.2 Time resolution and maximum count rates in different pn science modes for avoiding pile-up. 57

3.1 The sample of *XMM-Newton* EPIC-pn observations. 66
3.2 The redshifts, Galactic absorption columns and iron line classes of the sample of *XMM-Newton* EPIC-pn observations. 69
3.3 The XSPEC model components and parameters for each model. . . . 72
3.4 The 99% threshold $\Delta\chi^2_{\rm NBR-Y}$ relative to Model NBR to determine the presence of blurred reflection for each observation and model that we test. 73
3.5 The best-fit χ^2/degree of freedom of Model NBR and the change ($\Delta\chi^2_{\rm NBR-Y}$/d.o.f.) in goodness-of-fit for Models N07, ION, SRC and SRI relative to Model NBR. 74
3.6 Disc line parameters for the narrow-line observations derived using Model ION. 77
3.7 Disc line parameters for the narrow-line observations derived using Model SRC. 80
3.8 Disc line parameters for the narrow-line observations derived using Model SRI. 82
3.9 The 99% threshold $\Delta\chi^2$ relative to Model NBR for the non-relativistic-line observations. 87
3.10 Disc line parameters derived for the non-relativistic observations using Model SRC. 88
3.11 Disc line parameters derived for the non-relativistic observations using Model SRI. 90
3.12 Comparison of optical line and iron line widths. 102

4.1 Power-law fits to the $\sigma_{\rm rms}$- and mean energy spectra. 111
4.2 Significances of the variability excesses in the iron line bands. 118

5.1 List of observations and segments in the variability sample. 141
5.2 The sample sources and their black hole mass estimate. 142
5.3 The classification of the $\sigma^2_{\rm nvar}$-spectra in the sample. 147
5.4 Coefficients of variation for the $\sigma^2_{\rm nvar}$ and $M_\bullet\sigma^2_{\rm nvar}$ distributions in each energy band. 150
5.5 The parameters of the time-averaged spectra of Models 1 and 2. . . . 156
5.6 Classifications of the $\sigma^2_{\rm mod}$-spectra. 166
5.7 The variable parameters of the models we test and their ranges of variation. 167

A.1 Fits of Model ION to the N07 observations with a broad iron line (relativistic and non-relativistic). 185

List of Figures

1.1 Typical 350 – 750 nm rest-frame optical spectra of a variety of AGN. 19
1.2 The standard picture of AGN unification. 21
1.3 Possible geometries for the accretion disc and Comptonising corona. . 26
1.4 A Monte Carlo simulation of X-ray reflection by a cold and semi-infinite slab of gas. 27
1.5 Theoretical ionised reflection spectra. 29
1.6 The processes involved in producing a broad and skewed iron line profile. 31
1.7 The dependence of the iron line profile on the disc inclination (*left*) and black hole spin (*right*). 32
1.8 The dependence of the iron line profile on the slope of the emissivity power-law. 32
1.9 The first robust detection of a broadened iron line profile in MCG-6-30-15. 34
1.10 Model emissivity profiles for torqued accretion discs. 37
1.11 The flux-flux plot (*left*) and difference spectrum (*right*) for an observation of MCG-6-30-15. 41
1.12 *Left*: The iron line equivalent width, reflection component flux and continuum flux as a function of source height in a light bending model. *Right*: The reflection component flux vs the continuum flux. 42
1.13 An artificial soft excess due to ionised absorption. 45
1.14 A reflection model applied to the broadband spectrum of 1H0707-495. 46

2.1 The launch of *XMM-Newton*. 49
2.2 The path taken by X-rays in the *XMM-Newton* telescope with a pn detector at its focus. 50
2.3 The effective areas of the pn, MOS and RGS detectors. 51
2.4 The quantum efficiency of the pn chip as a function of energy. 52
2.5 Layout of the 12 CCDs in the EPIC pn camera. 53

2.6 The encircled energy fraction as a function of angular radius at different energies. 53
2.7 The arrangement of the source and background regions used to extract events in an observation of MCG-6-30-15. 55
2.8 List of PATTERN types for the pn camera. 57
2.9 `EPATPLOT` plots for an *XMM-Newton* observation of IC 4329A 59
2.10 The background light curve of an *XMM-Newton* observation of NGC 526A. 60

3.1 Continuum and blurred REFLIONX spectra with (top panel) $r_{\rm in} = 6r_{\rm g}$ and $q = 3$ and (bottom panel) $r_{\rm in} = 1.24r_{\rm g}$ and $q = 6$. 79
3.2 The unfolded 2.5 – 10 keV spectrum and data/model ratio for the seven narrow-line observations that are well-fit with strongly smeared reflection and an ionised disc. 86
3.3 The unfolded 2.5 – 10 keV spectrum and data/model ratio for the 6/8 non-relativistic-line observations that are well-fit with strongly smeared reflection and an ionised disc. 92
3.4 Histograms of the disc reflection strengths (top panel) and reflected flux fractions (bottom panel) of the observations in the sample. . . . 94
3.5 The unfolded 2.5 – 10 keV spectrum and data/model ratio for the 4/11 narrow-line observations that do not show a significant improvement when fit with strongly smeared reflection and/or an ionised disc. 97
3.6 The unfolded 2.5 – 10 keV spectrum and data/model ratio for the 2/8 non-relativistic-line observations that do not show a significant improvement when fit with strongly smeared reflection and an ionised disc. 98

4.1 Data/model ratios of the $\sigma_{\rm rms}$-spectra and mean energy spectra fitted with a power-law continuum. 116
4.2 The continuum slope of the mean energy spectrum plotted against the continuum slope of the rms spectrum. 124

5.1 Humped normalised variance-spectra of IRAS 13224-3809 and NGC 4051. 135
5.2 0.3 – 10 keV light curves of observations in the N07 sample. 140
5.3 The 0.3 – 10 keV $\sigma^2_{\rm nvar}$-spectra of the observations in the sample. . . . 145
5.4 $\sigma^2_{\rm nvar}$-spectra of segments of Ark 564, NGC 4593, MCG-6-30-15, NGC 7469 (top panel) and NGC 3783 (bottom panel). 146

5.5 The absolute $\sigma^2_{\rm nvar}$-spectra and $M_\bullet\sigma^2_{\rm nvar}$-spectra (top and bottom panels respectively) of all observations in the sample between 0.3 – 10 keV. 151
5.6 The 0.3 – 10 keV energy spectrum of Model 1. 154
5.7 The $\sigma^2_{\rm mod}$-spectra of Models 1(a), (b), (c), (d) and (e). 162
5.8 The $\sigma^2_{\rm mod}$-spectra of Models 2(a), (b), (c), (d) and (e). 165
5.9 Fits to the $\overline{\sigma^2_{\rm nvar}}$-spectrum of the Model 1(a), 1(d), 1(e) and 2(c) $\sigma^2_{\rm mod}$-spectra. 169

6.1 How the hot spots of Kα emission will appear as arcs in an *ATHENA* simulation of the time-energy plane. 183

A.1 The unfolded spectra centred around the iron line band (4 – 9 keV) for the entire N07 sample. 187

Declaration and Copyright

This thesis is my own work, except where explicitly indicated in the text.
This work is copyright to Shyam Bhayani. Full access is granted to this work for the purposes of study and research. All other rights reserved.

Shyam Bhayani
June 2011

Acknowledgements

It would have been impossible to complete my PhD without the help and motivation of others. My first and deepest thanks must go to my supervisor, Paul Nandra. To have studied X-ray astronomy under one of the most eminent names in the field has been a great honour. His unlimited source of ideas and unnerving ability to always find a solution to any problem have been crucial in taking me to the point where I could start writing this thesis.

My thanks also go to Iossif Papadakis for visiting Imperial to help me and then hosting me at the University of Crete. I am grateful to him for his patience, enthusiasm and always making sure that there was a good vegetarian option on the menu!

From the beginning to the end of my PhD, I have asked countless questions of my fellow X-ray group members. Special thanks go to Murray and Elise for always providing me with advice on everything from using XSPEC for the first time to their experiences of writing up. Though I did not work with Paul O'Neill, I must acknowledge him as his scripts have taught me much about *XMM-Newton* as well as the importance of being organised.

The highlight of my PhD has been spending time with the Astrophysics post-graduates. There has been no better escape from working than talking about everything under the Sun as well as discussing things much further away. I must give a special mention to the table-tennis guys for making me a more gracious loser when I (rarely) lose. I would also like to thank my fellow undergraduate Lampros for showing me that it is possible to enjoy physics, even if you hate lab-work! Finally, I have to include my friends Rahul and Srik. At times, our chats about football have involved a higher level of analysis than the work in this thesis.

Finally, I must thank my Mum, Dad and brother for their support over the past four years and more. They may not have understood in detail exactly what I do everyday, but without their encouragement, I would certainly not have embarked on a PhD or come close to finishing it.

Publications

- "Rms variability properties of the iron K alpha line in Seyfert galaxies." **Bhayani S.** & Nandra K., 2010, MNRAS, 408, 120
- "On the apparent absence of broad iron lines in Seyfert galaxies." **Bhayani S.** & Nandra K., 2011, MNRAS, 416, 629

Chapter 1

Introduction

Many galaxies have nuclei so bright that they cannot be powered by stellar processes as they outshine the rest of the galaxy. These compact cores are termed active galactic nuclei (AGN). The most luminous AGN subclass are the quasars, which have been observed at luminosities as high as 10^{48} erg s^{-1} (e.g. Wu et al., 2010). Another of their defining features is their rapid variability, which astonishingly indicates that AGN can be as small as our Solar System. The radiation from AGN cannot be thermal emission from stars as it encompasses all parts of the electromagnetic spectrum from radio waves to X-rays and often gamma rays. The only way to explain the immense energy production is accretion onto a supermassive black hole (SMBH) at the centre of the galaxy (Lynden-Bell, 1969; Rees, 1984). This is the process of transporting mass into the black hole and converting its gravitational potential energy into kinetic and radiative energy that we observe. To conserve angular momentum, material from the surrounding galaxy is likely to accrete via a flattened and rotating disc.

Nearly all galaxies are expected to possess a SMBH of mass $M \sim 10^5 - 10^{9.5}$ M$_\odot$ at their centre (Kormendy & Richstone, 1995; Magorrian et al., 1998) but the majority, such as our own, are classed as dormant as they now accrete very slowly. In the galaxies thought to host accreting AGN, the centre is the site of some of the most exotic areas of physics known: the interactions between matter moving at relativistic velocities, electromagnetic fields and the black hole spacetime. The event horizon at $\frac{2GM}{c^2}$ for a non-rotating black hole is the radius beyond which even light cannot escape the black hole. As the angular scales of the biggest horizons are $\sim 10^{-6}$ arcsec, imaging the central regions is still many years away. Fortunately, analysis of an AGN's X-ray spectrum and the prominent iron line in particular can provide an indirect view of the inner regions.

In this introductory chapter, I will begin with a short overview on the variety of

AGN and the unification theories that can link them together. I will then review the SEDs of Seyfert galaxies and focus on the information that the profile and variability of the iron line can provide us on black holes and accretion.

1.1 Taxonomy

The commonly-used term "AGN Zoo" reveals that there are many subclasses of AGN. They are separated by their observational properties such as luminosity and variability, but at the heart of each of them lies a SMBH. Our understanding of their diversity is not complete, but a major reason for their apparent differences is the way in which we observe them. This is expanded upon in Section 1.2. In this section I introduce the different types of AGN that have been discovered.

The Seyfert class of AGN form up to 10% of all galaxies (Maiolino & Rieke, 1995; Ho et al., 1997). They were discovered in 1943 by Carl Seyfert when he selected a group of galaxies with stellar-appearing cores (Seyfert, 1943) and found that the optical spectra were dominated by broadened and high-excitation emission lines. Khachikian & Weedman (1974) realised that there are two types of Seyferts that are distinguished by the width of the optical emission lines. Type 1 Seyferts possess both narrow (hundreds of $\mathrm{km\,s^{-1}}$) and broad lines (up to 10,000 $\mathrm{km\,s^{-1}}$) in their optical spectra whereas Type 2s only display narrow lines. Figure 1.1 shows the optical spectra of Seyfert galaxies and the other AGN classes discussed below. As the broad-line region (BLR) is of higher density ($n_\mathrm{e} \geq 10^9$ cm^{-3}) than the narrow-line region (NLR) ($n_\mathrm{e} \sim 10^{3-5}$ cm^{-3}), broad lines are found only in the permitted lines (Koski, 1978; Ferland & Netzer, 1983; Stasińska, 1984). In contrast, both permitted and forbidden transitions are seen in the narrow lines. Classification schemes have been devised (e.g. Osterbrock, 1981) to account for the cases where the relative strength of the broad and narrow components in the optical is less clear. As the broad component of Hβ becomes weaker compared to the narrow component, the Seyfert classification changes from 1.2 to 1.5 to 1.8. A further type of 1.9 accounts for Seyferts with weak broad wings visible on the Hα line but not on the Hβ line. The assumption that all Seyfert 2s lack broad lines has since been revealed not to be completely correct (Antonucci & Miller, 1985). Miller et al. (1991) found that the optically polarised spectra of some Seyfert 2s do have broad lines that are scattered into our line of sight (Tran et al., 1992). This implies that Seyfert 2s may only differ from Seyfert 1s because of their orientation to the observer and the presence of obscuring matter between the NLR and BLR. This agrees with unification theories that had first been stipulated over a decade before and are discussed further in

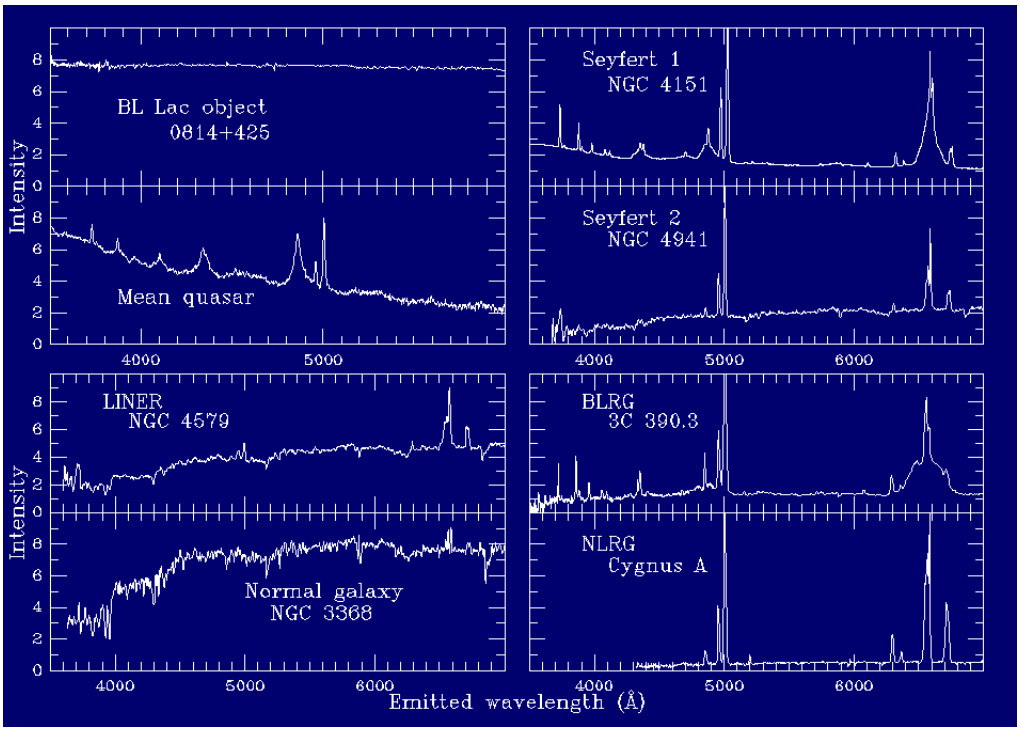

Figure 1.1: Typical 350 – 750 nm rest-frame optical spectra of a variety of AGN. The Hα(656.3 nm) and Hβ(486.1 nm) lines show both broad and narrow components in the Seyfert 1 spectrum but the Seyfert 2 spectrum displays only narrow lines. A similar classification is seen in the broad-line radio galaxy (BLRG) and narrow-line radio galaxy (NLRG). The BL Lac object displays a featureless continuum. The quasar spectrum has similar broad lines but weaker narrow lines compared to those of the Seyfert 1 spectra. Figure taken from http://www.astr.ua.edu/keel/agn/spectra.html.

Section 1.2.

This thesis includes Narrow Line Seyfert 1s (NLS1s), which are a subset of AGN with similar optical/UV spectra as Seyfert 1s but with remarkably narrow permitted lines (FWHM (Hβ) < 2000 km s^{-1}, Osterbrock & Pogge, 1985). Their X-ray properties also make them distinctive as they possess very steep soft X-ray spectra and exhibit large amplitude variability on short time-scales (Boller et al., 1996). Their extreme properties are compatible with relatively small black hole masses (Boller et al., 1996; Boroson, 2002) if the broad Hβ emitting region is gravitationally dominated by the black hole. To account for the relatively normal observed luminosities (Pounds et al., 1995), the accretion rates must be close to Eddington (Boroson & Green, 1992). Alternative models to explain their behaviour include winds and density effects (Lawrence et al., 1997), metallicity (Mathur, 2000) and ionised absorption (Komossa & Meerschweinchen, 2000).

Like Seyferts, the elliptical radio galaxies can be split into broad-line (BLRG)

and narrow-line (NLRG) types according to their optical spectra. Their structure invariably consists of two radio lobes either side of the AGN that extend to megaparsec scales and are connected to the core by collimated jets of relativistic particles (Bridle & Perley, 1984). Quasars are extremely luminous and mostly radio-quiet (Schmidt, 1963), though the first to be discovered were actually of the radio-loud variety. Quasars have been found as far as $z = 7.09$ (Mortlock et al., 2011), making them important cosmological probes. While high luminosity QSOs ($L_{2-10\ \mathrm{keV}} = 10^{45} - 10^{47}$ ergs s^{-1}) peak at a redshift of 2 (Warren et al., 1994; Schmidt et al., 1995; Kennefick et al., 1995; Shaver et al., 1996), lower luminosity AGN ($L_{2-10\ \mathrm{keV}} = 10^{41} - 10^{43}$ ergs s^{-1}) peak in their comoving space density at a lower redshift, $z \lesssim 1$ (Cowie et al., 2003; Steffen et al., 2003; Ueda et al., 2003; Barger et al., 2005). Quasar spectra are similar to those of Seyfert galaxies, which suggests that quasars are more distant and higher luminosity versions of Seyfert galaxies as postulated by Weedman (1976). The AGN classification also includes the radio-loud and rapidly variable Blazars (e.g. PKS2155-304 Ghisellini & Tavecchio, 2008), which possess a relativistically-beamed jet close to the line of sight. At the low end of the luminosity scale are the Low-Ionisation Nuclear Emission Regions (LINERs, Heckman, 1980) that have been detected in many nearby bright galaxies (Ho et al., 1997; Kauffmann et al., 2003).

1.2 Radio-quiet unification

The unification scheme for AGN is based on the assumption that there is less intrinsic diversity among them than we observe. Instead, the wide variety of AGN phenomena is due to a combination of real differences in a small number of physical parameters such as luminosity, combined with apparent differences in observer-dependent parameters such as orientation. Since this thesis is focused on Seyfert galaxies, this section focuses only on the unification of their two classes.

Rowan-Robinson (1977) and Osterbrock (1978) made the first suggestions that both types of Seyferts are physically the same but that the BLR is obscured from our view in Seyfert 2s. The obscuration is likely to arise from a dusty torus surrounding the central source so that the classification of the Seyfert galaxy is dependent on the orientation of the torus relative to the observer's line of sight to the nucleus (Antonucci & Miller, 1985; Miller & Goodrich, 1990; Antonucci, 1993). As shown in Figure 1.2, a Seyfert galaxy is classed as Type 1 if the observer views the central source and BLR along the axis of the torus whereas a Seyfert 2 is identified if the BLR is inaccessible to lines of sight through the obscuring torus. The space density

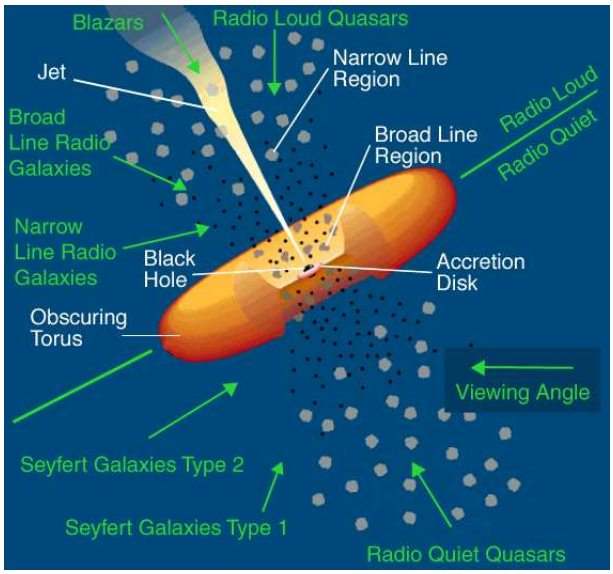

Figure 1.2: The standard picture of AGN unification showing how our orientation could reconcile different AGN into a single class. Figure taken from Urry & Padovani (1995).

of Seyfert 2s is 1 – 3 times that of Seyfert 1s (Maiolino & Rieke, 1995), which suggests that the torus blocks out around 1/2 of the sky as seen by the central source.

The first direct evidence of a torus has come with interferometric mid-infrared observations of NGC 1068 that resolve the dust structure (Jaffe et al., 2004). Further indirect evidence for a dusty torus came from thermal bumps in the infrared spectra of Seyfert 2s (Barvainis, 1987) and cone-shaped NLRs in well-resolved cases (Pogge, 1989; Evans et al., 1991; Wilson & Tsvetanov, 1994). Obscuration in AGN can also explain the spectrum of the X-ray background, which can be described by a power law with a spectral slope of $\Gamma \approx 1.4$ (Kushino et al., 2002; Lumb et al., 2002; De Luca & Molendi, 2004), while most AGN have a steeper spectral slope of $\Gamma = 1.9$ once Compton reflection is taken into account (Mushotzky et al., 1993; Nandra et al., 2007). The X-ray background can instead be built up by summing the spectra of many obscured AGN and taking into account their redshifts, luminosities and absorbing column densities. This has been confirmed by the resolving of the hard X-ray component into individual X-ray sources in deep X-ray observations with the *Chandra X-ray observatory* and *XMM-Newton* (Mushotzky et al., 2000; Brandt & Hasinger, 2005; Worsley et al., 2005).

Unifying Seyfert galaxies with the obscuring torus is not yet complete as there are still a few unresolved problems. One example is that only 50% of Seyfert 2s show broad lines in their polarisation spectra (Tran et al., 1992). The remaining half may have no broad line region at all (Pappa et al., 2001; Bianchi et al., 2008a;

Brightman & Nandra, 2008). Another problem is that no highly polarised Seyfert 2s have been found even though the polarisation level should reach 50% for edge-on sources (Miller & Goodrich, 1990).

1.3 Accretion

The only feasible process that can provide the sustained energy release seen in bright AGN is accretion. Put simply, accretion is the conversion of gravitational energy into electromagnetic radiation and kinetic energy as matter falls inward at rate $\dot{M}$ towards the central black hole. As the matter accretes from large distances, it possesses substantial angular momentum that must be conserved. This can occur if the gas accretes via a disc as the differential motion and viscosity transfer angular momentum outwards. The viscous stresses are thought be associated with turbulence arising from the magnetorotational instability (Balbus & Hawley, 1991).

The Eddington luminosity ($L_{\rm Edd}$) is used to identify a practical limit to the luminosity of disc-like accretion flows even though it strictly applies only to spherical accretion. It is found by equating the inwards gravitational force acting on the accreting gas to the outwards radiation force:

$$L_{\rm Edd} = \frac{4\pi G c m_p}{\sigma_{\rm T}} M, \tag{1.1}$$

where m_p is the proton mass, M is the black hole mass and $\sigma_{\rm T}$ is the Thompson scattering cross-section. If the luminosity exceeds $L_{\rm Edd}$, then the radiation will overwhelm gravity and prolonged accretion becomes impossible. From the Eddington luminosity, it is possible to identify the Eddington accretion rate $\dot{M}_{\rm E}$, which is the mass accretion rate required to sustain the Eddington luminosity:

$$\dot{M}_{\rm E} = \frac{L_{\rm Edd}}{\eta c^2} \approx 1.4 \times 10^{18} (M/{\rm M}_\odot) {\rm g\ s}^{-1}, \tag{1.2}$$

where η is the efficiency of converting the infalling mass into energy that is radiated away.

At sufficiently high fractions of $L_{\rm Edd}$, accretion in AGN is thought to proceed through a geometrically thin accretion disc (Shakura & Sunyaev, 1973). The main assumptions involved are that the medium is optically thick and the energy of a particle at distance r from the central source is dissipated locally. Gravitational potential energy is released at the rate $\frac{GM\dot{M}}{r}$ and half of this is radiated away at rate $L_{\rm disc}$ while the other half heats up the disc. The local emission can be approximated as a blackbody so:

$$L_{\rm disc} = \frac{GM\dot{M}}{2r} = 2\pi r^2 \sigma T^4, \tag{1.3}$$

where σ is the Stefan-Boltzmann constant. This can be solved for the disc temperature at r. Taking into account energy dissipated in the disc through viscosity, the temperature is:

$$T(r) = \left(\frac{3GM\dot{M}}{8\pi\sigma r^3} \left[1 - \left(\frac{r_{\rm in}}{r} \right)^{1/2} \right] \right)^{1/4}. \tag{1.4}$$

where $r_{\rm in}$ is the inner boundary to the disc. The lower limit of $r_{\rm in}$ depends on the spin of the black hole. The radius of marginal stability, $r_{\rm ms}$, is the distance within which circular test particles are no longer stable and material plunges into the black hole. The Schwarzchild metric describes space-time around a static black hole where $r_{\rm ms} = 6r_{\rm g}$ ($2r_{\rm g} = \frac{2GM}{c^2}$ is the event horizon for a non-rotating black hole, otherwise known as the Schwarzchild radius, $R_{\rm S}$). With a spinning black hole, $r_{\rm ms}$ reaches even closer to the black hole. The minimum radius of $r_{\rm ms} = 1.24r_{\rm g}$ occurs when the black hole spins at its maximum value of $a = 0.998$ (where $a = \frac{cJ}{GM^2}$ and J is the angular momentum of the black hole, Bardeen et al., 1972; Thorne, 1974). Strong emission is not expected within $r_{\rm ms}$ because the gas should be hot and highly ionised (Young et al., 1998). A non-rotating black hole with $r_{\rm in} = 6r_{\rm g}$ can achieve an efficiency of $\eta = 0.06$, which is seven times smaller than for a maximally rotating black hole with $r_{\rm in} = 1.24r_{\rm g}$.

For $r \gg r_{\rm in}$, Equation 1.4 can be simplified and put in terms of $R_{\rm S}$:

$$T(r) = \left[\frac{3GM\dot{M}}{8\pi\sigma R_{\rm S}^3} \right]^{1/4} \left(\frac{r}{R_{\rm S}} \right)^{-3/4}. \tag{1.5}$$

Substituting for the first factor of $R_{\rm S}$ with $\frac{2GM}{c^2}$ leaves:

$$T(r) = \left[\frac{3c^6}{64\pi\sigma G^2} \right]^{1/4} \dot{M}^{1/4} M^{-1/2} \left(\frac{r}{R_{\rm S}} \right)^{-3/4}. \tag{1.6}$$

Finally, using Equation 1.2, the dependence of the disc temperature on accretion rate, black hole mass and radius is given as:

$$T(r) \propto (\dot{M}/\dot{M}_{\rm E})^{1/4} M^{-1/4} \left(\frac{r}{R_{\rm S}} \right)^{-3/4}. \tag{1.7}$$

This shows that a disc around a supermassive black hole of mass 10^{7-8} $M_\odot$ that is accreting at the Eddington rate will emit mostly at a temperature of $10^5 - 10^6$ K,

making them optical and UV sources. However, an accreting stellar-mass black hole will emit in the higher energy X-ray region of the spectrum.

The non-relativistic nature of the Shakura-Sunyaev model makes it a very good but crude approximation to real accretion discs. Relativistic generalisations have been modelled by Novikov & Thorne (1973), Page & Thorne (1974) and Eardley & Lightman (1975). These relativistic, geometrically thin and radiatively efficient discs are described as the "standard model" for black hole accretion discs. They include a natural choice for $r_{\rm in}$ at $r_{\rm ms}$ where the torque is assumed to vanish. This is referred to as the zero-torque boundary condition as material within $r_{\rm ms}$ plunges into the black hole, conserving energy and angular momentum.

1.4 Accretion disc coronae

The standard model predicts an optical/UV dominated quasi-thermal spectrum for AGN but one of their defining observational characteristics is that they are copious X-ray emitters. The X-ray spectrum typically features a power-law that extends to hard X-ray energies before rolling over exponentially at hundreds of keV. The most likely mechanism for producing the X-rays is inverse Compton scattering of the soft optical/UV photons in a hot (10^9 K) and tenuous corona that surrounds the disc (Sunyaev & Titarchuk, 1980; Thorne & Price, 1975; Sunyaev & Truemper, 1979; Zdziarski et al., 1994). If the thermal energy (T_e) of the relativistic electrons in the corona is greater than the photon energy (E), there will be a transfer of energy from an electron to a photon of:

$$\Delta E \approx (4kT_e - E)\frac{E}{m_e c^2} \tag{1.8}$$

where m_e is the electron mass. In the standard model, low-to-moderate optical depth electrons can reach virial temperatures of tens to hundreds of keVs in the innermost regions. Multiple scatterings of photons off these electrons is exponentially unlikely, but when they do occur, there are exponential energy gains for the photons. Overall, this results in a power-law spectrum of the form $E^{-\Gamma}$ where Γ is the photon index and gives the slope of the power-law. As the photon energy approaches that of the thermal electrons, the energy transfer decreases and eventually a sharp rollover should be seen in the spectrum when equality is reached. Thus, observing the cut-off can inform us of the temperature of the underlying electron distribution.

While the X-ray power-law is understood to be produced by Comptonisation, the mechanism for heating the electrons is not completely known. Possibilities

include magnetic processes such as flux tubes rising above the disc and dissipating energy in the corona (Galeev et al., 1979; Nayakshin & Kazanas, 2001). Another unknown property of the corona is its geometry. An often used geometry is the "sphere + disc" configuration where a disc surrounds the central corona. In this geometry, the hot, inner corona receives only a fraction of the soft optical/UV flux from the outer, cool disc. This ensures it is not strongly Compton cooled and can remain hot enough to produce hard spectra (Dove et al., 1997). Other coronal models are based on a co-spatial disc and corona (Ostriker et al., 1976; Liang & Price, 1977) where the dissipation of energy takes place mostly within the corona. A simpler model is one where the corona sandwiches the accretion disc (Haardt & Maraschi, 1991; Haardt et al., 1994, 1997), but even under the extreme conditions of a maximised coronal optical depth and complete dissipation of the accretion energy in the corona, Γ cannot be less than ~ 2 (Stern et al., 1995), which contradicts many X-ray observations (e.g. Nandra & Pounds, 1994). As the accretion disc will reprocess incident X-rays into soft thermal radiation, the corona will be cooled further (Haardt et al., 1994). Thus, successful models must prevent this feedback loop from cooling the corona too much, otherwise hard X-ray spectra will not be produced.

Illustrations of some geometries are shown in Figure 1.3. A point source located above the accretion disc is the simplest geometry. However, all geometries for the disc and corona translate into a radial disc emissivity. We parametrise the disc emissivity in this thesis as a broken power-law (referred to as the lamppost emissivity) or single power-law, without assuming any particular geometry. The aim is to use the form of the radial emissivity to learn about the geometry of the accretion disc and corona.

1.5 Disc reflection

Standard, radiatively efficient accretion discs are optically thick so all the radiation that is observed from the disc has been reprocessed through the outer few Thompson depths. The discs may be "cold", which means that only hydrogen and helium are fully ionised while other elements are neutral, or the metals may be partially ionised (see Section 1.5.3). In the latter case, radiative recombination continua also contribute to the reflection spectrum. The power-law continuum produced by the corona irradiates the disc, which results in the formation of a reflection component. A hard X-ray photon entering the disc is subject to two possible fates. The first is Compton scattering by the free electrons from the ionised gases or the

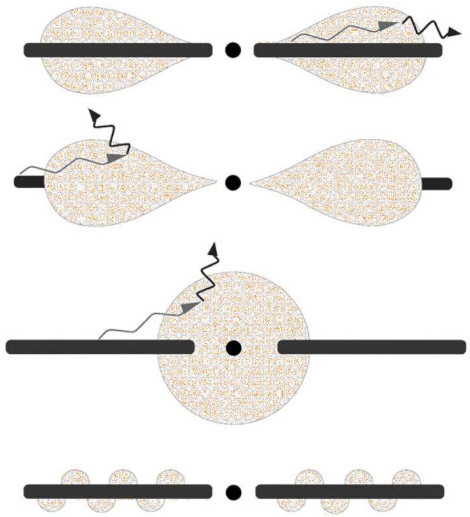

Figure 1.3: Possible geometries for the accretion disc and Comptonising corona. The top configuration is denoted as the "sandwich" geometry but produces spectra that are too soft. The remaining three geometries predict harder spectra as the corona is less effectively cooled by soft disc photons. The middle two geometries are referred to as "sphere + disc" while the bottom is described as a "patchy corona". Figure taken from Reynolds & Nowak (2003).

bound electrons of neutral metals. The second is photoelectric absorption by one of the neutral atoms which can only ensue if the photon is more energetic than the threshold energy for the particular photoelectric transition. Absorption is either followed by fluorescent line emission or Auger de-excitation.

Figure 1.4 shows the expected continuum and reflection spectrum. It is based on a Monte-Carlo simulation that models reflection from an illuminated slab (Reynolds, 1996) using calculations by George & Fabian (1991) and Matt et al. (1991). Photoelectric absorption is dominant over Compton scattering for softer X-rays whereas hard photons are rarely absorbed and are Compton scattered back out of the slab. The spectral curvature above 10 keV is due to Compton recoil reducing the backscattered photon flux. Below 10 keV, the spectrum exhibits many fluorescent Kα emission lines. They are produced when one of the two K-shell (i.e. n = 1) electrons of a metal's atom are ejected following photoelectric absorption. The resulting ion can de-excite with an L-shell (n = 2) electron dropping into the vacancy in the K-shell and the excess energy being radiated as a Kα line photon. Alternatively, another L-shell electron could be ejected to carry away the excess energy which effectively destroys the incident ionising photon. This is Auger de-excitation and the probability that an excited ion undergoes fluorescence instead is given by the fluorescence yield.

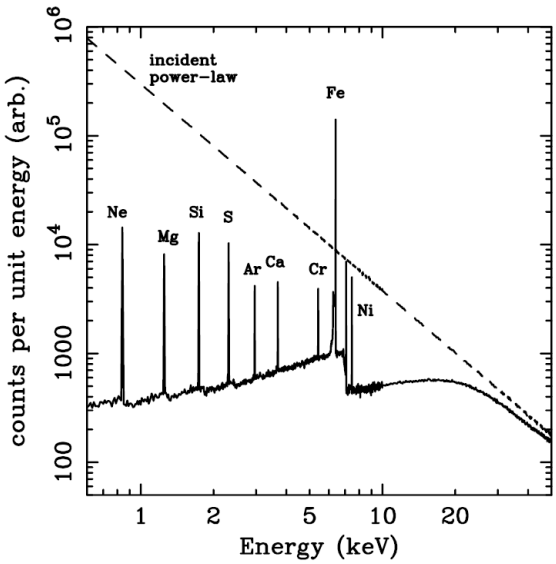

Figure 1.4: A Monte Carlo simulation by Reynolds & Nowak (2003) of X-ray reflection by a cold and semi-infinite slab of gas. The dashed line shows the incident power-law X-ray spectrum and the solid line represents the reflected spectrum. This is made up of fluorescent lines, of which the iron Kα line is the strongest, and the Compton hump that can be seen to peak at 30 keV.

Due to its large cosmic abundance, high fluorescence yield of 0.33 and small opacity, the cold iron Kα line at 6.4 keV is the most prominent. An iron edge at 7.1 keV is present because this is the photoelectric threshold for neutral iron. The line is actually a blend of two separate lines at 6.404 keV and 6.391 keV due to angular momentum splitting the L-shell, though the line is modelled only as a single component. As the reflection component is superposed on the direct powerlaw continuum, the iron line is the easiest fluorescent line to identify in X-ray spectra.

The strength of the iron line is measured by its equivalent width, which is the width of the continuum that contains the same flux as the line. The equivalent width of the iron line in Figure 1.4 is $\sim$ 180 eV. It is primarily a function of elemental abundances, the inclination angle at which the disc is observed, the ionisation state of the disc and the solid angle subtended by the disc as seen at the continuum source. Each of these is discussed below in more detail.

1.5.1 Elemental abundance

The greater the iron abundance, the greater the amount of Kα fluorescence that can occur. However a higher abundance of elements with smaller atomic number will lead to increased competition with iron for K-shell photoelectric absorption. These effects, along with saturation of the edge lead to a roughly logarithmic dependence

of the equivalent width on the iron abundance (Matt et al., 1997).

1.5.2 Inclination angle

The inclination angle (i) is defined as the angle the observer views the accretion disc relative to its normal i.e $i = 0°$ for a face-on disc and $i = 90°$ for an edge-on view. The equivalent width decreases as i increases because iron line photons will have a greater path length to escape and therefore encounter more absorption and scattering (George & Fabian, 1991; Ghisellini et al., 1994).

1.5.3 Ionisation of the disc surface

X-ray irradiation can photoionise the thin skin at the surface and affect the equivalent width of the iron line (Ross & Fabian, 1993; Ross et al., 1999). For ionised iron, there are less outer electrons to screen the inner K-shell electrons from the positive nuclear charge so the photoionisation threshold and line energy increases with ionisation state. The fluorescence yield is a weak function of state from neutral iron (Fe I) up to Fe XXIII. As the Auger effect requires a minimum of 2 L-shell electrons to occur, fluorescence dominates at the highest ionisation states. A useful quantification of the ionisation state of the disc is the ionisation parameter as it measures the rate of photoionisation to the recombination rate:

$$\xi(r) = \frac{4\pi F_{\rm x}(r)}{n(r)}, \tag{1.9}$$

where $F_{\rm x}(r)$ is the X-ray flux received per unit area of the disc and $n(r)$ is the comoving electron number density. Assuming a fixed density structure in the atmosphere of the disc, Matt et al. (1993) and Matt et al. (1996) investigated the dependence of the reflection component on ξ and found four regimes as displayed in Figure 1.5:

(1) $\xi < 100$ erg cm s^{-1}: Iron is weakly ionised so a cold iron line will be produced at 6.4 keV. The Compton-backscattered continuum is weak at 6 keV because the photoelectric opacity is strong below the small iron absorption edge at 7.1 keV.

(2) 100 erg cm s^{-1} $< \xi <$ 500 erg cm s^{-1}: Iron in this intermediate region is in the form of Fe XVII – Fe XXIII where there is a vacancy in the L-shell. This allows the ions to resonantly absorb the corresponding Kα line photons. Successive fluorescence emissions and resonant absorptions effectively trap the photons until they are destroyed by the Auger effect. Thus, the iron line is weak as few

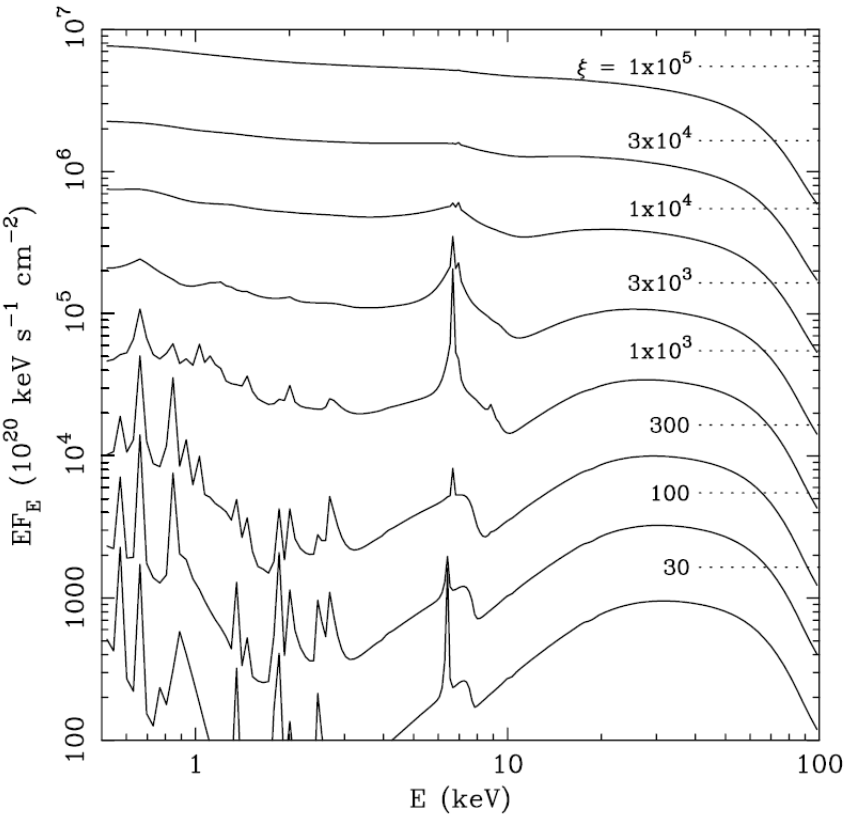

Figure 1.5: Theoretical ionised reflection spectra for different ionisation states of the accretion disc. The strength of ionisation, as determined by ξ, is shown to affect the iron line and edge as well as the shape of the Compton hump. Figure taken from Fabian et al. (2000) using the models of Ballantyne et al. (2001b).

line photons escape the disc but the iron edge is moderately strong because competing photoelectric absorption by oxygen and iron L decreases.

(3) 500 erg cm s^{-1}< ξ < 5000 erg cm s^{-1}: Iron is too highly ionised for the Auger effect to destroy the Kα line photons. Therefore, even though resonant scattering still occurs, more line photons will be able to escape than in (2). A hot iron line is seen at 6.67 (He-like) or 6.97 keV (H-like) and the iron absorption edge is also large. The increased ionisation level reduces the contribution of photoelectron absorption from the ionised low-Z elements while the additional Compton scattering from the increase in free electrons leads to smearing of the line and edge features. Furthermore, the Compton backscattered continuum can be seen at energies below 10 keV.

(4) ξ > 5000 erg cm s^{-1}. Iron is completely ionised so no line or edge is produced.

These calculations are applicable to an accretion disc with a fixed density struc-

ture. More realistic models relax this assumption and make the next simplest, but physical assumption that the disc atmosphere is in hydrostatic equilibrium (Nayakshin et al., 2000). In such a disc, a thermal instability arises that results in a cold, dense disc blanketed by an overlying low-density and highly ionised region. If the irradiation is weak, then the blanket will have no effect on the disc reflection but for strong illumination, the ionised blanket scatters and smears the reflection features. These complexities can make modelling reflection spectra very difficult. One solution is to use constant density models with variable ionisation parameters and reflection fractions to account for dilution by the ionised skin (Ballantyne et al., 2001b).

1.6 The profile of the broad iron line

Even though the iron line is intrinsically narrow, ~ 1 eV, (Pozdniakov et al., 1979), it has been found to be extremely broadened. This is because the line profile is shaped by the effects of Doppler shifts and gravitational redshifting, as demonstrated in Figure 1.6. A double horned line profile is produced at each radius of the disc because there is emission from both parts of the disc that approach (blueshifted) and recede (redshifted) away from the observer. The closer the line-emitting material to the black hole, the faster it orbits and this results in a broader line profile. The blue peak is stronger than the red peak because near the black hole, special relativistic beaming enhances the radiation emitted towards the observer. Finally the line emission is shifted to lower energies by the transverse Doppler effect and gravitational redshifting. The skewed and highly broadened line profile that is observed is formed by summing the line emission from all radii of the disc.

Figure 1.7 (*left*) from Fabian et al. (2000) shows line profiles emitted from an accretion disc around a non-rotating black hole viewed at disc inclinations of 10°, 30° and 60°. The outer radius is $30r_{\rm g}$ and the inner radius is set to $6r_{\rm g}$, the minimum for a Schwarzchild black hole. The inclination is the most single important factor that affects the blueward extent of the line. The redward extent is most sensitive to the inner radius of the disc. A disc extending to below $6r_{\rm g}$ can only do so if the black hole is spinning, which means the breadth of the red wing is associated with the black hole spin. Figure 1.7 (*right*) shows that an iron line from a disc with an inner radius of $1.24r_{\rm g}$ is more smeared than one from a disc with an inner radius of $6r_{\rm g}$.

The local emissivity of the disc is often parametrised as a power-law of the form r^{-q} where q is the emissivity index. The line profiles for different emissivity indices

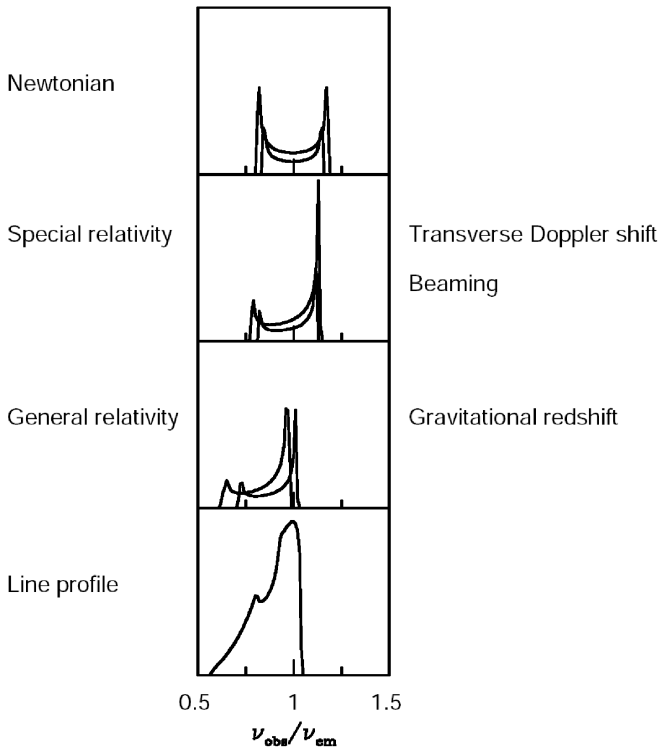

Figure 1.6: The profile of the broad and skewed iron line emanates from the interplay of Doppler and transverse Doppler shifts, relativistic beaming and gravitational redshifting. The first panel shows symmetric double-peaked profiles from two narrow annuli. The second panel displays an enhanced blue peak due to transverse Doppler shifting and relativistic beaming. The third panel shows how the lines move to lower energies because of gravitational redshifting. The sum of emission across the disc leads to the line profile in the fourth panel. Figure taken from Fabian et al. (2000).

are shown in Figure 1.8, also taken from Fabian et al. (2000). For large q, most of the iron line photons are emitted in the inner regions of the disc. This strongly broadens out the line and makes it difficult to ascertain the red and blue peaks. For $q < 2$, more of the emission arises in the outer regions, where relativistic broadening is less strong, and so it becomes more difficult to identify the red wing.

1.7 Alternatives to relativistic blurring

There have been some claims that the broadening of the iron line is not due to the gravitational effects of the black hole. The main argument involves warm absorber disc winds. Both the *Chandra* and *XMM-Newton* observatories have revealed spectra of Seyfert 1s rich in absorption lines and edges that are likely to be a result of absorption local to the AGN. If these warm absorbers can sufficiently change the

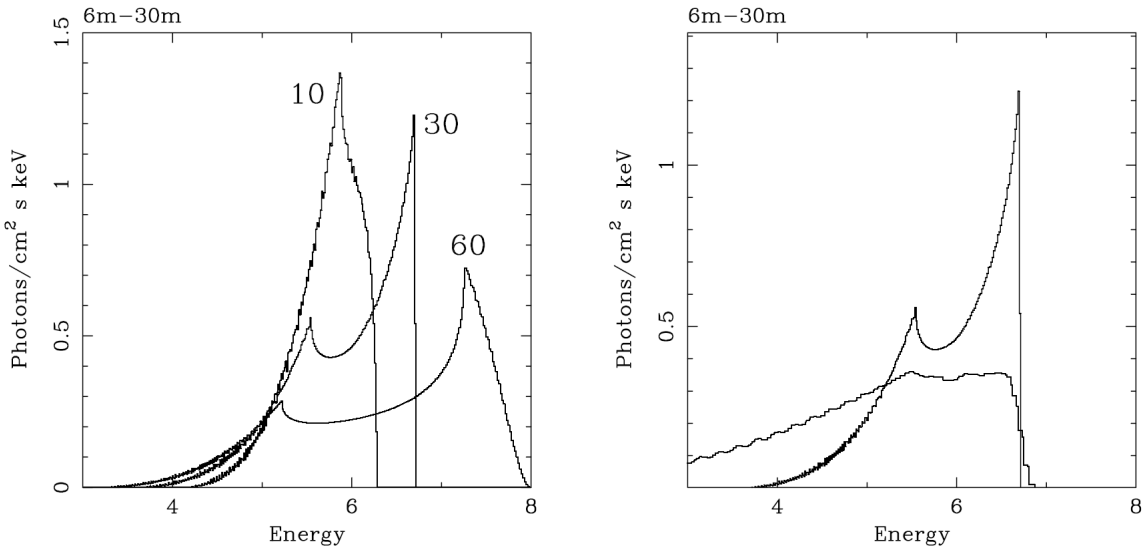

Figure 1.7: *Left*: Relativistic iron line profiles are shown for a non-rotating black hole where the inner radius extends down to $r_{\rm ms} = 6r_{\rm g}$. The effect of increasing the inclination is to broaden the line by increasing its high-energy extent. *Right*: A relativistic iron line from a disc around a maximally rotating black hole (shallower line) is compared to that from a disc surrounding a non-rotating black hole (double-peaked line). With the rotating case, the disc extends down to $1.24r_{\rm g}$, which results in a broader red wing that is shifted to lower energies by larger gravitational redshifts. Figure taken from Fabian et al. (2000).

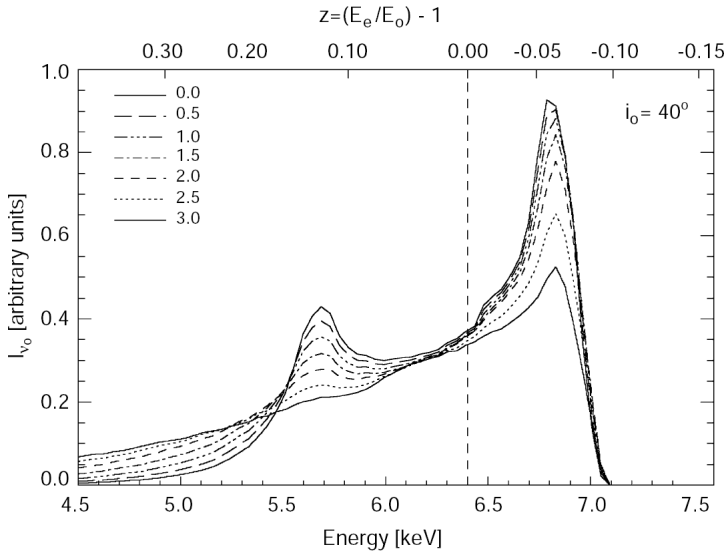

Figure 1.8: Relativistic iron line profiles as a function of emissivity index q (labelled in the panel). The assumptions are that the black hole is spinning with $a = 0.5$ and the disc extends down to $r_{\rm ms}$. As q increases, the disc emission becomes more centrally concentrated so the iron line broadens. Figure taken from Reynolds & Nowak (2003).

curvature of the 2 – 10 keV spectrum, it is possible that continuum curvature could mimic the broad red wing (Reeves et al., 2004; Turner et al., 2005). This is discussed further in the next section.

Other models include broadening of the line with Comptonisation (Misra & Kembhavi, 1998; Misra & Sutaria, 1999). This involves Compton downscattering narrow iron line photons in a surrounding cold ($kT < 0.5$ keV) cloud with a large optical depth of $\tau \sim 5$. However, there are several arguments ruling Comptonisation out, the foremost being that as the continuum must pass through the Comptonising gas, a break should be observed in the continuum spectrum at $511/\tau^2$ keV ($\sim$20 keV, see Figure 1 of Misra & Kembhavi, 1998). This has not been found to be the case (Guainazzi et al., 1999) and there has also been a lack of good fits by Comptonisation models (e.g. Ruszkowski et al., 2000). Another suggestion is that the red wing might be scattered and broadened in relativistic and optically-thick outflows (Titarchuk et al., 2003; Laming & Titarchuk, 2004; Laurent & Titarchuk, 2007). However, many observations show X-ray flux variability on time-scales corresponding to r_{ms}, which is unexpected if there is screening by an optically-thick outflow. Furthermore, the outflows require super-Eddington accretion rates to achieve substantial broadening (Miller et al., 2004).

1.8 Observations of the broad iron line

The archetypical object for broad iron line studies is the Seyfert 1, MCG-6-30-15 ($z = 0.008$). This was the first AGN where X-ray reflection from fairly neutral material was clearly detected by Nandra et al. (1989). They showed that the spectrum of a 2 day observation with the European satellite *EXOSAT* was more complex than the previously accepted power-law description. The detection of emission and absorption features from cold iron led them to suggest that an accretion disc could be responsible. Further evidence came from the composite spectrum of 12 Seyferts observed by the Japanese Satellite *GINGA*, which displayed a redshifted excess above the power-law and indications of an iron K edge (Pounds et al., 1990).

However, it was not until 1995 with the capabilities of the Advanced Satellite for Cosmology and Astrophysics (*ASCA*), that the first robust detection of a broad and skewed iron line was made in a long observation of MCG-6-30-15 (Tanaka et al., 1995). This is shown in Figure 1.9. The CCD detectors granted a spectral resolving power of $E/\Delta E = 50$ that was large enough to allow X-ray line widths to be resolved for the first time. The extremely broad iron line profile corresponded well with the profile expected from the surface of a relativistic accretion disc. Using a model of an

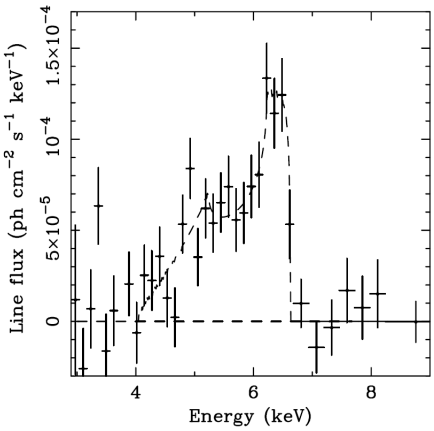

Figure 1.9: The first robust detection of a broadened iron line profile in the *ASCA* observation of MCG-6-30-15 (Tanaka et al., 1995). The line is skewed and peaks at 6.35 keV. The dashed line is the iron line model of Fabian et al. (1989) that assumes a non-rotating black hole, a disc inclination of 30° and an emissivity index of $q = 3$.

accretion disc around a non-rotating black hole, the inclination and inner radius were constrained to be 27° and $7r_{\rm g}$ respectively. The line was best-fit with an emissivity index of $q = 3$ and the line emission was found to peak within $20r_{\rm g}$.

Studying samples can be extremely informative, as shown by Nandra et al. (1997a, hereafter N97) who presented *ASCA* iron Kα data for 18 Seyfert 1 galaxies. Statistical evidence for broadening was found in 75% of the observations in the sample. Low inclinations were strongly preferred with a mean of 30°. This is expected as the higher inclined sources would be obscured and seen as Seyfert 2s. The mean emissivity index, $q = 2.5$, was consistent with that expected from a centrally illuminated disc where emission is strongly concentrated in the inner regions of the AGN. However, this slope of the emissivity power-law was not found to be universal throughout the sample. The average iron line of the sample peaked at 6.4 keV, suggesting a low state of ionisation. This is possible despite the strong central illumination as accretion discs are expected to be very dense.

No strong requirement for line emission from regions other than the disc was found by N97, but it was allowed by the data. Turner et al. (1998) studied a sample of Seyfert 2s where a significant contribution of a narrow line component in the iron line region was found. This is likely to arise from matter far away from the central black hole e.g. the molecular torus (Weaver & Reynolds, 1998). Further support came from observations of NGC 2992 (Weaver et al., 1996) and NGC 4051 (Guainazzi et al., 1998), which showed that the primary continuum source had faded away to leave only the narrow component that had not yet responded to the

vanishing continuum. The lack of variable, narrow iron line emission also agrees with a contribution from distant matter (Bhayani & Nandra, 2010, – Chapter 3).

Not all bright Seyfert 1s observed by *ASCA* were found to have a broadened iron line. One example was IC 4329A, which possessed a relatively narrow iron line (Done et al., 2000). It was modelled well with a disc that extended down to $\sim 50r_{\rm g}$. This could be because the disc within this radius is missing and so no blurred reflection is possible. Alternatively, Done et al. (2000) suggested that the inner disc may be present down to $r_{\rm ms}$ but is too highly ionised to form a broadened iron line.

Further observations of MCG-6-30-15 by Iwasawa et al. (1996) and Iwasawa et al. (1999) proved valuable in displaying significant and complex variations of the iron line in both profile and intensity. During the long 1994 observation, the iron line was quite narrow and possessed an unusually strong blue peak. This occurred during a bright flare when the emission might have been dominated by fairly large radii in the disc. Another flare occurred in 1997 and this led to the entire iron line extending below 6 keV, suggesting that the primary contribution came from radii $< 6r_{\rm g}$. During another part of the 1994 observation where the continuum flux fell below its average value by a factor of 2 – 3, the iron line appeared to become much broader and stronger. This implied that the black hole in MCG-6-30-15 is spinning. Dabrowski et al. (1997) placed a formal limit on the spin parameter of the black hole as $a > 0.94$. Reynolds & Begelman (1997) tried to account for this "deep minimum" observation with a Schwarzchild black hole by arguing that reflection within the plunging region can produce a large redshifted line. This disagrees with the standard model, which does not allow for angular momentum transport and dissipation of energy within the plunging region. Furthermore, the plunging zone is also likely to be highly ionised. This discussion over the origin of the reflection in MCG-6-30-15 was one of the key questions to be addressed by the next X-ray observatory, *XMM-Newton*.

1.8.1 *XMM-Newton*

The X-ray Multi-Mirror Mission (*XMM-Newton*) was launched by the European Space Agency (ESA) in 1999 and is still operating at the time of writing, playing an important role in X-ray astronomy. It consists of three grazing incidence X-ray telescopes with CCD detectors but its most important feature for iron line studies is the large collecting area both above and below the Fe K band. This is essential for disentangling the continuum from the iron line. A further advancement over previous missions is that the full reflection spectrum can be modelled instead of just

the iron line.

Wilms et al. (2001) conducted the first *XMM-Newton* observation of MCG-6-30-15, which also happened to be during a deep minimum state. In agreement with the *ASCA* observation, the line was found to be very broad and extremely skewed, with the red wing extending down to 3 keV. The line was fit well with a maximally spinning black hole, an accretion disc extending down to $r = 1.24r_{\rm g}$ and a very steep emissivity index, $4.5 < q < 6.0$. If the hard X-ray source is an isotropic emitter, the emissivity profile is consistent with magnetic energy being extracted from the black hole. Physically, it is more likely that MCG-6-30-15 is spinning rather than reflecting the continuum from within $r_{\rm ms}$, as this requires an implausibly large emissivity index, $q > 10$ (Brenneman & Reynolds, 2006).

These observations have shown that the broad iron line in MCG-6-30-15 requires a steep emissivity profile. Under the zero-torque boundary condition, the standard model predicts that the emissivity profile can only steepen as much as $\propto r^{-3}$. A larger emissivity index is possible if magnetically induced torques are involved (Page & Thorne, 1974). Agol & Krolik (2000), Krolik (1999) and Gammie (1999) have shown that magnetic fields may be effective at transporting angular momentum from material in the plunging region to the main body of the accretion disc and this will be accompanied by the liberation of the binding energy as local dissipation/radiation. As well as connecting the accretion disc and plunging region, Li (2002) has shown that the torque can link the disc to the spinning black hole. Figure 1.10 shows that the torque-induced disc emissivity profiles become more centrally concentrated as the spin parameter increases.

1.9 *XMM-Newton* survey of Seyfert galaxies

Nandra et al. (2007, hereafter N07) followed up the N97 analysis of the *ASCA* sample of Seyfert 1s with a systematic analysis of the iron line region in a large sample observed by *XMM-Newton*. The aim was to determine how common line broadening was and if it can be robustly and uniquely accounted for by a relativistic accretion disc. To accomplish this, spectral models were applied conservatively and systematically so as not to bias the detection of relativistic iron lines.

A key result was that contrary to the N97 survey, a narrow core representing reflection from distant matter was found to be ubiquitous. This was assumed to be associated with distant, optically thick material such as the molecular torus. Two thirds of the sample portrayed evidence for further, broadened emission in the iron K band with the inferred energy close to 6.4 keV. This implies that typically,

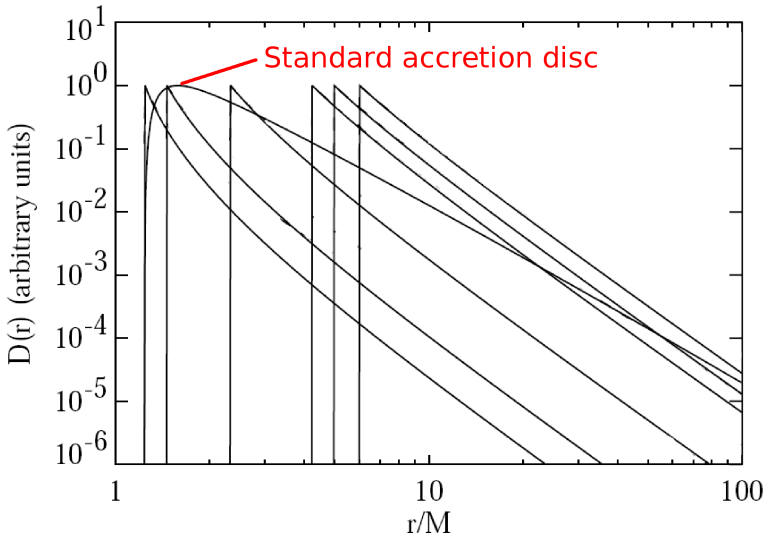

Figure 1.10: Model emissivity profiles, $D(r)$, for torqued accretion discs made by Reynolds & Nowak (2003). The labelled line is the emissivity profile for a standard accretion disc around a maximally spinning black hole. The thin lines show from left to right the torque-induced (at $r_{\rm ms}(a)$) profiles for spins parameters of $a = 0.998$, 0.99, 0.9, 0.5, 0.3 and 0. The torque-induced dissipation is expected to become more centrally concentrated as the spin parameter increases.

the accretion disc is cold in the sample. A model testing whether the broad lines could be explained by a blend of narrow, unshifted emission lines and zones of highly ionised gas in the line of sight was not as favourable as a relativistic disc line model. It is important to test whether complex absorption can mimic the red wings as this would explain broadened iron lines without recourse to relativistic effects. An extreme example of where complex low-energy absorption mimicking has been proposed is NGC 3783. A deep *XMM-Newton* spectrum was found to possess a strong absorption line that could be explained by a highly ionised warm absorber. Reeves et al. (2004) argued that this could introduce subtle spectral curvature below 6.4 keV that results in an apparently weak red wing. This agrees with an analysis of a long exposure by Yaqoob et al. (2005) who also found strong evidence for a small red extent to the iron line. N07 showed that the inclusion of a blurred reflection component to the warm absorbers greatly increased the quality of the fit compared to the pure absorption fit. Similarly, the reflection component was also found to be necessary in a second observation of NGC 3783, which suggests that a relativistic disc line is still strongly required even when there is strong absorption.

N07 assumed a power-law emissivity that breaks from $q_1 = 0$ to $q_2 = 3$ at the break radius, $r_{\rm br}$. This characteristic radius represents where the peak of the disc line flux occurs. The mean disc inclination of 40° was similar to that found

in N97. The mean break radius of $r_{\rm br} = 15r_{\rm g}$ illustrates that much of the emission is subject to gravitational redshifting and Doppler effects. However, the broad reflection was found to be only half as strong as expected from a flat disc illuminated by a point source. Only three observations showed evidence for a spinning black hole, though the difference between the Schwarzchild and Kerr models was generally small. Assessment of the spin is prohibited by the difficulty in deblending the red wing extension from the continuum. Furthermore, Miller (2007) argued that the prescription of a broken emissivity power-law makes it difficult to constrain the inner radius and black hole spin.

The break radius was used to define three classes of broad iron lines in the sample. The first group consists of 45% of the sample that have $r_{\rm br} < 50r_{\rm g}$. These observations are defined to possess a relativistically broadened iron line, which is expected by the standard model. The second group also possess a broad iron line but it is not as blurred as in the first group. The break radius is larger, $r_{\rm br} > 50r_{\rm g}$, for the 25% of the sample in this group. The last class includes the remaining 30% of the sample that show no evidence for blurred reflection at all. Nonetheless, it is difficult to exclude an accretion disc contribution in the narrow line objects as the disc may be highly inclined, which leads to weaker reflection. However, high inclination objects with $i > 60°$, should be seen as Seyfert 2s and these were excluded from the sample. N07 found that for a disc reflection strength of $R_{\rm disc}$= 1, expected for a flat accretion disc subtending a solid angle of 2π below a central point source, no observation in this group was consistent with $i < 60°$ at 99% confidence. On the other hand, if the average reflection strength is $R_{\rm disc}$= 0.5, then no observation can be excluded from having $i < 60°$. Therefore, either the reflection is much weaker than expected by the standard model or there are clearly objects where the disc line appears to be missing.

1.9.1 Weak or non-existent broad emission

It is puzzling why all Seyfert 1s do not show broad iron lines. All that is required is a large amount of mass flowing into the SMBH and a spatially compact X-ray source located close to the SMBH. That AGN have high luminosities and display rapid X-ray variability shows that these conditions are easily satisfied. However, there are several reasons why the iron line may be absent or not as strong or broad as the standard model predicts. These are discussed below.

1.9.1.1 Geometrical effects

Reflection is maximised in the scenario where the X-ray source is above the disc as the disc sees all of the X-ray emission and in turn, the observer sees all of the accretion disc. Other geometries such as a central spherical source surrounded by a cool disc (Zdziarski et al., 1999) can lead to weaker reflection as a smaller solid angle is subtended by the disc. A similar scenario is possible if the X-ray source is embedded by cloudlets that can self-cover (Nandra & Pounds, 1994).

1.9.1.2 Abundance effects

$R_{\rm disc}$ can be underestimated if the iron abundance is less than solar. Even with solar abundances, there should be significant Compton reflection at high energies and the manifestation of this could be concave spectra, as seen in the N07 sample.

1.9.1.3 Extreme relativistic blurring

If the emission is strongly concentrated in the inner regions, the blurring of the line could be extreme enough to make it indistinguishable from the continuum. The line is also extremely broad if the disc is viewed edge-on. Reflection should still be seen in good quality high-energy data while the iron line and edge will appear stronger and broader compared to the low-abundance scenario.

1.9.1.4 Anisotropy

Anisotropical effects such as the bulk motion of the X-ray emitting plasma away from the disc can culminate in beaming of the continuum, (Beloborodov, 1999). In this case, the observed power-law emission is overestimated by models that assume only isotropic X-ray emission and as a result, the disc reflection appears weaker than it is. There may also be anisotropy due to gravitational effects in the central regions such as light bending (Miniutti & Fabian, 2004).

1.9.1.5 Ionisation

The accretion disc should be sufficiently dense that the surface is not highly ionised and can be regarded as cold under illumination from the X-ray source. However, if the irradiation is sufficiently intense that an ionised skin forms on the surface, it is possible for the line be scattered and smeared out. This can occur only if the X-ray emission originates very close to the surface of the disc such as in magnetic flare

models. Both disc ionisation and extreme relativistic blurring effects are investigated in Chapter 3.

1.10 Variability

A unique property of AGN is their variability in all regions of the electromagnetic spectrum. The fastest X-ray variability should arise close to the black hole. Since this is where relativistic disc lines are predicted to form under illumination by the corona, the lines should also be variable. The simplest prediction is that variations in the hard X-ray continuum should be followed by similar variations in the reflection spectrum with the degree of variability being similar in both components. This prediction has been tested in several Seyfert 1s with different methods that have shown the continuum-line variability to be far more complicated.

Vaughan et al. (2004) found a correlation between the 1 – 2 keV and 3 – 10 keV fluxes in an *XMM-Newton* observation of MCG-6-30-15 when it was in a normal state. Perhaps more significantly, they also discovered a constant offset in the higher energy band, as shown in Figure 1.11 (*left*). To identify the variable and constant components, they split the observation into segments and subtracted the lowest flux spectrum from the rest. These difference spectra (Fabian & Vaughan, 2003) exhibited only a power-law with no evidence for an iron line as it is cancelled out. One of the difference spectra is shown in Figure 1.11 (*right*). This showed that the iron line was constant during the observation while the spectral variability was due only to the power-law. This is referred to as the two-component model (McHardy et al., 1999; Shih et al., 2002) as the variability arises only from changes in the normalisation of the power-law while the reflection component remains relatively constant. A correlation, known as spectral softening, between the 2 – 10 keV power-law slope and flux was also found in MCG-6-30-15 using flux-resolved spectra. This complies with the two-component model as the contribution of the constant component relative to the variable component increases when the total flux decreases. Therefore at low fluxes, the spectrum becomes harder above 2 keV and a more prominent iron line is present in the energy spectrum.

Reynolds et al. (2004) analysed the deep-minimum observation of MCG-6-30-15 and found that in this case, the iron line did vary with the power-law continuum. Nearly all of the difference spectra in this observation displayed a broad iron line of the same equivalent width. This means that the response of the iron line to the continuum variations is of the same magnitude, in agreement with the standard model. At higher luminosities, there then appears to be a decoupling of the power-

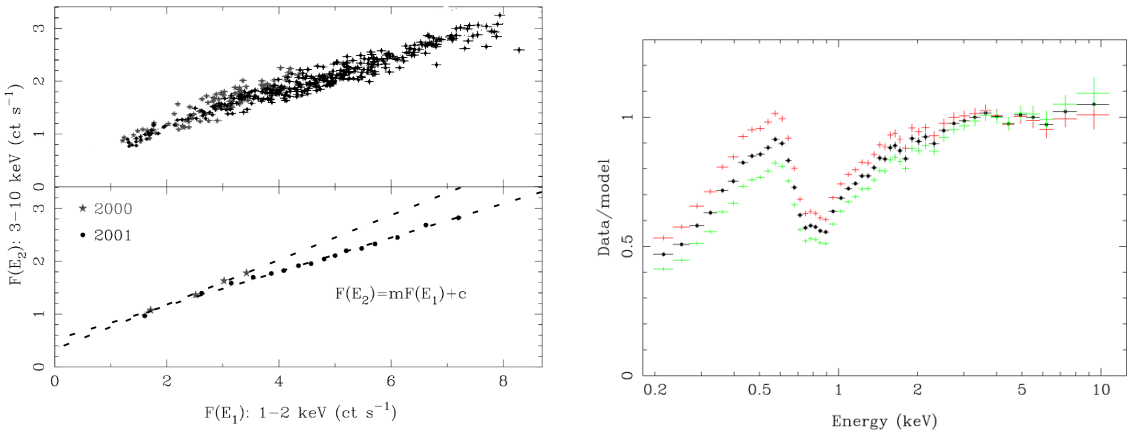

Figure 1.11: *Left*: The top panel shows a tight correlation between the fluxes in the 1 – 2 and 3 – 10 keV bands of an *XMM-Newton* observation of MCG-6-30-15 using 1 ks bins. For clarity, the bottom panel averages the data in the top panel with bins of 20 points. The correlation is due to variations in the normalisation of the power-law continuum. An offset is visible in the 3 – 10 keV band, which insinuates the presence of a constant spectral component between 3 – 10 keV. *Right*: Examples of difference spectra of MCG-6-30-15 are shown as a ratio to a power-law model. No iron line is seen, which implies that it does not respond to variations in the continuum. Both figures taken from Vaughan et al. (2004).

law continuum and iron line as described above. This is in agreement with *Suzaku* observations that reveal the entire reflection spectrum up to 45 keV to be less variable than the continuum (Miniutti et al., 2007). Complex and variable absorption models were ruled out for MCG-6-30-15 because 47 of the 51 soft X-ray absorption lines seen with *XMM-Newton* are invariant with respect to the varying brightness (Turner et al., 2004a) and there was no evidence of progressive partial covering in the flux-selected spectra.

1.10.1 Light bending

The extremely broad red wing of MCG-6-30-15 implies that there is significant emission from the innermost parts of the accretion disc, $\sim 2r_g$. For there to be a decoupling between the reflection and the power-law continuum, the intrinsic X-ray emission must be anisotropic. Gravitational light bending can explain the anisotropy as the gravitational field of the black hole bends continuum photons away from the observer and towards the disc. It is not accounted for by the standard disc model but is likely to be important in spinning black holes with discs that extend close to the black hole. The model (Miniutti & Fabian, 2004) assumes a centrally-concentrated corona that can change its height above a black hole. The light bending is strongest at a low coronal height as the reflection component is enhanced relative to the

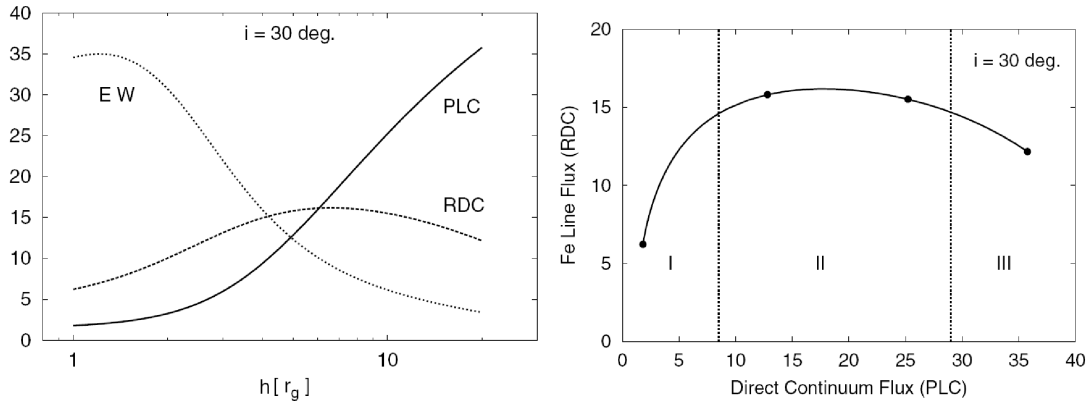

Figure 1.12: *Left*: The iron line equivalent width (EW), reflected component flux (RDC) and power-law continuum flux (PLC) are plotted as a function of source height, h, in the gravitational light bending model. At low heights, the continuum photons are bent onto the disc and the reflection component is enhanced. As the height of the corona increases, less photons are bent onto the disc and the power-law continuum strengthens over the reflection component. *Right*: A plot of the reflected component flux against the continuum flux reveals three regimes. The first two are the most interesting as regime 1 predicts a correlation between the fluxes while a decoupling is suggested for regime 2. The dots represent source heights of 1, 5, 10, 20$r_{\rm g}$ from left to right. Both figures are taken from Miniutti & Fabian (2004)

reduced power-law component. As the height of the corona above the disc increases, less continuum photons are deflected onto the disc and so more of them reach the observer directly. Miniutti & Fabian (2004) investigated the effects of gravitational light bending in a toy model and found that changes in the the coronal height, h, lead to three different regimes:

(1) $1r_{\rm g} < h < 4r_{\rm g}$: The observed continuum flux is very low as the primary radiation from the source undergoes very strong light bending. This causes the total spectrum to be reflection dominated at the lowest source heights, though the continuum recovers as h increases. A broad and redshifted iron line is produced because the irradiation is concentrated in the inner regions and so has a steep emissivity profile. Regarding the variability, the iron line and continuum fluxes are positively correlated.

(2) $4r_{\rm g} < h < 10r_{\rm g}$: The direct continuum varies by a factor of ~ 4 while the reflection component changes by less than 10%. Therefore the line can be considered to be non-variable in this regime. This results in an anti-correlation between the equivalent width and continuum flux. The reflection component flux reaches a maximum in this regime.

(3) $10r_g < h < 20r_g$: Light bending is less effective but still present. The iron line flux is anticorrelated with the continuum flux as less continuum photons are bent away from the observer. Illumination of the accretion disc becomes more isotropic so iron line photons arise further from the black hole. Thus, a narrower iron line is produced in this regime. For $h >> 30r_g$, light bending no longer affects the emission.

The left panel of Figure 1.12 shows the behaviour of the continuum and reflected fluxes as a function of coronal height and the right panel displays the three regimes discussed above. The decoupling of the iron line and continuum variability in the deep minimum observation of MCG-6-30-15 can be explained by the scenario in regime 2. Furthermore, if the height of the corona is reduced into regime 1, the iron line is expected to be as variable as the continuum, which matches with the Reynolds et al. (2004) observation.

The assumption of a corona on the central axis is perhaps too simplistic and better data are needed to constrain the model. Furthermore, the intrinsic coronal luminosity is assumed to be constant, which most likely is not the case (Zoghbi et al., 2010). Nonetheless, in cases where much of the X-ray luminosity originates from within a few r_g of the black hole, light bending will be important. Other AGN where light bending is thought to be involved include NGC 4051 (Ponti et al., 2006; Reeves et al., 2006), 1H 0707-495 (Fabian et al., 2004; Zoghbi et al., 2010) and MCG-5-23-16 (Reeves et al., 2007).

1.10.2 Narrow line variability

As well as a broad iron Kα line, narrow redshifted iron lines have also been found e.g. in NGC 3516 (Turner et al., 2002) and Mrk 766 (Turner et al., 2004a). The lines could arise from a flare illuminating a specific part of the disc or they could indicate that certain radii close to the black hole are illuminated preferentially. Support for the flare model was given by Iwasawa et al. (2004) who found that the narrow line component in an *XMM-Newton* observation of NGC 3516 moved between 5.7 and 6.5 keV in four 25 ks cycles. This is consistent with the illumination of a spot on the disc by a co-rotating flare between $7 - 16r_g$ that produces an iron line modulated by Doppler shifts and gravitational redshifting. The line variability was used to estimate a black hole mass of $1 - 5 \times 10^7$ $M_\odot$, which agrees with reverberation mapping results (Onken et al., 2003). Numerous other narrow lines have been reported, though Vaughan & Uttley (2008) suggested that there is a correlation between the estimated line strength and its uncertainty. Such an effect would be

expected from false detections. Future X-ray missions (e.g. the Advanced Telescope for High Energy Astrophysics (*ATHENA*) and General Relativistic Astrophysics Via Timing and Spectroscopy (*GRAVITAS*)) with superior collecting areas and energy resolution will be more suited to detecting the narrow lines.

1.11 Soft excess

Two distinct components dominate the the optical to X-ray spectra of AGN. They are the big bump in the optical/UV bands, which is associated with thermal emission from the optically thick accretion disc, and the power-law X-ray tail seen to hundreds of keVs. The standard model predicts that the maximum temperature of the disc is 20 eV for a 10^8 $M_\odot$ black hole accreting at its Eddington luminosity. However in type 1 AGN, an extrapolation of the power-law yields a strong broad soft excess below 2 keV (Arnaud et al., 1985). The first attempts at modelling the soft excess focused on thermal emission from the disc, but the model blackbody temperatures were deemed too high (Bechtold et al., 1987) considering the black hole masses and accretion rates. Furthermore the shape of the soft excess is smoother than the sharp peak typical of a disc spectrum (Czerny et al., 2003; Gierliński & Done, 2004).

Another possible continuum origin of the soft excess is Comptonisation of the disc emission by low-temperature electrons (Czerny & Elvis, 1987; Kawaguchi, 2003), perhaps produced by a hot skin forming over the cooler disc (Czerny et al., 2003). The problem with Comptonisation is that the temperature of the skin is remarkably constant at 0.1 – 0.2 keV across AGN that are four magnitudes in mass apart (Czerny et al., 2003; Gierliński & Done, 2004; Crummy et al., 2006). Dewangan et al. (2007) investigated a two-component corona with different Comptonising regions for the power-law and soft excess but found that the soft corona still suffered from a near-constant temperature while the disc temperature varies by a factor of 10 (Gierliński & Done, 2004). Alternatively, Coppi (1999) suggested that a single plasma with a hybrid thermal/non-thermal electron distribution may give rise to both the soft excess and power-law.

The universal shape of the soft excess and its constant temperature intimates an origin in atomic processes. In particular, there is a strong jump in opacity associated with the lines and edges of ionised O VII, O VIII and iron between 0.7 – 2 keV. Gierliński & Done (2004) suggested that the soft excess could arise artificially if there is relativistically smeared absorption between 0.7 – 3 keV. A successful model requires the absorbing gas to be partially ionised and smeared in a high velocity wind as no characteristic absorption features are detected. An example of the soft

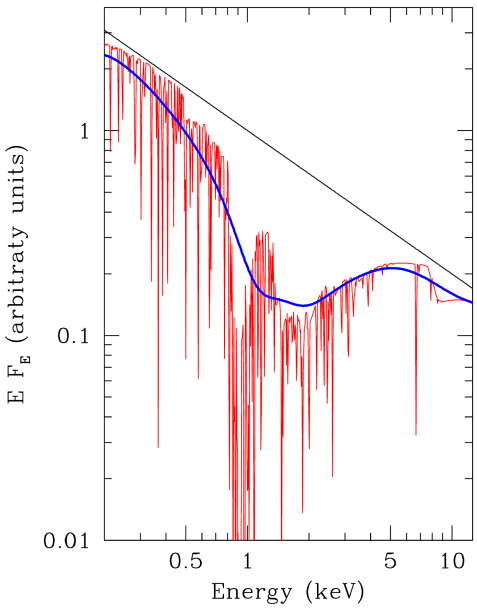

Figure 1.13: An illustration of an artificial soft excess due to ionised absorption. The black line is the underlying power-law with $\Gamma = 2.7$. The red line shows the multiple absorption features predicted by a model that fits the quasar PG 1211+143 with $N_{\rm H} = 33 \times 10^{22}$ cm^{-2} and $\xi = 460$ erg cm s^{-1}. The blue line shows the absorption convolved with a Gaussian of $\sigma/E = 0.28$ to represent the smearing. Figure taken from Gierliński & Done (2004).

excess forming via ionised absorption is shown in Figure 1.13. It has proved difficult to model a realistic accretion disc wind as the velocity dispersions demanded are extreme ($> 0.8c$, Schurch & Done, 2007; Schurch et al., 2009).

As well as absorption, the soft excess could be associated with partially ionised reflection (Ballantyne et al., 2001b; Crummy et al., 2006). As the probability of reflection depends on the balance between electron scattering and photoelectric absorption, the decrease in opacity below 0.7 keV increases the reflection fraction if the disc is ionised. The intrinsic emission lines could be O VII/VIII Lyman-α between 0.6 – 0.7 keV as well as Lyman-α from C, N and Fe L transitions. Similarly to the absorption model, there must be a strong smearing of the emission lines to produce the smooth soft excess. This can naturally be accounted for by the gravitational effects of the black hole if the lines arise in the inner disc regions. Sobolewska & Done (2007) found that quasi-isotropic emission from the disc limits the size of the soft excess to less than a factor of 3 above the power-law continuum. Soft excesses much larger than this are seen so there must be a strong suppression of the intrinsic continuum such as expected in gravitational light bending.

Suzaku observations have attempted to discriminate between the reflection and absorption models for the soft excess. Ponti et al. (2010) found that the strong soft

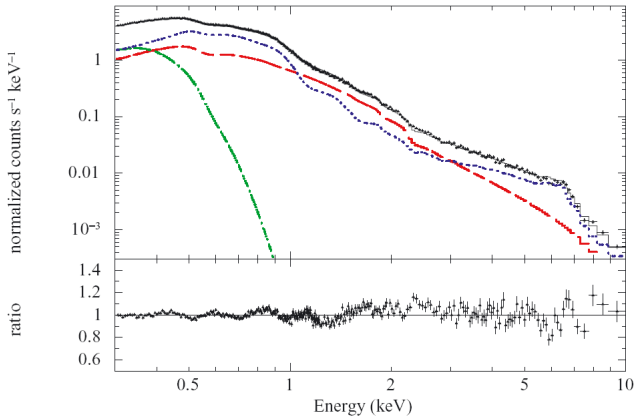

Figure 1.14: The reflection model applied to the *XMM-Newton* broadband spectrum of 1H0707-495 (black). The power-law continuum is shown in red while the disc reflection is displayed in blue. The model provides a good fit to both the soft excess and iron line although a low temperature blackbody (green) is also required to fit a small excess below 0.5 keV. This differs from the higher temperature blackbodies previously used to fit the soft excess and is consistent with emission from the disc. Figure taken from Zoghbi et al. (2010).

excess in IRAS13224-3809 is fit well with ionised reflection while the absorption models are insufficient unless there is an inclusion of soft blackbody components. This is similar to 1H0707-495 (Fabian et al., 2009) where a time lag is detected between the direct continuum and the soft band that can be accounted for by reverberation from reflecting material between $2 - 5r_{\rm g}$ from the black hole. An application of the blurred reflection model to the broadband spectrum of 1H 0707-495 (Zoghbi et al., 2010) is shown in Figure 1.14. Interestingly, Larsson et al. (2008) found that the reflection spectrum of Mrk 335 needs two reflectors; an inner, heavily blurred, ionised reflector for the soft excess and an outer, almost neutral reflector for the moderately weak iron line. The existence of two reflectors could be due to two X-ray sources at different heights or beaming of the continuum from a source very close to the black hole. The absorption model was ruled out as it underpredicted the $14 - 40$ keV flux.

1.12 Aims

The aim of this thesis is to use the time-averaged energy spectra and X-ray light curves of local Seyferts to gain further knowledge of the environment around the central black hole and the X-ray emission mechanisms in AGN. Details of the *XMM-Newton* data reduction are given in Chapter 2. This is followed by an analysis in Chapter 3 of the iron line region in observations where a relativistically broadened

iron line has not been detected previously in the energy spectra. Such behaviour is puzzling as one of the results of matter accreting onto a central, supermassive black hole should be the production of an iron line that is relativistically broadened by the strong Doppler effects and gravitational field around the black hole. The possibility that the line only appears to be missing because the accretion disc is ionised or there are strong relativistic effects that blur the iron line into the continuum are tested.

The analysis of the iron line with a time-averaged energy spectrum can be complemented by studying variance-spectra. For example, an iron line produced close to the black hole is expected to respond to changes in the X-ray continuum that illuminates the disc. However, as discussed with MCG-6-30-15 in Section 1.10, cases have been found where the iron line is constant and does not respond to the continuum. Comparing the time-averaged spectrum directly with the variance-spectrum provides a simple way of testing if parts or all of the iron line are variable or constant. Using variance-spectra to investigate the iron line is also useful because in certain circumstances, it can distinguish between the accretion disc model that naturally broadens the red wing of the iron line via gravitational effects and the warm absorption model, which can artificially broaden the red wing. Furthermore, the variance-spectra of multiple observations of the same object can indicate if the iron line variability behaviour changes with time and this can be compared to changes in the corresponding energy spectra.

The study of the spectral variability across the iron line region can be extended to the broadband X-ray energy range between 0.3 – 10 keV. This encompasses the soft excess, warm absorption, the power-law continuum, the iron line and the associated reflection continuum. In particular, further information can be gained concerning the X-ray emission mechanisms, such as the origin of the soft excess. Many of the variance-spectra shown in other works exhibit a humped peak between 1 – 2 keV that is thought to be due to the increased atomic opacity of iron and oxygen around this energy range. By calculating broadband variance-spectra over the same time-scales, the shapes of the variance-spectra can be analysed to determine if the humped feature is common to most objects or if there is more diversity to the profile. The smeared wind absorption and relativistically blurred disc reflection models both give a good fit to the broadband energy spectrum and they can be tested to see if they can also explain the variance-spectra that are observed in the sample.

Chapter 2

XMM-Newton

2.1 Overview

The High Throughput X-ray Spectroscopy Multi-Mirror Mission was initially proposed in 1984 with development work beginning in 1996. The project involved a collaboration spanning 35 European countries to make it the largest science satellite ever built in Europe. Figure 2.1 shows the mission launch in French Guiana on 10th of December, 1999. The observatory was kept in safe mode until January 4th, 2000 to avoid possible complications associated with the Millennium Bug. A month later, it was renamed as *XMM-Newton* to commemorate the founder of spectroscopy, Sir Isaac Newton. At the time of writing, *XMM-Newton* has spanned 2850 refereed publications in many areas of astrophysics such as galaxy clusters 10 million light years away (Stanford et al., 2006), 60m wide hotspots in neutron stars (De Luca et al., 2005) and the evolution of dark matter (Tozzi & Norman, 2001). As the proposed launch of *ATHENA* is still more than ten years away, *XMM-Newton* will continue to contribute substantially to X-ray astronomy until at least 2018 (Parmar et al., 2008). In this chapter, I review the capabilities of *XMM-Newton* and describe the techniques involved in reducing the data.

2.2 Key features

The defining features of *XMM-Newton* are:

- **Simultaneous operation:** All six *XMM-Newton* science instruments function simultaneously if they are not constrained by the target brightness. The instruments can be operated independently and in different modes of data acquisition.

Figure 2.1: The launch of *XMM-Newton* from Kourou, French Guiana, at 15:32 Paris time on 10 December. Photograph courtesy of ESA.

- **Large collecting area:** The effective area of the focusing telescopes in *XMM-Newton* is the largest of any X-ray observatory currently in operation. In total the effective area is 4650 cm^2 at 1.5 keV for the three X-ray telescopes.

- **Angular resolution:** High sensitivity is ensured by the use of 56 nested mirror shells in each X-ray telescope. The point-spread function (PSF) has a full-width half-maximum (FWHM) of $\sim 6''$ and a half energy width of $\sim 15''$.

- **Spectral resolution:** The imaging spectrometers achieve a moderate spectral resolution of $E/\Delta E = 20 - 50$ while the reflection grating spectrometer (RGS) has a superior resolution of $E/\Delta E = 60 - 500$.

- **Long and continuous visibility of target:** *XMM-Newton* follows a high eccentricity ($e = 0.59$) orbit around Earth and takes 48 hours to complete a single revolution. This is favourable for increasing the efficiency of exposures and recording the variability of sources.

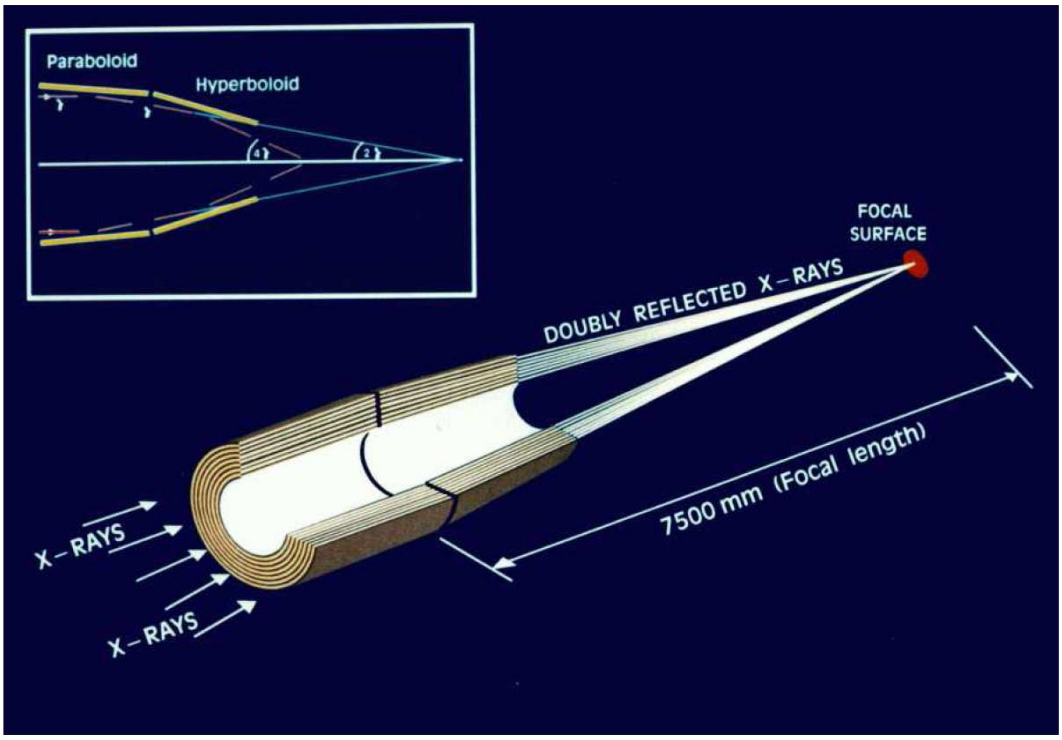

Figure 2.2: The path taken by X-rays in the telescope with a pn detector at its focus. Figure taken from the *XMM-Newton* User's Handbook.

2.3 Telescopes

XMM-Newton accommodates two types of telescopes: three Wolter-type X-ray telescopes and a 30 cm optical/UV telescope. The focal plane of the X-ray telescopes is home to the three European Photon Imaging Camera (EPIC) CCD detectors: pn, MOS1 and MOS2. These cameras are suitable for moderate resolution spectroscopy, X-ray imaging and photometry. Also present are the two detectors of the RGS, which perform high-resolution spectroscopy and spectro-photometry. The telescopes bring X-rays to a focus with a paraboloid-hyperboloid arrangement of 58 grazing-incidence mirrors that doubly reflect the X-rays. The pn camera is at the focus of one of the X-ray telescopes and receives the X-rays unobstructed whereas the two other X-ray telescopes possess both MOS and RGS detectors. A grating assembly permits 44% of the incoming light to advance to the MOS cameras at the primary focus and disperses another 40% to the CCDs of the RGS at the secondary focus. The remaining 16% is absorbed by support structures. Figure 2.2 displays the light path in the X-ray telescope with a pn camera.

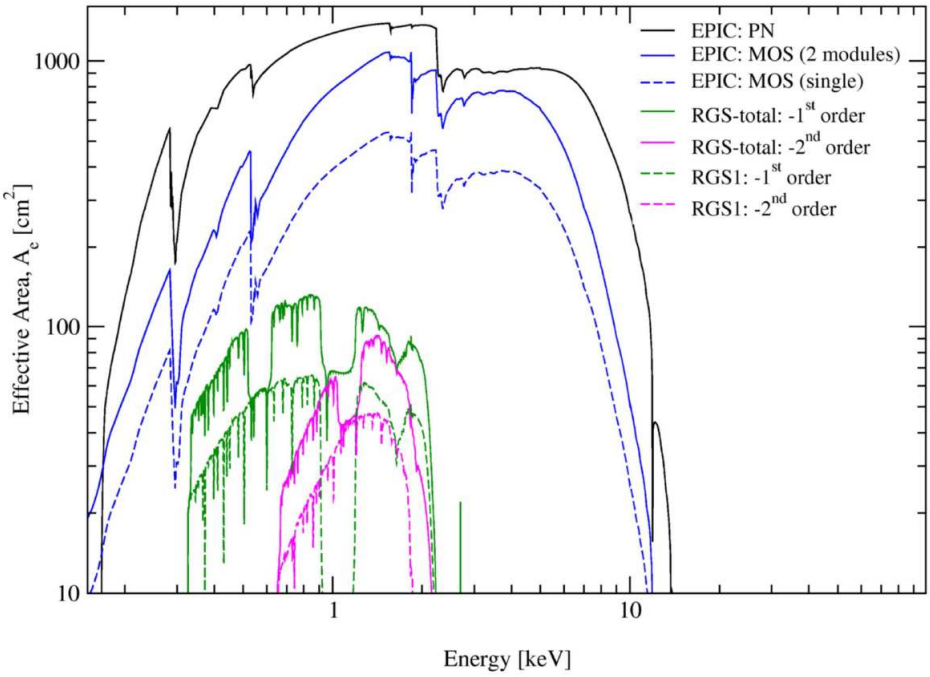

Figure 2.3: The effective areas of the pn, MOS and RGS detectors after folding through the response of each focal instrument. Figure taken from the *XMM-Newton* User's Handbook.

2.3.1 EPIC detectors

This thesis only uses data from the pn camera. This is primarily due to the superior statistical quality and effective area of the pn detector across the 0.2 – 10 keV energy range compared to that of the MOS detectors. A comparison of the effective areas of the MOS and pn CCDS is shown in Figure 2.3. The effective area reaches a maximum at $\sim$ 1.5 keV and there is a pronounced feature near 2 keV due to the Au M edge. The hard X-ray response function of the pn CCDs exceeds the MOS response while the high energy passband of the MOS detectors is limited by the quantum efficiency (QE). The QE is the fraction of photons that hit the surface of the CCD and produce an electron-hole pair. Figure 2.4 displays the QE of the pn chip as a function of energy. The QE of the pn camera is greater at higher energies than the MOS chips because the former is back-illuminated whereas the latter are front-illuminated. The pn detector also copes better with pile-up (see Section 2.4.3) as each pixel column has its own readout buffer, which leads to faster readout times.

As shown in Figure 2.5, the pn camera is composed of 12 CCD chips integrated onto a single wafer and arranged such that it is slightly offset with respect to the optical axis of the X-ray telescope. This ensures that the on-axis observing position of a point source does not fall onto the central chip boundary and that over 90%

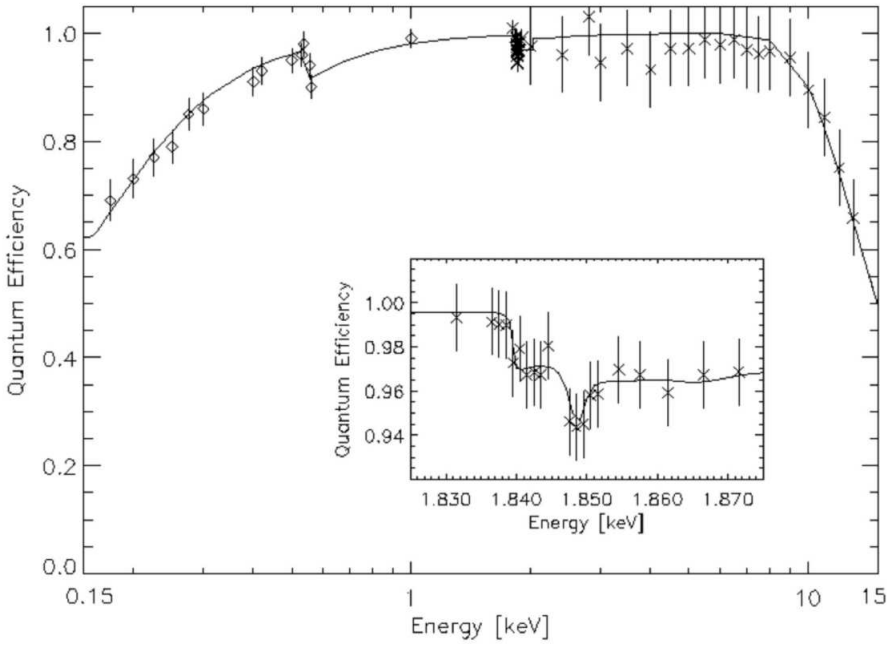

Figure 2.4: The QE of the pn chip as a function of energy. Figure taken from the *XMM-Newton* User's Handbook.

of the energy is collected on one CCD chip. The detectors can be operated in different "Window Modes" of data acquisition. The Full and Extended Full Frames cover the entire field of view and involve all the pixels of every CCD. Regarding the partial window modes, the Large Window utilises half the area of the 12 CCDs and the Small Window mode only collects data in a small part of the central CCD. A further option for the pn camera is the timing mode where imaging is processed in one dimension and the data are read out at high speed.

2.3.2 X-ray point-spread function

Along with the effective area, another critical parameter that affects the quality of a telescope is the X-ray point-spread function (PSF). This is the ability of a telescope to focus photons and is one of *XMM-Newton*'s strongest points. The core of the on-axis PSF is narrow, varies little over the energy range 0.1 – 6 keV and only becomes slightly energy dependent above 6 keV. The PSF also deteriorates as the off-axis angle increases. The encircled energy fraction (EEF) is the integral of the PSF. Figure 2.6 shows the EEF as a function of the on-axis angular radius for the pn camera. As the angular radius increases, a slight energy-dependent divergence is seen with higher energies having a larger EEF than lower energies. This is because a large fraction of the high energy photons are redistributed into the wings of the

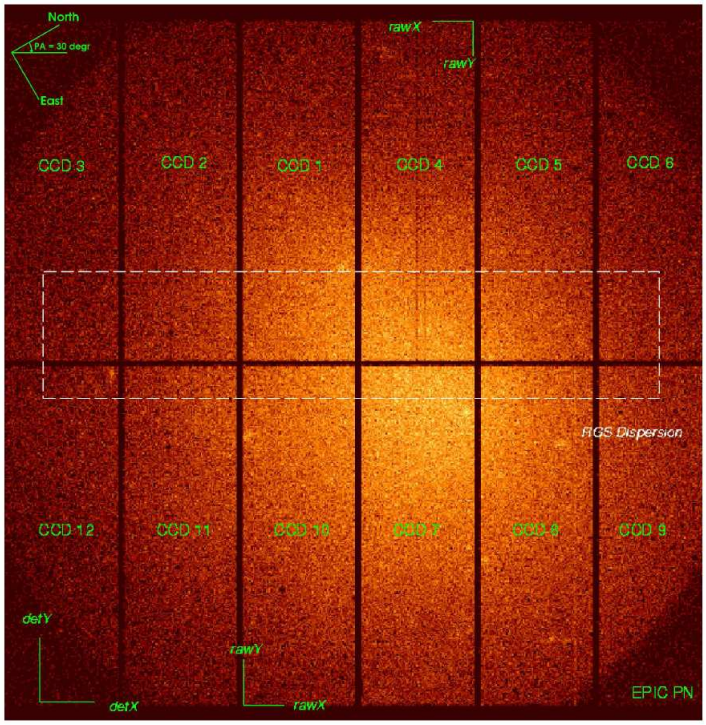

Figure 2.5: The layout of the 12 CCDs in the EPIC pn camera. Figure taken from the *XMM-Newton* User's Handbook.

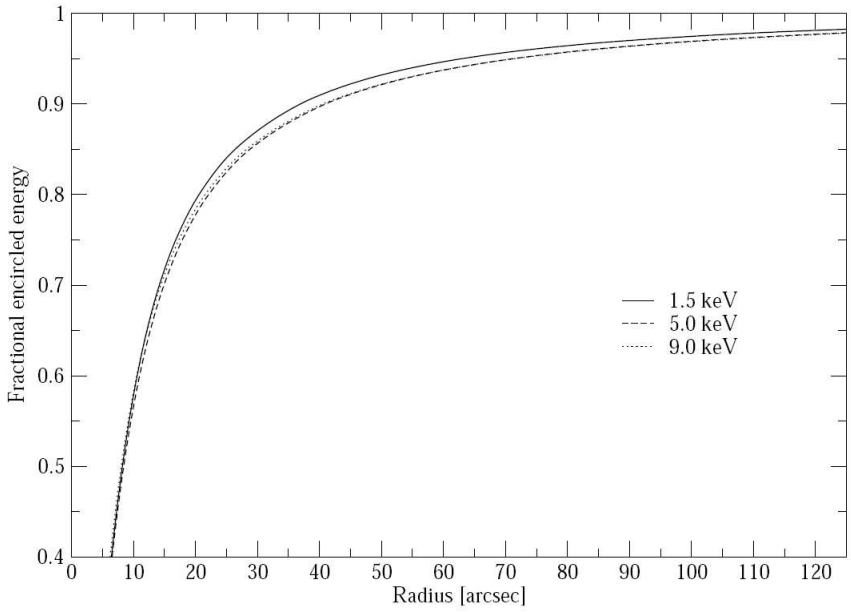

Figure 2.6: The encircled energy fraction (EEF) as a function of angular radius at different energies. 90% of the energy of a point source is encircled at an angular radius of 35″. Figure taken from the *XMM-Newton* User's Handbook.

PSF by X-ray scattering. The PSF also determines the angular resolution of the pn camera as the pixel size of 150 microns corresponds to 4.1″ on the sky, which slightly under-samples the core of the PSF.

The EPIC CCDs are sensitive to IR, visible and UV light as well as X-ray photons. To prevent contamination by sources with a high optical flux, aluminised optical blocking filters are a necessity. A thick filter minimises the throughput of optical light but also reduces the soft X-ray response. Therefore, medium and thin filters are additionally available as a compromise between diminishing the optical contamination and boosting the X-ray response.

2.4 Data reduction

A pipeline devised by Dr Paul O'Neill and described by N07 was used to reduce all the *XMM-Newton* observations involved in this thesis. Version 11 of the Science Analysis Software (SAS) was employed along with the latest calibration files as of July 2011. I now describe in detail the pipeline reduction.

2.4.1 Preparation

The *XMM-Newton* dataset for a single observation consists of the observation data files (ODF) and the data products generated by the Pipeline Processing Subsystem (PPS). The ODF data includes the raw event science files, the instrument housekeeping files, the radiation monitor files and the spacecraft files. The PPS files permit a first look at the data as they contain calibrated photon event lists, source lists and images.

The SAS tasks require up-to date calibration information, which is stored in the Current Calibration File (CCF). `cifbuild` is used to produce an index file that can access the relevant files from the CCF. Another task, `odfingest` is required to extend the ODF summary file with data extracted from the housekeeping files and the calibration database. At the start of the analysis, the data were more than a year old so the PPS files could not be used as they were processed with older versions of SAS and CCF. The next task is producing calibrated photon event files, which is the aim of `epchain`. An events list is created per exposure for the central chip only. Following Nandra et al. (2007), exposures from consecutive orbits are merged together if the science mode and filter do not change.

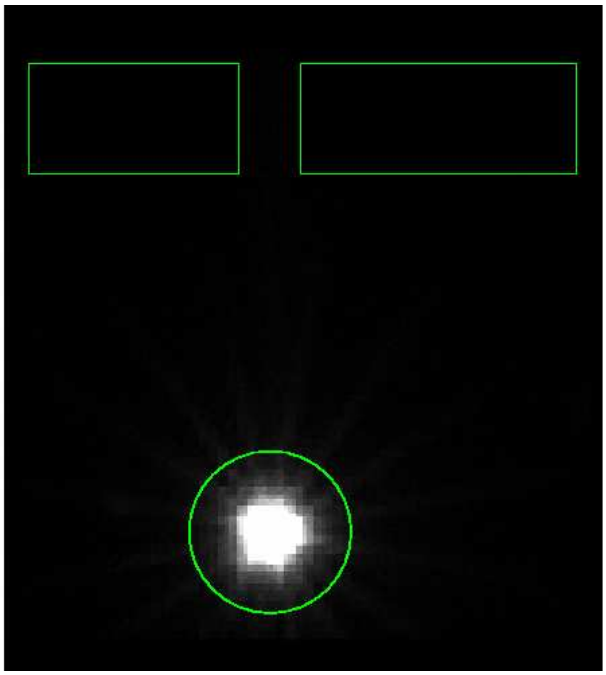

Figure 2.7: The arrangement of the source and background regions used to extract events in an observation of MCG-6-30-15.

2.4.2 Event and region filtering

The next step is to filter the single-event list by region, flag and event type. The appropriate tool to accomplish this is `evselect`. The typical arrangement of source and background regions in an observation of MCG-6-30-15 (OBSID 0111570101) is shown in Figure 2.7. The nominal source position in detector coordinates is derived using the RA and DEC co-ordinates from the NASA/IPAC Extragalactic Database. The source region is defined as a circle of radius 700 detector pixels (35″) centred on the source position. As the Small Window frame is a subset of the Large Window and Full Frame areas, the background regions were chosen within the boundary of the Small Window. The background was selected as two rectangles located away from the nominal on-axis source with a total area of 3.7 times the source area. Additionally, the two regions were separated to avoid the out-of-time events strip, an artefact of photons registering during the readout of the CCDs. If necessary, the source region was decreased to avoid the chip edges and the background regions were decreased if they were found to be situated too close to the source.

The epchain process assigns a FLAG and PATTERN value to each event. The possible attributes for each are shown in Table 2.1 and Figure 2.8. The FLAG parameter identifies "bad" events such as a bad pixel or an event at the edge of a CCD. Such events are flagged with a non-zero value so `evselect` was instructed to

select only FLAG = 0 events. PATTERN stores the number of pixels that respond to a single event as the charge cloud released by a photon can be distributed over one or many pixels. An event with pattern 0 corresponds to only a single pixel registering a charge whereas energy distributed on two (doubles), three (triples) or four (quadruples) pixels are classed as patterns 1 – 4, 5 – 8 and 9 – 12 respectively. It is recommended to only use single or double events (PATTERN less than 4) as the spectral responses are well calibrated for these patterns.

Table 2.1: The XMM-Newton FLAG attributes, taken from the *XMM-Newton* User's Handbook.

FLAG value	Brief Description	Detailed Description
#XMMEA_0	INVALID_PATTERN	Event part of a pattern that cannot be produced by a single photon. Caused by pile-up or remnant of charged particle events.
#XMMEA_2	CLOSE_TO_CCD_WINDOW	Event immediately next to a border of the current CCD window.
#XMMEA_3	ON_OFFSET_COLUMN	Event immediately on a column with a higher lower threshold than the rest of the CCD.
#XMMEA_4	NEXT_TO_OFFSET_COLUMN	Event immediately next to a column with a higher lower threshold than the rest of the CCD.
#XMMEA_5	CLOSE_TO_ONBOARD_BADPIX	Event immediately next to a bad pixel declared on board.
#XMMEA_6	CLOSE_TO_BRIGHTPIX	Event immediately next to a bright pixel not declared on board.
#XMMEA_8	CLOSE_TO_DEADPIX	Event immediately next to a dead pixel, so that part of its discharge may be lost.
#XMMEA_11	IN_SPOILED_FRAME	Event detected in a frame where other events were detected in wrong readout order or with illegal coordinates.
#XMMEA_16	OUT_OF_POV	Event detected outside the nominal field of view of XMM.
#XMMEA_17	IN_BAD_FRAME	Event detected in a frame where something was incoherent, hinting at corrupted data.
#XMMEA_19	COSMIC_RAY	Event detected within a large PATTERN. It was most likely a particle event (MIP).
#XMMEA_20	MIP_ASSOCIATED	Event detected in columns that contain high-energy particle events (MIPs) or in adjacent columns.
#XMMEA_21	ON_BADPIX	Event detected at the location of a registered bad pixel.
#XMMEA_22	SECONDARY	Event a second event in a pattern and all the relevant event information is stored with the main event after the pattern recombination.
#XMMEA_23	TRAILING	Event most likely re-emission of an event occurring immediately next to it towards the XAMEX and just above the threshold.
#XMMEA_25	OUT_OF_CCD_WINDOW	Event detected outside the CCD or the current window.
#XMMEA_EP	Select good PN events	Keeps in #XMMEA_0 to #XMMEA_11 inclusive and #XMMEA_25. Filters out #XMMEA_16 to #XMMEA_23 inclusive.

2.4.3 Pile-up

Pile-up is a common problem in X-ray data reduction, especially if the source brightness is high. It occurs when incoming X-rays strike two neighbouring pixels or the same pixel more than once in a single read-out cycle. Instead of recognising two separate events, the energies of the two events are combined to form a single entity. As a result, it is possible for a spectrum to become skewed to higher energies.

The simplest way to estimate whether pile-up is present is to consider the source count rate. Table 4.2 shows the maximum count rates in different modes for which

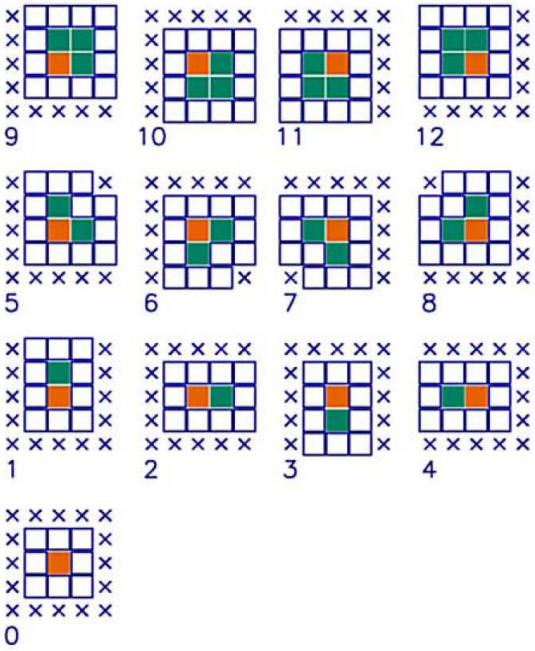

Figure 2.8: List of PATTERN types for the pn camera. The patterns are centred on a red pixel, which has the highest charge. The other pixels with a charge above the threshold level are coloured green and those pixels with insufficient charge to register are coloured white. Diagonal formations (patterns 5 – 12) are not expected from a genuine X-ray and are more likely due to the pile-up of monopixel events. Figure taken from the *XMM-Newton* User's Handbook.

Table 2.2: Time resolution and maximum count rates in different pn science modes for avoiding pile-up. The count rates include the background.

Mode	Time resolution [ms]	Max. count rate [s^{-1}]
Full Frame	73.4	6
Extended Full Frame	199.1	1
Large Window	47.7	6
Small Window	5.7	50

pile-up should not be a problem. Another method is to study an image filtered for diagonal patterns only. This is because diagonal bipixels are almost solely produced by the pile-up of two single-pixel events.

The most often used method of detecting pile-up is with `EPATPLOT`. By assuming no pile-up, this task predicts the fractions of single- and double-pixel events as a function of energy and compares it to the real fractions. If pile-up is present, there would be a deficit of single-pixel events and an excess of double-pixel events relative to the model fractions. The fractions are energy dependent with higher energy photons producing less single-event pixels due to the increasing size of the electron cloud. An example of a piled-up observation of IC 4329A (OBSID 0101040401) is shown in Figure 2.9. In cases where pile-up is found, spectra were extracted using only single-pixel events and not doubles. It is possible that the pile-up of two incident photons on the same pixel can contribute to the pattern 0 events but this is less likely than pile-up involving double pixels (Ballet, 1999).

2.4.4 Low background

Before source and background spectra can be extracted, periods of high background in the light curve associated with proton flares must be removed. It is likely that the soft protons, with energies less than a few 100 keV, originate in clouds populating the Earth's magneto-sphere. They are funnelled towards the detectors by the X-ray mirrors and can distort the spectral analysis if not addressed. An example of background flares in the light curve of NGC 526A (OBSID 0150940101) is shown in Figure 2.10. The flares can be discarded by defining a background count rate limit below which there is no evidence for intrinsic background variability. The most suitable variability measure is the excess variance (Nandra et al., 1997a; Edelson et al., 2002), $\sigma^2_{\rm XS}$, as it subtracts the variability due to the Poisson measurement errors from the total variance to give the intrinsic variability of a light curve. We used the prescription given by Vaughan et al. (2003) to estimate $\sigma^2_{\rm XS}$ as follows. Considering a light curve with N time bins, count rates and uncertainties in each time bin of X_i and $\sigma_{{\rm err},i}$ respectively and a mean count rate of μ_E, the variance of the light curve is:

$$S^2 = \frac{1}{N-1}\sum_{i=1}^{N}(X_i - \mu_E)^2. \tag{2.1}$$

$\sigma^2_{\rm XS}$ is defined by subtracting the contribution from measurement errors:

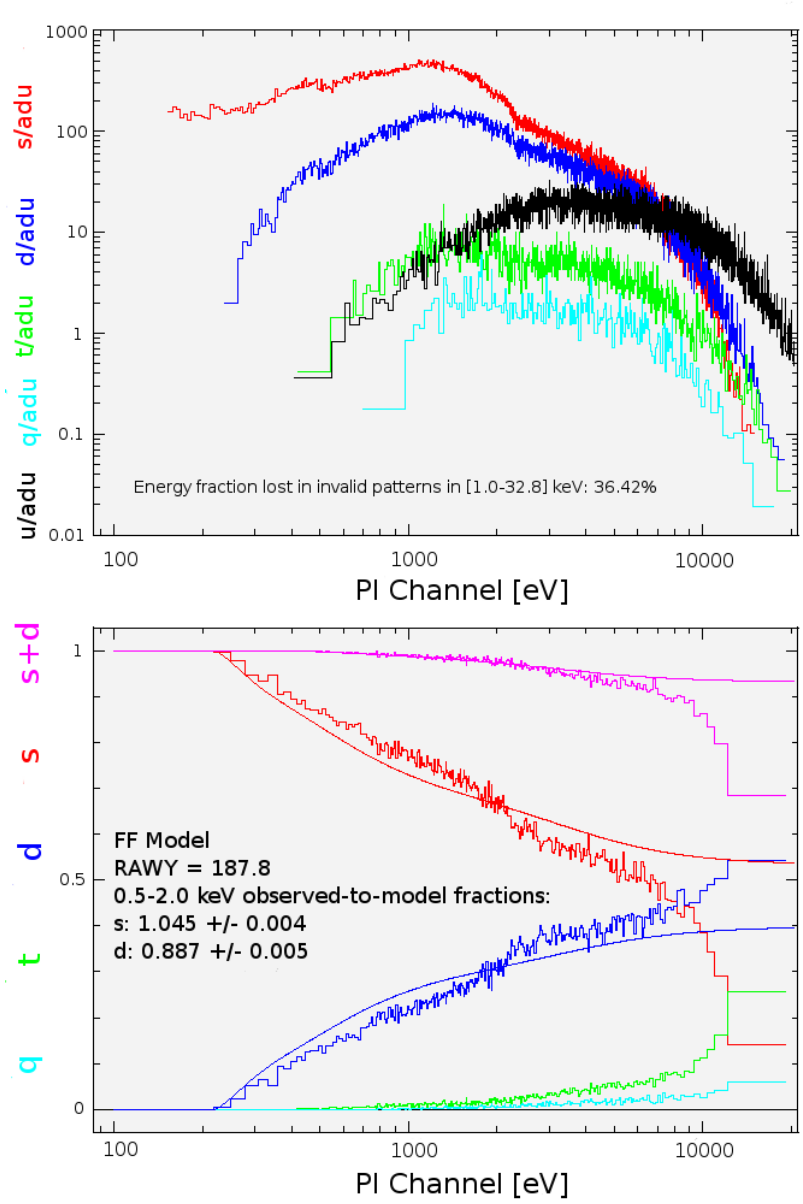

Figure 2.9: `EPATPLOT` plots of the distributions and fractions of single-, double-, triple- and quadruple-pixel events as a function of energy for the piled-up source IC 4329A. The model fractions are shown as solid lines in the bottom panel. There is a deficit of single-pixel events and an excess of double-pixel events relative to a model for a source free of pile-up.

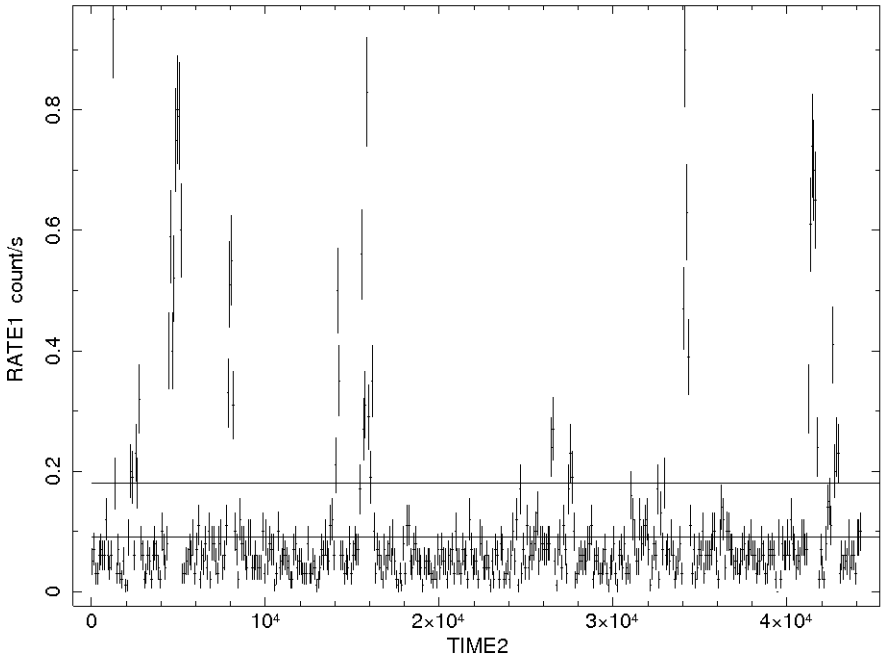

Figure 2.10: The background light curve of the NGC 526A observation. The lower horizontal line reflects the count rate at which the excess variance is zero. The higher horizontal line is at twice the count rate and and is set as the threshold for low background intervals.

$$\sigma_{\rm XS}^2 = S^2 - \frac{1}{N}\sum_{i=1}^{N}\sigma_{{\rm err},i}^2. \tag{2.2}$$

The high background count rate is found by decreasing the permitted background count rate until the excess variance reaches zero and there is no intrinsic variability. The adopted background limit is set to twice this threshold to allow for modest background variations. The time bins when the background is low are classed as good time intervals (GTIs) and are used by `evselect` to filter both the source and background events files.

2.4.5 Spectral extraction

Source and background spectra are extracted with `evselect` using only events recorded during the GTIs and with energies in the range 0.2 – 10 keV. In the following chapters, models are fit to the energy spectrum with the software package XSPEC (Arnaud, 1996) and this requires two additional files, the Redistribution Matrix File (RMF) and the Auxiliary Response File (ARF). They are produced by

the tasks `rmfgen` and `arfgen` respectively and are necessary because the output from the pn detector is a convolution of the real spectrum with the response of the CCDs. More specifically, photon counts $C(I)$ are assigned to specific energy-dependent instrument channels, I. The relationship between the real, $f(E)$, and observed spectra are:

$$C(I) = \int_0^\infty f(E)R(I,E)\,d(E) \tag{2.3}$$

where the instrumental response, $R(I,E)$, gives the probability that a photon of energy E will be detected in channel I. The response is a combination of the RMF, which distributes the real spectrum into a distribution of pulse heights due to the finite energy resolution, and the ARF, which accounts for the effective area, filter and quantum efficiency of the detectors. It is not possible to invert the equation and retrieve the real spectrum as the inversion is non-unique. Instead, a model spectrum such as a power-law ($f(E) \propto E^{-\Gamma}$) is selected and the software folds it through the response to give a model counts spectrum $C_{\rm P}(I)$. This is then fitted to the observed counts data using a fit statistic such as chi-squared, χ^2:

$$\chi^2 = \sum \frac{(C(I) - C_{\rm P}(I))^2}{\sigma(I)^2} \tag{2.4}$$

where $\sigma(I)$ is the error in $C(I)$. Finally, the spectral channels are grouped with the `grppha` tool. Two conditions are applied to decide the width of the new channels. First, the grouped channels must be at least as wide as the HWHM of the detector's response at the channel energy. Secondly, the channels must each possess a minimum of 20 counts. This ensures that the errors are approximately Gaussian, which is a requirement of using the χ^2 statistic.

2.5 Summary

In this Chapter, I have reviewed the capabilities of the *XMM-Newton* observatory and in particular, the characteristics of the pn camera. The large collection area, hard X-ray response and good energy resolution of the detector makes it ideal for modelling the iron line. The steps involved in reducing the data were described including the creation of events lists, the designation of source and background regions, the detection of pile-up, and the creation of low-background spectra. These techniques are all used in analysing the Seyfert galaxies presented in the next chapter.

Chapter 3

On the apparent absence of relativistically broadened iron lines in Seyfert galaxies

3.1 Overview

An important discovery from *XMM-Newton* data was the apparent absence of broad relativistic iron lines in some AGN. These objects represent a challenge to the established paradigm for AGN, where a relatively cold accretion disc feeds the central black hole. In that paradigm, X-ray illumination of the accretion disc should lead to continuum and fluorescence emission from iron which is broadened and shifted by relativistic effects close the hole. We extend the work of Nandra et al. (2007), who found no evidence for such a relativistically broadened component in an earlier analysis of these objects, by testing a variety of more complex relativistic reflection models. Specifically, we consider the possibility that the disc is highly ionised, and/or that the reflection is heavily blurred by strong relativistic effects in a Kerr geometry. We find that in 7/11 of the observations with no apparent broad iron line, the fit is significantly improved when an ionised or strongly blurred reflector is included, and that all 11 observations allow for such a component. A similar fraction of the observations that N07 classified as possessing a non-relativistic iron line are found to instead display a relativistic line if there is additional iron line emission from the optical broad line region. The disc inclinations of both groups are found generally to be greater than 40°, which when combined with a steep emissivity profile results in strong relativistic blurring of the reflection, rendering the Kα line difficult to distinguish from the underlying continuum. Nevertheless, relativistic reflection

does appear to be present, and the strength of the smeared reflection is similar to that expected from a flat disc illuminated by a point source. In some cases. a steep radial emissivity profile is necessary to enhance the blurring of the line, which is consistent with the gravitational light bending of continuum photons close to the black hole. Some of the work presented here appears in Bhayani & Nandra (2011).

3.2 Introduction

Since the first clear example of a strong iron line with a broad red wing in the *ASCA* spectrum of MCG-6-30-15 (Tanaka et al., 1995), subsequent analysis of an AGN sample observed by *ASCA* suggested that this phenomenon was common (Nandra et al., 1997b). On the other hand, the *ASCA* spectra already hinted at a diversity in the iron line profiles. For example, the spectra showed a range of radial emissivity profiles, which is commonly used to parametrise how close to the central black hole the line flux is generated.

Subsequent observations with better statistics and/or higher spectral resolution have been provided by *XMM-Newton*, *Chandra* and *Suzaku*. While revealing broad and skewed lines in many individual objects (see Chapter 1), they have also shown that broad iron lines of this kind are not always found. For example, the X-ray spectra in certain observations of NGC 7213 (Bianchi et al., 2008b), NGC 3227 (Markowitz et al., 2009) and NGC 5548 (Pounds et al., 2003a; Liu et al., 2010) seem to possess only the narrow iron line that is thought to originate in a distant reflector such as the molecular torus (Krolik & Kallman, 1987). These observations highlight the important issue of why the broad and relativistic iron line appears to be missing.

A systematic approach to this problem was provided via an *XMM-Newton* survey of local Seyfert 1 galaxies by Nandra et al. (2007, hereafter N07). As discussed in Chapter 1, this work revealed that $\sim 70\%$ of objects possessed a broadened iron line of some kind. However, out of these, in only around 70% could the broadening be classified as relativistic. Around a quarter of the sample showed an iron line that, while significantly broadened, was consistent with most of the emission originating beyond $50r_{\rm g}$ from the black hole. A similar question to that asked above also arises with these objects: why is there apparently no line emitting gas within $50r_{\rm g}$, where most of the accretion power — and X-ray emission — is generated? Perhaps most troublingly for the standard accretion disc model, a similar proportion ($\sim 30\%$) of the sample showed no evidence for broadened iron line emission at all, with only the narrow iron line from distant reflection being detectable.

The results of studying MCG-6-30-15 and other broad line sources (de La Calle

Pérez et al., 2010) have provided strong support for the standard paradigm for AGN, where an accretion disc feeds a central supermassive black hole, and indeed even for the existence of black holes themselves. Conversely, sources which lack such features challenge that paradigm. The presence of a relativistically broadened iron line is an almost inevitable consequence of the basic physical processes thought to operate in the central regions, and the absence of this feature makes it very difficult to fit all objects into a single unifying framework.

N07 suggested that the apparent lack of a disc line in some cases may be due to them being viewed at a high inclination as this is expected to lead to weaker reflection. In combination with low S/N spectra, it may then be difficult to detect the reflection component in these observations. The latter conclusion has been strongly supported by de La Calle Pérez et al. (2010), who clearly demonstrated that very high signal-to-noise ratio spectra are needed to detect the broad emission. Alternatively, a relativistically broadened iron line would not be able to form if the accretion disc is highly ionised (Ross & Fabian, 1993; Zycki & Czerny, 1994). This could occur if the X-ray emission originates in magnetic flares close to the surface of the disc.

It is also possible that instead of being missing, the iron line in some objects is broadened to such an extent that it is difficult to distinguish from the continuum. This can also occur if the accretion disc is viewed at a high inclination. Similarly, an iron line will be heavily smeared if there is a strong concentration of X-ray emission in the central regions. For example, this is possible in a Kerr geometry via light bending (Miniutti & Fabian, 2004).

The cases of high ionisation and extreme smearing of the line in a Kerr geometry were not considered by N07, who limited themselves to the simpler cases of a neutral disc, and a broken emissivity power-law in which the emission is spread over a wide range of disc radii. The aim of this Chapter is to extend the analysis of N07 by exploring these possibilities.

3.3 The sample and data reduction

In this section, the selection of the objects forming the N07 sample and the reduction of their data is described. N07 selected only observations available in the *XMM-Newton* public archive as of January 1st 2006 and cross-correlated with the Véron-Cetty & Véron (2001) AGN catalogue. A redshift cut-off of $z < 0.05$ was imposed to restrict the sample to nearby objects only. Seyfert 2 galaxies were excluded apart from those that displayed broad emission lines in the near-infrared (Blanco et al.,

1990). Intermediate types (1.8 and 1.9) were included but NGC 1365 was excluded as it has been shown to possess a highly complex spectrum that is occasionally Compton-thick (Risaliti et al., 2005).

We used only the observations taken with the EPIC-pn CCD camera. Studying the iron line requires high signal-to-noise ratio (S/N) in the hard X-ray band so the final criterion of the sample selection was a minimum of 30,000 counts in the 2 – 10 keV spectrum after background subtraction and screening for flares. This left a sample of 37 observations from 26 sources, detailed in Table 3.1. The redshifts, Galactic absorption columns and iron line classes of the sample are given in Table 3.2. Column 4 lists the classification of the iron line as given by N07 (R: relativistically broadened iron line, N: non-relativistically broadened iron line and X: no evidence for blurred reflection).

The observations were reduced as described in Chapter 2. It should be noted that exposures of a given source were merged if taken from the same or consecutive orbits. The exception is NGC 4151 where the CCD mode changed within an orbit. Four observations: NGC 2992, MCG-5-23-16(1), MCG-5-23-16(2) and IC 4329A(2) displayed evidence for pile-up so only grade 0 events were used for these four. Grade 0 – 4 events were extracted for the remaining 33 observations. The analysis was restricted to the 2.5 – 10 keV energy range as the focus of this Chapter is on the broad iron line and the associated reflection continuum. The choice of lower bound is justified by the fact that there are calibration-related residuals near the mirror Au M shell edge and detector Si edge between 1.8 – 2.5 keV.

3.4 Model NBR

We focus first on the 11 "narrow-line" observations that were found by N07 not to require an accretion disc component in their time-averaged spectrum ("X" in Column 4 of Table 3.2). The models that we tested are compared to a model that lacks a broad iron line and its associated reflection component (Model NBR - "No Blurred Reflection"). In XSPEC terminology, Model NBR is described as:

$$\text{Model NBR} = \text{WABS} \times (\text{POWERLAW} + \text{PEXMON}) \times \text{CWA18}. \qquad (3.1)$$

Table 3.1: The sample of *XMM-Newton* EPIC-pn observations. Column (1): name and observation number. Column (2): *XMM-Newton* observation ID. Column (3): *XMM-Newton* revolution. Column (4): observation date. Column (5): duration of observation before screening (ks). Column (6): exposure time after screening and accounting for detector deadtime (ks). Column (7): EPIC-pn read-out mode: FF = Full Frame, LW = Large Window, SW = Small Window. Column (8): filter in place during observation. Column (9): event grades used in the analysis.

Name	OBSID	Rev.	Date	Duration (ks)	Exposure (ks)	Mode	Filter	Grades
(1)	(2)	(3)	(4)	(5)	(6)	(7)	(8)	(9)
NGC 526A	0150940101	647	2003-06-21	47.9	37.0	LW	Thin1	0 – 4
Mrk 590	0201020201	837	2004-07-04	225.3	51.9	SW	Thin1	0 – 4
Ark 120	0147190101	679	2003-08-24	112.1	57.4	SW	Thin1	0 – 4
NGC 2110	0145670101	593	2003-03-05	59.5	34.0	LW	Thin1	0 – 4
MCG+8-11-11	0201930201	794	2004-04-09	38.5	20.2	SW	Medium	0 – 4
Mrk 6	0144230101	619	2003-04-26	59.0	31.6	FF	Medium	0 – 4
Mrk 110	0201130501	904	2004-11-15	47.4	32.5	SW	Thin1	0 – 4
NGC 2992	0147920301	630	2003-05-19	28.9	21.8	FF	Medium	0
MCG-5-23-16(1)	0112830301	261	2001-05-13	76.9	9.3	FF	Medium	0
MCG-5-23-16(2)	0112830401	363	2001-12-01	24.9	19.6	FF	Medium	0
NGC 3516(1)	0107460601	245	2001-04-10	130.2	37.9	SW	Thin1	0 – 4
NGC 3516(2)	0107460701	352	2001-11-09	130.0	81.5	SW	Thin1	0 – 4
NGC 3783	0112210201	371	2001-12-17	413.5	173.3	SW	Medium	0 – 4
HE 1143-1810	0201130201	824	2004-06-08	34.1	21.7	SW	Thin1	0 – 4

Continues on next page

Table 3.1 – continued from previous page

Name	OBSID	Rev.	Date	Duration	Exposure	Mode	Filter	Grades
NGC 4051	0109141401	263	2001-05-16	122.0	41.2	SW	Medium	0 – 4
NGC 4151(1)	0112310101	190	2000-12-21	33.0	20.6	SW	Medium	0 – 4
NGC 4151(2)	0112830501	190	2000-12-22	85.4	68.6	FF	Medium	0 – 4
NGC 4151(3)	0143500101	633	2003-05-25	56.9	31.8	SW	Medium	0 – 4
Mrk 766(1)	0096020101	82	2000-05-20	58.8	24.3	SW	Medium	0 – 4
Mrk 766(2)	0109141301	265	2001-05-20	129.9	72.4	SW	Medium	0 – 4
Mrk 766(3)	0304030101	1004	2005-05-23	523.0	303.1	SW	Medium	0 – 4
NGC 4395	0142830101	728	2003-11-30	113.4	90.4	FF	Medium	0 – 4
NGC 4593	0059830101	465	2002-06-23	87.2	50.6	SW	Medium	0 – 4
MCG-6-30-15(1)	0111570101	108	2000-07-11	112.7	64.0	SW	Medium	0 – 4
MCG-6-30-15(2)	0029740101	301	2001-07-31	349.3	204.5	SW	Medium	0 – 4
IC 4329A(1)	0101040401	210	2001-01-31	13.9	9.3	FF	Medium	0 – 4
IC 4329A(2)	0147440101	670	2003-08-06	136.0	68.4	SW	Thin1	0
NGC 5506(1)	0013140101	211	2001-02-02	20.0	13.7	LW	Medium	0 – 4
NGC 5506(2)	0013140201	382	2002-01-09	13.8	9.9	LW	Medium	0 – 4
NGC 5548(1)	0109960101	191	2000-12-24	26.1	15.9	SW	Medium	0 – 4
NGC 5548(2)	0089960301	290	2001-07-09	135.0	66.2	SW	Thin1	0 – 4
Mrk 509	0130720101	161	2000-10-25	31.6	16.6	SW	Thin1	0 – 4
NGC 7213	0111810101	269	2001-05-29	49.6	29.3	SW	Medium	0 – 4
NGC 7314	0111790101	256	2001-05-02	44.7	25.6	SW	Medium	0 – 4
Ark 564	0206400101	930	2005-01-05	101.8	67.4	SW	Medium	0 – 4

Continues on next page

Table 3.1 – continued from previous page

Name	OBSID	Rev.	Date	Duration	Exposure	Mode	Filter	Grades
NGC 7469(1)	0112170101	192	2000-12-26	43.6	28.3	SW	Medium	0 – 4
NGC 7469(2)	0207090101	912	2004-11-30	164.1	112.2	SW	Medium	0 – 4

Table 3.2: The redshifts, Galactic absorption columns and iron line classes of the sample of *XMM-Newton* EPIC-pn observations. Column (1): name and observation number. Column (2): redshift from the NASA/IPAC Extragalactic Database (NED). Column (3): Galactic absorption column from Elvis et al. (1989), Stark et al. (1992) and Dickey & Lockman (1990). Column (4): classification of the iron line (IL): R, broad and relativistic; N, broad but non-relativistic and X, no evidence for disc reflection.

Name	Redshift	$N_{\rm H}$ (Gal) (10^{20} cm^{-2})	IL Class
(1)	(2)	(3)	(4)
NGC 526A	0.019	2.2	R
Mrk 590	0.035	4.1	X
Ark 120	0.033	12.6	N
NGC 2110	0.007	18.3	X
MCG+8-11-11	0.020	20.9	X
Mrk 6	0.019	6.4	X
Mrk 110	0.036	1.5	X
NGC 2992	0.008	5.3	R
MCG-5-23-16(1)	0.008	8.4	N
MCG-5-23-16(2)	0.008	8.4	R
NGC 3516(1)	0.009	2.9	R
NGC 3516(2)	0.009	2.9	R
NGC 3783	0.010	8.5	R
HE 1143-1810	0.033	3.5	X
NGC 4051	0.002	1.3	R
NGC 4151(1)	0.003	2.1	N
NGC 4151(2)	0.003	2.1	N
NGC 4151(3)	0.003	2.1	R
Mrk 766(1)	0.013	1.6	R
Mrk 766(2)	0.013	1.6	R
Mrk 766(3)	0.013	1.6	R
NGC 4395	0.001	1.4	R
NGC 4593	0.009	2.0	N
MCG-6-30-15(1)	0.008	4.1	R
MCG-6-30-15(2)	0.008	4.1	R

Continues on next page

Table 3.2 – continued from previous page

Name	Redshift	$N_{\rm H}$ (Gal)	IL Class
IC 4329A(1)	0.016	10.4	X
IC 4329A(2)	0.016	10.4	N
NGC 5506(1)	0.007	3.8	X
NGC 5506(2)	0.007	3.8	R
NGC 5548(1)	0.017	1.7	X
NGC 5548(2)	0.017	1.7	N
Mrk 509	0.034	4.2	R
NGC 7213	0.006	2.1	X
NGC 7314	0.005	1.5	R
Ark 564	0.025	6.4	N
NGC 7469(1)	0.017	4.8	X
NGC 7469(2)	0.017	4.8	R

A description of the model components is given below.

3.4.1 The continuum and ionised absorption

The X-ray continuum is represented by the "POWERLAW" component, which has two parameters, the slope, Γ, and the normalisation. WABS accounts for the neutral absorption and the Galactic $N_{\rm H}$ values that we use are given in Column 3 of Table 3.2 and taken from Elvis et al. (1989), Stark et al. (1992) and Dickey & Lockman (1990). 4/11 of the narrow-line observations: NGC 2110, Mrk 6, IC 4329A(1) and NGC 5506(1) also required ionised absorption and this is modelled by "CWA18". This is a table model calculated by N07 from the photoionisation code `XSTAR`[†] (version 21kn) of Kallman et al. (2004). The assumptions of the model are: an illuminating powerlaw continuum of slope $\Gamma = 2$, a hydrogen nucleus density of 10^6 cm^{-3}, solar abundances and a turbulent velocity of 100 km s^{-1}. The two free parameters of the model are the ionisation parameter, $\xi_{\rm abs}$, and the column density, $N_{\rm H}$, which are free to vary between $20 < \log N_{\rm H} < 24$ cm^{-2} and $-4 < \log \xi_{\rm abs} < 4$ erg cm s^{-1} respectively. If the absorber has sufficient column density, it can modify the curvature of the spectrum above 2.5 keV. N07 ascertained the presence of a warm absorber by testing if a fit to the continuum with the POWERLAW model improves

[†]http://heasarc.gsfc.nasa.gov/docs/software/xstar/xstar.html

with the inclusion of the CWA18 model. The presence of an additional screen of ionised absorption was tested for by N07 (i.e. a multizone absorber) with only NGC 4151(2) showing evidence for such a component. With this particular observation, a second CWA18 model is included in all fits.

3.4.2 Compton reflection

The "PEXMON" component in Model NBR accounts for continuum reflection by the distant torus, which was found by N07 to be ubiquitous in their sample. It was developed by N07 to self-consistently account for both the iron line and Compton reflection continuum. The neutral reflection is modelled by the "PEXRAV" model (Magdziarz & Zdziarski, 1995), which assumes a slab geometry. The parameters of PEXMON are the incident power-law slope, the upper exponential cut-off energy, $E_{\rm Cut}$, the inclination of the slab, i, the elemental abundances and the reflection strength, R. The last parameter gives the solid angle ($2\pi \times R$) covered by the reflecting material from the view of the X-ray source. For a canonical flat slab illuminated from above by the source, the solid angle is expected to be 2π i.e. $R = 1$. The incident power-law slope is set to that of the POWERLAW model while a high cut-off to the continuum of $E_{\rm Cut} = 1$ MeV is assumed, although this is unimportant as the spectra extend only as far as 10 keV. Solar abundances are adopted. A slab inclination of $i_{\rm dist} = 60^{\circ}$ was assumed for the distant torus.

To model the neutral iron line, a narrow 6.4 keV emission line is added with the strength determined from the results of George & Fabian (1991). A Compton shoulder to the line is also included by approximating it as a Gaussian with energy 6.315 keV. As neutral Fe Kβ (7.05 keV) and Ni Kα (7.47 keV) lines are expected to arise via fluorescence, they are added to the model with 11.3% and 5% of the iron line flux respectively.

N07 also tested the iron band for narrow lines (see Table 7 in N07 for a list of detected lines) and if these were deemed to be present, they were also included in Model NBR. The model components and parameters of Model NBR and the subsequent models are listed in Table 3.3. The best-fit χ^2/d.o.f. of Model NBR to the 2.5 – 10 keV energy spectra are shown in Column 1 of Table 3.5. The fits of all the models that we tested are compared to Model NBR so we list the $\Delta\chi^2$ of the models relative to Model NBR in columns 2 – 6.

Table 3.3: The XSPEC model components and parameters for each model. Part (a) of the table lists the components with parameters that are the same in all five models and part (b) gives the model components that differ between the models. X denotes parameters that are dependent on the AGN and **f** represents parameters that are free to vary. — is used when a model component is not included and "red" denotes a redundant parameter i.e. the break radius for KDBLUR2 when $q_1 = q_2$.

(a)

Model component	Parameter	All models
WABS	$N_{\rm H}$	X
POWERLAW	Γ	**f**
	Normalisation	**f**
PEXMON (torus)	$E_{\rm Cut}$ (keV)	1000
	z	X
	Abundance	1.0
	$i_{\rm dist}$ ($^\circ$)	60
	$R_{\rm dist}$	**f**
CWA18 (if necessary)	$\log(N_{\rm H})$	**f**
	$\log(\xi_{\rm abs})$	**f**

(b)

Model component	Parameter	Model				
		NBR	N07	ION	SRC	SRI
PEXMON (disc)	$E_{\rm Cut}$ (keV)	—	1000	—	1000	—
	z	—	X	—	X	—
	Abundance	—	1.0	—	1.0	—
	$R_{\rm blur}$	—	**f**	—	**f**	—
REFLIONX	Abundance	—	—	1.0	—	1.0
	$\xi_{\rm blur}$	—	—	**f**	—	**f**
	z	—	—	X	—	X
	Normalisation	—	—	**f**	—	**f**
KDBLUR2	q_1	—	0	0	**f**	**f**
	q_2	—	3	3	$= q_1$	$= q_1$
	$i_{\rm blur}$	—	**f**	**f**	**f**	**f**
	$r_{\rm in}$ ($r_{\rm g}$)	—	6	6	1.24	1.24
	$r_{\rm out}$ ($r_{\rm g}$)	—	400	400	400	400
	$r_{\rm br}$ ($r_{\rm g}$)	—	**f**	**f**	red	red

Table 3.4: The 99% threshold $\Delta\chi^2_{\rm NBR-Y}$ relative to Model NBR (i.e. $\Delta\chi^2_{\rm NBR-Y} = \chi^2_{\rm NBR} - \chi^2_{\rm Y}$ where Y is the model of interest) to determine the presence of blurred reflection for each observation and model that we test.

Name	99% threshold limit			
	$\Delta\chi^2_{\rm NBR-N07}$	$\Delta\chi^2_{\rm NBR-ION}$	$\Delta\chi^2_{\rm NBR-SRC}$	$\Delta\chi^2_{\rm NBR-SRI}$
Mrk 590	8.1	10.6	9.8	11.5
NGC 2110	6.4	6.7	6.6	6.8
MCG+8-11-11	7.5	8.4	7.8	8.9
Mrk 6	6.5	6.9	6.8	7.2
Mrk 110	9.6	11.5	10.2	13.1
HE 1143-1800	6.7	8.1	7.0	8.7
IC 4329A(1)	6.5	9.0	8.8	9.4
NGC 5506(1)	6.8	7.0	6.9	7.6
NGC 5548(1)	7.9	9.7	8.3	12.1
NGC 7213	8.4	9.0	8.7	9.8
NGC 7469(1)	6.7	8.4	8.2	9.1

3.4.3 Significance of a blurred reflection detection

Errors are calculated at a confidence level of 90% for one interesting parameter. The significance of the improvement in the fits over Model NBR was assessed using Monte Carlo simulations, which is superior to the F-test in many cases (Protassov et al., 2002), and we followed the approach of N07. For each observation, we created 1000 synthetic spectra using the *fakeit* task in XSPEC. Each synthetic spectrum was based on Model NBR with parameters set to those found by N07 for the particular observation. The simulated spectra also had the same number of counts between 2.5 – 10 keV as the observed spectrum and Poisson noise was added. These simulated spectra were refit with Model NBR and the change in χ^2 after fitting with the model of interest was recorded e.g. if Models NBR and N07 give $\chi^2_{\rm NBR} = 87.6$ and $\chi^2_{\rm N07} = 83.1$ respectively, then $\Delta\chi^2_{\rm NBR-N07} = \chi^2_{\rm NBR} - \chi^2_{\rm N07} = 4.5$. The 1000 $\Delta\chi^2_{\rm NBR-N07}$ values were ranked in order of size and the 990^{th} largest value (i.e. 99%) was chosen as the threshold $\Delta\chi^2_{\rm NBR-N07}$ for a significant detection of an iron line at 99% confidence level with Model N07. The 99% threshold $\Delta\chi^2$ for each observation and model that we test are shown in Table 3.4. Observations with a significant detection at a confidence level of 99% are shown in bold in Table 3.5.

Table 3.5: Column (1): the best-fit χ^2/degree of freedom (d.o.f.) of Model NBR. Columns (2) – (6): the change in goodness-of-fit ($\Delta\chi^2_{\rm NBR-Y}$) and the extra degrees of freedom in Models N07, ION, SRC and SRI relative to Model NBR. Significant improvements at a confidence level of 99% are shown in bold.

Name (1)	$\chi^2_{\rm NBR}$ (2)	$\Delta\chi^2_{\rm NBR-N07}$ (3)	$\Delta\chi^2_{\rm NBR-ION}$ (4)	$\Delta\chi^2_{\rm NBR-SRC}$ (5)	$\Delta\chi^2_{\rm NBR-SRI}$ (6)
Mrk 590	95.9/98	3.2/3	3.2/4	1.8/3	1.9/4
NGC 2110	99.1/100	2.6/3	4.7/4	**9.8/3**	**9.9/4**
MCG+8-11-11	94.6/99	**7.6/3**	**11.5/4**	**9.7/3**	**13.8/4**
Mrk 6	97.6/92	**7.0/3**	**8.8/4**	**7.3/3**	**8.1/4**
Mrk 110	116.0/100	3.7/3	**12.1/4**	**14.7/3**	**20.5/4**
HE 1143-1800	94.0/99	3.0/3	5.1/4	**8.4/3**	**12.8/4**
IC 4329A(1)	76.2/103	1.6/3	1.8/4	1.2/3	1.3/4
NGC 5506(1)	91.3/99	**7.1/3**	4.2/4	6.6/3	**8.0/4**
NGC 5548(1)	84.1/100	0.2/3	0.0/4	0.1/3	1.7/4
NGC 7213	111.7/99	1.1/3	7.4/4	0.7/3	0.7/4
NGC 7469(1)	122.0/100	**8.2/3**	**13.6/4**	**13.2/3**	**14.9/4**

3.5 Model N07

In addition to the model components in Model NBR, the best-fitting model in N07 (either their Model E or F) includes reflection from the accretion disc. This is defined as Model N07 and its XSPEC description is:

$$\begin{aligned}\text{Model N07} = \text{WABS} \times (\text{POWERLAW} + \text{PEXMON} + \text{KDBLUR2} \times \text{PEXMON}) \\ \times \text{CWA18}.\end{aligned} \tag{3.2}$$

N07 investigated a cold accretion disc, so PEXMON can also be used to model reflection of the continuum by the accretion disc. As there is reflection from the inner part of the accretion disc, it should be blurred by Doppler effects and the strong gravitational field of the central black hole. This can be modelled with "KDBLUR2", which convolves a spectrum with the kernel from the relativistic accretion disc line model of Laor (1991). It has six parameters: the inner and outer disc radii, $r_{\rm in}$ and $r_{\rm out}$, the inclination, $i_{\rm blur}$, the two emissivity indices, q_1 and q_2, and the break radius, $r_{\rm br}$. N07 fixed $r_{\rm out} = 400r_{\rm g}$, the maximum radius allowed in the Laor (1991) model, and $r_{\rm in} = 6r_{\rm g}$ was adopted as it is the radius of marginal stability for a Schwarzchild black hole. The inclination parameter is tied to that of the PEXMON

model. N07 considered a broken power-law for the radial disc emissivity, which approximately corresponds to the emissivity profile expected for an X-ray source at a height h above the illuminated accretion disc in a Newtonian geometry (e.g. Vaughan et al., 2004). In this scenario, the emissivity can be characterised as r^{-q} with slope $q \propto h/(r^2 + h^2)^{3/2}$. Taking limits of $r << h$ and $r >> h$ allow the emissivity slopes to be approximated as $q_1 = 0$ and $q_2 = 3$ inside and outside the break radius, $r_{\rm br}$. This radius is a key parameter as it represents where the peak of the line flux originates and is therefore used by N07 in their classification of the iron line. An observation with $r_{\rm br} < 50r_{\rm g}$ is defined to have a relativistically broadened iron line while one with $r_{\rm br} > 50r_{\rm g}$ has a broad but non-relativistic iron line. N07 allowed the break radius to vary below the inner radius of the disc though the line profile is no different to that derived for $r_{\rm br} = 6r_{\rm g}$.

A significant detection of the blurred reflection can be made in four narrow-line observations with Model N07: MCG+8-11-11, Mrk 6, NGC 5506(1) and NGC 7469(1). These observations did not show a large enough improvement with the F-test method used by N07 to compare the fits with that of Model NBR, although the improvements in the fits with Model N07 over Model NBR were close to being significant. In no case could the disc inclination be constrained with Model N07, although three out of four do have a best-fit break radius of $< 50r_{\rm g}$. This hints at relativistic reflection, so we allow the four observations to remain in the narrow-line sample to test if our models are superior to Model N07.

3.5.1 Ionised disc – Model ION

As discussed in Chapter 1, the equivalent width of the iron line is dependent on the ionisation state of the accretion disc. For example, if the ionisation parameter is in the range $\xi = 100 - 500$ erg cm s^{-1}, the iron line is weak as the Kα line photons are resonantly absorbed. As Model N07 tested only neutral accretion disc reflection, our first extension to the N07 analysis was to determine if an ionised accretion disc model can reveal the reflection in the apparent narrow-line spectra. This model is termed Model ION and differs from Model N07 only in the replacement of the cold disc model, PEXMON, with the ionised reflection model, "REFLIONX" (Ross & Fabian, 2005) for the blurred reflection. In REFLIONX, the ionisation state of the disc is parametrised by the ionisation parameter, defined as $\xi_{\rm blur} = L/nr^2$, where L is the luminosity of the ionising continuum, n is the hydrogen number density and r is the distance to the X-ray source. The REFLIONX model also includes soft X-ray emission lines below 2 keV, but as the time-averaged spectra are modelled between

2.5 – 10 keV, we do not believe that the soft excess affects the fitting of the higher energy reflection continuum and iron line. REFLIONX does not parametrise the reflection strength. To obtain it, we use the reflection model of Ballantyne et al. (2001a) and fix its parameters to those found with REFLIONX to find $R_{\rm blur}$. The XSPEC description of Model ION is:

$$\begin{aligned}\text{Model ION} = \text{WABS} \times (\text{POWERLAW} + \text{PEXMON} + \text{KDBLUR2} \times \text{REFLIONX}) \\ \times \text{CWA18}. \end{aligned} \quad (3.3)$$

3.6 Fit of Model ION to the data

The best-fit parameters for Model ION are given in Table 3.6. Evidence for a broad and ionised reflection component at $> 99\%$ confidence is found in four observations: MCG+8-11-11, Mrk 6, Mrk 110 and NGC 7469(1). All four of these observations display an iron line that is relativistically broadened, as their characteristic break radii are less than $50r_{\rm g}$. The REFLIONX ionisation parameters of these four observations are mild, ranging from $\xi_{\rm blur} = 99 - 200$ erg cm s^{-1}. Nonetheless, accounting for the ionisation state of the disc may be very important, as even in a mildly ionised disc, Compton scattering can contribute to additional broadening (Ross et al., 1999).

The REFLIONX reflection strengths of the accretion disc in MCG+8-11-11, Mrk 6, Mrk 110 and NGC 7469(1) are between $R_{\rm blur} = 0.55 - 0.97$, which is slightly less than the strength, $R = 1$, expected by a flat accretion disc subtending a solid angle of 2π below a central point source. They are however, typical of reflection fractions for the objects with visible and detectable neutral broad lines in the N07 sample.

The disc inclination is well determined in the case of Mrk 110, at $i = 36^{\circ}{}^{+19^{\circ}}_{-12^{\circ}}$. MCG+8-11-11 and Mrk 6 are much less well determined, but the best-fit values are 45° and 26° respectively. These are close to the average disc inclination for the N07 broad line sources. Hence the spectra of MCG+8-11-11, Mrk 6 and Mrk 110 show properties entirely typical of sources with broad, relativistic reflection components, with the sole difference being that the reflector is ionised. The inclination of the disc in NGC 7469(1) pegs at the model limit of 85° and thus the detection in this case cannot be considered robust. If the disc inclination is high, the reflection would be expected to be very weak and broad. An alternative possibility, that we examine in the following section, is that the extreme broadening is due to stronger relativistic effects than assumed by the models in N07.

Table 3.6: Disc line parameters for the narrow-line observations derived using Model ION. Column (1): observation name. Column (2): spectral slope. Column (3): reflection fraction of the blurred REFLIONX component. Column (4): inclination of the slab representing the blurred reflector. Column (5): break radius for the emissivity law. Column (6): ionisation parameter of the blurred reflector. Column (7): reflection fraction of the distant PEXMON component. Column (8): $\Delta\chi^2_{\rm N07-ION}$ for 3 additional d.o.f.. Column (9): $\Delta\chi^2_{\rm NBR-ION}$ for 4 additional d.o.f.. Detections of blurred reflection with Model ION at a significance level of 99% are shown in bold.

Name	Γ	$R_{\rm blur}$	$i_{\rm blur}$	$r_{\rm br}$	$\xi_{\rm blur}$	$R_{\rm dist}$	$\Delta\chi^2_{\rm NBR-N07}$	$\Delta\chi^2_{\rm NBR-ION}$
		$(\Omega/2\pi)$	$(^\circ)$	$(r_{\rm g})$	(erg cm s^{-1})	$(\Omega/2\pi)$		
(1)	(2)	(3)	(4)	(5)	(6)	(7)	(8)	(9)
Mrk 590	$1.7^{+0.1}_{-0.1}$	$0.5^{+0.2}_{-0.2}$	47^{+38}_{-47}	$1.2^{+68}_{-0.0}$	10^{+2860}_{-0}	$0.3^{+0.2}_{-0.2}$	3.2	3.2
NGC 2110	$1.7^{+0.1}_{-0.1}$	$0.5^{+0.2}_{-0.4}$	0^{+51}_{-0}	$3.1^{+397}_{-1.9}$	205^{+876}_{-195}	$0.8^{+0.1}_{-0.1}$	2.6	4.7
MCG+8-11-11	$1.8^{+0.0}_{-0.0}$	$0.6^{+0.2}_{-0.2}$	45^{+40}_{-8}	$4.6^{+395}_{-3.4}$	201^{+1232}_{-191}	$0.8^{+0.1}_{-0.1}$	7.7	**11.5**
Mrk 6	$1.7^{+0.1}_{-0.1}$	$0.6^{+0.4}_{-0.4}$	26^{+59}_{-7}	22^{+378}_{-21}	12^{+127}_{-2}	$0.3^{+0.2}_{-0.2}$	7.1	**8.8**
Mrk 110	$1.8^{+0.1}_{-0.1}$	$0.7^{+0.2}_{-0.2}$	36^{+19}_{-12}	$1.2^{+400}_{-0.0}$	99^{+113}_{-89}	$0.2^{+0.1}_{-0.1}$	3.7	**12.1**
HE 1143-1810	$1.8^{+0.1}_{-0.0}$	$0.5^{+0.2}_{-0.2}$	0^{+85}_{-0}	$4.0^{+396}_{-2.8}$	97^{+582}_{-90}	$0.3^{+0.1}_{-0.2}$	3.0	5.1
IC 4329A(1)	$1.8^{+0.0}_{-0.1}$	$0.2^{+0.2}_{-0.1}$	61^{+23}_{-62}	106^{+294}_{-105}	21^{+165}_{-11}	$0.2^{+0.1}_{-0.1}$	1.6	1.8
NGC 5506(1)	$1.9^{+0.1}_{-0.1}$	$0.1^{+0.1}_{-0.1}$	53^{+32}_{-53}	190^{+210}_{-188}	556^{+301}_{-546}	$0.5^{+0.1}_{-0.1}$	7.1	4.2
NGC 5548(1)	$1.7^{+0.0}_{-0.1}$	$0.03^{+0.2}_{-0.03}$	3^{+82}_{-3}	259^{+142}_{-257}	5739^{+4280}_{-5730}	$0.4^{+0.1}_{-0.1}$	0.2	0.0
NGC 7213	$1.8^{+0.0}_{-0.0}$	$0.1^{+0.1}_{-0.1}$	$0^{+64}_{-0.0}$	344^{+56}_{-310}	496^{+638}_{-286}	$0.5^{+0.1}_{-0.1}$	1.1	7.4
NGC 7469(1)	$2.0^{+0.1}_{-0.1}$	$1.0^{+0.3}_{-0.3}$	85^{+0}_{-49}	$2.8^{+397.2}_{-1.5}$	105^{+474}_{-80}	$0.7^{+0.2}_{-0.1}$	8.2	**13.6**

3.6.1 Strong relativistic effects – Model SRC

Our next set of models test if the iron line is heavily blurred by concentrating the line emission in the central regions. This is accomplished firstly by modifying the emissivity profile to a single power-law with the index, q, now a parameter free to vary between $3 < q < 9$. For example, if $q = 3$, 89.3% of the emission arises within $50r_{\rm g}$. A steeper profile with $q = 6$ has 99.9796% of the iron Kα photons originating within the same radius and 90% within $10.8r_{\rm g}$. Therefore, the choice of the emissivity profile is very important in determining how strongly blurred the reflection is.

Secondly, we assume a maximally spinning black hole by fixing the inner radius of the accretion disc to $1.24r_{\rm g}$. This allows emission in the very inner regions of the AGN whereas no emission can arise within $6r_{\rm g}$ in Model N07. Figure 3.1 shows example continuum and blurred REFLIONX spectra for (i) $r_{\rm in} = 6r_{\rm g}$ and $q = 3$ and (ii) $r_{\rm in} = 1.24r_{\rm g}$ and $q = 6$. A spectral slope of $\Gamma = 1.9$, disc inclination of $i_{\rm blur} = 40^{\circ}$, ionisation parameter of $\xi_{\rm blur} = 21$ erg cm s^{-1} and reflection strength of $R_{\rm blur}$= 1 are assumed. In the first case, the red wing and blue peak of the iron line can be separated and the line is identifiable in the total spectrum. However in the latter scenario, the line is so heavily blurred that it is not easily possible to distinguish the line from the remainder of the reflection component or the continuum. Nevertheless, the curvature of the 2 – 10 keV spectrum is still affected by the reflection.

We first assume a cold accretion disc (PEXMON) to model the blurred disc reflection, with the ionised version investigated in the next section. This model is referred to as Model SRC ("Strong Relativistic effects with a Cold disc"). Compared to Model N07, the break radius is a redundant parameter, as the two emissivity indices are tied together. However, since the emissivity slope is now a free parameter, unlike in Model N07 where it was fixed, the number of free model parameters is the same in Models SRC and N07.

The best-fit parameters of Model SRC for the narrow-line observations are given in Table 3.7. A significant detection of a blurred reflection component is made in 6/11 observations at a confidence level of 99%: MCG+8-11-11, Mrk 6, Mrk 110, NGC 7469(1), NGC 2110 and HE 1143-1800. The first four objects also gave a detection of disc reflection with Model ION, which does not require a spinning black hole or a steep emissivity profile. Mrk 110 is the only one of these observations with a lower χ^2 compared to Model ION, although Model SRC has one less degree of freedom. NGC 2110 and HE 1143-1800 are the two observations that give a significant detection of the blurred reflection with Model SRC, but not with Model ION.

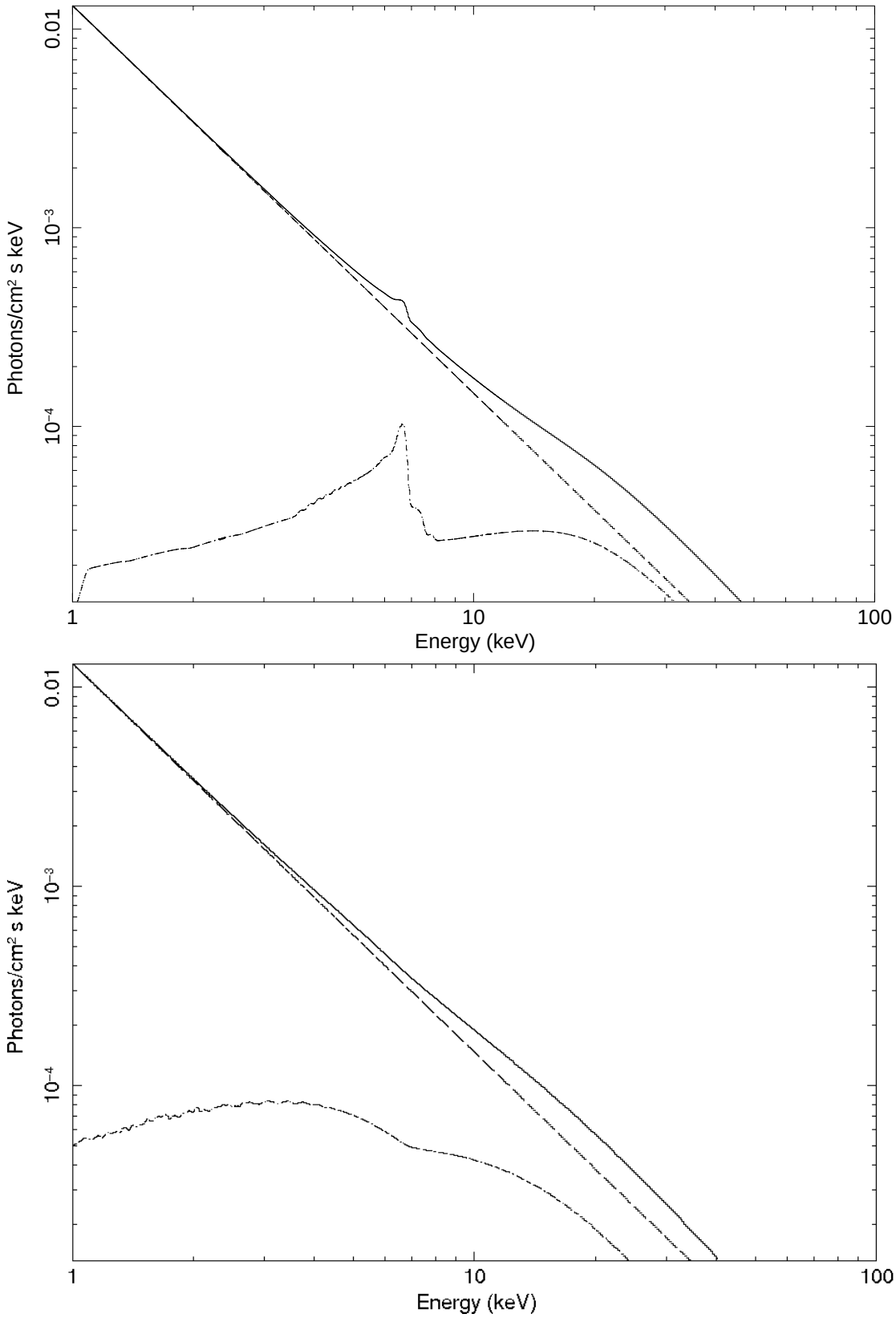

Figure 3.1: Continuum (dashed) and blurred REFLIONX (dot-dashed) spectra with (top) $r_{\rm in} = 6r_{\rm g}$ and $q = 3$ and (bottom) $r_{\rm in} = 1.24r_{\rm g}$ and $q = 6$. The remaining parameters are a spectral slope of $\Gamma = 1.9$, disc inclination of $i_{\rm blur} = 40°$, ionisation parameter of $\xi_{\rm blur} = 21$ erg cm s^{-1} and reflection strength of $R_{\rm blur}$= 1. The total spectrum is shown as a solid line.

Table 3.7: Disc line parameters for the narrow-line observations derived using Model SRC. Column (1): observation name. Column (2): spectral slope. Column (3): reflection fraction of the blurred REFLIONX component. Column (4): inclination of the slab representing the blurred reflector. Column (5): reflection fraction of the distant PEXMON component. Column (6): emissivity index. Column (7): $\Delta\chi^2_{\rm N07-SRC}$ for 2 additional d.o.f.. Column (8): $\Delta\chi^2_{\rm NBR-SRC}$ for 3 additional d.o.f.. Detections of blurred reflection with Model SRC at a significance level of 99% are shown in bold.

Name	Γ	$R_{\rm blur}$ $(\Omega/2\pi)$	$i_{\rm blur}$ $(^\circ)$	$R_{\rm dist}$ $(\Omega/2\pi)$	q	$\Delta\chi^2_{\rm NBR-N07}$	$\Delta\chi^2_{\rm NBR-SRC}$
(1)	(2)	(3)	(4)	(5)	(6)	(7)	(8)
Mrk 590	$1.7^{+0.4}_{-0.1}$	$0.4^{+0.9}_{-0.4}$	48^{+37}_{-48}	$0.3^{+0.3}_{-0.2}$	$3.0^{+6.0}_{-0.0}$	3.2	1.8
NGC 2110	$2.2^{+0.3}_{-0.3}$	$8.2^{+18}_{-6.1}$	61^{+2}_{-14}	$0.9^{+0.1}_{-0.2}$	$8.9^{+0.1}_{-2.6}$	2.6	**9.8**
MCG+8-11-11	$2.0^{+0.2}_{-0.1}$	$3.0^{+3.6}_{-2.3}$	73^{+6}_{-11}	$0.8^{+0.2}_{-0.2}$	$7.3^{+1.7}_{-2.6}$	7.7	**9.7**
Mrk 6	$1.8^{+0.3}_{-0.1}$	$0.9^{+5.4}_{-0.6}$	29^{+21}_{-10}	$0.4^{+0.2}_{-0.2}$	$3.0^{+2.3}_{-0.0}$	7.1	**7.3**
Mrk 110	$2.1^{+0.2}_{-0.1}$	$3.7^{+4.1}_{-0.7}$	60^{+7}_{-4}	$0.3^{+0.1}_{-0.1}$	$7.3^{+1.3}_{-2.2}$	3.7	**14.7**
HE 1143-1810	$2.2^{+0.2}_{-0.3}$	$6.4^{+1.9}_{-5.6}$	58^{+7}_{-58}	$0.3^{+0.1}_{-0.1}$	$8.6^{+0.4}_{-5.0}$	3.0	**8.4**
IC 4329A(1)	$1.9^{+0.2}_{-0.1}$	$0.3^{+2.3}_{-0.2}$	42^{+35}_{-42}	$0.3^{+0.1}_{-0.1}$	$3.0^{+6.0}_{-0.0}$	1.6	1.2
NGC 5506(1)	$2.0^{+0.1}_{-0.1}$	$0.7^{+0.5}_{-0.4}$	46^{+4}_{-4}	$0.6^{+0.3}_{-0.1}$	$3.0^{+1.0}_{-0.0}$	7.1	6.6
NGC 5548(1)	$1.7^{+0.2}_{-0.0}$	$0.1^{+5.7}_{-0.1}$	64^{+21}_{-64}	$0.6^{+0.2}_{-0.2}$	$3.0^{+6.0}_{-0.0}$	0.2	0.1
NGC 7213	$1.9^{+0.3}_{-0.2}$	$1.6^{+2.7}_{-1.6}$	71^{+14}_{-71}	$0.6^{+0.2}_{-0.4}$	$9.0^{+0.0}_{-6.0}$	1.1	0.7
NGC 7469(1)	$2.1^{+0.1}_{-0.1}$	$3.6^{+2.4}_{-2.0}$	81^{+4}_{-6}	$0.8^{+0.2}_{-0.2}$	$8.0^{+1.0}_{-5.0}$	8.2	**13.2**

For the six observations where a blurred reflection component is detected with Model SRC, the fit to the time-averaged spectrum is better than for Model N07. However, with MCG+8-11-11 and Mrk 6, the improvements are smaller than $\Delta\chi^2_{\rm N07-SRC} = 2$. An advantage of Model SRC over Model N07 is that better constraints are generally obtained on the model parameters. The disc inclinations for MCG+8-11-11, Mrk 110 and NGC 7469(1) pegged at 85° with Model N07 while the lower limit of 0° was preferred for NGC 2110 and HE 1143-1800. The inclinations of these five observations no longer peg at the model boundaries as they range from $i_{\rm blur} = 58° - 81°$. While the disc inclination of Mrk 6 does not change significantly from the Model N07 best-fit value, better constraints on the errors are obtained with Model SRC. Apart from Mrk 6, the five other well-fit observations have disc inclinations that are much higher than those typical of the N07 broad line sources ($\langle i_{\rm blur}\rangle = 34.0° \pm 6.4°$), and hint at another reason why no broad line is clearly visible in these objects. The reflection strengths of these five observations are remarkably strong with $\sim R_{\rm blur} > 3$.

The degree of blurring is revealed by the emissivity index. A steep emissivity profile with $q > 7.3$ is found in the same five cases, which is indicative of very strong blurring. For NGC 2110, MCG+8-11-11, Mrk 110 and HE 1143-1800, the uncertainty of the emissivity index is not compatible with $q = 3$, which explains why reflection could not be detected with Model N07. The best-fit reflection strength of Mrk 6 is smaller than the five other well-fit observations, although the upper limit is consistent with being very strong. Furthermore, Mrk 6 requires less concentrated emission from the central regions as its best-fit emissivity slope pegs at $q = 3$.

3.6.2 Strong relativistic effects and ionisation of the accretion disc – Model SRI

In this section, we test if a combination of strong relativistic effects and disc ionisation can reveal the blurred disc reflection in the narrow-line observations. This is achieved by replacing PEXMON in Model SRC with the ionised disc model REFLIONX. This model is termed Model SRI ("Strong Relativistic effects and an Ionised accretion disc"). Compared to Model N07, the black hole is maximally spinning, the accretion disc is ionised and the emissivity slope can be steeper than $q = 3$. The best-fit parameters of Model SRI are given in Table 3.8.

Model SRI provides a significant detection of the blurred reflection in the same 6/11 observations that are well-fit with Model SRC. A further observation, NGC 5506(1) is also well-fit by Model SRI at a confidence level of 99%. Overall, Model

Table 3.8: Disc line parameters for the narrow-line observations derived using Model SRI. Column (1): observation name. Column (2): spectral slope. Column (3): reflection fraction of the blurred REFLIONX component. Column (4): inclination of the slab representing the blurred reflector. Column (5): ionisation parameter of the blurred component. Column (6): reflection fraction of the distant PEXMON component. Column (7): emissivity index. Column (8): $\Delta\chi^2_{\rm N07-SRI}$ for 3 additional d.o.f.. Column (9): $\Delta\chi^2_{\rm NBR-SRI}$ for 4 additional d.o.f.. Detections of blurred reflection with Model SRI at a significance level of 99% are shown in bold.

Name	Γ	$R_{\rm blur}$ $(\Omega/2\pi)$	$i_{\rm blur}$ $(^\circ)$	$\xi_{\rm blur}$ (erg cm s^{-1})	$R_{\rm dist}$ $(\Omega/2\pi)$	q	$\Delta\chi^2_{\rm NBR-N07}$	$\Delta\chi^2_{\rm NBR-SRI}$
(1)	(2)	(3)	(4)	(5)	(6)	(7)	(8)	(9)
Mrk 590	$1.7^{+0.4}_{-0.1}$	$0.7^{+0.2}_{-0.2}$	48^{+37}_{-48}	10^{+864}_{-0}	$0.3^{+0.2}_{-0.2}$	$3.2^{+5.8}_{-0.2}$	3.2	1.9
NGC 2110	$2.3^{+0.2}_{-0.5}$	$5.0^{+5.0}_{-0.3}$	62^{+2}_{-11}	19^{+671}_{-9}	$0.8^{+0.1}_{-0.1}$	$9.0^{+0.0}_{-4.7}$	2.6	**9.9**
MCG+8-11-11	$2.0^{+0.1}_{-0.1}$	$2.7^{+0.3}_{-0.2}$	74^{+2}_{-11}	28^{+200}_{-19}	$0.8^{+0.1}_{-0.1}$	$8.8^{+0.2}_{-5.8}$	7.7	**13.8**
Mrk 6	$1.8^{+0.2}_{-0.1}$	$1.2^{+0.6}_{-0.6}$	30^{+14}_{-9}	11^{+96}_{-1}	$0.3^{+0.2}_{-0.2}$	$3.0^{+1.8}_{-0.0}$	7.1	**8.1**
Mrk 110	$2.3^{+0.1}_{-0.1}$	$0.8^{+1.0}_{-0.8}$	64^{+1}_{-6}	54^{+47}_{-18}	$0.2^{+0.1}_{-0.1}$	$8.9^{+0.1}_{-3.5}$	3.7	**20.5**
HE 1143-1810	$2.1^{+0.3}_{-0.2}$	$3.0^{+0.4}_{-0.3}$	58^{+12}_{-19}	77^{+116}_{-54}	$0.3^{+0.1}_{-0.2}$	$6.9^{+2.1}_{-3.1}$	3.0	**12.8**
IC 4329A(1)	$1.9^{+0.2}_{-0.2}$	$0.5^{+0.3}_{-0.3}$	85^{+0}_{-85}	220^{+904}_{-210}	$0.2^{+0.1}_{-0.1}$	$3.0^{+6.0}_{-0.0}$	1.6	1.3
NGC 5506(1)	$2.0^{+0.1}_{-0.1}$	$0.7^{+0.3}_{-0.4}$	46^{+5}_{-4}	10^{+15}_{-0}	$0.5^{+0.1}_{-0.1}$	$3.0^{+0.8}_{-0.0}$	7.1	**8.0**
NGC 5548(1)	$1.6^{+0.3}_{-0.6}$	$0.8^{+0.3}_{-0.3}$	4^{+65}_{-4}	4415^{+3960}_{-4405}	$0.4^{+0.1}_{-0.1}$	$3.5^{+5.2}_{-0.5}$	0.2	1.7
NGC 7213	$1.8^{+0.1}_{-0.4}$	$0.1^{+0.1}_{-0.1}$	69^{+16}_{-69}	1352^{+8670}_{-1330}	$0.5^{+0.1}_{-0.1}$	$9.0^{+0.0}_{-6.0}$	1.1	0.7
NGC 7469(1)	$2.0^{+0.1}_{-0.1}$	$1.3^{+0.3}_{-0.3}$	76^{+7}_{-23}	100^{+142}_{-90}	$0.7^{+0.2}_{-0.1}$	$7.1^{+1.9}_{-4.1}$	8.2	**14.9**

SRI performs better than Model SRC for all seven observations but with one more degree of freedom, Model SRI outperforms Model SRC by $\Delta\chi^2_{\rm SRC-SRI} > 3$ in only 3 observations: MCG+8-11-11, Mrk 110 and HE 1143-1800. This suggests that disc ionisation may be the most important factor in revealing the blurred disc reflection in these 3 observations, whereas strong relativistic effects may be the dominant factor in the 3 other observations that are well-fit by Models SRC and SRI. In no case is a disc ionisation higher than $\xi_{\rm blur} = 100$ erg cm s^{-1} preferred across the seven observations. Model SRI is also superior to Model ION for 6 of the 7 well-fit observations. The exception is Mrk 6, which marginally prefers Model ION over Model SRI. As with Model SRC, a steep emissivity index of $q > 6.9$ is preferred in 5/7 observations apart from Mrk 6 and NGC 5506(1), where it pegged at $q = 3$. This is unsurprising in the case of NGC 5506(1) as the fit of Model N07, where the emissivity slope cannot be steeper than $q = 3$ is comparable to that of Model SRI. Likewise, the disc inclinations found with Model SRI are very close to those given by Model SRC. They are higher than $i_{\rm blur} = 54^\circ$ for 5/7 of the well-fit observations, although Mrk 6 and NGC 5506(1) have lower inclinations, consistent with the 18 "relativistic-line" observations classified by N07. Unlike Model SRC, the upper error on the inclination for NGC 7469(1) does not extend to the model limit but it is still the highest of all the narrow-line observations. Another difference with Model SRC is that the REFLIONX reflection strengths of the 7 well-fit observations span a smaller range of $0.7 < R_{\rm blur} < 5.0$, although in most cases, this is still stronger than expected in the standard model.

The unfolded spectra of Model SRI for the seven well-fit narrow-line observations are shown in Figure 3.2. The strength of blurring required can be seen to be very strong as in most cases, it is difficult to identify the iron line in the reflection component. However, the reflection component clearly does change the spectral curvature across 2 – 10 keV, without which there would be no improvement in the quality of fits compared to Model NBR.

3.7 Non-relativistic iron lines

The focus of this section is on the 8 observations that are classed by N07 as possessing a non-relativistically broadened iron line. This class of observations is made up of those that have a break radius of $r_{\rm br} > 50 r_{\rm g}$ in Model N07. A similar question as asked of the narrow-line observations can be applied to the non-relativistic group: why is the iron line not relativistically broadened? The solution may be the same in that the accretion disc reflection is heavily blurred and therefore difficult to detect.

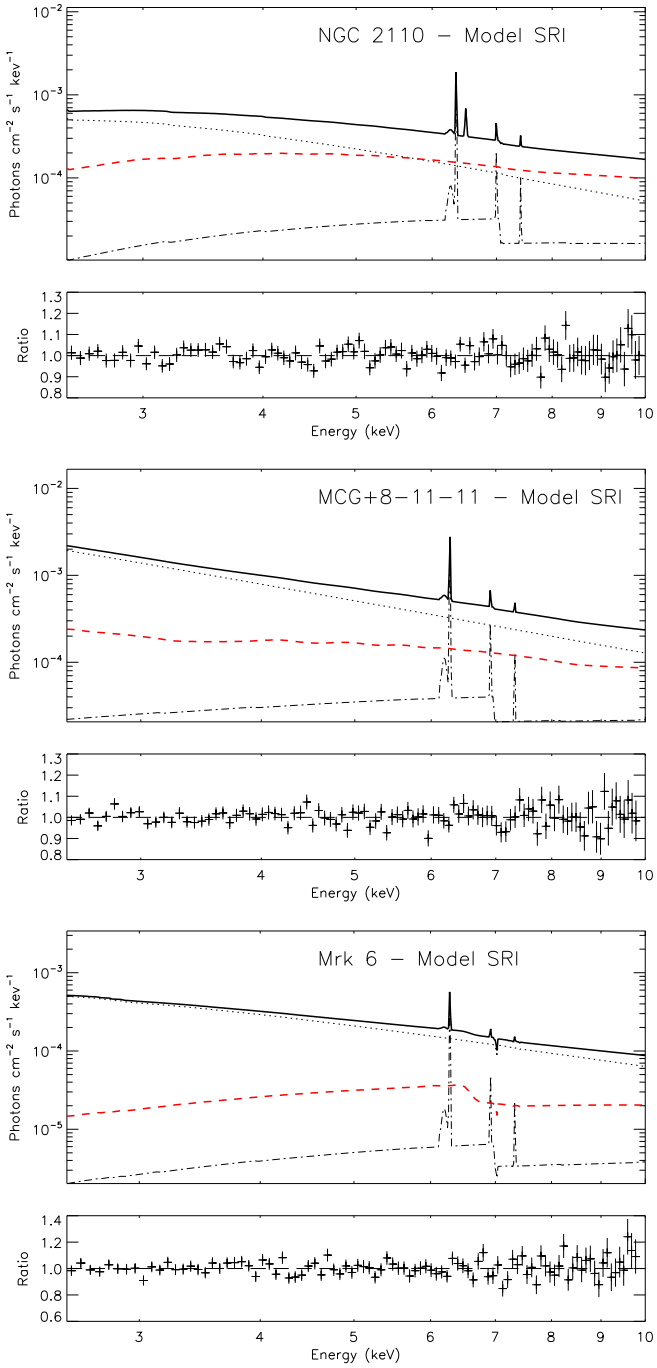
NGC 2110 – Model SRI
Photons cm^{-2} s^{-1} kev^{-1}
Ratio
Energy (keV)
MCG+8–11–11 – Model SRI
Photons cm^{-2} s^{-1} kev^{-1}
Ratio
Energy (keV)
Mrk 6 – Model SRI
Photons cm^{-2} s^{-1} kev^{-1}
Ratio
Energy (keV)

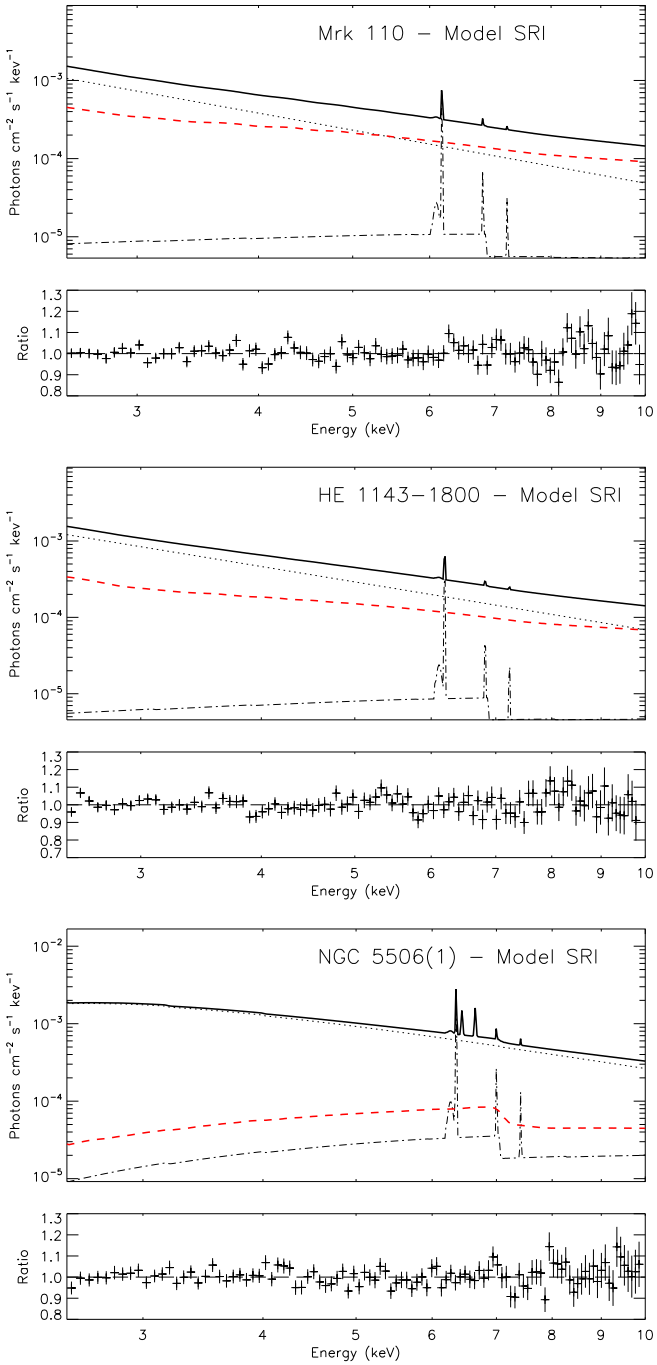
Mrk 110 – Model SRI
Photons cm^{-2} s^{-1} kev^{-1}
Ratio
Energy (keV)
HE 1143–1800 – Model SRI
Photons cm^{-2} s^{-1} kev^{-1}
Ratio
Energy (keV)
NGC 5506(1) – Model SRI
Photons cm^{-2} s^{-1} kev^{-1}
Ratio
Energy (keV)

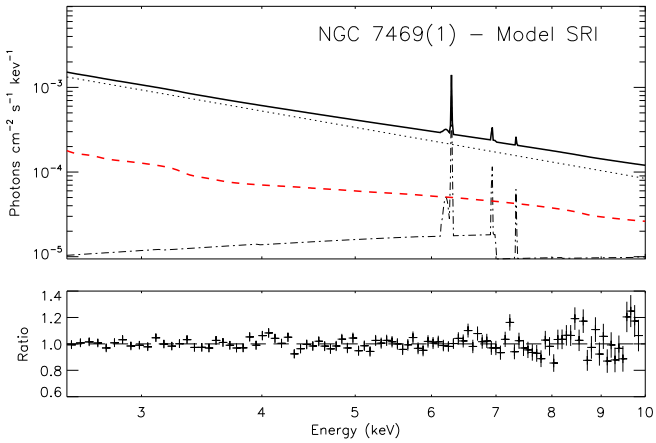

Figure 3.2: The unfolded 2.5 – 10 keV spectrum and data/model ratio for the seven narrow-line observations that are well-fit with strongly smeared reflection and an ionised disc. The power-law continuum is shown with a dotted line. The blurred and distant reflection are shown with red dashed and dash-dotted lines respectively. The total spectrum is shown as a solid line.

In this case, the additional problem is to determine the origin of the iron line.

The line is unlikely to originate in the torus as the typical width of ~ 0.24 keV is too large to be produced so far away from the nucleus. A possible alternative is production in gas closer to the black hole that would be subject to stronger gravitational forces. If this gas is associated with the optical BLR instead of the accretion disc or torus, the iron line will be accompanied by a much fainter Compton reflection component as the BLR is expected to be Compton-thin (Bianchi et al., 2008b). In this scenario, assuming that the gas is present at distance r from the central black hole, the width of the iron line component, $\sigma_{\rm Fe}$ would be:

$$\sigma_{\rm Fe} = \frac{\Delta E}{2.4} = \frac{6.4v}{2.4c} = \frac{6.4}{2.4c}\sqrt{\frac{GM_\bullet}{r}} \tag{3.4}$$

where ΔE is the FWHM of the iron line (in keV) and v is the Keplerian velocity at radius r. For example, for gas present at $\sim 100r_{\rm g}$, the width of the line would be 0.27 keV. We add a Gaussian model component, "ZGAUSS" to Models SRC and SRI and apply both to the "non-relativistic-line" observations. We adopt $100r_{\rm g}$ as the smallest reasonable radius for the BLR clouds. The width of the line is allowed to be less than 0.27 keV however, as the gas may be present at a larger distance. The energy of the line is fixed to 6.4 keV as the iron line emission is expected to be cold.

The significance of a detection of the blurred reflection in the non-relativistic observations can be determined in a similar way as for the narrow-line observations

(see Section 3.4.3). The only difference is that Model NBR now also includes a ZGAUSS component to model the BLR iron line, as with Models SRC and SRI. The width and normalisation of the Gaussian is set to that found by the best-fit of the model being considered for each observation. The 99% confidence thresholds are shown in Table 3.9.

Table 3.9: The 99% threshold $\Delta\chi^2_{\rm NBR-Y}$ relative to Model NBR for the non-relativistic-line observations, where Y is the model of interest. A Gaussian component is also included to model iron line emission from BLR-type gas.

Name	99% threshold limit	
	$\Delta\chi^2_{\rm NBR-SRC}$	$\Delta\chi^2_{\rm NBR-SRI}$
Ark 120	8.4	8.7
MCG-5-23-16(1)	10.2	10.8
NGC 4151(1)	9.3	9.4
NGC 4151(2)	11.3	11.7
NGC 4593	7.9	8.2
IC 4329A(2)	10.5	11.0
NGC 5548(2)	9.6	9.8
Ark 564	12.1	13.0

3.7.1 Model SRC

The best-fit parameters of Model SRC for the non-relativistic-line observations are shown in Table 3.10. A blurred disc component is significantly detected in 6/8 cases with MCG-5-23-16(1) and IC 4329A(2) providing the exceptions. Overall, the goodness-of-fits are better than for Model N07 with a mean improvement of $\Delta\chi^2_{\rm N07-SRC} \sim 8.7$ for two additional degrees of freedom, excluding MCG-5-23-16(1) which is fit less well than with Model N07.

As mentioned above, the width of the BLR iron line is related to the distance of the line-producing gas. In half the cases with Model SRC, the width pegged at the maximum, suggesting an origin closer than $100r_{\rm g}$. In reality, this is probably due to degeneracies in fitting the BLR and relativistic lines simultaneously, coupled with the finite resolution of the EPIC-pn detector. For the four remaining observations, the emitting gas is present between $330-739r_{\rm g}$. As with the narrow-line observations (see Section 3.6.1), a steep emissivity profile is essential for the blurred reflection component with $q > 6.3$ preferred in 5/6 of the well-fit observations. A lower best-fit emissivity index of $q = 3.8$ is found for NGC 4151(1), which also differs from the

Table 3.10: Disc line parameters derived for the non-relativistic observations using Model SRC. Column (1): observation name. Column (2): spectral slope. Column (3): reflection fraction of the blurred component. Column (4): inclination of the slab representing the blurred reflector. Column (5): reflection fraction of the distant component. Column (6): width of the broad Gaussian iron line (keV). Column (7): emissivity index. Column (8): $\Delta\chi^2_{\rm N07-SRC}$ for 2 additional d.o.f.. Column (9): $\Delta\chi^2_{\rm NBR-SRC}$ for 3 additional d.o.f.. Detections of blurred reflection with Model SRC at a significance level of 99% are shown in bold.

Name	Γ	$R_{\rm blur}$ $(\Omega/2\pi)$	$i_{\rm blur}$ $(^\circ)$	$R_{\rm dist}$ $(\Omega/2\pi)$	$\sigma_{\rm Fe}$ (keV)	q	$\Delta\chi^2_{\rm N07-SRC}$	$\Delta\chi^2_{\rm NBR-SRC}$
(1)	(2)	(3)	(4)	(5)	(6)	(7)	(8)	(9)
Ark 120	$2.2^{+0.1}_{-0.1}$	$5.3^{+2.0}_{-1.9}$	84^{+1}_{-5}	$0.3^{+0.2}_{-0.1}$	$0.3^{+0.0}_{-0.0}$	$9.0^{+0.0}_{-3.0}$	15.6	**54.0**
MCG-5-23-16(1)	$1.9^{+0.4}_{-0.1}$	$0.9^{+6.9}_{-0.9}$	41^{+16}_{-41}	$0.1^{+0.7}_{-0.0}$	$0.1^{+0.2}_{-0.0}$	$3.0^{+6.0}_{-0.0}$	-1.1	5.9
NGC 4151(1)	$1.9^{+0.1}_{-0.1}$	$4.0^{+3.0}_{-1.8}$	43^{+3}_{-3}	$1.9^{+1.0}_{-0.8}$	$0.1^{+0.1}_{-0.0}$	$3.8^{+0.7}_{-0.2}$	15.3	**23.7**
NGC 4151(2)	$1.8^{+0.1}_{-0.2}$	$3.8^{+0.7}_{-1.9}$	60^{+2}_{-13}	$2.1^{+0.9}_{-0.3}$	$0.3^{+0.0}_{-0.3}$	$7.5^{+1.5}_{-0.9}$	4.1	**69.7**
NGC 4593	$2.0^{+0.1}_{-0.2}$	$2.3^{+2.3}_{-1.8}$	60^{+19}_{-10}	$0.4^{+0.2}_{-0.3}$	$0.1^{+0.1}_{-0.1}$	$6.3^{+2.0}_{-2.8}$	7.2	**11.7**
IC 4329A(2)	$1.8^{+0.1}_{-0.1}$	$0.7^{+1.1}_{-0.7}$	73^{+13}_{-73}	$0.3^{+0.0}_{-0.1}$	$0.3^{+0.0}_{-0.1}$	$8.9^{+0.1}_{-6.1}$	3.0	1.8
NGC 5548(2)	$2.0^{+0.1}_{-0.1}$	$3.1^{+3.6}_{-1.8}$	63^{+2}_{-63}	$0.3^{+0.2}_{-0.2}$	$0.2^{+0.1}_{-0.1}$	$9.0^{+0.0}_{-2.8}$	12.8	**12.9**
Ark 564	$2.7^{+0.1}_{-0.1}$	$3.4^{+1.8}_{-2.5}$	$73^{+6.}_{-15}$	$0.0^{+0.1}_{-0.0}$	$0.3^{+0.0}_{-0.1}$	$7.6^{+1.4}_{-2.2}$	3.6	**14.8**

other five observations as it is fit with a low disc inclination of $i_{\rm blur} = 43°$. However, it is consistent with the 18 N07 relativistic-line observations. There is an agreement of a high disc inclination ($i_{\rm blur} > 60°$) between the narrow-line and non-relativistic-line observations fit well with Model SRC. However, the disc inclination can only be constrained in 4/6 of the well-fit cases. Another similarity with the narrow-line observations is that the reflection strengths of all six are stronger than found with Model N07.

3.7.2 Model SRI

The best-fit parameters of Model SRI for the non-relativistic-line observations are shown in Table 3.11. A blurred and ionised disc component is detected in the same 6/8 observations that are found to possess blurred reflection with Model SRC. The only cases where Model SRI produces a better fit than Model SRC by $\Delta\chi^2_{\rm SRC-SRI} > 5$ are Ark 120 and NGC 4593, primarily as these are the only two observations that are well-fit with an ionisation parameter of $\xi_{\rm blur} > 100$ erg cm s^{-1}.

The best-fit model parameters differ between Models SRC and SRI. Compared to Model SRC, the width of the BLR iron line now only pegs at the model limit for Ark 120. Interestingly, 5/6 of the well-fit observations have a disc inclination less than 49° with only Ark 120 preferring a higher inclination. Similarly, the disc reflection strengths are also lower in Model SRI with only three of the well-fit observations having reflection strengths of $R_{\rm blur} > 1.5$: Ark 120, NGC 4151(1) and NGC 4151(2). The disc reflection in Ark 564 is very weak and this observation also stands out for its steep continuum slope of $\Gamma = 2.62$. Both NGC 4593 and NGC 5548(2) have a reflection strength of $R_{\rm blur} \sim 1$, consistent with the relativistic-line observations. NGC 4151(1), NGC 4151(2), NGC 4593, NGC 5548(2) and Ark 564 are best-fit with smaller emissivity indices of $q < 4.5$, compared to the larger indices found with Model SRC.

The unfolded Model SRI spectra of the six well-fit non-relativistic-line observations are shown in Figure 3.3. As with the narrow-line observations, the blurred iron line is difficult to discern from the remainder of the accretion disc reflection component. NGC 4151(2) is a good example of the advantage Model SRI has over Model N07 as the strengths of the BLR iron line and the disc reflection are allowed to be different.

Table 3.11: Disc line parameters derived for the non-relativistic observations using Model SRI. Column (1): observation name. Column (2): spectral slope. Column (3): reflection fraction of the blurred component. Column (4): inclination of the slab representing the blurred reflector. Column (5): ionisation parameter of the blurred component. Column (6): reflection fraction of the distant component. Column (7): width of the broad Gaussian iron line (keV). Column (8): emissivity index. Column (9): $\Delta\chi^2_{\rm N07-SRI}$ for 3 additional d.o.f.. Column (10): $\Delta\chi^2_{\rm NBR-SRI}$ for 4 additional d.o.f.. Detections of blurred reflection with Model SRI at a significance level of 99% are shown in bold.

Name	Γ	$R_{\rm blur}$	$i_{\rm blur}$	$\xi_{\rm blur}$	$R_{\rm dist}$	$\sigma_{\rm Fe}$	q	$\Delta\chi^2_{\rm N07-SRI}$	$\Delta\chi^2_{\rm NBR-SRI}$
		$(\Omega/2\pi)$	$(^\circ)$	(erg cm s^{-1})	$(\Omega/2\pi)$	(keV)			
(1)	(2)	(3)	(4)	(5)	(6)	(7)	(8)	(9)	
Ark 120	$2.1^{+0.1}_{-0.1}$	$1.8^{+0.2}_{-0.2}$	76^{+2}_{-13}	100^{+69}_{-75}	$0.3^{+0.2}_{-0.1}$	$0.3^{+0.0}_{-0.0}$	$8.6^{+0.4}_{-2.1}$	25.5	**63.9**
MCG-5-23-16(1)	$2.0^{+0.3}_{-0.6}$	$1.8^{+0.8}_{-0.8}$	43^{+25}_{-4}	10^{+191}_{-0}	$0.3^{+0.2}_{-0.3}$	$0.3^{+0.0}_{-0.3}$	$3.5^{+5.5}_{-0.5}$	-2.7	4.3
NGC 4151(1)	$1.9^{+0.1}_{-0.1}$	$4.3^{+5.7}_{-1.1}$	43^{+4}_{-3}	14^{+159}_{-4}	$2.0^{+0.8}_{-0.8}$	$0.1^{+0.0}_{-0.0}$	$3.7^{+0.8}_{-0.5}$	14.3	**22.6**
NGC 4151(2)	$1.8^{+0.1}_{-0.2}$	$3.5^{+0.9}_{-0.4}$	48^{+18}_{-5}	64^{+115}_{-42}	$2.0^{+1.1}_{-1.0}$	$0.1^{+0.1}_{-0.1}$	$4.5^{+3.8}_{-0.8}$	3.9	**70.0**
NGC 4593	$1.9^{+0.3}_{-0.0}$	$0.9^{+0.3}_{-0.2}$	43^{+32}_{-9}	147^{+54}_{-108}	$0.4^{+0.3}_{-0.3}$	$0.1^{+0.1}_{-0.0}$	$3.2^{+4.6}_{-0.2}$	14.0	**18.1**
IC 4329A(2)	$1.8^{+0.0}_{-0.1}$	$0.5^{+0.1}_{-0.1}$	46^{+7}_{-3}	12^{+58}_{-2}	$0.2^{+0.1}_{-0.1}$	$0.1^{+0.1}_{-0.1}$	$3.0^{+6.0}_{-0.0}$	4.0	2.9
NGC 5548(2)	$1.9^{+0.2}_{-0.1}$	$1.0^{+0.1}_{-0.1}$	29^{+26}_{-29}	10^{+107}_{-0}	$0.3^{+0.2}_{-0.3}$	$0.2^{+0.1}_{-0.1}$	$3.9^{+1.6}_{-0.9}$	11.5	**11.5**
Ark 564	$2.6^{+0.1}_{-0.1}$	$0.1^{+4.9}_{-0.1}$	46^{+6}_{-14}	46^{+263}_{-24}	$0.0^{+0.2}_{-0.0}$	$0.3^{+0.0}_{-0.1}$	$3.0^{+0.6}_{-0.0}$	8.3	**19.4**

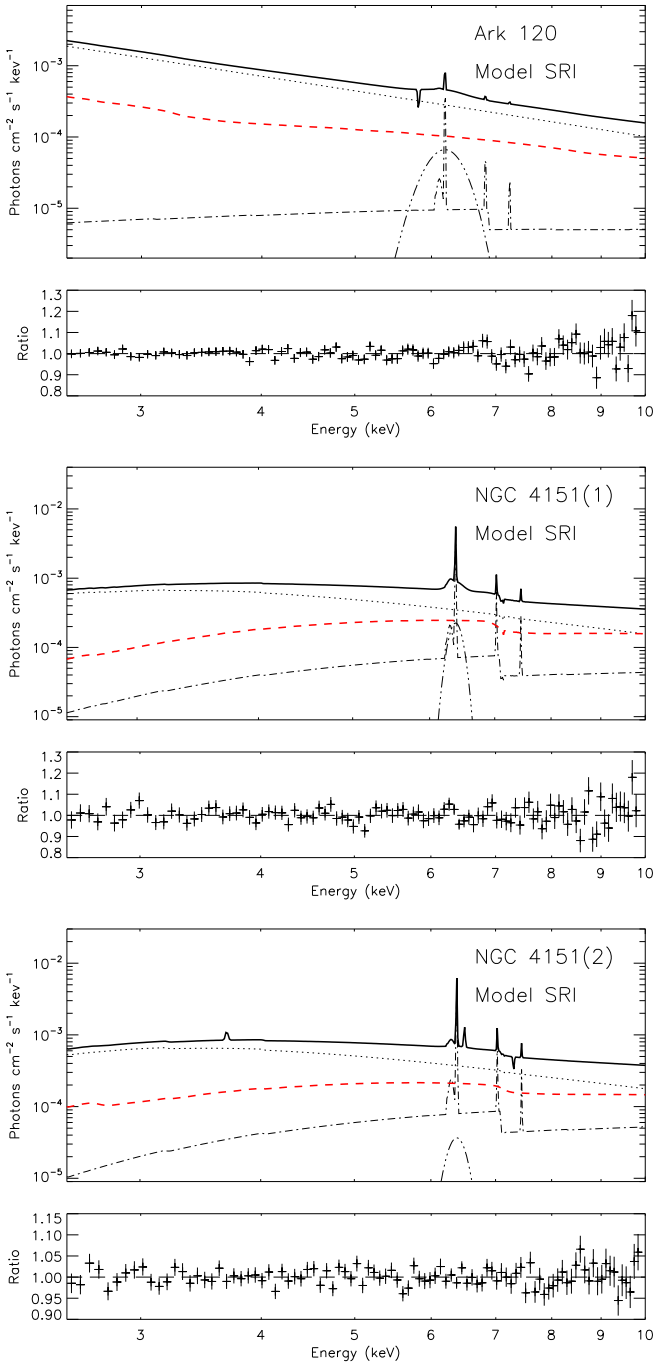
Ark 120
Model SRI
Photons cm^{-2} s^{-1} kev^{-1}
Ratio
Energy (keV)
NGC 4151(1)
Model SRI
Photons cm^{-2} s^{-1} kev^{-1}
Ratio
Energy (keV)
NGC 4151(2)
Model SRI
Photons cm^{-2} s^{-1} kev^{-1}
Ratio
Energy (keV)

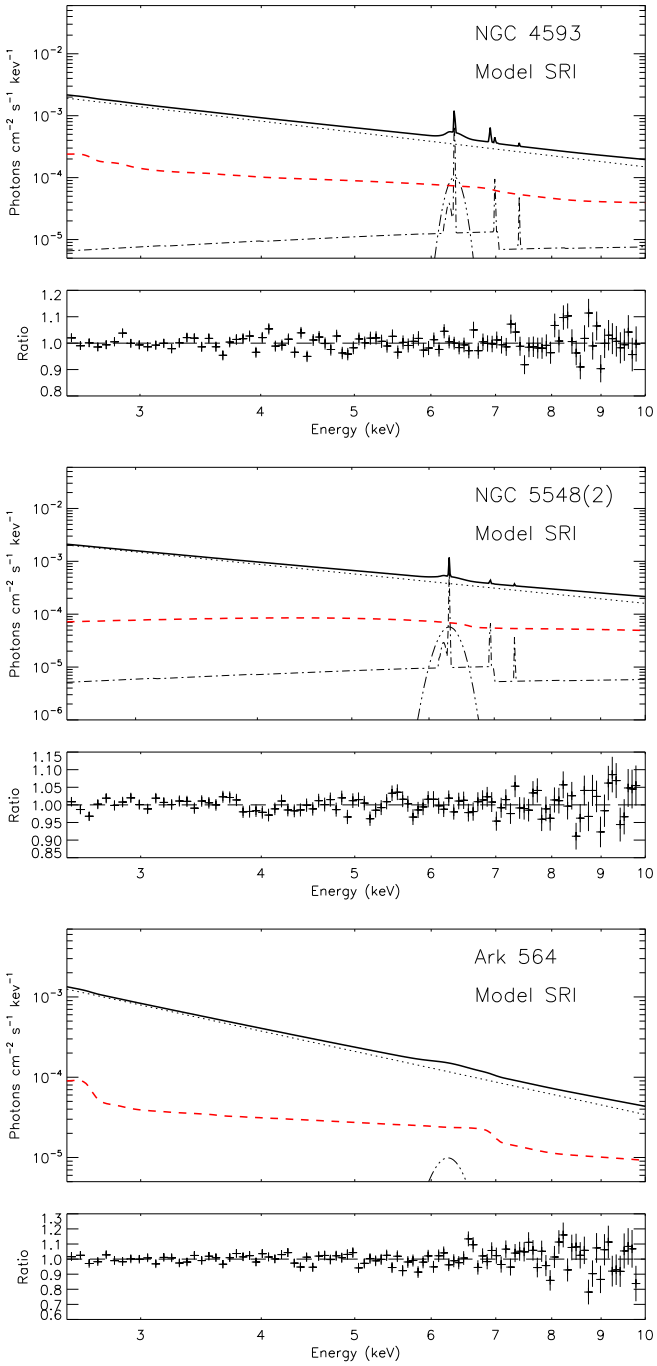

Figure 3.3: The unfolded 2.5 – 10 keV spectrum and data/model ratio for the 6/8 non-relativistic-line observations that are well-fit with strongly smeared reflection and an ionised disc (Model SRI). The identification of the model components is the same as for Figure 3.2. In addition, the BLR iron line is shown with a dashed-dot-dot-dot line.

3.7.2.1 Reflection strength

The disc reflection strengths derived from Model SRI, which includes both strong relativistic effects and disc ionisation, can be compared to those of the 18 N07 observations with a relativistically broadened iron line. Model SRI is used as it generally gave the best fit to most of the observations and all 19 narrow- and non-relativistic-line observations are considered. Using the maximum likelihood method of Maccacaro et al. (1988), the narrow-line observations have a mean reflection strength of $\langle R_{\rm blur} \rangle = 1.65 \pm 0.42$ with an intrinsic spread of $\sigma_{R_{\rm blur}} = 1.51 \pm 0.36$. This is slightly larger than the reflection strengths of the non-relativistic observations, which have a mean of $\langle R_{\rm blur} \rangle = 1.41 \pm 0.51$ and spread of $\sigma_{R_{\rm blur}} = 0.77 \pm 0.53$. However, both groups exhibit much stronger reflection than the relativistic-line observations of N07, who showed an average reflection strength of $\langle R_{\rm blur} \rangle = 0.79 \pm 0.11$ with an intrinsic spread of $\sigma_{R_{\rm blur}} = 0.23 \pm 0.14$ with Model N07. A histogram of the reflection strengths of the three groups is shown in the top panel of Figure 3.4. Thus, on the face of it (and somewhat paradoxically), the observations with no apparent relativistically broadened line seem to have *stronger* reflection than those in which the broad, skewed line can be seen.

Before drawing this conclusion, however, we consider the fact that the narrow- and non-relativistic-line observations also exhibit on average a higher disc inclination, $\langle i_{\rm blur} \rangle = 62.9^\circ \pm 7.6^\circ$ and $\langle i_{\rm blur} \rangle = 49.5^\circ \pm 9.0^\circ$ respectively, than the relativistic-line observations, for which $\langle i_{\rm blur} \rangle = 34.1^\circ \pm 6.3^\circ$. For the narrow-line observations in particular, this in itself provides a partial explanation for the difficulty in detecting the broad lines in N07, as the higher inclination sources will suffer stronger Doppler effects that further blend the line into the continuum. The fact that the higher inclination sources also show larger reflection fractions is somewhat suspicious, as it implies the total strength of the reflection is similar, whereas it should be weaker in the case of the highly inclined sources. Reflection fractions greater than one imply that the emission from the power-law source is anisotropic. To compare these more directly, we follow Crummy et al. (2006) and use a more robust measure of the reflection strength, which we call the reflected flux fraction (RFF). This is the ratio of the blurred reflected flux to the continuum flux between 2.5 – 10 keV. The mean RFF of the narrow- and non-relativistic-line observations are $\langle {\rm RFF} \rangle = 0.17 \pm 0.08$ and $\langle {\rm RFF} \rangle = 0.14 \pm 0.04$ with intrinsic dispersions of $\sigma_{\rm RFF} = 0.12 \pm 0.04$ and $\sigma_{\rm RFF} = 0.06 \pm 0.01$ respectively. These are now more consistent with the N07 relativistic-line observations, which have a mean RFF of $\langle {\rm RFF} \rangle = 0.13 \pm 0.04$ with an intrinsic dispersion of $\sigma_{\rm RFF} = 0.03 \pm 0.01$. A histogram of the RFFs of the observations are shown in the bottom panel of Figure 3.4. Therefore, after accounting for

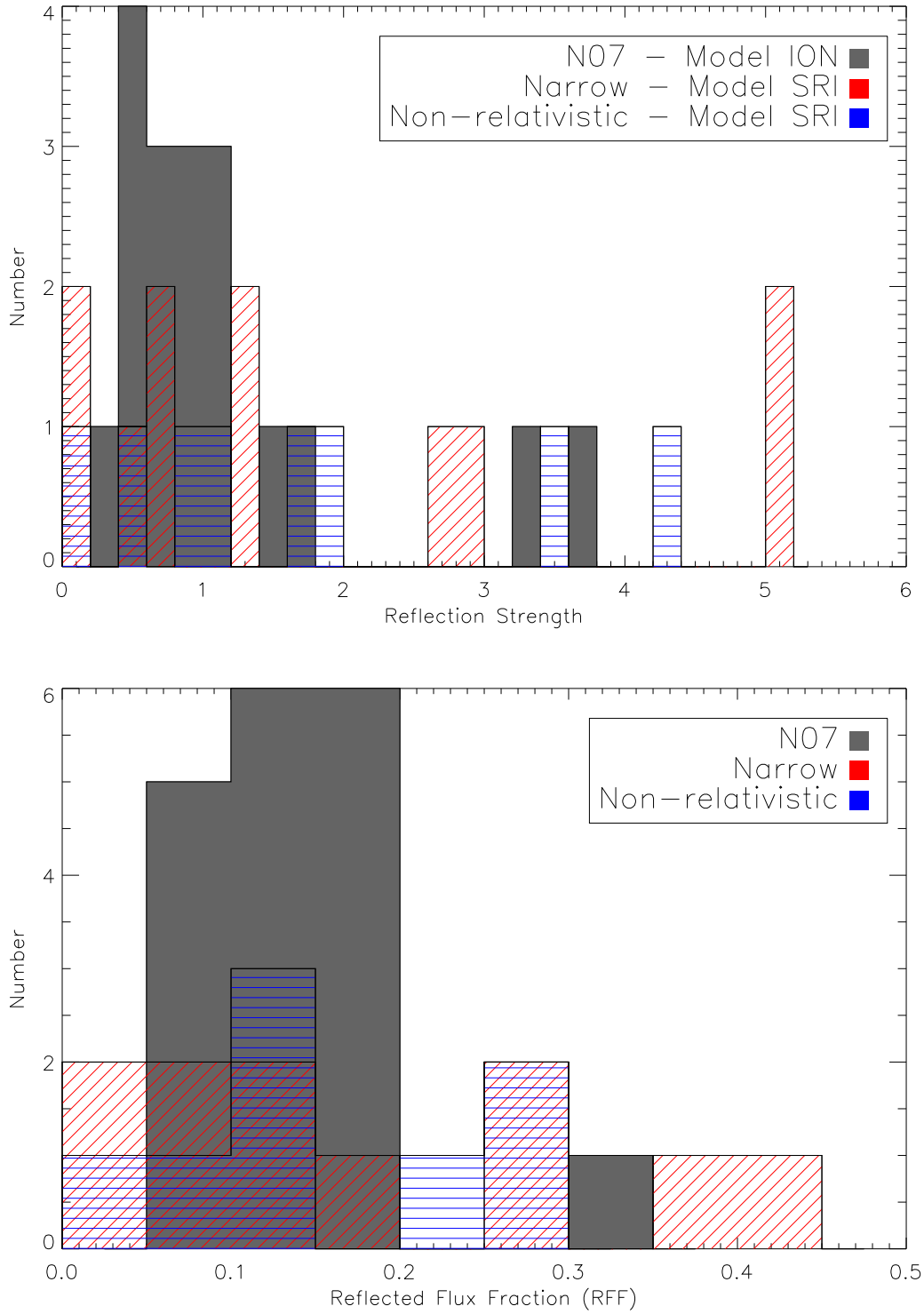

Figure 3.4: Histograms of the disc reflection strengths (top panel) and RFFs (bottom panel) of the observations in the sample. The reflection strengths and RFFs of the narrow- (red line) and non-relativistic-line (blue line) observations are obtained from the best-fits of Model SRI. The reflection strengths and RFFs of the relativistic-line observations (grey shaded) are calculated using Model ION (see the Appendix for a fit of Model ION to the relativistic-line observations).

inclination effects, we conclude that the strength of the blurred disc reflection in the narrow- and non-relativistic-line observations is similar to that of the observations with a relativistically broadened iron line.

3.7.3 The N07 relativistic-line observations

As some of the narrow-line and non-relativistic-line observations have shown evidence for ionised and/or strongly blurred disc reflection, we test if these effects are also evident in the 18 N07 relativistic-line observations. The fits of Model ION to the observations are detailed in the Appendix. As Model ION has the extra free parameter to account for the disc ionisation state compared to Model N07, the majority of the relativistic-line observations are better fit by Model ION than Model N07. However, in only three cases is the fit better than $\Delta\chi^2_{\rm N07-ION} = 5$: NGC 4151(3), MCG-6-30-15(1) and MCG-6-30-25(2). The ionisation parameter in all 3 cases is less than $\xi_{\rm blur} = 21$ erg cm s^{-1}, which is relatively mild. The presence of strong relativistic effects and a cold accretion disc (Model SRC) does not improve the fit more than marginally except in the case of NGC 3516(1), where $\Delta\chi^2_{\rm N07-SRC} = 8$. The emissivity slope is best-fit by $q = 3.3$ which is slightly steeper than the maximally allowed value of $q = 3$ in Model N07. Similarly, only MCG-6-30-15(2) shows a strong improvement when strong relativistic effects and an ionised accretion disc (Model SRI) are considered, with $\Delta\chi^2_{\rm N07-SRI} = 16$ relative to Model ION. As with NGC 3516(1), the best-fit emissivity slope of $q = 3.2$ is not as steep as found with some of the non-relativistic line and narrow-line observations. Overall, nearly all of the N07 relativistic-line observations are fit best by a combination of a cold accretion disc and an emissivity slope that is no steeper than expected from the standard model.

3.7.4 Objects with no detected blurred reflection

Four narrow-line observations do not show evidence for ionised and/or strongly blurred reflection: Mrk 590, IC 4329A(1), NGC 5548(1) and NGC 7213. Equivalently, such reflection is also not detected in two non-relativistic-line observations: MCG-5-23-16(1) and IC 4329A(2). The unfolded Model SRI spectra of these observations are shown in Figures 3.5 and 3.6 where the 90% upper limit on the blurred reflection component is also displayed. While, there is no significant detection of the blurred disc reflection, the upper limit is stronger than the distant reflection so it appears that the upper limits are at least consistent with the detection of blurred reflection in the well-fit cases.

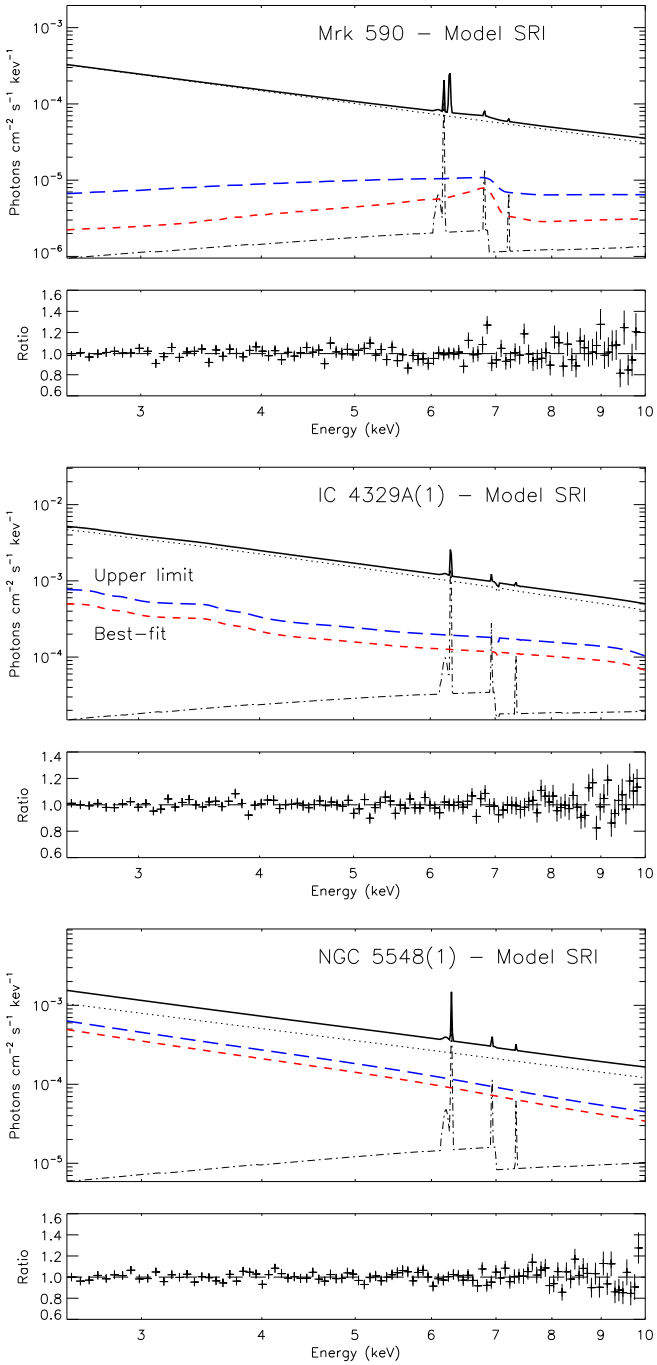
Mrk 590 – Model SRI
Photons cm^{-2} s^{-1} kev^{-1}
Ratio
Energy (keV)
IC 4329A(1) – Model SRI
Upper limit
Best–fit
Photons cm^{-2} s^{-1} kev^{-1}
Ratio
Energy (keV)
NGC 5548(1) – Model SRI
Photons cm^{-2} s^{-1} kev^{-1}
Ratio
Energy (keV)

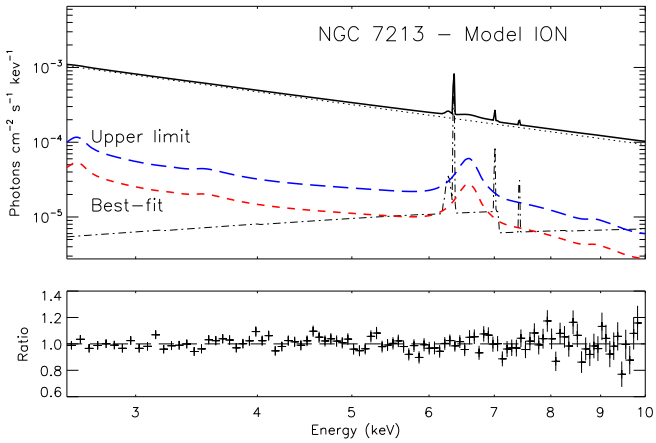

Figure 3.5: The unfolded 2.5 – 10 keV spectrum and data/model ratio for the 4/11 narrow-line observations that do not show a significant improvement when fit with strongly smeared reflection and/or an ionised disc. The spectrum of Model SRI is shown for Mrk 590, IC 4329A(1) and NGC 5548(1) with the identity of the model components being the same as in Figure 3.2. The Model ION spectrum is plotted for NGC 7213 as this model is superior to Model SRI. The blue long-dashed line shows the 90% upper limit on the REFLIONX model component.

High ionisation parameters with Model SRI could explain why no disc reflection is detected in NGC 5548(1) and NGC 7213. Mrk 590 and IC 4329A(1) are similar to Mrk 6 and NGC 5506(1) in that they are best-fit with a small reflection strength and an emissivity index close to $q = 3$. However, while Mrk 590 has a moderate disc inclination, our view of the disc in IC 4329A(1) is edge-on in Model SRI. In this case, if it is true that the disc inclination is high but the relativistic effects are not strong, the reflection and iron line would be expected to be faint and extremely difficult to identify in *XMM-Newton* spectra. IC 4329A is unique in the sample as the only object that does not display a relativistically broadened iron line in multiple observations. A high inclination does not seem to be preferred in the second, non-relativistic-line observation, as it is fit with a lower disc inclination of $i_{\rm blur} = 30°$ and 50° by both Models N07 and SRI respectively. MCG-5-23-16 differs from IC 4329A in that one of its observations is found by N07 to have a relativistic line. MCG-5-23-16(1) may possibly appear to lack relativistic reflection due to low S/N as it has the second smallest exposure in the sample.

3.8 Discussion

We have re-analysed 19 *XMM-Newton* spectra of the Seyfert galaxies classified by N07 as not requiring an accretion disc iron line that is relativistically broadened in

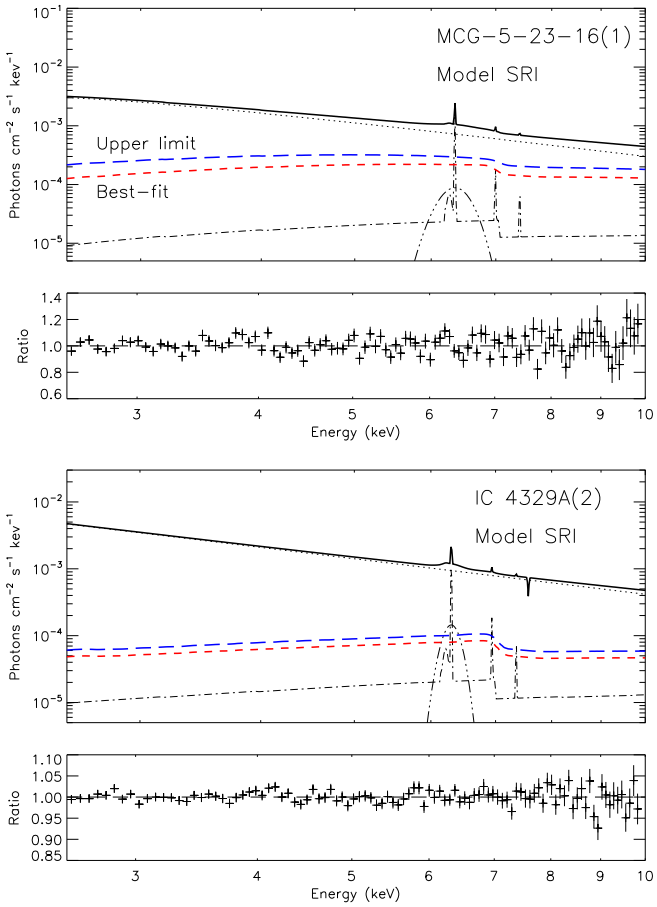

Figure 3.6: The unfolded 2.5 – 10 keV spectrum and data/model ratio for the 2/8 non-relativistic-line observations that do not show a significant improvement when fit with strongly smeared reflection and an ionised disc. The spectrum of Model SRI is shown with the identity of the model components being the same as in Figure 3.5

a simple analysis. By fitting models which allow the disc to be ionised, or to have stronger relativistic effects in a Kerr geometry, we have found that 7/11 narrow-line observations and 6/8 non-relativistic-line observations, in fact, do show evidence for a significant blurred reflection component. The reflection may appear to be missing because the most obvious feature in the reflection spectrum — the broad iron Kα line — is rendered indistinguishable from the underlying continuum, by a combination of blending and Comptonisation in an ionised disc, strong relativistic effects and, in some cases, a high disc inclination. With the non-relativistic-line observations, there is a requirement for iron line emission from more distant BLR-type gas. In total, the number of N07 observations that can now be considered to display evidence of relativistically smeared disc reflection is 31/37 ($\sim$ 84%) and the remainder are consistent with having it.

Although the models and parameters are rather degenerate and somewhat difficult to disentangle, the most important effect seems to be that of strong relativistic blurring. A mildly ionised reflection component can be detected in MCG+8-11-11, Mrk 6, Mrk 110 and NGC 7469(1) without the need for a steep emissivity power-law or a spinning black hole. On the other hand, twelve observations can be well-fit with a cold disc as long as the emission is concentrated in the very innermost regions where the Kerr metric holds sway. In reality, it seems that both effects are likely at play in many cases. For example, the strongest detection of blurred reflection in the narrow-line observations is made in Mrk 110 with a combination of both ionisation and strong gravity.

3.8.1 Comparison with *Suzaku* data

The heavily blurred iron lines are associated with strong Compton humps in the narrow- and non-relativistic-line observations that are well-fit with Models SRC or SRI. Indeed, in eight cases, the reflection hump is stronger than the continuum above 10 keV. While the bandpass of *XMM-Newton* is limited to 12 keV, *Suzaku* is suited to observing high energy X-ray spectra above 10 keV. The only two narrow- or non-relativistic-line objects that have been observed with *Suzaku* are NGC 7469 and NGC 2110. The ratio of the X-ray flux above and below 10 keV can be compared to the predictions of Models SRI and Model NBR, which excludes the blurred reflection, to determine if the hard reflection flux is as strong as predicted. It should be noted that the ratios are sensitive to changes in the continuum slope.

The *Suzaku* X-ray spectrum of NGC 7469 has been studied by Patrick et al. (2010). The ratio of the 15 – 50 keV flux to the 2 – 10 keV flux of their observation is 1.53. Model SRI predicts a ratio of 1.35 ± 0.25 (90% error), which is compatible within the error, but Model NBR predicts a lower value of 1.21 ± 0.06 i.e. the model without relativistic reflection under-predicts the hard flux. The same test can be applied to the *Suzaku* spectrum of NGC 2110, which showed no evidence for a disc line component or reflection (Reeves et al., 2006). The ratio of the 15 – 100 keV flux to the 2 – 10 keV is 2.57. The ratio is predicted to be 2.55 ± 0.56 for Model SRI and 4.10 ± 0.52 for Model NBR. The latter ratio is high because the model with no disc reflection estimates the spectral slope to be flat, $\Gamma \sim 1.70$, and therefore over-predicts the hard X-ray flux. The close agreement of the observed and predicted hard fluxes in NGC 7469 and NGC 2110 with Model SRI therefore supports our results that both objects exhibit strongly smeared reflection.

3.8.2 Steep emissivity profiles

The blurred disc reflection in the narrow- and non-relativistic line observations is as strong, if not slightly stronger, as it is in the N07 observations that are well-fit with a relativistically broadened iron line. Furthermore, a steep emissivity profile is found in the majority of the observations that give a significant detection of the reflection spectrum. The emissivity slope of the non-relativistic observations has a mean of $\langle q \rangle = 4.1$, which corresponds to 90% of the reflection component photons arising within $3.7 r_{\rm g}$. The mean slope of the seven narrow-line observations that are well-fit with Model SRI is $\langle q \rangle = 5.9$. In this case, 90% of the emission is produced within a smaller annulus of the disc, $r < 2.2 r_{\rm g}$. Such steep emissivity profiles are not unique to this analysis as indices of $q = 5.2$ (Ark 120, Nardini et al., 2011) and $q = 4.5$ (MCG-6-30-15, Wilms et al., 2001) have been identified in previous observations.

In, standard accretion disc models (Novikov & Thorne, 1973; Riffert & Herold, 1995), the sole energy source for the radiation of the disc is its gravitational energy. In this case, the emissivity is predicted to peak at $r \sim 1.6 r_{\rm g}$ and steepen gradually to $r^{-3.5}$, independent of the BH spin. Therefore, the standard model is not compatible with the steeper emissivity profiles that are necessary to sufficiently blur the disc reflection component. Analysing the very broad red wing of MCG-6-30-15, Wilms et al. (2001) suggested that irradiating the disc more centrally than predicted by the standard model requires an additional X-ray source such as X-rays associated with the magnetic extraction of the black hole's spin energy (Blandford & Znajek, 1977). A quantitative treatment of the balance and transportation of energy and angular momentum assuming a magnetic coupling between the disc and black hole is provided by Li (2002). The magnetic coupling allows the black hole to exert a torque on the disc and so provides a pathway for the transfer of the black hole's rotational energy to the disc. In their model, Li (2002) find that the emissivity index (see their Figure 5) can reach $q = 6$ at $r = 1.5 r_{\rm g}$ and increases further as r decreases.

A combination of strongly blurred reflection and a centrally concentrated disc emissivity is also consistent with gravitational light bending (see Figure 3 of Miniutti & Fabian, 2004). This predicts that if the X-ray source is close to the plane of the disc, continuum photons will be bent towards the accretion disc and black hole instead of escaping to infinity. As a result, the intrinsic continuum is suppressed and the anisotropic illumination of the disc can produce highly smeared reflection. The strength of the reflection can also vary much more from source-to-source than in a simple Newtonian geometry, because it depends on the degree of light bending and relativistic focusing.

As we have shown, a centrally concentrated emissivity can strongly blur the iron line. If the emissivity is strongly peaked, the implication is that the X-ray source is very compact, which would lead to shorter variability time-scales compared to the scenario where the X-ray source is more extended. This would also have an effect on the energy spectrum, accretion rate and time-delays although further investigation is needed.

3.8.3 Comparison with optical lines

If the visible iron line in the non-relativistic-line observations arises via reflection in the BLR, it can be compared to optical lines to test if they are produced in the same BLR material. An agreement between the FWHM of the iron and Hα lines has been found in MCG+8-11-11 (Bianchi et al., 2010) and NGC 7213 (Bianchi et al., 2008b) although these observations were classified by N07 as not requiring a blurred reflection component. Table 3.12 lists the FWHM of the Hβ line ($\lambda = 486.1$ nm) of the eight non-relativistic-line observations in Column 2 and the corresponding distance of the optical BLR gas from the black hole in Column 3, calculated with Equation 3.4. The distance of the iron line-producing region of the BLR is listed in Column 4, calculated from the width of the iron line in Model SRI.

The BLR gas that produces the Hβ photons is an order of magnitude further from the black hole than the iron line gas. In reality, the BLR does not have a single radius as inner parts produce highly ionised lines and the outer parts are the origin of the lower ionisation lines. All parts of the BLR are capable of emitting iron line photons. The widths of the line from different regions of the BLR will depend on their proximity to the black hole. Therefore, the breadth of the iron line that we measure in the spectrum will be determined by the photons originating from the part of the BLR closest to the black hole so agreement with the width of the optical lines is not necessarily expected. Instead, the measurement of the BLR iron line width may be important in constraining the inner radius of the BLR.

3.9 Conclusions

In this Chapter, we have investigated 19 *XMM-Newton* observations that either showed evidence for non-relativistic accretion disc reflection or no reflection at all. The aim was to test if the expected relativistic disc reflection is actually present in the 2.5 – 10 keV energy spectra, but appears to be hidden because the disc is ionised and/or that the reflection is heavily blurred by strong relativistic effects in a Kerr

Table 3.12: Comparison of optical line and iron line widths. Column (1): observation. Column (2): FWHM of the optical Hβ line. Column (3): corresponding radius of the Hβ line-producing BLR region. Column (4): radius of the BLR-type gas that produces the iron line, calculated with Equation 3.4. Column (5): reference that provides $\mathrm{FWHM_{optical}}$.

Name	$\mathrm{FWHM_{optical}}$ ($\mathrm{km\,s^{-1}}$)	$\mathrm{R_{H\beta}}$ (r_g)	$\mathrm{R_{Fe}}$ (r_g)	Reference
(1)	(2)	(3)	(4)	(5)
Ark 120	6595	2069	101	Wang et al. (2009)
MCG-5-23-16(1)	1450	42806	116	Lutz et al. (2002)
NGC 4151(1)	6354	2229	741	Wang et al. (2009)
NGC 4151(2)	6354	2229	377	Wang et al. (2009)
NGC 4593	3654	6741	510	Wang et al. (2009)
IC 4329A(2)	6431	2176	377	Peterson et al. (2004)
NGC 5548(2)	10312	846	293	Wang et al. (2009)
Ark 564	3649	6759	114	Wang et al. (2009)

geometry. The key results of the analysis are:

- An ionised disc model with a broken power-law emissivity provides a good fit to 4/11 of the narrow-line observations. However a high disc ionisation is not generally required and the model parameters are not well-constrained.
- 7/11 of the narrow-line observations are well-fit by a model that incorporates line emission concentrated in the inner disc regions, with either a cold or an ionised disc except in the case of NGC 5506(1) where the latter is necessary. With the ionised disc model, a low state of disc ionisation is generally found showing that the most dominant component of the blurred reflection is the strong relativistic effects rather than the disc ionisation.
- 6/8 of the non-relativistic-line observations are also well-fit by a model that consists of centrally-concentrated disc emission. In this case, an additional source of iron line emission is necessary from BLR-type gas.
- Both the narrow- and non-relativistic-line observations in which blurred disc reflection is detected appear to have a higher disc reflection strength than the

relativistic-line observations. However, accounting for their higher disc inclinations shows that the narrow- and non-relativistic-line observations have a similar fraction of reflection-to-continuum emission as the relativistic-line observations. The steep disc emissivities found in these observations is consistent with the gravitational light bending of continuum photons near the black hole or the extraction of the black hole's spin-energy.

- Accounting for the above effects, the fraction of the N07 sample that show some form of smeared disc reflection is 86% (31/37). While in a couple of cases, the detection may be marginal, this Chapter has shown that in others, there is significant evidence of ionised and strongly blurred reflection in the regions close to the central black hole.

Chapter 4

Root mean square variability of iron lines in Seyferts

4.1 Overview

In this Chapter, we investigate the root mean squared (rms) variability of the iron line region in 18 observations from the N07 sample as it can complement analysis of the time-averaged energy spectra. This model-independent method of analysing spectral variability allows us to test if the expected behaviour of variations in the iron line following those in the continuum occurs across the sample of Seyferts. Around $\sim$ 50% of the rms spectra show variability within the iron line region, but only two observations show the expected continuum-line correlated variability. Instead, a diversity of variability behaviour is seen in the sample with, for example, two observations possessing a broad iron line that is more variable than the continuum and another three observations displaying variability only on the blue side of the line. This is interpreted as arising from the accretion disc or emission and absorption by photoionised gas close to the nucleus.

Eight observations in total show no variability across the iron line region but are known to have iron lines with broad red wings from the results of other works and Chapter 3. This indicates that there must be a decoupling between the disc reflection and the continuum, which is possible if the continuum emission is affected by gravitational light bending or other anisotropic effects. Similarly, the evidence of no iron line variability or line variability that is stronger than the continuum rules out an absorption origin for the iron line in sources such as NGC 3516 and NGC 4151. This is a key result as absorption and reflection models for the iron line can be difficult to distinguish when analysing only the energy spectrum, but the

combination of energy and rms spectra shows that the reflection model is superior in NGC 3516(2) and NGC 4151(3).

The diversity in the iron line variability extends to multiple observations of the same source in that the iron line variability profile changes in 3/4 objects for which we have two rms-spectra. One feature shared by each variance spectrum is that the narrow core of the line at 6.4 keV is non-variable. This is expected as continuum variations should be washed out before they reach the distant torus. Overall, the great diversity of iron line variability properties indicated by the rms-spectra makes it extremely difficult to interpret the variability in any simple framework. Instead, the implication is that the central regions of AGN close to the black hole are extremely complex, with the central accretion flow being chaotic and highly variable. Anisotropy and strong gravitational effects are also most likely in effect. The majority of the results in this Chapter have been presented in Bhayani & Nandra (2010).

4.2 Introduction

In Chapter 3, we examined the time-averaged properties of the iron line in observations where a relativistically broadened iron line was not previously detected. This can be complemented by studying the variance-spectrum of the iron line region as this may reveal variability across the red wing, even if the red wing is difficult to detect in the time-averaged spectrum. Furthermore, in the observations that have a clear red wing i.e. the relativistic-line observations from Chapter 3, the prediction by the standard model that the iron line is as variable as the continuum can easily be tested with variance-spectra. In this section, the rms spectrum is introduced as the tool to measure spectral variability.

The continuum emission of typical AGN is variable over both short and long time-scales. This type of variability is often described as stochastic as it is random and aperiodic. Therefore, it is valuable to study the *average* properties of light curves. A tool that is commonly utilised to do this is the power spectral density (PSD, $\mathcal{P}(f)$). This portrays the amount of variability power as a function of temporal frequency. At high frequencies, the PSD for Seyfert 1s is represented well by a power-law ($\mathcal{P}(f) \propto f^{-\alpha}$) with slope $\alpha = 1 - 2$ (Green et al., 1993; Lawrence & Papadakis, 1993; Markowitz et al., 2003). This is known as "red" noise. To avoid a divergence of power at the smallest frequencies, the PSD breaks to a shallower power-law at a characteristic break frequency (Edelson & Nandra, 1999).

The integral of the PSD between two frequencies, f_1 and f_2, is the *true* variance,

$\langle S^2 \rangle$, due to variations between the two corresponding time-scales, $t_1 = 1/f_1$ and $t_2 = 1/f_2$:

$$\langle S^2 \rangle = \int_{f_1}^{f_2} \mathcal{P}(f) df. \tag{4.1}$$

The determination of the PSD of a source requires even sampling of its light curve at many frequencies. This makes it difficult to study the variability of these observations with PSDs. Instead the intrinsic variance can be estimated directly from the light curve with the excess variance, $\sigma^2_{\rm XS}$, which is given in Equation 2.2. This takes into account that a light curve possesses finite uncertainties due to measurement errors i.e. Poisson noise in our case of X-ray photon counting detectors. To retrieve the intrinsic source variance, the variance due to these uncertainties must be subtracted from the total variance.

The square root of the excess variance is the rms, $\sigma_{\rm rms}$, which can be favourable over $\sigma^2_{\rm XS}$ as it is a linear statistic. The spectral variability of the X-ray continuum and iron line can be studied with a variance spectrum. This tool gives the rms, $\sigma_{\rm rms}(E)$, as a function of X-ray energy, E, and its main benefit is to allow a direct comparison of the variability profile of the iron line with its profile in the mean energy spectrum. The $\sigma_{\rm rms}$-spectrum is calculated by first splitting the X-ray light curve into energy bands and determining the variability amplitude of each light curve with Equation 2.1. The $\sigma_{\rm rms}$-spectrum will contain features due to the instrumental response but these can be accounted for by using the same effective area and response matrix employed in the time-averaged spectra.

Analysis of variability in the iron line region with variance spectra has not been been carried out for many sources apart from MCG-6-30-15. An excess above the continuum variability is seen in the variance-spectrum of an *XMM-Newton* observation of MCG-6-30-15 (Ponti et al., 2004) between 4.7 – 5.8 keV. It is most likely due to the variability of the broad, redshifted iron line component emitted from an accretion disc surrounding a spinning black hole. MCG-6-30-15 is a good example of an AGN that has shown changes in its $\sigma_{\rm rms}$-spectrum with time. For example, a later and longer *XMM-Newton* observation showed a dearth of variability around the iron Kα line (Vaughan et al., 2004). The broad-band instruments aboard *Suzaku* have been used by Miniutti et al. (2007) to study the variance-spectrum of MCG-6-30-15 across a wider energy range. They found that the variability decreased with energy above 3.0 keV with a dip in variability at 6.4 keV. Therefore, as with the results of Vaughan et al. (2004), the interpretation of the variance spectrum is that the reflection component in that observation was less variable than the continuum.

These spectra of MCG-6-30-15 have shown that the picture of correlated variability between the iron line and continuum predicted by the standard model does not always hold as expected. Instead, this AGN has been used as a strong case to support the two-component model, which predicts that a variable power-law with a constant slope is superimposed on a hard reflection component that is nearly constant (McHardy et al., 1999; Shih et al., 2002; Taylor et al., 2003; Fabian & Vaughan, 2003).

The $\sigma_{\rm rms}$-spectra are particularly useful as they can be compared directly with the time-averaged spectrum. It is then relatively simple to find the interesting cases where a broad red wing can be seen in the time-averaged spectrum, but there is no excess variability above the continuum across the energy range. This shows that the reflection is constant and agrees with the two-component model. Another example of their use is with the observations from Chapter 3, where the blurred reflection was detected if an ionised disc or strong relativistic effects are considered. If excess variability relative to the continuum is found across the red wing region in these observations, this would support the presence of disc reflection as it is expected to be variable.

Examples were given in Chapter 1 of objects where warm absorption has been suggested to produce an apparently broad red wing in AGN including MCG-6-30-15 (Miller et al., 2008) and NGC 4151 (Schurch et al., 2003). As the warm absorber is in the line of sight, any variations in the continuum should also be seen in the apparent red wing. If a broad red wing to the line is not variable, or is more variable than the continuum, then this suggests that absorption is not responsible for artificially broadening the iron line. Comparing the rms spectrum to the time-averaged spectrum in objects such as MCG-6-30-15 and NGC 4151 can easily determine if the absorption model is also capable of explaining the variability across the red wing.

The combination of variability spectra and other variability techniques such as flux-flux plots in MCG-6-30-15 have shown that while the time-averaged spectrum can be explained by a blurred disc reflection model, the spectral variability is not as simple to understand. Indeed, the two-component model above has increased our understanding of the central regions of AGN and led to models of gravitational light bending. The aim of this Chapter is to analyse the $\sigma_{\rm rms}$-spectra of the Seyfert galaxies in the N07 sample so that we can determine the proportion of cases where, as expected, iron line variations follow changes in the continuum or instead, the reflection is non-variable. Furthermore, we can test if the $\sigma_{\rm rms}$-spectra can distinguish between absorption and reflection models of the broad red wing of the iron line

and multiple observations of the same source can reveal if the iron line variability behaviour is constant or changes with time.

4.3 The $\sigma_{\rm rms}$-spectrum

The energy range is restricted to 2.5 – 10 keV to minimise the effects of photoelectric absorption and the soft excess component, which is investigated in Chapter 5. This is justifiable as we are primarily interested in the iron line and its relationship with the continuum. According to Equation 2.2, it is possible for the excess variance to be negative if, due to statistical fluctuations, the intrinsic variability is small and outweighed by the measurement errors. The rms cannot then be defined. If this is the case for the light curve of even a single energy band, we do not include the $\sigma_{\rm rms}$-spectrum of the observation in the sample. The major consequence of this problem is in the choice of the energy bands. With small bands, many observations will be rejected because of negative rms values and thus reduce the sample size. On the other hand, if the bands are too large, there will be insufficient resolution to differentiate the line variations from those of the continuum. To strike a balance between the resolution of the spectra around the iron line and a large sample size, we adopted the same set of 11 energy bins between 2.5 – 10 keV for each spectrum. The resolution at the iron band (4.5 – 7.5 keV) is 400 eV, which is sufficient to distinguish between the variability of both the broad and narrow components of the line. Our final sample consists of fully-defined $\sigma_{\rm rms}$-spectra for a total of 18 observations of 14 objects. The $\sigma_{\rm rms}$-spectra were calculated using light curves binned to 1000s.

4.3.1 Error on $\sigma_{\rm rms}$ due to measurement errors

It can be difficult when examining a $\sigma_{\rm rms}$-spectrum to determine if changes in the amplitude with energy represent the real energy dependence of the intrinsic variability or if they are caused by random errors in the light curves. This is especially important when searching for features in the $\sigma_{\rm rms}$-spectra as their presence is not significant if they are a result of random errors. Therefore, it is important to assess the uncertainty generated by the finite measurement errors of Poisson noise on the individual fluxes. The errors on the $\sigma_{\rm rms}(E)$ values will then enable a determination of spectral variability i.e. if the $\sigma_{\rm rms}(E)$ values do not overlap within their errors, the variability amplitude is dependent on energy.

The calculation of the error of an $\sigma_{\rm rms}$ value has been addressed by many previous works. The first determination of the error assumed that the dominant variance

of Equation 2.1 is associated with the sample variance, S^2, so that the error term, $\overline{\sigma_{\rm err}^2}$, can be neglected in comparison (Nandra et al., 1997a; Turner et al., 1999; Edelson et al., 2002). However, this depends on the assumption that the light curves of different bands are uncorrelated and governed by Gaussian statistics. This is contrary to typical AGN light curves as they are strongly correlated at different energies and are not Gaussian. Vaughan et al. (2003) applied a Monte Carlo approach to quantify the effect of measurement errors on estimates of $\sigma_{\rm rms}$, which is given in their Equation 11. Their strategy was to calculate the excess variance of simulated light curves that only differed from the real light curve by the addition of Poisson noise. 10,000 light curves were simulated in this way with the spread of their excess variances influenced solely by Poisson noise. The error of $\sigma_{\rm rms}$ was then taken as the standard deviation of the simulated excess variances.

We cannot use the formula from Vaughan et al. (2003) to calculate errors for negative excess variances, which are encountered in Chapter 5. Therefore, we followed a similar approach in calculating the uncertainties in $\sigma_{\rm rms}$ due to Poison errors with simulations. For each energy band, Monte Carlo light curves were simulated with the same number of time bins and 1000s bin size as the observed light curve. A Gaussian distribution was devised for each time bin with the mean and standard deviation set to the observed counting rate and uncertainty respectively in that time bin. This is appropriate as each time bin was required to have a minimum of 20 counts in the original data reduction. The counting rate for each simulated light curve bin was decided by drawing a random deviate from the bin's distribution. 10,000 synthetic light curves were simulated in this way for each energy band and a $\sigma_{\rm rms}$ value calculated for each simulated light curve. Finally, the 1σ uncertainty in the $\sigma_{\rm rms}$ for each energy band was set to the standard deviation of the 10,000 $\sigma_{\rm rms}$ values for that energy band. The differences between the errors of Vaughan et al. (2003) and our method are typically less than 5%.

4.4 Results

As with the time-averaged spectra, the 2.5 – 10 keV $\sigma_{\rm rms}$-spectra of the 18 observations in our sample broadly follow a power-law form. The variability around the iron line region is easier to study by taking the ratio of the $\sigma_{\rm rms}$-spectrum to a model of the continuum. This effectively normalises the total intrinsic variability by the continuum variability and portrays more clearly the iron line variability, if any exists at all. A continuum fit to the 2.5 – 10 keV energy range was obtained in XSPEC while ignoring the 4.5 – 7.5 keV region to exclude any variability due to the iron Kα line.

The power-law slope was left to vary as a free parameter. Neutral Galactic absorption was included using the WABS model with the $N_{\rm H}$ values listed in Table 1.2 of Chapter 3. N07 found that some of the observations in our sample show additional effects of ionised absorption local to the AGN. We accounted for this in cases where it was required using the XSTAR table model CWA18 (described further in Chapter 3), with parameters fixed to those found by N07 to avoid over-parametrisation of the fits. If there is absorption variability, it would be parametrised by a change in the fitted slope. The best-fit power-law slope, $\Gamma_{\rm rms}$, and χ^2 after the model is extrapolated across the iron line region are listed in Table 4.1. The data/model ratios are shown in Figure 4.1. To compare the $\sigma_{\rm rms}$-spectrum with the mean energy spectrum, we fitted a continuum model to the time-averaged spectrum in the same manner as we did to the $\sigma_{\rm rms}$-spectrum. The power-law slopes for this model, $\Gamma_{\rm en}$, are also listed in Table 4.1 from N07, where the iron line region between 4.5 – 7.5 keV has been excluded. All errors are quoted at a confidence level of 90%.

A first look at the data/model ratios of the $\sigma_{\rm rms}$-spectra appears to show that many observations have excesses and deficits in variability relative to the continuum variability. However, 11/18 of the $\sigma_{\rm rms}$-spectra are well-fit with the power-law model in a χ^2 test at a confidence level of 99%. This is not a good method of testing the iron line variability as a real excess in only one energy band would give an acceptable fit with a power-law model. Therefore, an alternative method is necessary to assess the significances of any excesses.

4.4.1 Significance of a variability excess

In this Chapter, we interpret features in the energy bands of an rms spectrum that are close in energy. Assuming that the bands are highly correlated, the light curves of nearby energy bands represent the same realisation of the underlying random process. This means that differences in the variability of the light curves should not be due to red-noise. This assumption is likely to hold well for the relatively close energy bands across the 2 – 10 keV energy range. Any differences in the rms variability of the energy bands can then be considered as intrinsic to the source.

We can make a more precise estimate of the significance of any iron line variability by comparing the real $\sigma_{\rm rms}$-spectrum to simulated variability spectra of a continuum model. As no reflection component is included, we can find the range of variances expected in the iron line energy bands if only the continuum was variable. A continuum light curve was simulated by using the *fakeit* function in XSPEC to create a power-law spectrum for each 1000s time bin. The model is the same

Name	$\Gamma_{\rm rms}$	χ^2/d.o.f.	Probability	$\Gamma_{\rm en}$
(1)	(2)	(3)	(4)	(5)
MCG-5-23-16(2)	1.74	33.4/6	0.00	$1.74^{+0.05}_{-0.07}$
NGC 3516(2)	1.72	27.9/6	0.00	$1.90^{+0.08}_{-0.08}$
NGC 3783	1.85	20.5/6	0.00	$1.72^{+0.03}_{-0.05}$
NGC 4051	2.42	7.7/8	0.96	$2.04^{+0.05}_{-0.05}$
NGC 4151(2)	1.45	18.4/6	0.00	$1.44^{+0.06}_{-0.06}$
NGC 4151(3)	2.15	7.6/6	0.27	$1.70^{+0.02}_{-0.05}$
Mkn 766(2)	2.20	9.6/8	0.29	$2.23^{+0.05}_{-0.05}$
Mkn 766(3)	2.37	26.7/8	0.00	$2.12^{+0.07}_{-0.07}$
NGC 4395	1.80	7.7/6	0.26	$1.48^{+0.11}_{-0.09}$
NGC 4593	1.97	13.5/8	0.10	$1.81^{+0.03}_{-0.02}$
MCG-6-30-15(1)	2.19	33.8/6	0.00	$2.2^{+0.13}_{-0.06}$
MCG-6-30-15(2)	2.17	12.9/6	0.04	$2.30^{+0.04}_{-0.07}$
NGC 5506(1)	1.95	7.6/6	0.27	$1.90^{+0.16}_{-0.05}$
NGC 5506(2)	2.24	1.50/6	0.96	$1.79^{+0.06}_{-0.08}$
NGC 5548(2)	2.26	21.9/8	0.00	$1.67^{+0.09}_{-0.04}$
NGC 7314	2.23	16.4/6	0.01	$2.08^{+0.07}_{-0.07}$
Ark 564	2.51	8.0/8	0.43	$2.60^{+0.06}_{-0.05}$
NGC 7469(2)	1.46	5.4/8	0.71	$2.04^{+0.06}_{-0.06}$

Table 4.1: Power-law fits to the $\sigma_{\rm rms}$- and mean energy spectra. The iron line region (4.5 – 7.5 keV) is excluded and a warm absorber is included if necessary. Column (1): name and observation number. Column (2): the best-fit power-law slope, $\Gamma_{\rm rms}$, for the $\sigma_{\rm rms}$-spectrum. Column (3): χ^2/d.o.f. for the model after it is extrapolated across the iron line region. Column (4): null hypothesis probability that this χ^2 is acceptable by chance. Column (5): the best-fit power-law slope, $\Gamma_{\rm en}$, for the mean energy spectrum.

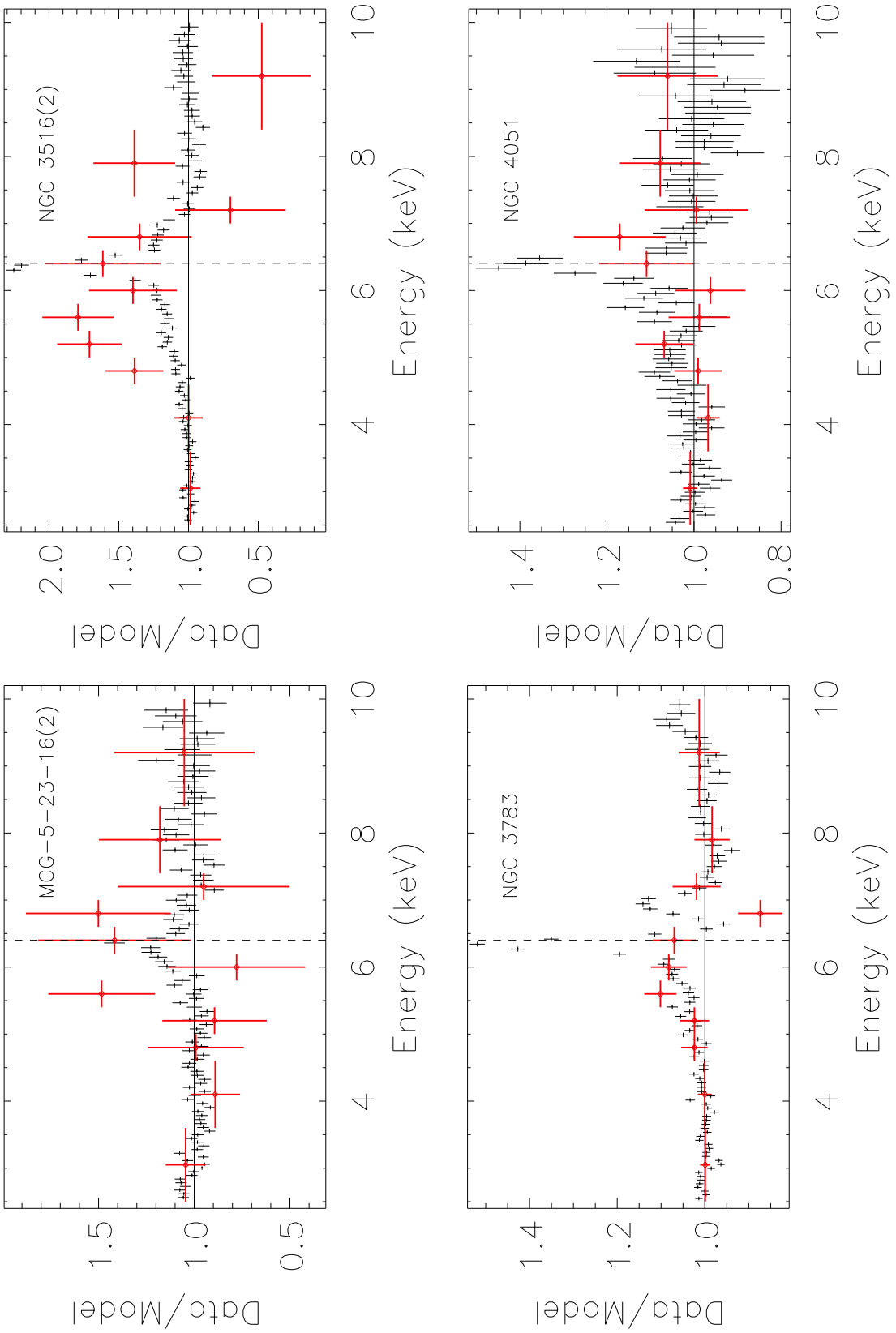
NGC 3516(2)
NGC 4051
MCG−5−23−16(2)
NGC 3783
Data/Model
Energy (keV)

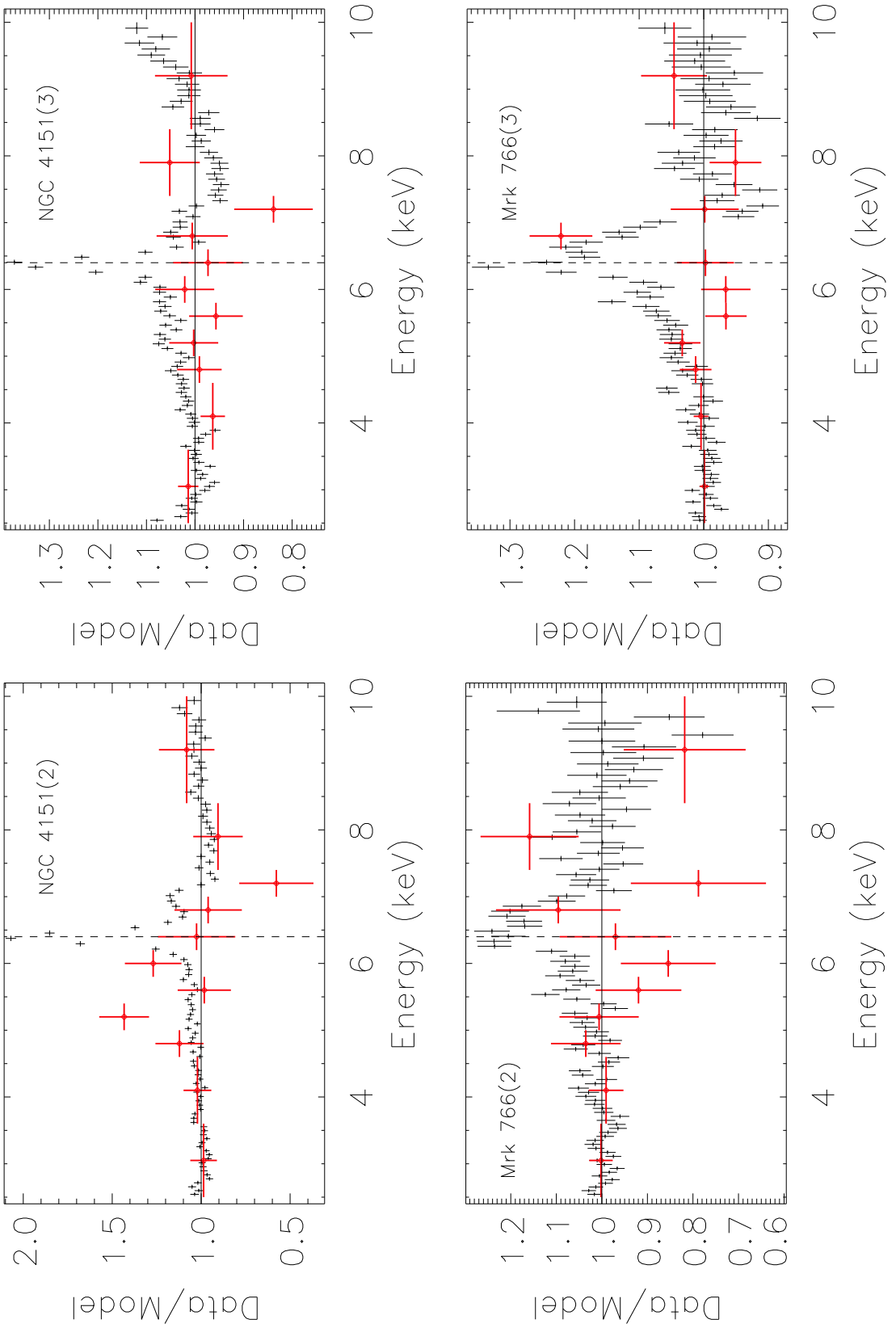
NGC 4151(3)
Mrk 766(3)
NGC 4151(2)
Mrk 766(2)
Data/Model
Energy (keV)

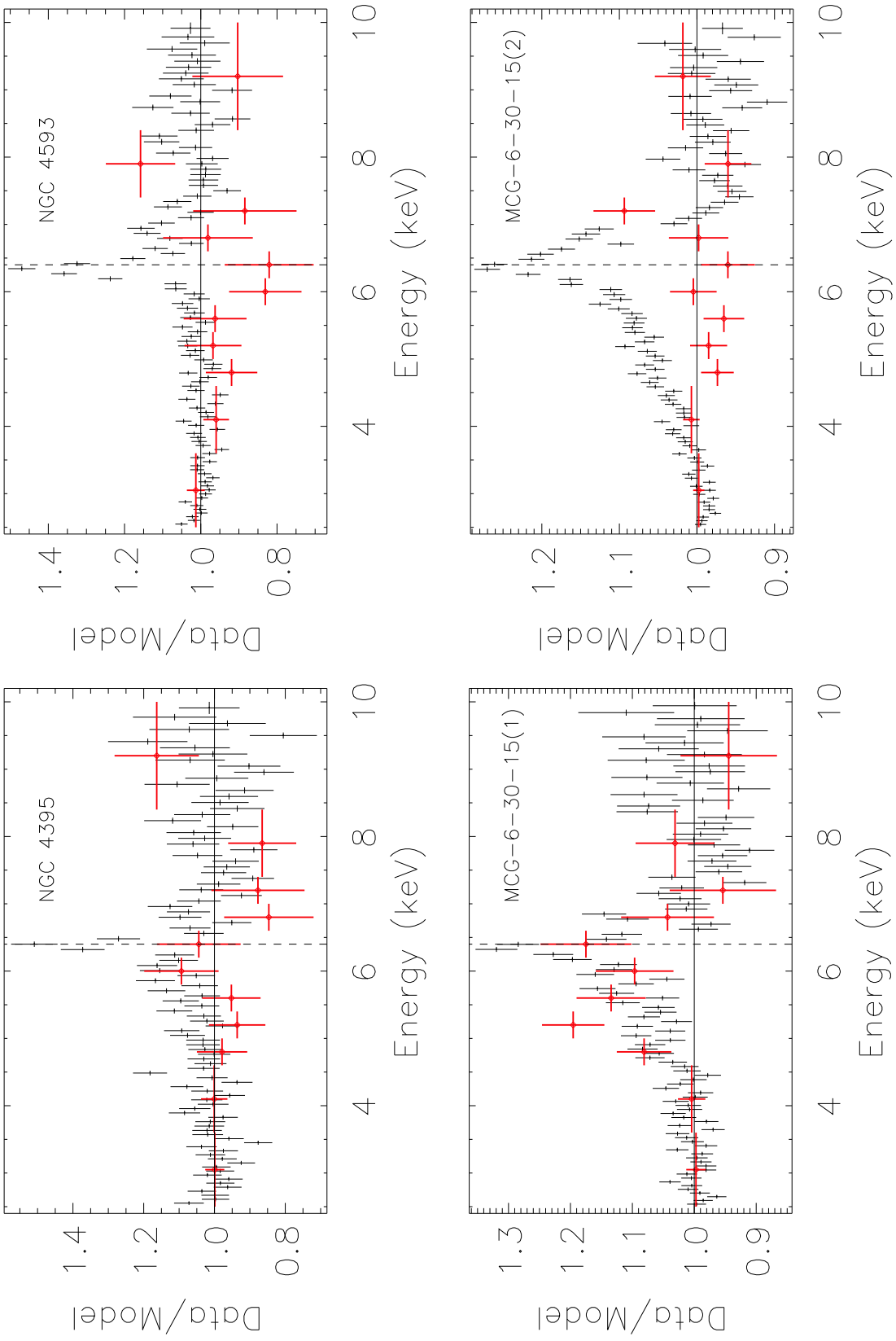
NGC 4593
MCG−6−30−15(2)
NGC 4395
MCG−6−30−15(1)
Data/Model
Energy (keV)

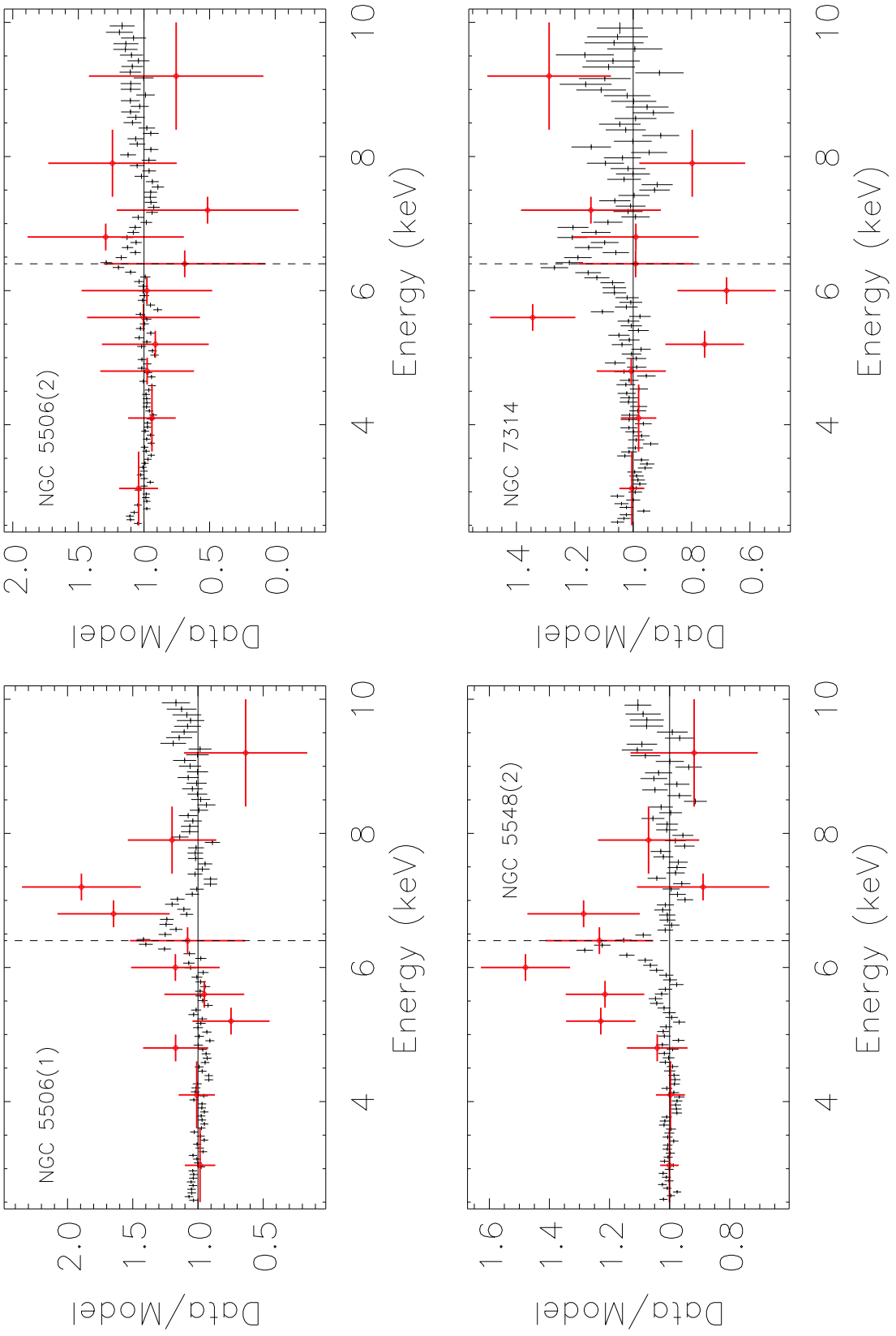
NGC 5506(2)
NGC 7314
NGC 5506(1)
NGC 5548(2)
Data/Model
Energy (keV)

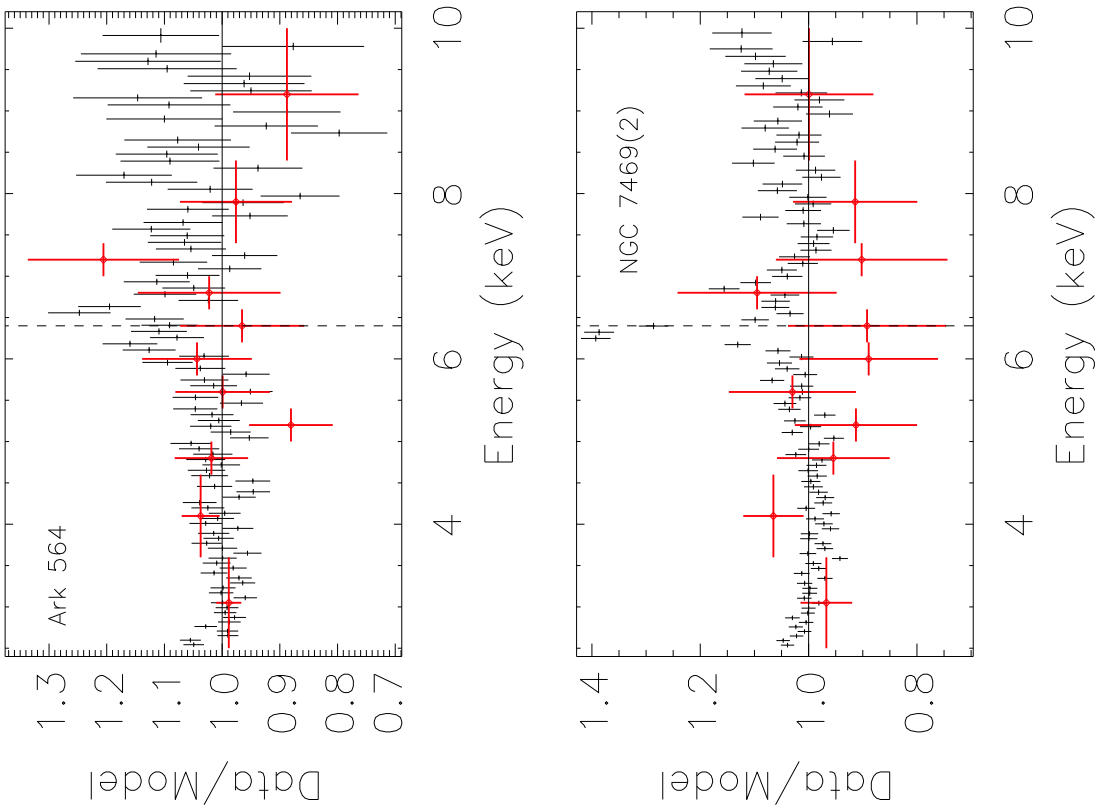

Figure 4.1: Data/model ratios of the $\sigma_{\rm rms}$-spectra (red) and mean energy spectra (black) fitted with a power-law continuum. Neutral Galactic absorption is included and the 4.5 – 7.5 keV energy range is excluded. A warm absorber was also included if found necessary by N07 with parameters fixed to their values. The vertical dashed lines mark the rest-frame energy of the iron Kα line from neutral iron at 6.4 keV.

as the continuum model (power-law and absorption) used to fit the observed $\sigma_{\rm rms}$-spectrum, but the normalisation of the power-law for each time bin was set such that the total count rate of the four continuum energy bands (i.e. those between 2.5 – 4.6 keV and 7.4 – 10.0 keV) matched the observed count rate in this energy range. The 4.6 – 7.4 keV interval is excluded as this will contain any contribution by line components, whereas the rest of the energy range should only show continuum emission. The simulations yield a continuum light curve in each of the 11 energy bands between 2.5 – 10 keV. For each energy band, Poisson noise is added to each time bin in the same way as for the calculation of the error bar on the rms (see Section 4.3.1). The excess variance is calculated for each energy band to form an excess variance-spectrum for the continuum. This is repeated 1000 times to obtain 1000 values of the continuum excess variance in each energy band. For each energy band, we can then compare how many times the excess variance of the continuum

model exceeds that of the observed $\sigma_{\rm rms}$-spectrum, which contains the iron line. This yields the probability that the observed variance exceeds the continuum variance by chance, and hence the significance of the line variations.

As there are 7 energy bands between 4.6 – 7.4 keV, at a confidence level of 99% we would expect ∼0.07 false detections of significant variability per observation and 1.3 false detections for the entire sample of 18 observations (i.e. 126 energy bands). At a lower confidence level of 95%, 0.4 energy bands per observation and 6 across the whole sample are expected to be false detections. Therefore, excesses that are variable at a confidence level of greater than 99% are are considered to be real and bands with a confidence level of greater than 95% are also discussed, albeit with caution, as several adjacent bins with moderately high confidence might indicate a broad variability excess. The significances of the energy bands that have excess variability above the continuum at a confidence level of greater than 95% are given in Table 4.2.

4.5 Analysis of the iron line variability

A simple disc reflection model predicts that the broad iron line should respond rapidly to changes in the illuminating continuum as the inner part of the accretion disc is close to the X-ray source. This would result in a $\sigma_{\rm rms}$-spectrum with an iron line profile excess that is as broad and strong as the profile found in the time-averaged spectrum. However, in contrast, the $\sigma_{\rm rms}$-spectra in Figure 4.1 display a range of iron line variability profiles. This is an important result as our sample reveals no clear overall trend between the time-averaged and $\sigma_{\rm rms}$-spectra.

Only 7/18 of the observations of our sample show at least one energy band with significant line variability at a confidence level of 99%, while two further observations have excesses that are variable at greater than 95%. Two observations, NGC 3516(2) and MCG-6-30-15(1) show definitive broad line variability, in that there are two adjacent bins with excess variations at $> 99\%$ confidence. At a lower confidence level of 95%, NGC 3783 and NGC 5548(2) also show signs of broad red wing variability. NGC 4151(2), Mrk 766(3), MCG-6-30-15(2) and NGC 7314 show significant but narrow excesses.

The diversity of behaviour increases further when the strength of the variability excess is compared to the time-averaged line profile. The correspondence is generally poor. For example, NGC 3516(2) and NGC 5548(2) have line variability, especially in the red wing, that is stronger than the mean energy spectrum. MCG-6-30-15(1) has a variable, broad iron line that is as strong as the time-averaged line profile,

Name	Energy (keV)						
	4.6 – 5.0	5.0 – 5.4	5.4 – 5.8	5.8 – 6.2	6.2 – 6.6	6.6 – 7.0	7.0 – 7.4
MCG-5-23-16(2)							
NGC 3516(2)		100	100				
NGC 3783			98.1	95.3			
NGC 4051							
NGC 4151(2)		100					
NGC 4151(3)							
Mkn 766(2)							
Mkn 766(3)						100	
NGC 4395							
NGC 4593							
MCG-6-30-15(1)	95.2	100	99.8	96.4	99.9		
MCG-6-30-15(2)							99.4
NGC 5506(1)							
NGC 5506(2)							
NGC 5548(2)		97.9	96.2	100			
NGC 7314			99.5				
Ark 564							95.7
NGC 7469(2)							

Table 4.2: Significances (%) of the variability excesses in the seven iron line energy bands (4.6 – 7.4 keV) of the $\sigma_{\rm rms}$-spectra. Only excesses detected at a confidence level of greater than 95% are shown.

as does NGC 3783 (although its iron line red wing is not as strong as in MCG-6-30-15). Sometimes, a broad iron line and red wing is seen in the time-averaged spectrum, but the variability excess is narrow, and tends to the blue side of the line. The strongest examples are Mrk 766(3) and MCG-6-30-15(2) with Ark 564 being more marginal. NGC 4151(2) is unique in displaying a significantly variable narrow component to the red side of the line that is greatly in excess of the time-averaged profile. The largest group of observations are those that show no evidence for line variability at all, despite many of them displaying clear emission (narrow and/or broad) in their time-averaged spectra.

The $\sigma_{\rm rms}$-spectra can crudely be classified into three non-exclusive groups. The first class are those with red wing variability, the second, those with blue excess variations, and lastly there are those with little or no evidence for broad or energy-shifted iron line variations at all. Here we discuss each class in turn, but before doing so, we consider the core of the iron line at 6.4 keV. This is suspected to arise much further away from the central region of the AGN than the broad iron line.

4.5.1 6.4 keV iron line core

N07 found that a narrow component of the iron line at 6.4 keV was ubiquitous throughout their sample. The fact that it is narrow and found at the non-redshifted energy of fluorescence for neutral iron suggests that it originates at a large distance from the black hole e.g. at the molecular torus. As this distant reflector is far away from the central X-ray source (several years for a typical pc-scale torus), variations in the continuum are expected to be averaged out over the light-crossing time. Therefore, the narrow iron line component should not be able to respond to any variations in the continuum. This agrees with the fact that only MCG-6-30-15(1) shows significant iron line variability in the 6.2 – 6.6 keV band, as this is part of a broader variability excess instead of being due to a narrow torus iron line. In all cases, the variability at 6.4 keV is suppressed compared to the time-average spectrum. Clearly the narrow core of the iron line is far less variable than the continuum, supporting an origin in distant material.

4.5.2 Red wing variability

A number of observations in Table 4.2 show variability excesses that extend below 6.4 keV. In many cases, the excesses are observed in multiple, consecutive bins. Some of these observations have a red wing to the iron line that is as variable as the continuum, e.g. NGC 3783 and MCG-6-30-15(1), but in others, the line is more

variable e.g. NGC 3516(2), NGC 5548(2) and NGC 7314. The observation that the red wing is as variable as the continuum is consistent with the simplest interpretation of disc reflection.

The excess in the $\sigma_{\rm rms}$-spectrum of NGC 3783 is similar in strength to the broad iron line in the time-averaged spectrum, so in the accretion disc model, the line and continuum vary together. Reeves et al. (2004) and N07 found an ionised H-like line at 6.97 keV that is not seen to be variable in the $\sigma_{\rm rms}$-spectrum. This offers support for the speculation of N07 that the line originates from hot gas filling the torus, which is not expected to be variable. Turning to MCG-6-30-15, N07 found a strong requirement for a blurred accretion disc component in the time-averaged spectrum (as in several previous studies, e.g. Tanaka et al., 1995; Fabian et al., 2002). The first observation, MCG-6-30-15(1), follows the simple disc interpretation as the variability line profile matches well with the time-averaged line profile. However, there is a large change between this and the variability profile of the second observation (see Section 4.5.5). NGC 3783 and MCG-6-30-15(1) are the only observations in our sample which show both clear evidence for broad line variations and an amplitude consistent with the continuum, although there are others where the S/N prevents definitive conclusions.

There are four observations that show variability of the iron line redward of the core that exceeds that of the time-averaged spectrum. NGC 3516(2) and NGC 5548(2) are the clearest cases, along with NGC 4151(2) and NGC 7314, which show narrower excesses. If the red wing is indeed more strongly variable than the continuum, it is a compelling indicator that relativistic effects are in play (Ponti et al., 2004; Miniutti & Fabian, 2004). N07 did not find evidence in either NGC 5548(2) or NGC 4151(2) for strong gravitational effects in their time-averaged spectra. NGC 5548(2) is the most puzzling case, with a non-relativistic iron line but a strong, broad variable excess that extends down to 5.0 keV, a much lower energy than the time-averaged profile covers. NGC 3516(2) and NGC 7314 are different in that they possess relativistically broad iron lines, as well as having strong variability excesses across the red wing. This means that the iron line is more variable than the continuum and is likely to be explained by relativistic effects such as beaming or emission from iron moving with a large bulk velocity. However, in both of these cases, it is difficult to explain why the entire red wing is not variable.

4.5.3 Blue excesses

The second class of observations exhibit the majority of their variability blueward of the line core. These include Mrk 766(3), MCG-6-30-15(2) and the marginal case of Ark 564.

In Mrk 766(3), the variability excess in the 6.6 – 7.0 keV band is narrow compared to the broad time-averaged iron line and at a higher energy than the narrow core at 6.4 keV. The time-averaged spectrum is fit well with only an accretion disc model, but the $\sigma_{\rm rms}$-spectrum suggests that the iron Kα region can be split into two bands of high and low ionisation. The high ionisation band varies with the continuum, while the low ionisation band representing disc emission is nearly constant.

MCG-6-30-15(2) largely has a flat $\sigma_{\rm rms}$-spectrum apart from a significant excess in the 7.0 – 7.4 keV band. No emission or absorption is found in this energy band by N07, but Fabian et al. (2002) do find complexity around 7.0 keV that can be explained by an edge at 7.38 keV if there is thick material partially covering the line of sight. The variability could then be due to changes in the covering rather than being attributable to the accretion disc. Alternatively, the complexity could be due to an H-like recombination emission line at 6.97 keV, but then it is puzzling that there is no significant variability in the 6.6 – 7.0 keV bin. Ark 564 was found by N07 to be equally well-fit by a blend of narrow lines (He- and H- like iron lines) and a multizone warm absorber as by a blurred reflector. The single 95% variability excess is in the 7.0 – 7.4 keV band so it does not appear to be associated with either of the narrow lines fitted to the time-averaged spectrum by N07. This may argue in favour of the blurred reflection interpretation.

4.5.4 Constant iron lines

A large group of observations show clear evidence for a red wing of the iron line in their time-averaged spectra, but have no evidence for variability of that emission component in their $\sigma_{\rm rms}$-spectrum. This group can be split into MCG-5-23-16(2), NGC 4051, NGC 4151(3), Mrk 766(2), NGC 4395, NGC 4593, NGC 5506(2) and NGC 7469(2), which have no evidence for variability across the entire iron line region and MCG-6-30-15(2), Mrk 766(3) and Ark 564, which have blue but no red variability. NGC 5506(1) is also not significantly variable across the iron line region, but unlike the other observations, it was not found by N07 to show any iron line emission from the accretion disc (see Section 4.9).

The apparent lack of red wing variability in NGC 5506(2) and Mrk 766(2) could simply be a result of poor statistics. The rms-spectrum of MCG-5-23-16(2) appears

to show three bands with excess variability above the continuum but none of these are at a confidence level of 95% or more. Arguably the most interesting cases are where there is a clear broad red wing of emission, but a flat $\sigma_{\rm rms}$-spectrum. The most obvious examples are NGC 4051, NGC 4151(3), Mrk 766(3), NGC 4395, MCG-6-30-15(2) and NGC 7469(2). These observations are those where the reflection component appears constant while the continuum is the only variable component.

Three observations, NGC 4593, NGC 7314 and NGC 7469(2) appear to have dips in the iron line region of their $\sigma_{\rm rms}$-spectra. Dips do not mean anything physically and may be indicative of incorrect modelling of the continuum. The time-averaged spectrum of NGC 7469(2) was not fit well with a reflection component, though there is a significant improvement when a blurred reflector is included. N07 proposed that this could be due to a black hole with an extreme spin that blurs the line to such a large extent that it can be difficult to separate from the continuum. This could make the continuum outside the iron line region concave, and thus the use of only a power-law in fitting the continuum is too simplistic. In Chapter 3, we found that NGC 4593 is consistent with possible strongly blurred disc reflection and a BLR iron line. If this is the case, a better model for the continuum is also needed in NGC 4593. Unfortunately, not enough bands are available to do this for these two observations. NGC 7314 has both variability dips and an excess across the red wing while the rest of the iron line does not appear variable. The time-averaged spectrum is well fit with a disc reflection model but clearly the $\sigma_{\rm rms}$-spectrum of this observation is different. NGC 7314 was not found to have any obvious additional continuum complexity, which makes the extremes in variability more difficult to understand.

4.5.5 Objects with multiple observations

There are four objects where we are able to compute $\sigma_{\rm rms}$-spectra for more than one observation: MCG-6-30-15, Mrk 766, NGC 5506 and NGC 4151. They provide an opportunity to test if the variability of the iron line has changed with the time-averaged spectra or has remained the same. Arguably one of the most puzzling results of our analysis is that the rms variability properties appear to change in most of these cases.

The largest difference in variability profile of the iron line across a pair of observations occurs with MCG-6-30-15, as already discussed. The second observation is flat below 7.0 keV, which agrees with other studies of this object (mostly based on this long observation; Fabian et al., 2002; Larsson et al., 2007), where the line

has been proposed to be nearly constant while the power-law is the main driver of variability. On the other hand, the earlier observation, MCG-6-30-15(1), shows a highly variable red wing, as originally noted by Ponti et al. (2004). This variability behaviour is inconsistent with the two-component model that has been popularised based on this object. Furthermore, the only variable band in the $\sigma_{\rm rms}$-spectrum of MCG-6-30-15(2) is the 7.0 – 7.4 keV band which is not variable in the first observation. An important difference between the two observations is that the mean 2 – 10 keV flux for the second observation is 35% higher than for the first observation. The lack of iron line variability at low fluxes in MCG-6-30-15 has led to the development of gravitational light bending models (see Section 4.6). A similar combination of flux and iron line variability has been found in NGC 4051, which is fit well by an accretion disc model in N07. The iron line is not found to be variable in the $\sigma_{\rm rms}$-spectrum, which is in agreement with the results of Ponti et al. (2006) for the same observation. They also studied a lower flux observation and found that in this case, the iron line did vary with the continuum.

The other objects with multiple observations, while less statistically compelling, also appear to show changing variability behaviour. Like MCG-6-30-15(1), NGC 4151(2) shows evidence for excess variability between 5.0 – 5.4 keV, whereas the $\sigma_{\rm rms}$-spectrum of NGC 4151(3) is flat. Interestingly, N07 found that the third observation, NGC 4151(3), strongly requires a broad and relativistic iron line but the first two observations of this object, while being consistent with a broad line, did not need one. The presence of the variability excess around 5 keV in NGC 4151(2) points towards relativistic effects being important, despite there being no evidence of this in the time-averaged spectrum. Similarly, the third observation would be expected to show some variability across the iron line region due to the region of line formation being close to the black hole. As with MCG-6-30-15, the flux of the observation with the variable iron line is lower than the observation with the constant line.

There is no red wing variability in either observation of Mrk 766, but there is blue variability in Mrk 766(3) that is not significant in Mrk 766(2). In this instance, this may simply be due to poor statistics in the case of Mrk 766(2). NGC 5506 is the only object in the sample with two rms-spectra that show no differences. The low significance of the excess above 6.4 keV in NGC 5506(1) may be down to low S/N but if the iron line is indeed constant, the similarity between the rms spectra matches the similarity of the two time-averaged spectra.

4.5.6 The continuum

The power-law shape of the $\sigma_{\rm rms}$-spectra shows that the continuum is variable. A quick comparison in Table 4.1 appears to show that generally $\Gamma_{\rm rms}$ is steeper than $\Gamma_{\rm en}$. This is shown more clearly in Figure 4.2, which plots the slopes against each other. The solid line represents a one-to-one mapping of the rms and time-averaged continuum slopes and error bars are omitted for clarity. While five observations have $\Gamma_{\rm rms} \sim \Gamma_{\rm en}$, the majority of the sample have a steeper $\Gamma_{\rm rms}$.

This may be due to a few reasons. Firstly, reflection that is quasi-constant may add to the hard flux up to the 10 keV limit, but would not contribute any variability to the hard rms. This could result in the mean flux spectrum being flatter than the rms spectrum. As noted above, the difference in slopes may be an indication that the absorption is varying across the length of the observation. Alternatively,there may be an intrinsic change in the shape of the continuum.

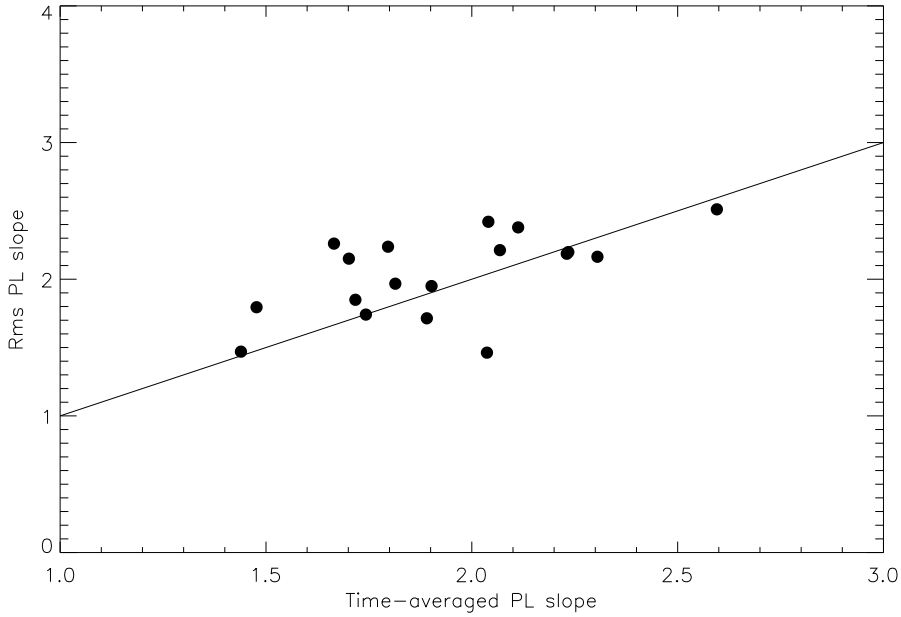

Figure 4.2: The continuum slope of the mean spectrum, $\Gamma_{\rm en}$, plotted against the slope of the continuum variability, $\Gamma_{\rm rms}$, in the rms spectrum. The solid line represents a one-to-one mapping between the slopes, $\Gamma_{\rm rms} = \Gamma_{\rm en}$. For presentation purposes, error bars are omitted.

4.6 Discussion

We have presented the rms variability spectra of 18 observations of 14 Seyfert galaxies from our *XMM-Newton* sample, concentrating on their iron Kα line variability. The most striking result of our analysis is the extraordinary diversity in the $\sigma_{\rm rms}$-spectra. Different objects clearly display different variability properties around the iron line. A direct comparison between the $\sigma_{\rm rms}$- and time-averaged spectra has shown that there is sometimes suppressed variability around the iron line, and enhanced variability in other sources. The variability or non-variability across the red wing of the iron line is in some cases able to argue against warm absorption artificially broadening the red wing. Finally, objects observed at more than one epoch show changes in their $\sigma_{\rm rms}$-spectra, indicating that there are different variability modes at different times even in the same object. In the cases of MCG-6-30-15 and NGC 4051, this may be related to the flux level of the observation, as only the observations at lower flux levels appear to show a variable iron line. The diversity in the rms variability at the iron line throughout the sample shows that it is unlikely that there is a universal line formation mechanism. Indeed our results are extremely difficult to explain in any single theoretical framework.

4.7 Non-variable distant reflection

One robust and easily-interpreted result is that in all observations, we find a lack of variability at the neutral iron line energy of 6.4 keV. Nearly all of the objects were found by N07 to contain a narrow line at this energy. The lack of variability of the line core in the $\sigma_{\rm rms}$-spectra supports the interpretation that it arises from material far from the central black hole, for example in the molecular torus. The core is expected to be constant because variations in the power-law continuum will be averaged out over the light crossing time of the torus and therefore emission from the torus should not have any effect on the rms.

4.8 Red wing variability

The broad iron line emission and its variability are far more puzzling. The simple disc interpretation for the broad line is that variations should follow those in the continuum, as the line emitting region is close to the production site of the power-law continuum, the corona. This would result in an $\sigma_{\rm rms}$-spectrum that shows a variable broad line that matches the time-averaged spectrum. This is seen only in a

very few objects. Variability in the red wing region is not uncommon in the sample, however, being present in 6/18 observations. This includes at least two observations where variations in the red wing exceed those of the continuum and is indicative that in these objects, beaming, light bending or other relativistic effects may be in play.

4.8.1 Artificial broadening of the red wing by warm absorption

Some of the objects that display broad iron line variability have been suggested to possess absorption layers that can mimic the red wing e.g. MCG 6-30-15 (Miller et al., 2008). A partial covering absorber, when combined with distant reflection, can produce a hump in the energy spectrum between 3 – 7 keV, which is then taken to be an emission feature. This requires no relativistic component as the absorption zones are $> 100r_{\rm g}$ from the black hole and the weak narrow iron line arises from distant reflection. Another example is NGC 3783, where there has been some controversy over whether or not a broad red wing is present. Reeves et al. (2004) suggested that much of the broad red wing may be an artefact of a warm absorber adding curvature to the continuum, although they and N07 both concluded that some disc reflection was also present. Nonetheless the spectrum is very complex, with two zones of ionised gas, a strong H-like emission line and a blurred Compton reflection component. The effect of absorption on the variability is not completely clear but if the red wing is a product of partial covering absorption or distant scattered components, then the rms variability of the red wing cannot be larger than that of the continuum. This is compatible with NGC 3783, but disagrees with the suggestion that thick warm absorbers can mimic the red wing in NGC 3516(2) (Turner et al., 2005) as the variability of the iron line is much stronger than the continuum. The $\sigma_{\rm rms}$-spectrum is thus better explained with the blurred reflection model (N07) if relativistic effects are enhancing the variability of the red wing. A similar argument can be applied to the observations where complex absorption has been suggested to be the sole cause of spectral curvature in the red wing but a flat $\sigma_{\rm rms}$-spectrum reveals a non-variable broad line and constant disc reflection. For example, Schurch et al. (2003) have suggested that the red wing in NGC 4151(3) might be accounted for purely by complex absorption. In this case the excess photons seen in our time-averaged spectrum between 4 – 6 keV are continuum photons, which should naturally show the same variability as the remainder of the 4 – 6 keV continuum, over which the red wing is seen. We are able to reject this

possibility using the flat $\sigma_{\rm rms}$-spectrum for NGC 4151(3) and conclude that when invariant, the broad red wing must therefore be a distinct additional component, almost certainly from reflection.

4.8.2 Decoupling between the continuum and iron line

As mentioned above, a non-variable iron line has been found previously in, e.g. MCG-6-30-15 (Vaughan & Fabian, 2004). This has been taken as evidence of a decoupling between the continuum and line. With MCG-6-30-15, the peak of the reflected emission forms close to the black hole, so for the reflection component to not be strongly associated with the direct power-law component, the intrinsic X-ray emission must be anisotropic. Gravitational light bending has been proposed to explain this as the anisotropy can result from the gravitational field of the black hole bending power-law photons away from the observer and towards the disc. As explained in Chapter 1, this light bending is most severe when the height of the corona over the disc is small. Instead of reaching us, the continuum photons will be reflected off the disc, which enhances the disc component. As the coronal height increases, less photons are deflected onto the disc and so more reach us directly. Figure 1.12 of Chapter 1 shows how the intensities of the direct and reflection components may vary with the coronal height in a simple toy model (Miniutti & Fabian, 2004). At a low coronal height, both components are predicted to vary together, which would give an $\sigma_{\rm rms}$-spectrum with an excess that matches the time-averaged iron line profile e.g. MCG-6-30-15(1). The continuum flux level will also be lower when the coronal height is small, which agrees with MCG-6-30-15(1) having a lower mean count rate than MCG-6-30-15(2). As the height increases further, another regime is reached where the direct flux varies by a factor of 3 or 4, but the reflection component changes by less than 10%. Thus, this could correspond to flat $\sigma_{\rm rms}$-spectra such as that of MCG-6-30-15(2). As the two observations of MCG-6-30-15 are separated by a year, the light bending interpretation suggests that there is a large change in the coronal height within a relatively small amount of time. The observations where the variability excess is stronger than the red wing of the time-averaged iron line could also be explained by gravitational light bending if relativistic effects such as relativistic beaming enhance the variability of the disc reflection component. Along with MCG-6-30-15, the two other objects with multiple observations, NGC 4151 and Mrk 766 show a change in the variability at the iron line between their two observations. This demonstrates the complexity of variability in Seyfert 1s as there is not only a range of behaviour found between objects, but also within objects themselves.

The implication is that the inner accretion flow is highly unstable and chaotic, with changes in illumination and/or geometry occurring on relatively short time-scales (months-years). Relativistic, transient lines could be a cause of differences in the variability of the iron line region between multiple observations especially if they are strongly variable. Mrk 766(2) was found by Turner et al. (2004b) to have such a spectral component between 5.60 – 5.75 keV but this band shows no excess rms variability. NGC 3516(2) also showed evidence of narrow, transient iron lines at 5.6 keV and 6.2 keV (Turner et al., 2002) and these bands are variable in the $\sigma_{\rm rms}$-spectra though it is likely that this is mainly due to the variable broad iron line. Furthermore, the lines are narrower than the 0.4 keV-wide energy bands of the $\sigma_{\rm rms}$-spectra so the variability of the transient lines may be washed out. Longer observations with high S/N are needed to investigate the variability of transient iron lines.

There are alternatives to gravitational light bending in explaining a flat $\sigma_{\rm rms}$-spectrum. The reduced variability of the line could also be due to the inner disc being absent or suppressed so the line is unable to form close to the black hole where it would be more variable. This could be because the inner disc is highly ionised, radiatively inefficient or truncated. The bulk of the observed line flux would then arise from the outer region of the disc. However, the majority of the observations with a constant iron line have very broad iron lines, with profiles indicating that the emission is concentrated close to the black hole, so non-variability of the line should not be down to a lack of inner disc emission.

4.8.3 Narrow variability excesses

The origin of the narrower variability excesses, typically seen blueward of the line core, are also difficult to explain. When they are seen there is generally no variability at the red wing, so if the blue emission is the high energy wing of the disc line, it is hard to understand why the red part is not also variable: the red wing of the line should originate closer to the black hole where strong gravitational redshifting effects are present. An alternative is that the blue variability is due to absorption or emission by ionised iron close to the central source, but not too close so as to be broadened. This has been suggested for Mrk 766(3) by Miller et al. (2006). They split the iron K band into high and low ionisation bands and find only the former is variable. This agrees with the $\sigma_{\rm rms}$-spectrum showing an excess in the 6.6 – 7.0 keV band that is as large as the time-averaged component. Mrk 766(2) does not show such a strong excess at a similar energy and Pounds et al. (2003b) do not find any complexity around 7 keV in the spectrum. In addition there are also observations

with clear evidence for relatively narrow, ionised lines in their time-averaged spectra (e.g. NGC 3783, NGC 4593), which show no evidence for blue variability, indicating a more distant origin for these lines. Even if absorption or emission by photoionised gases does contribute, simple models would find it difficult to explain the varying strengths of the excesses. NGC 4151(2) and NGC 7314 are unusual in that they show a narrow excess redward of the line core. If the red variability excesses are real, they may be indicative of emission from a relatively isolated "hot spot" i.e. only a narrow range of radii in the relativistic region of the disc is illuminated.

It is interesting to compare our work to that of de Marco et al. (2009, DM09), who have studied the iron Kα line variability of a sample of nearby radio-quiet AGN by searching for excess emission in the time-energy plane. Twelve of their observations overlap with $\sigma_{\rm rms}$-spectra from our work: MCG-5-23-16(2), NGC 3516(2), NGC 3783, NGC 4051, Mrk 766(2), NGC 4593, MCG-6-30-15(1), MCG-6-30-15(2), NGC 5548(2), NGC 7314, Ark 564 and NGC 7469(2). Their method differs from ours in that it is optimised to search for narrow, transient features in the excess maps, whereas ours will characterise any variability, or lack thereof. Comparing the overlapping sample, the excess maps of eight out of the twelve showed no significant variability in any narrow transient line across the iron K band. This includes NGC 3516(2) in which we found variability across the iron line region that must then be due to a variable broad line, rather than narrow transient lines.

DM09 found significant variability in four observations for which we also have $\sigma_{\rm rms}$-spectra. NGC 7314 showed significant variations in the 5.4 – 5.8 keV band. Our $\sigma_{\rm rms}$-spectrum of this observation is difficult to understand because of some strong dips but there is a significant variability excess in the 5.4 – 5.8 keV band that could be a redshifted Fe Kα component as found in a 2002 Chandra observation (Yaqoob et al., 2003). Both observations of MCG-6-30-15 were found to exhibit Fe K band variability in the excess maps of DM09. This agrees broadly with our result for MCG-6-30-15(1), although we note that the variability across the iron line region in this observation is unlikely to be due solely to narrow line components as the excess extends down to 4.6 keV and it overlaps well with the time-averaged line profile. The $\sigma_{\rm rms}$-spectrum of the second MCG-6-30-15 observation shows narrow variability to the blue side. Comparison with the excess maps is more difficult in this case, as DM09 considered each of the three *XMM-Newton* revolutions separately, whereas we have combined them. However, we note that at least one of these does show blue variability, which is consistent with our result. Finally NGC 3783 has a variability excess in its $\sigma_{\rm rms}$-spectrum that corresponds to the weak broad and redshifted iron line in the time-averaged spectrum. DM09 also find significant variability between

5.4 – 6.1 keV in this source, in agreement with the $\sigma_{\rm rms}$-spectrum. Overall our results confirm the work of DM09 in the sense that both studies show that, contrary to some previous reports, variations in the iron Kα band are not uncommon. They also confirm that work in the sense that these variations are extremely difficult to interpret.

4.9 Variability of the heavily blurred disc reflection

NGC 5506(1) is the only narrow-line observation from Chapter 3 for which we have been able to calculate the $\sigma_{\rm rms}$-spectrum. Blurred disc reflection was significantly detected if it was both ionised and heavily blurred. There is no significant variability on the red wing side of the iron line, which may argue against blurred disc reflection but could also mean that the iron line is non-variable as found with MCG-6-30-15(2) and many other observations above. The strongest support for heavily blurred disc reflection is in NGC 5548(2), which is a non-relativistic-line observation. In this case, heavily blurred disc reflection was significantly detected in Chapter 3, if there was additional iron line emission from the BLR. Three bands between 5.0 – 6.2 keV possess excess variability above the continuum, which would be difficult to explain if the iron line is non-relativistic as the red wing does not extend below 5.8 keV. Instead, the variability could arise from the heavily blurred iron line responding to the continuum. The $\sigma_{\rm rms}$-spectra of two other non-relativistic-line observations, NGC 4593 and Ark 564 show no significant red wing variability. Whether the iron line is non-relativistically or heavily broadened, it is not variable. Interestingly, a good fit with heavily blurred disc reflection was obtained with NGC 4151(2), but only the 5.0 – 5.4 keV band showed significant variability. If the iron line is heavily blurred, it is surprising that either there is no variability across the iron line region or there is variability across the entire 5.0 – 6.4 keV energy range.

4.10 Conclusions

In this Chapter, we have studied the variability of the iron line and X-ray continuum between 2.5 – 10 keV in the N07 sample of Seyfert galaxies using $\sigma_{\rm rms}$-spectra. 18/37 observations have sufficient S/N to produce fully defined $\sigma_{\rm rms}$-spectra with no negative excess variances. The key results are:

- While $\sim$ 50% of the sample shows evidence for variations within the iron K-

band, only four observations have a broad variability profile. Furthermore, the prediction that variations in the iron line follow those in the continuum is only confirmed in two cases.

- Instead, there is a remarkable diversity in the shapes of the rms variability profiles of the iron Kα lines. 2/18 observations have a broad iron line that is more variable than the continuum and extends down to $\sim$ 5 keV. In contrast, 3/18 observations exhibit only bluewards variability that could arise from the accretion disc, or may be due to emission or absorption by other hot or photoionised gas close to the nucleus.

- The most interesting class of observations are the 11/18 that display a broad iron line in the time-averaged spectra but have an invariant red wing. Out of these, eight show no variability across the entire iron line region. The non-variable iron lines indicate a decoupling of the continuum and reflection component. This requires the intrinsic emission to be anisotropic, which is consistent with the expectations of gravitational light bending. This theory can also explain the MCG-6-30-15 observations, where the iron line is only variable in the observation with the lower mean 2 – 10 keV X-ray flux, although it is less clear if this applies more generally.

- There is a change in the iron line variability properties for 3/4 objects that have two observations. This shows that the variability of the iron line is not only different for individual objects, but it also changes from time to time for the same object.

- Mimicking of the broad red wing by complex absorption effects in objects such as NGC 3516 and NGC 4151 does not agree with their $\sigma_{\rm rms}$-spectra, which is either flat at the red wing or shows variations that are stronger than the continuum. Instead, the variability is more likely to be explained by a combination of anisotropy and strong gravitational effects, which is expected in the complex, central regions of AGN close to the black hole.

- The narrow core of the iron line at 6.4 keV is not found to be variable in all 18 observations. This agrees with the expectation that continuum variations will be averaged out before they are reflected by the outer disc or torus.

- The slope of the continuum variability profile is often steeper than the slope of the continuum in the time-averaged spectrum, which indicates that either the absorption may be variable, the non-variable reflection adds to the hard

flux but not the hard rms, or the continuum intrinsically softens as the 2.5 – 10 keV flux increases.

Chapter 5

On the origin of the X-ray spectral variability in Seyfert galaxies

5.1 Overview

In this Chapter, the focus is on the broadband X-ray variability in our sample of Seyferts on short time-scales of $\sim$ 40 ks. This extends the variability analysis of the iron line to the 0.3 – 10 keV energy range so that the soft excess, warm absorption, the continuum and the iron line and associated reflection continuum are all involved. Previous works have shown that the relativistically blurred disc reflection and smeared wind absorption models can produce a soft excess and explain the broad red wing of the iron line in the energy spectra of AGN. Both models also predict a normalised 0.3 – 10 keV variance-spectrum that peaks in variability between 0.7 – 2 keV so our first objective was to determine how many objects in the sample showed such a shape. We found that there is a diversity in both the shapes and amplitudes of the 51 normalised variance-spectra across the sample. The humped shape was visible in $\sim$ 50% of the spectra while flat, soft and hard profiles were also found to be common.

As the normalised excess variance of an AGN is expected to be inversely proportional to its black hole mass, we tested if the scatter in the amplitudes of the variance-spectra could be explained by the wide range of black hole masses in the sample. While the scatter did decrease between the black hole mass $\times$ normalised variance-spectra, the range of amplitudes across the sample is still large. The variety of amplitudes and shapes suggest that there are intrinsic differences in the spectral variability of both separate objects and within objects themselves as well, which is in agreement with the different types of iron line variability found in Chapter 4.

The second aim was to investigate the possible variance-spectrum profile shapes that can arise in the disc reflection and wind scenarios. In total, all four profile shapes: flat, humped, soft and hard can be produced by the five models that we test for each scenario. The average variance-spectrum of the humped group of variance-spectra is investigated further by testing if the models can explain both the amplitude and the shape. The only model capable of explaining the humped spectral variability is that where only the X-ray continuum varies in the reflection model, while the distant reflection, the relativistically blurred reflection and the warm absorption remain constant. The change in the continuum is of the form where the spectral slope steepens linearly by $\sim \Delta\Gamma = 0.07$ while the continuum flux changes by a factor of 1.4 relative to its minimum value.

5.2 Introduction

In Chapter 4, we investigated the variability of the iron line region in the N07 sample of observations of local Seyfert 1s. This was found to complement the analysis of the iron line region in the corresponding time-averaged spectra. The iron line variability is one diagnostic of the variability in the central regions of AGN, but we can also study the broadband X-ray spectral variability between 0.3 – 10 keV to learn more about the X-ray emission mechanisms. The extended energy range allows us to investigate the spectral variability of the direct power-law continuum above 2 keV, the reflection continuum consisting of the iron line and Compton hump, and also the soft excess.

As discussed in Chapter 1, the soft excess is too hot to be standard disc emission from a supermassive black hole. The possibility of a Comptonising region appears to be ruled out by the constant temperature of such a region across AGN that vary in their black hole mass across several orders of magnitude. The most recent scenarios support an atomic origin with either disc reflection or a velocity-smeared wind. Both mechanisms are based on the increase in opacity associated with lines and edges of O VII, O VIII and iron at $\sim$ 0.7 keV. In the reflection model, the decrease in opacity below $\sim$0.7 keV leads to a strong increase in reflection below this energy. The soft X-ray emission lines from reflection must be smeared by relativistic effects in order to produce the smooth shape of the soft excess. Alternatively, the wind absorption model can explain the soft excess if the absorption features between 0.7 – 2 keV are produced by winds with relativistic velocities, which will smear out the characteristic absorption features. The absorption produces a hole in the energy spectrum, which can then lead to an apparent soft excess below 0.7 keV and a harder spectrum at

Figure 5.1: Humped normalised variance-spectra of IRAS 13224-3809 (left) and NGC 4051 (right). Figures taken from Gallo et al. (2004) and Ponti et al. (2006) respectively.

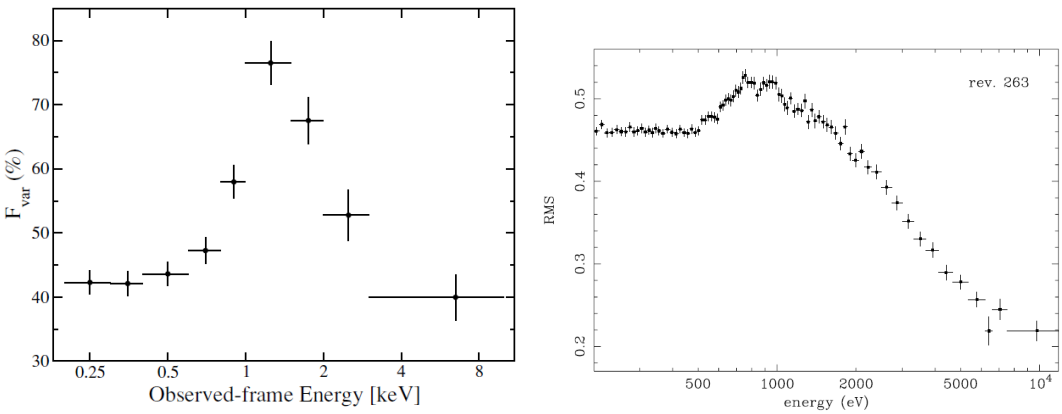

higher energies.

It has been difficult to separate between the two models when fitting to the energy spectra of local Seyfert 1s. Both models predict a hump in the normalised variance spectrum between 0.7 – 2 keV, where the opacity is higher, if the reflection is constant in the reflection scenario (Ponti et al., 2006) or if the variability originates from changes in the ionisation state of the wind absorber (Gierliński & Done, 2006). Such humped variance-spectra have been found in observations of Seyfert 1s such as: MCG-6-30-15 (Vaughan & Fabian, 2004; Ponti et al., 2004), 1H 0707-495 (Gierliński & Done, 2006), NGC 4051 (Ponti et al., 2006), RX J0136.9-3510 (Jin et al., 2009), IRAS 13224-3809 (Gallo et al., 2004). Two examples are shown in Figure 5.1. However, in other cases, the variance profiles have been found to be flat e.g. Mrk 335 (O'Neill et al., 2007) and hard e.g. Ark 120 (Vaughan et al., 2004) and RE J1034+396 (Middleton et al., 2009).

The first aim of this Chapter is to determine the normalised variance-spectra for the N07 sample across 0.3 – 10 keV. In order to ensure a fair analysis, the variance-spectra are calculated over time-scales of between 30 – 40 ks. The shapes of the variance profiles will be classified so as to find out how common the humped profiles are compared to the other shapes. The second aim is to investigate the various models involved in the wind absorption and disc reflection scenarios that can produce spectral variability and test if they can explain the observed broadband spectral variability in the sample.

5.3 Normalised excess variance-spectrum

As with the analyses of Chapters 3 and 4, our sample comprised the 37 observations of 26 Seyfert 1 galaxies used by N07. Given the red-noise nature of AGN X-ray light curves, a fair comparison of the spectral variability of different observations requires the bin size and duration of the light curves to be similar. Therefore, as in Chapter 4, the light curves of all sources in each band were binned to a resolution of 1000s, which ensures Gaussian statistics. In addition, we split the light curves into equal-sized segments. This differs from the analysis of the iron line rms variability in Chapter 4 where we used the whole light curve so as to compared the rms-spectrum directly to the time-averaged energy spectrum for each observation. In this study, we aimed to obtain as many variance-spectra as possible and so divided the light curve of each observation if it was sufficiently long enough. The segment length is important as segments of longer duration sample higher amplitudes of variability and reduce the Poisson measurement uncertainty in the calculation of $\sigma^2_{\rm nvar}$. On the other hand, shorter durations result in a larger number of segments and ensure a more accurate determination of the average variance. Following O'Neill et al. (2005), segments of length 30 – 40 ks were used as a trade-off between these considerations. As they have light curves of duration less than 30 ks, NGC 2992, NGC 5506 and Mrk 509 were excluded from the final sample.

The division into segments begins with selecting the first 40 ks long segment of the light curve (or $\geq 30 - 40$ ks if the light curve is less than 40 ks long). If the light curve is long enough, the next fully exposed bin is chosen as the start of the second segment. This continued until less than 30 ks of data is available at the end of the light curve.

Time bins where monitoring occurs during periods of high background (see Section 2.4.4) are classed as "fractionally-exposed" as opposed to "fully-exposed" time bins where the background is low throughout. The fractionally-exposed time bins are not included in this analysis as their count rates will be lower than expected if the bin was fully-exposed and so will affect the determination of the excess variance. To ensure that segments are not under-sampled across their entire length, we only retained segments with a minimum of 20 fully-exposed bins. MCG+8-11-11, Mrk 6 and MCG-5-23-16 did not have any segments with 20 or more fully-exposed bins so we removed these objects from the sample. The 0.3 – 10 keV light curve of each observation in the sample and the selection of the segments is shown in Figure 5.2. Time bins that are fractionally-exposed are shaded in blue and segments that were not used because of a lack of bins are shaded in grey. Remaining gaps in the light

curve are due to periods of time when observing did not occur. Segment boundaries are plotted with dashed lines. The observations that form our sample and the lengths of their segments are listed in Table 5.1.

The full band light curves for most observations appear to be variable over both short and long time-scales. Our final criterion of the segment selection was to test the whole 0.3 – 10 keV light curve for a constant count rate with a simple χ^2 test at a confidence level of 90%. The results are given in Columns 4 and 5 of Table 5.1. As expected, the majority of the segment light curves are badly fit by a constant, but three segment light curves were found to be non-variable. They are the segments of Mrk 590, NGC 2110 and NGC 7213. As they are the only segments of their respective objects, they were excluded from the sample. All other objects were found to have variable light curves and they formed the final sample of 17 objects and 51 segments.

The objects in our sample and estimates of their black hole mass are listed in Table 5.2. For 11 objects, we used "reverberation mapping" $M_\bullet$ estimates and these were obtained directly from the references listed in column 4. We explicitly calculated the black hole mass of 5 objects using the latest $M_\bullet - \sigma_\star$ relationship of Gültekin et al. (2009):

$$\log\left(\frac{M_\bullet}{\mathrm{M}_\odot}\right) = (8.12 \pm 0.08) + (4.24 \pm 0.41) \times \log\left(\frac{\sigma_\star}{200 \text{ km s}^{-1}}\right). \tag{5.1}$$

For these objects, column 4 gives the references for the adopted $\sigma_\star$ measurements. Finally, for HE 1143-1800, we used the relationship between $M_\bullet$, Hα width, $\mathrm{FWHM}_{\mathrm{H}\alpha}$, and luminosity, $L_{\mathrm{H}\alpha}$ (Greene & Ho, 2005):

$$M_\bullet = (2.0^{+0.4}_{-0.3}) \times 10^6 \left(\frac{L_{\mathrm{H}\alpha}}{10^{42} \text{ ergs s}^{-1}}\right)\left(\frac{\mathrm{FWHM}_{\mathrm{H}\alpha}}{10^3 \text{ km s}^{-1}}\right). \tag{5.2}$$

The reference in column 4 provides estimates of both $\mathrm{FWHM}_{\mathrm{H}\alpha}$ and the Hα flux, while the luminosity distance was taken from the NASA Extragalactic Database.

5.3.1 Estimation of the normalised excess variance-spectrum

The normalised excess variance is calculated in each energy band by dividing the excess variance of Equation 2.2 with the mean count rate, $\sigma^2_{\mathrm{nvar}}(E) = \sigma^2_{\mathrm{XS}}(E)/\mu_E$. The 1σ errors of σ^2_{nvar} arising from measurement uncertainties are calculated in the same way as for σ_{rms} (described in Section 4.3.1). Our main aim in this Chapter is to

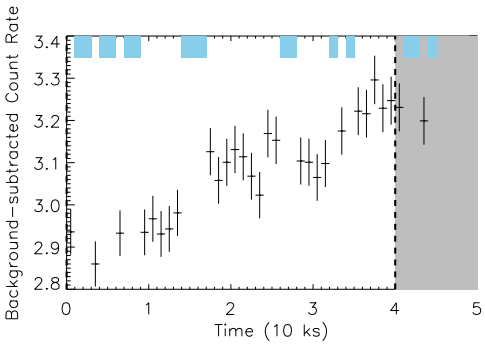

NGC 526A

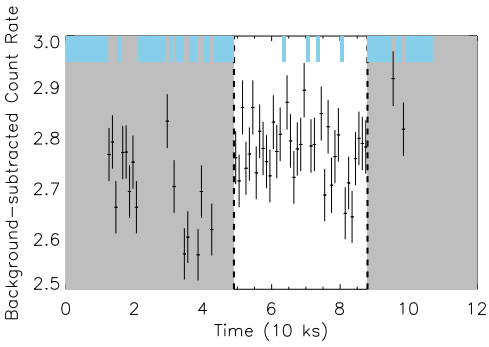

Mrk 590

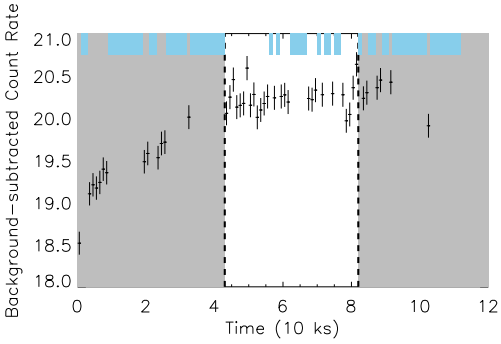

Ark 120

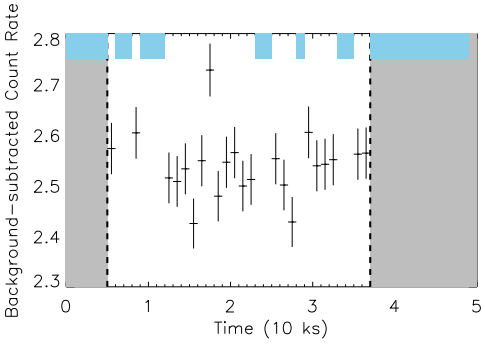

NGC 2110

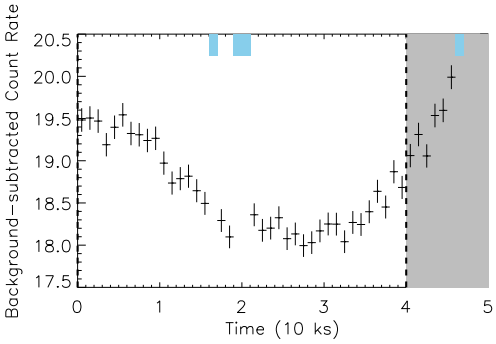

Mrk 110

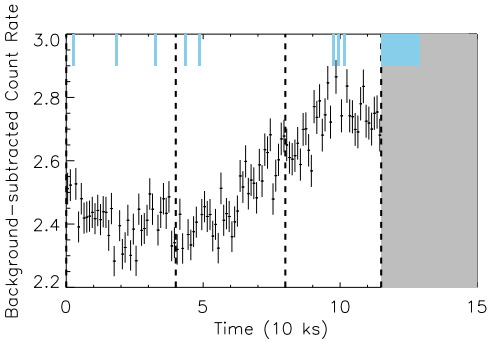

NGC 3516(2)

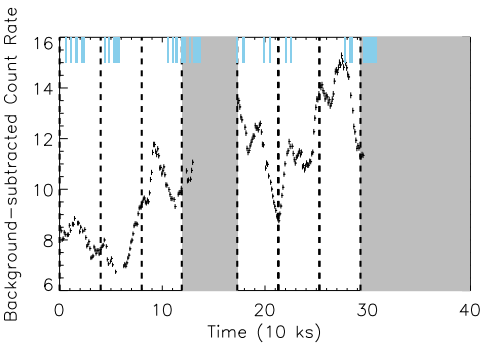

NGC 3783

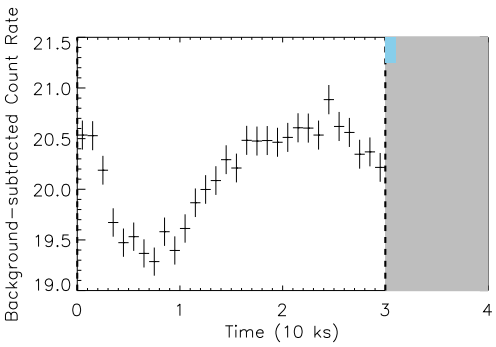

HE 1143-1800

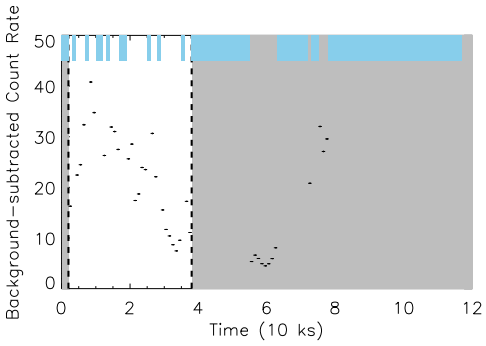

NGC 4051

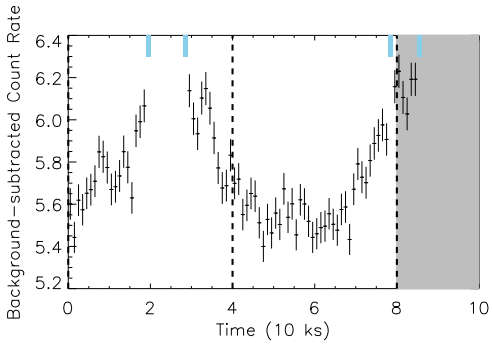

NGC 4151(2)

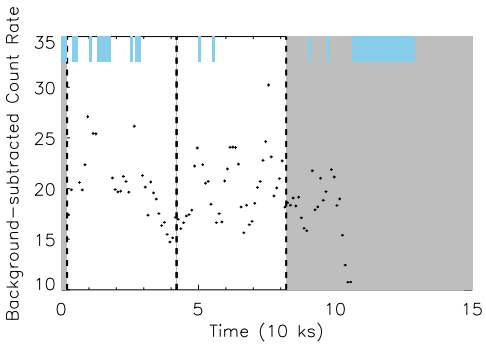

Mrk 766(2)

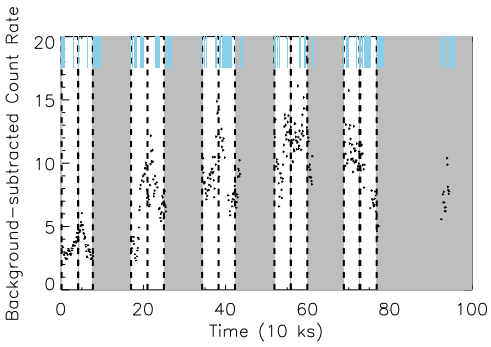

Mrk 766(3)

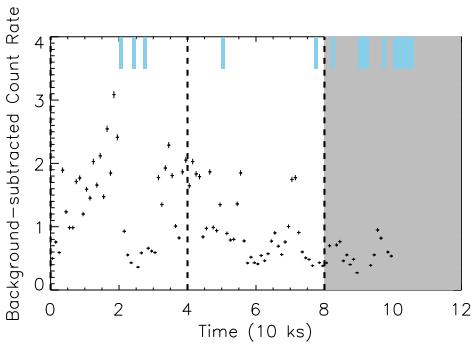

NGC 4395

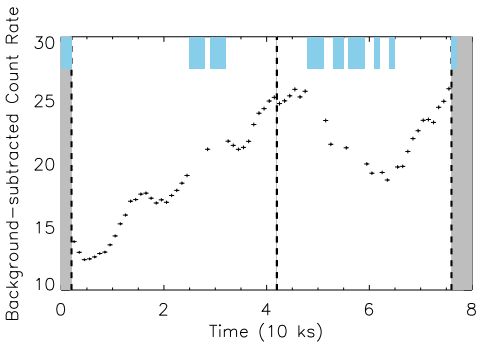

NGC 4593

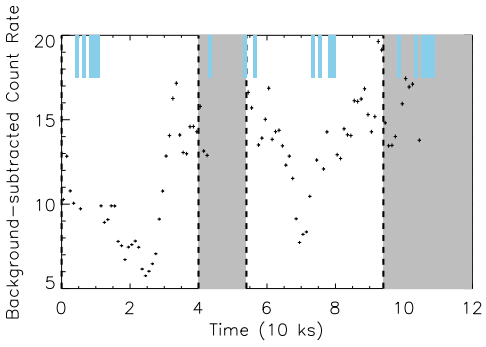

MCG-6-30-15(1)

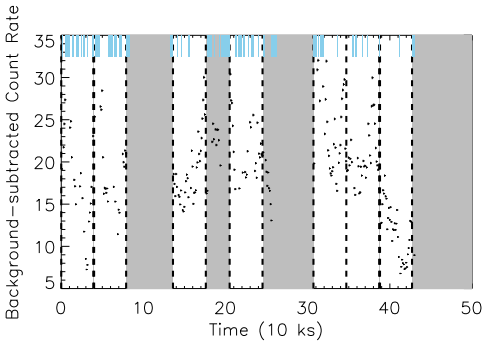

MCG-6-30-15(2)

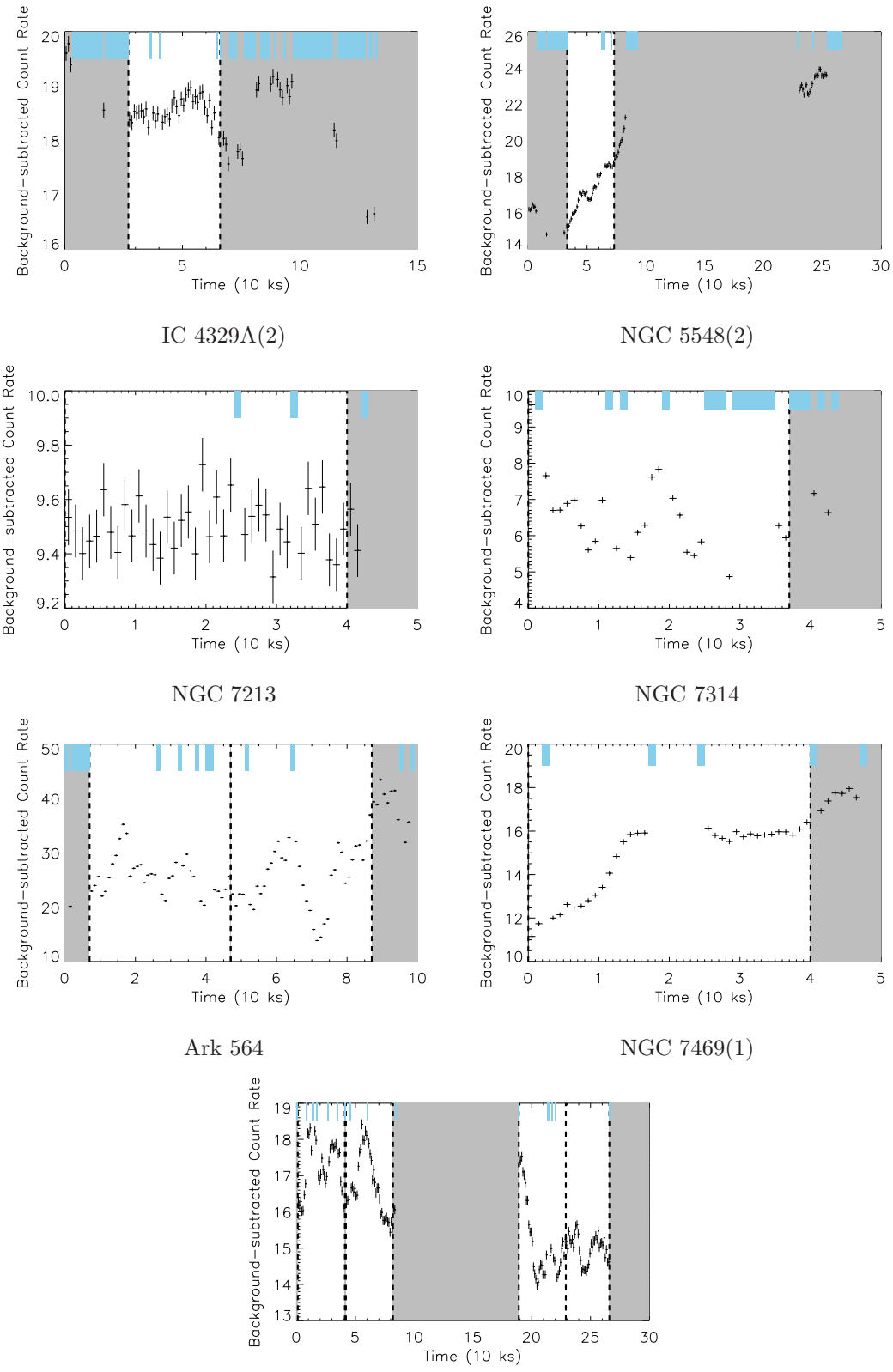

Figure 5.2: The 0.3 – 10 keV light curves of observations in the N07 sample with a minimum of one acceptable segment. Segments have a length between 30 – 40 ks and are separated by dashed lines. Time bins that are fractionally-exposed are shaded in blue and segments with a lack of 20 fully-exposed bins are shaded in grey.

Table 5.1: Our sample of EPIC-pn observations with at least one acceptable segment. Column (1): observation. Column (2): number of segments. Column (3): minimum and maximum lengths of segments (ks). Column (4): χ^2 and degrees of freedom for a fit of a constant count rate to the 0.3 – 10 keV light curve. column (5): probability of obtaining χ^2 by chance. Observations with a constant light curve at a confidence level of 90% are shown in bold.

Name (1)	Segments (2)	Min - Max Length (3)	χ^2/d.o.f. (4)	Prob (5)
NGC 526A	1	40	70/28	0.00
Mrk 590	**1**	**39**	**64/51**	**0.11**
Ark 120	1	39	150/45	0.68
NGC 2110	**1**	**32**	**25/21**	**0.26**
Mrk 110	1	40	199/42	0.00
NGC 3516(2)	3	35 – 40	711/106	0.00
NGC 3783	6	39 – 40	25176/33	0.00
HE 1143-1810	1	30	72/29	0.00
NGC 4051	1	36	12728/37	0.00
NGC 4151(2)	2	40	993/73	0.00
Mrk 766(2)	2	40	5313/88	0.00
Mrk 766(3)	10	36 – 40	70518/364	0.00
NGC 4395	2	40	5114/89	0.00
NGC 4593	2	34 – 40	5709/57	0.00
MCG-6-30-15(1)	2	40	14349/80	0.00
MCG-6-30-15(2)	7	39 – 40	70856/227	0.00
IC 4329A(2)	1	39	451/59	0.00
NGC 5548(2)	1	40	3276/77	0.00
NGC 7213	**1**	**40**	**49/39**	**0.13**
NGC 7314	1	37	1620/25	0.00
Ark 564	2	40	7466/83	0.00
NGC 7469(1)	1	40	487/36	0.00
NGC 7469(2)	4	37 – 40	2029/146	0.00

Table 5.2: The sample sources and their black hole mass estimate. Column (1): source name. Column (2): black hole mass estimate. Column (3): method of estimation: R, reverberation mapping; S, stellar velocity dispersion; L, relationship between $M_\bullet$, Hα width and luminosity. Column (4): reference: 1, Peterson et al. (2004); 2, Denney et al. (2009); 3, Bentz et al. (2006); 4, Bentz et al. (2009a); 5, Peterson et al. (2005); 6, Denney et al. (2006); 7, weighted mean of Bentz et al. (2007) and Bentz et al. (2009b); 8, Garcia-Rissmann et al. (2005); 9, Woo et al. (2010); 10, Cid Fernandes et al. (2004); 11, Botte et al. (2004); 12, Oliva et al. (1999); 13, Rodríguez-Ardila et al. (2000).

Name	Log(Mass) ($M_\odot$)	Method	Reference
(1)	(2)	(3)	(4)
NGC 526A	8.3	S	8
Ark 120	8.1	R	1
Mrk 110	7.4	R	1
NGC 3516	7.6	R	1
NGC 3783	7.5	R	1
HE 1143-1810	7.3	L	13
NGC 4051	6.2	R	2
NGC 4151	7.6	R	3
Mrk 766	6.2	R	4
NGC 4395	5.6	R	5
NGC 4593	7.0	R	6
MCG-6-30-15	6.3	S	9
IC 4329A	8.3	S	12
NGC 5548	7.8	R	7
NGC 7314	5.9	S	10
Ark 564	7.0	S	11
NGC 7469	7.1	R	1

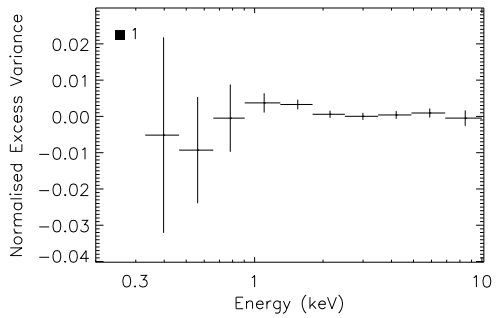

NGC 526A

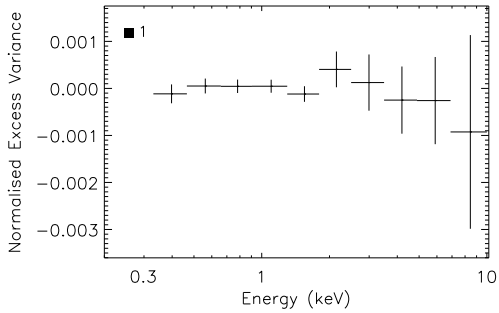

Ark 120

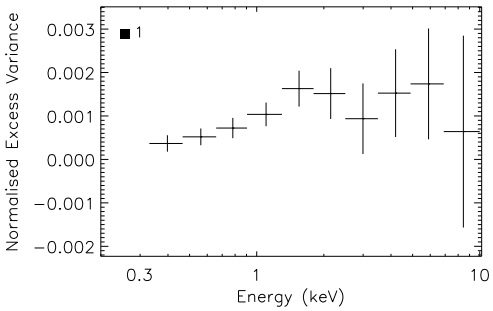

Mrk 110

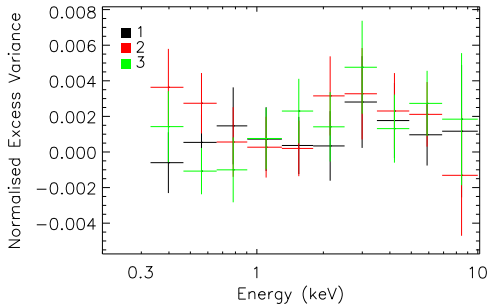

NGC 3516(2)

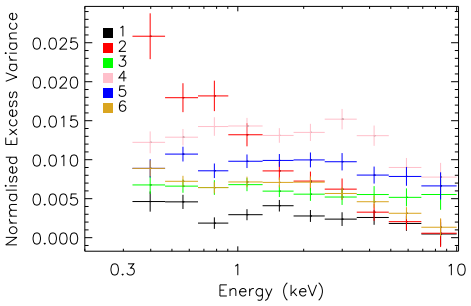

NGC 3783

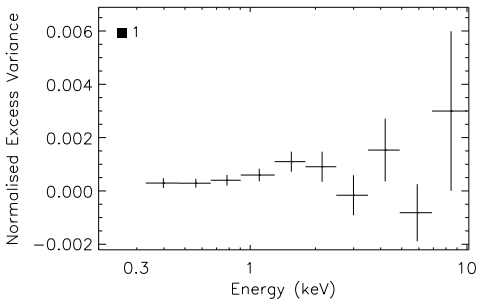

HE 1143-1800

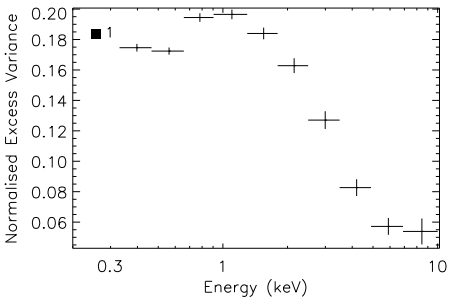

NGC 4051

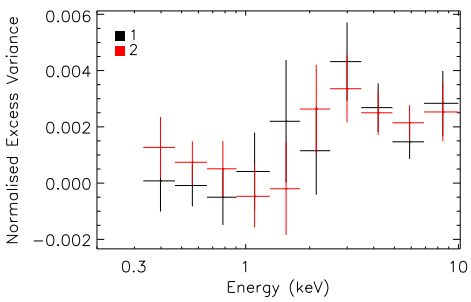

NGC 4151(2)

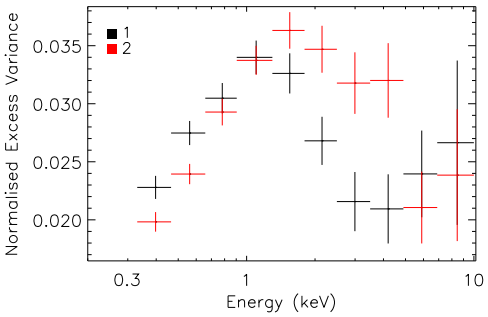

Mrk 766(2)

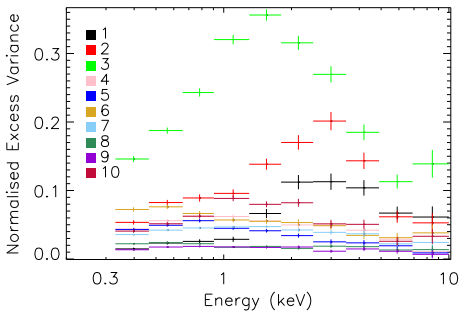

Mrk 766(3)

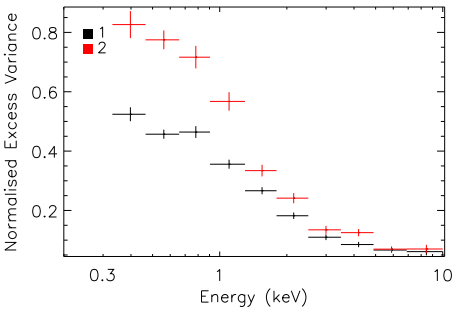

NGC 4395

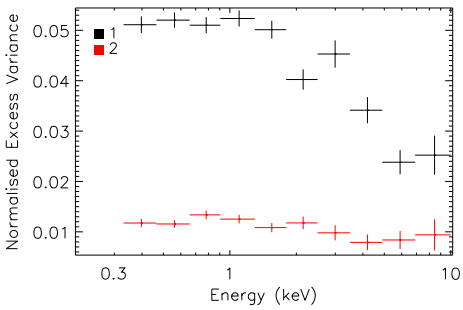

NGC 4593

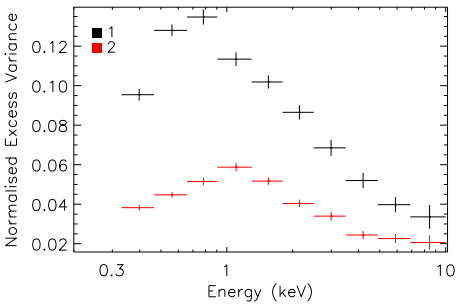

MCG-6-30-15(1)

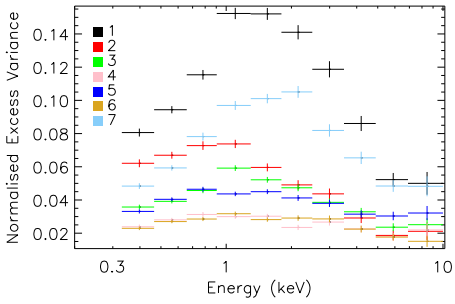

MCG-6-30-15(2)

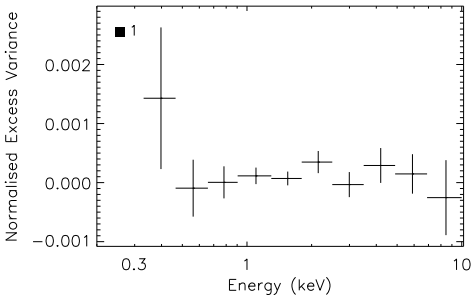

IC 4329A(2)

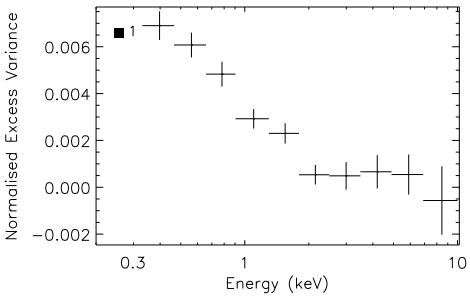

NGC 5548(2)

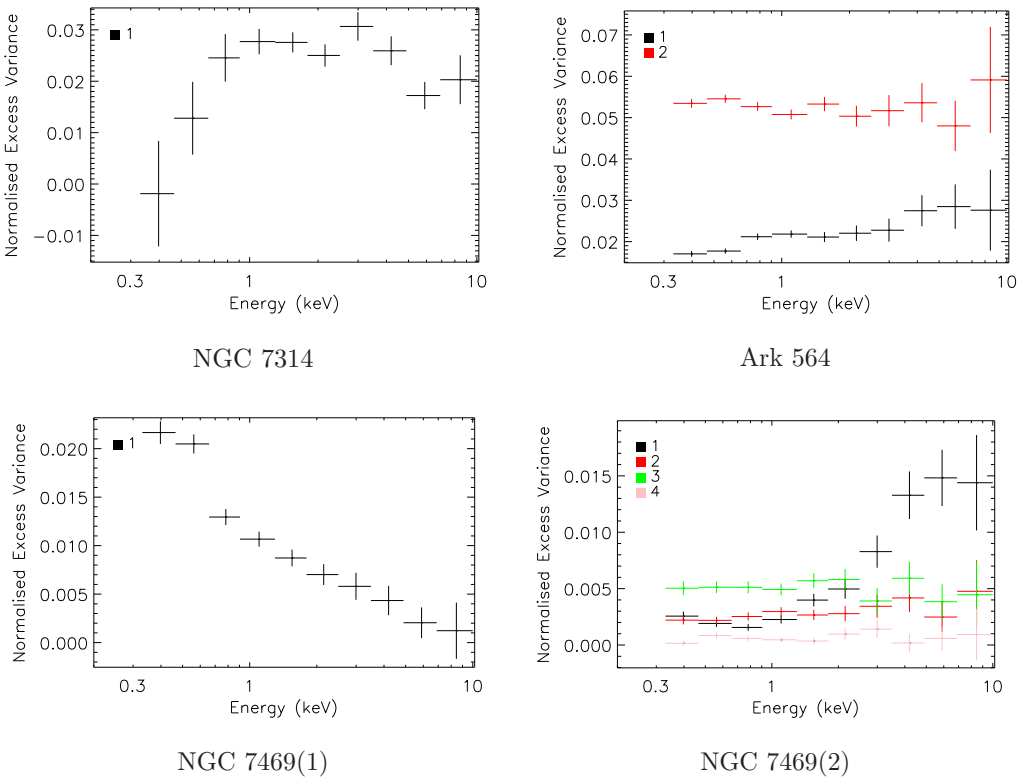

Figure 5.3: The 0.3 – 10 keV $\sigma^2_{\rm nvar}$-spectra of the observations in the sample. The spectra of multiple segments are plotted on the same axis in different colours.

study the dependence of the broadband spectral variability amplitude between 0.3 – 10 keV. Therefore we selected 10 energy bands from 0.3 to 10 keV in such a way that $\Delta E/E_{\rm l} = 0.4$, where ΔE is the band size and $E_{\rm l}$ is the lower energy bound of the band. The bands are smaller at lower energies to increase the resolution, while the variability of the reflection component at higher energies is still observable in the larger energy bands.

The 0.3 – 10 keV $\sigma^2_{\rm nvar}$-spectra have been calculated for each segment and are shown in Figure 5.3 with multiple segment spectra plotted in different colours. It should be noted that the $\sigma^2_{\rm nvar}$ values in some bands are negative for a few segments. However, these values are consistent with positive $\sigma^2_{\rm nvar}$ values once the 1σ Poisson uncertainty is taken into account.

A key result of this Chapter is the clear diversity in the shape of the $\sigma^2_{\rm nvar}$ profiles throughout the sample. To illustrate this, the top panel of Figure 5.4 shows the $\sigma^2_{\rm nvar}$-spectrum of segments of Ark 564, NGC 4593, NGC 7469 and MCG-6-30-15. The profiles can be broadly classified into four categories: "flat" e.g. Ark 564, "soft" e.g. NGC 4593, "hard" e.g. NGC 7469 and "humped" e.g. MCG-6-30-15.

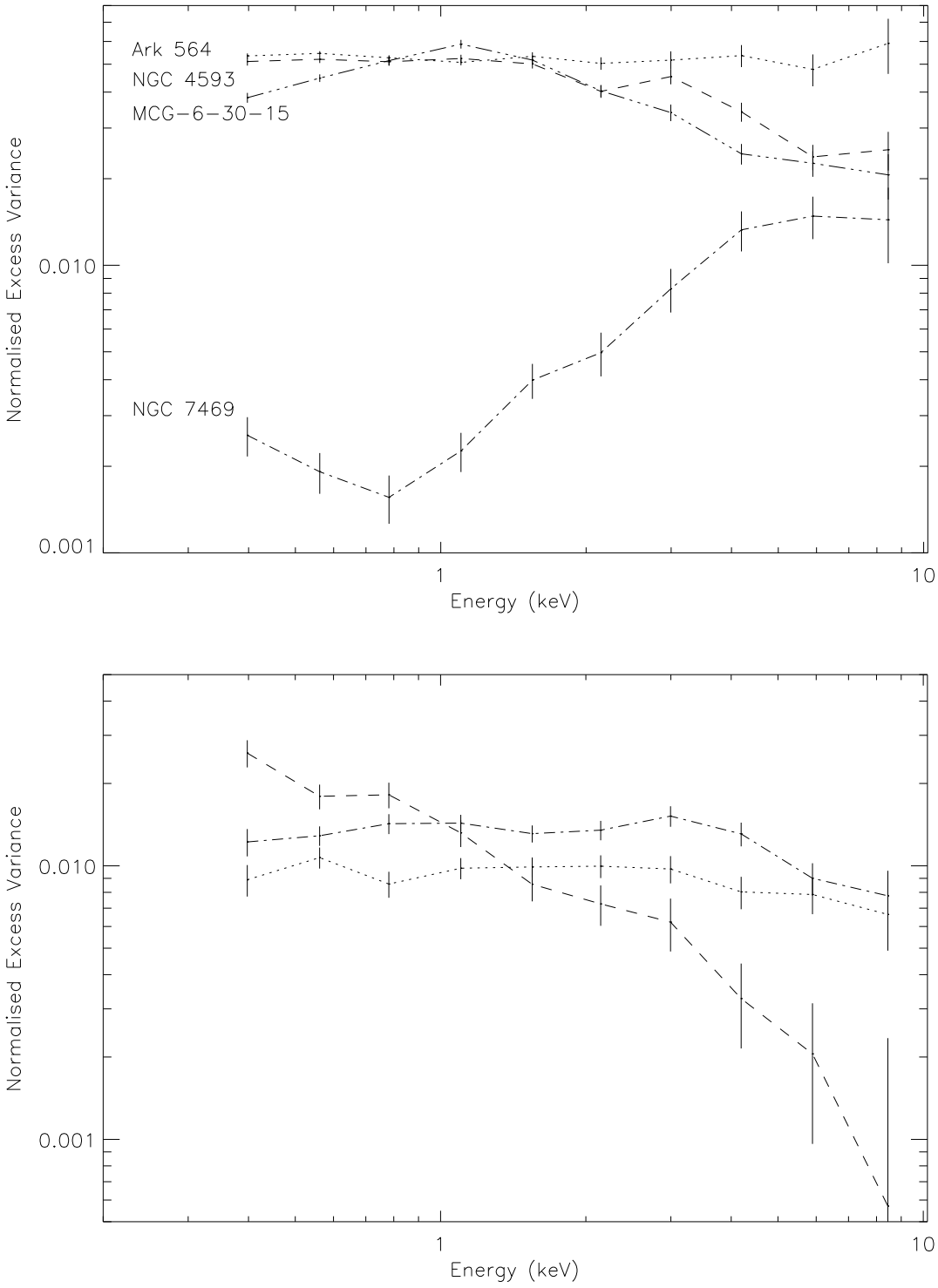

Figure 5.4: $\sigma^2_{\rm nvar}$-spectra of segments of Ark 564, NGC 4593, MCG-6-30-15, NGC 7469 (top panel) and NGC 3783 (bottom panel) showing the diversity in their profiles and amplitudes. Error bars on the energy bands are omitted for clarity.

While some difference in the *amplitudes* of the spectra is expected from the anti-correlation between $\sigma^2_{\rm nvar}$ and the black hole mass, the different profile *shapes* suggest that there are intrinsic differences between the spectral variability of the objects. Furthermore, the non-similarity of the profile shapes extends to $\sigma^2_{\rm nvar}$-spectra of the same object. For example, the bottom panel of Figure 5.4 displays the $\sigma^2_{\rm nvar}$-spectra from three segments of NGC 3783. Two of the spectra have a similar shape but different amplitudes, which cannot be explained by a varying black hole mass, but could possibly be explained by red-noise effects. However, the shape of these two $\sigma^2_{\rm nvar}$-spectra varies from the third spectrum, which is soft. Differences in profile shapes cannot be due to red-noise effects, so the intrinsic differences in spectral variability extend to $\sigma^2_{\rm nvar}$-spectra of the same object. There appears to be no relationship between the changes in the $\sigma^2_{\rm nvar}$-spectra and the 2 – 10 keV flux as the first and second segments of NGC 3783 are at a similar flux level, but have flat and soft profile shapes respectively and different amplitudes.

Table 5.3 shows the classification of the shape of each variance-spectrum. A spectrum was determined to be flat if it could be fit with a constant $\sigma^2_{\rm nvar}$ at a confidence level of 99%. This group was made of 18 $\sigma^2_{\rm nvar}$-spectra. The remaining $\sigma^2_{\rm nvar}$-spectra naturally appear to fall into three groups. The largest is that containing the 24 humped $\sigma^2_{\rm nvar}$-spectra. The soft and hard classes consist of 7 and 2 $\sigma^2_{\rm nvar}$-spectra respectively. While the humped profiles have commonly been found in local Seyferts, this analysis shows only $\sim 50\%$ of the variance-spectra have such a shape over time-scales of 30 – 40 ks. Multiple $\sigma^2_{\rm nvar}$-spectra from the same observation such as NGC 3783, NGC 4593, Mrk 766, Ark 564 and NGC 7469(2) also show different shapes, but the spectra of MCG-6-30-15 show no change in shape between segments or even observations.

Table 5.3: The classification of the $\sigma^2_{\rm nvar}$-spectra in the sample. Column (1): source name. Column (2): segment number. Column (3): χ^2 of a fit with constant $\sigma^2_{\rm nvar}$. The degrees of freedom is 9 and the confidence level is 99%. Column (4): Class of the $\sigma^2_{\rm nvar}$-spectrum. Flat $\sigma^2_{\rm nvar}$-spectra are those that are well-fit with a constant $\sigma^2_{\rm nvar}$. If the $\sigma^2_{\rm nvar}$-spectrum is not flat, it is judged to be either soft, hard or humped, depending on the shape of the profile.

Name	Segment	χ^2	Class
(1)	(2)	(3)	(4)
NGC 526A	1	6.4	Flat
Ark 120	1	2.7	Flat

Continues on next page

Table 5.3 – continued from previous page

Name	Segment	χ^2	Class
Mrk 110	1	14	Flat
NGC 3516(2)	1	1.8	Flat
NGC 3516(2)	2	4.9	Flat
NGC 3516(2)	3	7.4	Flat
NGC 3783	1	14	Flat
NGC 3783	2	171	Soft
NGC 3783	3	3.7	Flat
NGC 3783	4	25	Humped
NGC 3783	5	9.6	Flat
NGC 3783	6	52	Soft
HE 1143-1810	1	9.2	Flat
NGC 4051	1	1070	Humped
NGC 4151(2)	1	18	Flat
NGC 4151(2)	2	13	Flat
Mrk 766(2)	1	68	Humped
Mrk 766(2)	2	176	Humped
Mrk 766(3)	1	271	Humped
Mrk 766(3)	2	321	Humped
Mrk 766(3)	3	1100	Humped
Mrk 766(3)	4	89	Humped
Mrk 766(3)	5	147	Humped
Mrk 766(3)	6	94	Humped
Mrk 766(3)	7	66	Humped
Mrk 766(3)	8	34	Humped
Mrk 766(3)	9	21	Humped
Mrk 766(3)	10	196	Humped
NGC 4395	1	1350	Soft
NGC 4395	2	1220	Soft
NGC 4593	1	198	Soft
NGC 4593	2	198	Flat
MCG-6-30-15(1)	1	742	Humped
MCG-6-30-15(1)	2	320	Humped
MCG-6-30-15(2)	1	837	Humped
MCG-6-30-15(2)	2	433	Humped

Continues on next page

Table 5.3 – continued from previous page

Name	Segment	χ^2	Class
MCG-6-30-15(2)	3	267	Humped
MCG-6-30-15(2)	4	53	Humped
MCG-6-30-15(2)	5	103	Humped
MCG-6-30-15(2)	6	69	Humped
MCG-6-30-15(2)	7	591	Humped
IC 4329A(2)	1	4.4	Flat
NGC 5548(2)	1	165	Soft
NGC 7314(1)	1	27	Humped
Ark 564	1	45	Hard
Ark 564	2	45	Flat
NGC 7469(1)	1	277	Soft
NGC 7469(2)	1	104	Hard
NGC 7469(2)	2	6.5	Flat
NGC 7469(2)	3	3.7	Flat
NGC 7469(2)	4	6.6	Flat

As mentioned above, apart from the diversity in shape, there is also a large range in the amplitudes of the $\sigma^2_{\rm nvar}$-spectra. This scatter cannot be explained by the uncertainty associated with Poisson noise as the error bars on $\sigma^2_{\rm nvar}$, in nearly all the bands, do not overlap. It is possible that the scatter in amplitudes may be due to the different black hole masses (e.g. Lu & Yu, 2001; Bian & Zhao, 2003; Papadakis, 2004). The 2 – 10 keV $\sigma^2_{\rm nvar}$-black hole mass relationship of 16/26 of the objects in our sample have been studied by O'Neill et al. (2005), with an inverse proportionality found over the same 30 – 40 ks time-scales as the segments in this work. As the AGN light curves in various X-ray energy bands are strongly correlated (see for example: Papadakis & Lawrence (1995) and McHardy et al. (2004) for NGC 4051, Nandra & Papadakis (2001) for NGC 7469, Markowitz et al. (2007) for Mrk 766 and Vaughan et al. (2004) for MCG-6-30-15), we expect that a similar relationship will probably hold in each energy band between 0.3 – 10 keV.

All the $\sigma^2_{\rm nvar}$-spectra of all the sources in the sample are plotted together in the top panel of Figure 5.5 with the $\sigma^2_{\rm nvar}$ values in each band connected with dots. For presentation purposes, error bars are omitted. As for Figure 5.4, a logarithmic y-axis is used for presentation purposes. This requires that absolute $\sigma^2_{\rm nvar}$ values are plotted in each band so negative $\sigma^2_{\rm nvar}$ values are shown with larger black dots. In

Table 5.4: Coefficients of variation (σ/mean) for the $\sigma^2_{\rm nvar}$ and $M_\bullet\sigma^2_{\rm nvar}$ distributions in each energy band. Column (1): energy band. Column (2): $\sigma^2_{\rm nvar}$ coefficient of variation. Column (3): $M_\bullet\sigma^2_{\rm nvar}$ coefficient of variation.

Energy band (keV) (1)	$\sigma^2_{\rm nvar}$ σ/μ (2)	$M_\bullet\sigma^2_{\rm nvar}$ σ/μ (3)
0.33 – 0.47	0.35	0.26
0.47 – 0.66	0.32	0.43
0.66 – 0.9	0.29	0.15
0.9 – 1.3	0.26	0.15
1.3 – 1.8	0.22	0.14
1.8 – 2.5	0.20	0.13
2.5 – 3.5	0.20	0.13
3.5 – 4.9	0.18	0.13
4.9 – 6.9	0.16	0.14
6.9 – 10.0	0.17	0.20

the bottom panel of Figure 5.5, we show the $\sigma^2_{\rm nvar}$-spectra multiplied by the AGN $M_\bullet$ (for comparison reasons, the y-axis has the same maximum/minimum range as the plot of the $\sigma^2_{\rm nvar}$-spectra). The scatter in $M_\bullet\sigma^2_{\rm nvar}$ is clearly smaller than the scatter in $\sigma^2_{\rm nvar}$ for nearly every energy band. The normalised measure of dispersion in each energy band can be given by the "coefficients of variation" (standard deviation divided by the mean), and the values for all energy bands in both the $\sigma^2_{\rm nvar}$- and $M_\bullet\sigma^2_{\rm nvar}$-spectra are given in Table 5.4. The coefficients of variation confirm that apart from two bands, the scatter in the amplitudes of the $M_\bullet\sigma^2_{\rm nvar}$-spectra is less than that of the $\sigma^2_{\rm nvar}$-spectra. This result confirms that the black hole mass does indeed "normalise" the variance-spectra, i.e. in other words, the normalised excess variance is anti-correlated with the black hole mass in nearly all energy bands.

Even after normalisation by the black hole mass, a large amount of scatter is seen in the amplitudes of the $M_\bullet\sigma^2_{\rm nvar}$-spectra. It is possible that some part of the scatter in the amplitudes of the spectra may be due to the red-noise nature of variability in AGN. However, as each energy band is highly correlated, the light curves of each energy band are the same realisation of the underlying red-noise process. Therefore, red-noise effects cannot account for differences in the *shapes* of two $M_\bullet\sigma^2_{\rm nvar}$-spectra. This implies that while the red-noise variability could partially contribute to differences in the *amplitudes* of the $M_\bullet\sigma^2_{\rm nvar}$-spectra, the diversity in the *shapes* reflect intrinsic differences in the spectral variability of the objects. This applies both to different objects, and multiple $\sigma^2_{\rm nvar}$-spectra of the same source where

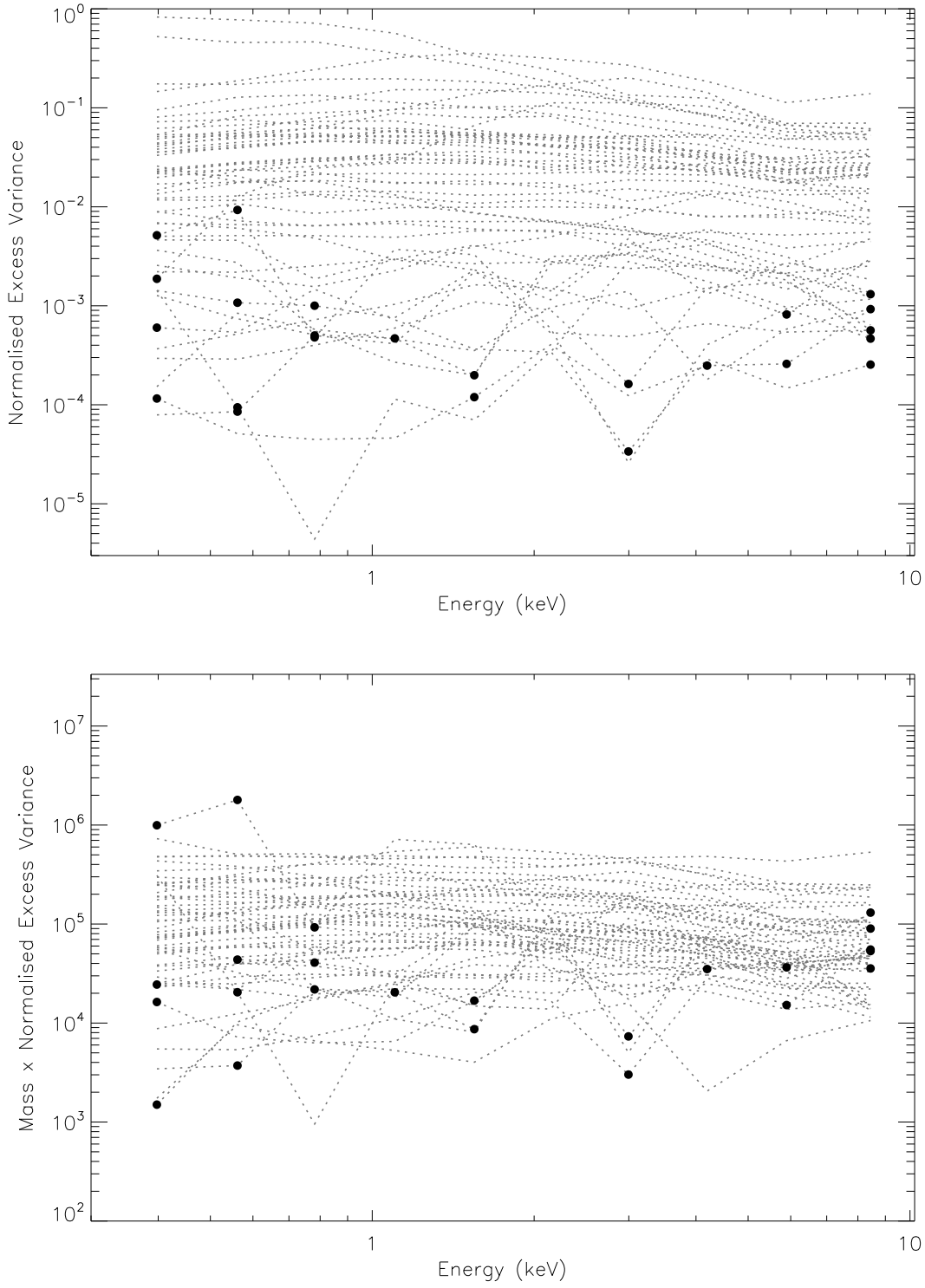

Figure 5.5: The absolute $\sigma^2_{\rm nvar}$-spectra and $M_\bullet\sigma^2_{\rm nvar}$-spectra (top and bottom panels respectively) of all observations in the sample between 0.3 – 10 keV (negative values are indicated with larger dots). Error bars are omitted for clarity.

the profile changes shape e.g. NGC 3783.

5.4 Profile shapes of the model variance-spectra.

The previous section showed that there are four distinct profile shapes in the $\sigma^2_{\rm nvar}$-spectra of the sample: flat, soft, hard and humped. The aim of this section is to test if these shapes can be explained by spectral variability that is invoked in disc reflection and wind absorption models. This is achieved by creating a model energy spectrum between 0.3 – 10 keV and varying one or model parameters uniformly over time to produce a model variance-spectrum. The shapes of the model variance-spectra can be classed to determine if the modelled spectral variability explains the various profile shapes that we see.

5.4.1 The time-averaged spectrum at hard X-rays

The first step is to set the "mean parameters" of the model time-averaged energy (MTE) spectrum. We use the observations that possess a humped-variance spectrum to set the mean parameters as this group is analysed in more detail in Section 5.5. It is important to note that the shapes of the model variance-spectra that we calculate depend more heavily on the variation of the model parameters rather than their mean values.

The group of 24 humped variance-spectra are made up of 7 observations of 5 objects: NGC 3783, NGC 4051(1), Mrk 766(2), Mrk 766(3), MCG-6-30-15(1), MCG-6-30-15(2) and NGC 7314. Evidence for reflection from a blurred reflection disc was found in each case in the analysis of N07. Furthermore, in these 7 observations, the broadening of the reflection was considered to display evidence for "strong gravity" as the characteristic emission radius (the break radius) was smaller than $20r_{\rm g}$. The best-fit disc inclination of the group varies between 22° – 42° with Model N07 and the disc reflection strength ranged between 0.56 – 1.72. Absorption due to ionised gas in the line of sight was detected in 4/7 of the observations and a narrow core to the iron line and an associated reflection component was ubiquitous in all of the energy spectra.

In Chapter 3, based on the best-fitting model of N07, we investigated the equivalent model with ionised disc reflection instead of neutral reflection (Model ION). In this Chapter, we approximate the MTE spectrum of the Seyferts in the humped group with a model that is identical to Model ION except that a single power-law emissivity with slope $q = 3$ is used instead of a broken power-law. This is labelled

Model 1 and it is very similar to Model ION as the small break radius preferred by all of the humped observations implies that a steep emissivity slope is a reasonable assumption. The ionised disc model is preferred over Model N07 because it can also model the soft X-ray spectrum below 2 keV (see Section 5.4.2). The form of Model 1 in XSPEC terminology is:

$$\begin{aligned}\text{Model 1} =&(\text{POWERLAW} + \text{REFLIONX} \times \text{KDBLUR} + \text{PEXMON}) \\ &\times \text{CWA18}\end{aligned} \tag{5.3}$$

In Chapter 3, Model ION was applied only to energy spectra of the narrow-line observations. It has also been fit to the remaining observations with the results given in the Appendix. The parameters of Model 1 are set to the weighted mean parameters of the humped observations with Model ION. Therefore, for the POWERLAW (PL) component, we adopted a slope of $\Gamma = 1.91$. The mean ionisation state of the disc for the group is low, $\xi_{\rm blur} = 25 \pm 8$ erg cm s^{-1}, which shows that there is not much difference between the fits of Models ION and N07 above 2 keV. The mean disc inclination across the group with Model ION is $34^\circ \pm 3^\circ$ and the mean disc and distant reflection strengths were found to be $R_{\rm blur} = 0.67 \pm 0.09$ and $R_{\rm dist} = 0.42 \pm 0.08$ respectively, similar to the values found by N07. These are the values we adopt for the parameters in the Model 1 MTE spectrum.

The smearing of the iron line and reflection continuum is implemented by the KDBLUR2 model component (Laor, 1991). The inner and outer disc radii are fixed to $r_{\rm in} = 6r_{\rm g}$ and $r_{\rm out} = 400r_{\rm g}$ respectively. Furthermore, like N07, we modelled the distant reflection spectrum with PEXMON, assuming an inclination of 60° and a reflection strength equal to that found with Model ION above. Finally, to account for warm absorption, we used the XSPEC table model CWA18. The parameters of this model are the column density, $N_{\rm H}$, and the ionisation parameter, $\xi_{\rm abs}$, for which we used the mean values from Model ION: $N_{\rm H} = 1.3 \times 10^{22}$ cm^{-2} and $\xi_{\rm abs} = 1.1$ erg cm s^{-1}.

Model 1, as defined with the mean parameter values that we listed in the previous paragraph, can be considered as the MTE spectrum for the sources in the humped group of variance-spectra. Before any model variance-spectra can be calculated, we have to consider the time-averaged model spectrum for the sources at soft X-ray energies as N07 focused only on X-ray spectra between 3 – 10 keV.

5.4.2 The time-averaged spectrum at soft X-rays

As discussed in the Introduction, in many cases, the X-ray spectra of Seyfert galaxies show emission in excess of the extrapolation of the 3 – 10 keV power-law continuum to lower energies. The origin of this soft-excess emission is still not completely understood, with the latest models assuming it arises via blurred disc reflection or smeared wind absorption. The former is modelled by REFLIONX, with the main advantage being that it can self-consistently account for the shape of the soft excess without the need to include a separate soft X-ray model component. This model takes into consideration several spectral signatures of ionised reflection, including multiple emission lines on top of a soft continuum between 0.3 – 3 keV. If the lines are smeared by strong Doppler and gravitational effects (as expected if they arise in the inner disc regions), they also contribute to the excess "soft" emission at energies below 3 keV. Therefore, Model 1, as defined by Equation 5.3, can be considered as representative of the time-averaged spectrum of the sources in the sample over the full, 0.3 – 10 keV band. The spectrum of Model 1 is shown in Figure 5.6.

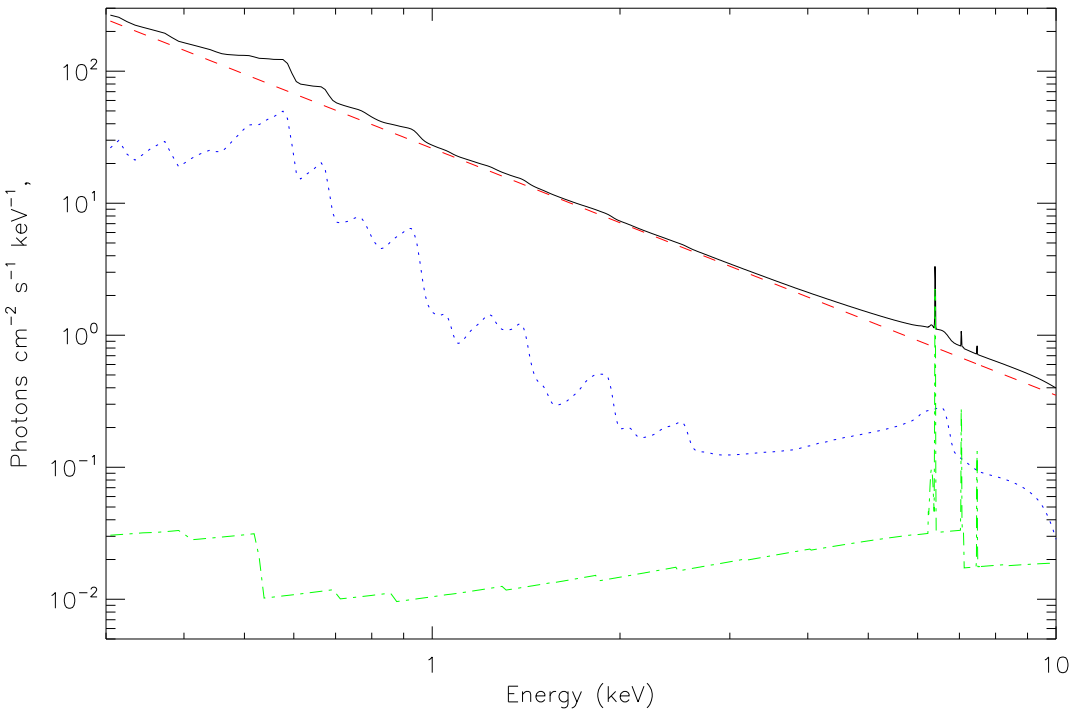

Figure 5.6: The 0.3 – 10 keV energy spectrum of Model 1. The parameters are set to the mean values found after application of Model ION to the entire N07 sample. The model consists of the PL (red dashed), REFLION (blue dot) and PEXMON (green dot-dashed) components. The solid black line is the combined total model.

Alternatively, heavy ionised absorption of the power-law continuum can artificially produce a soft excess if there is a large velocity dispersion to smear the absorption lines (Czerny et al., 2003; Gierliński & Done, 2004, hereafter GD04). Although the required smearing velocities are very high, and hence may be unrealistic (Schurch & Warwick, 2002; Schurch et al., 2009), we also considered the following model as representative of the 0.3 – 10 keV time-averaged spectrum of the Seyferts in the sample:

$$\text{Model 2} = (\text{POWERLAW} + \text{PEXMON}) \times \text{CWA18} \times \text{SWIND1} \tag{5.4}$$

This model consists of the PL continuum, the distant reflection component from the torus (PEXMON) and also includes the effects of warm-absorption (CWA18). Compared to Model 1, we have replaced the blurred reflection component with the "SWIND1" model of GD04, which was also developed using the photoionisation code XSTAR. The three parameters of this component are the column density and ionisation parameter of the wind, $N_{\rm H,wind}$ and $\xi_{\rm wind}$, respectively, and the width of the Gaussian kernel, $\sigma_{\rm vel}$, which governs the smearing of the absorption lines.

It is not straightforward to establish the parameter values in Model 2 that will determine the MTE spectrum for the objects in the humped group, as this model has not been fit to the individual spectra. To simplify matters, we used Model 1 with the average parameter values given above as a template to prescribe parameter values for Model 2. This ensures that the shape of the time-averaged spectra of Models 1 and 2 will be similar. To this end, we used the XSPEC *fakeit* command, together with the response of the pn detector, to produce a high-quality, Model 1 spectrum, which we then fitted with Model 2. We kept the CWA18 and PEXMON parameter values fixed to those used in Model 1, and the best-fit PL and SWIND1 model parameters were: $\Gamma = 1.94$, $N_{\rm H,wind} = 1.7 \times 10^{23}$ cm^{-2}, $\xi_{\rm wind} = 1900$ erg cm s^{-1} and $\sigma^2_{\rm vel} = 0.45$. They are in good agreement with the values found for a sample of Seyfert 1 galaxies by Middleton et al. (2007). We note that the power-law normalisation (PLN) in Model 2 increased by 50% compared to the PLN in Model 1. The parameters of the time-averaged spectra for Models 1 and 2 are listed in Table 5.5.

Having created MTE spectra for the sources in the humped group, based on disc reflection and a relativistically smeared wind, we can now consider various scenarios in which spectral variability is produced.

Table 5.5: The parameters of the time-averaged spectra of Models 1 and 2. Column (1): model. Column (2): model component. Column (3): parameter. Column (4): value of the parameter.

Model (1)	Component (2)	Parameter (3)	Value (4)
1	POWERLAW	Γ	1.91
1	REFLION	$R_{\rm blur}$	0.67
1	REFLION	$i_{\rm blur}$	34°
1	KDBLUR	q	3
1	KDBLUR	$r_{\rm in}$	$6r_{\rm g}$
1	KDBLUR	$r_{\rm out}$	$400r_{\rm g}$
1 & 2	PEXMON	$R_{\rm dist}$	0.42
1 & 2	PEXMON	$i_{\rm dist}$	60°
1 & 2	CWA18	$N_{\rm H}$	1.3×10^{22} cm^{-2}
1 & 2	CWA18	$\xi_{\rm abs}$	1.1 erg cm s^{-1}
2	POWERLAW	Γ	1.94
2	SWIND1	$N_{\rm H,wind}$	1.7×10^{23} cm^{-2}
2	SWIND1	$\xi_{\rm wind}$	1900 erg cm s^{-1}
2	SWIND1	$\sigma^2_{\rm vel}$	0.45

5.4.3 Model 1 variance-spectra

In this section, we consider possible scenarios that produce spectral variability in Model 1. The analogous scenarios for Model 2 are discussed in Section 5.4.4. Each of the models that we investigate involve changes in the PLN. We use an arbitrarily chosen "mean" PLN of 26 for Model 1, which is unimportant as the variance-spectra depend on the magnitude of the change in the mean PLN, and not the value of the mean PLN itself. We parametrise the factor change in the PLN with $A_{\rm PLN} = ({\rm PLN}_{\rm max} - {\rm PLN}_{\rm min})/{\rm PLN}_{\rm min}$. For most models, the size of $A_{\rm PLN}$ will primarily affect the amplitude of the model variance-spectrum but not the classification of the profile shape. Therefore, for all models, we consider a factor change of $A_{\rm PLN} = 1.0$. This means that in all of the Model 1 variance-spectra, the PLN varies from its minimum value of $= {\rm PLN}_{\rm min} = 17.3$ to its maximum value of ${\rm PLN}_{\rm max} = 34.7$. The five models of spectral variability that we consider for Model 1 are:

Model 1(a): The main driver of X-ray variability in Seyferts is thought to be the PL continuum variations. First, we tested the possibility that the PL component varies in normalisation only and the flux of all the other components in Model 1 remains constant. Although the PL varies in flux only, the presence of the other spectral components, whose flux remains constant, implies that the variability amplitude will be energy dependent.

Model 1(b): Energy-dependent variability is also expected to arise if the warm absorber responds to the variable continuum intensity. For example, the response may involve the ionisation parameter, $\xi_{\rm abs}$, of the absorber responding to the luminosity of the ionising continuum. If the hydrogen number density and the distance from the X-ray source to the absorber are constant, it is natural to expect that a change in the continuum luminosity will instigate a change in the ionisation parameter of the same factor, i.e. if the PLN doubles, then so does $\xi_{\rm abs}$. Therefore, to construct the variance-spectrum for Model 1(b), we assumed that $\xi_{\rm abs}$ varies proportionally with the PLN.

Model 1(c): If Model 1 is the correct representation of the time-averaged spectrum of Seyferts, it is possible that the blurred reflection component varies as well. For example, if the X-ray source illuminates the accretion disc from above, it is natural to expect that the reprocessed emission responds to changes in the PL continuum to some extent. We tested this possibility by coupling the strength of the blurred reflection to the PLN i.e. we assumed that $A_{\rm Refl} = A_{\rm PLN}$.

Model 1(d): It is also possible that both the PLN *and* the slope of the power-

law continuum are variable. We therefore tested the possibility that only the PL component varies, but both in amplitude and shape. In this case, the shape of the variance-spectrum depends on the magnitude of the change in Γ and its relationship with the PLN. We assumed a simple linear relationship between the PLN and Γ such that they both increase together i.e. $\Gamma = \alpha + \beta \times \mathrm{PLN}$, where α and β are both positive. This is in (qualitative) agreement with the "softer-when-brighter" behaviour of most radio-quiet AGN. For the model variance-spectrum, we considered $\Delta\Gamma = +0.05$ across the mean spectral slope as the PLN increases from its minimum to its maximum value. This size of $\Delta\Gamma$ should be large enough to observe the effect of a variable spectral slope.

Model 1(e): Instead of the softer-when-brighter behaviour of Model 1(d), it is also possible that the spectral slope hardens as the X-ray flux increases i.e. $\Gamma = \alpha - \beta \times \mathrm{PLN}$. To implement this behaviour, we considered a change of $\Delta\Gamma = -0.05$ across the mean spectral slope as the PLN increases from its minimum to its maximum value.

5.4.4 Model 2 variance-spectra

Models 2(a), (b) and (d): Models 1(a), (b) and (d) have obvious equivalent Model 2 counterparts. To construct the Model 2(a), (b) and (d) model variance-spectra, we considered the same $A_{\mathrm{PLN}} = 1.0$ variation as we did with the Model 1 variance-spectra. The only difference is that in this case, we considered PLN variations around a mean which is 1.5 times larger than the $\mathrm{PLN}_{\mathrm{mean}}$ we used in Model 1 (in agreement with the results of Section 5.4.2).

Model 2(c): Since there is no blurred reflection component in Model 2, Model 1(c) cannot be extended to Model 2. However, although it may not be realistic to expect significant variations in the column density of the partially ionised wind on the time-scales we consider in this work (less than half a day), its ionisation state may change in response to the PLN variations. We therefore constructed Model 2(c) to be the case where the ionisation state of SWIND1 responds linearly to the PLN variations i.e. a doubling of the PLN leads to a doubling in ξ_{wind}.

5.4.5 Shapes of the model variance-spectra

In order to determine the variance-spectrum for each Model, we used XSPEC to create 50 model spectra with Equations 5.3 or 5.4, by varying the parameters of interest as explained above. For each of the 50 runs, we used the *flux* command in XSPEC to calculate the flux in each of the ten energy bands we considered in

Section 5.3. Thus, in each band, we obtained 50 measurements of the flux and used these values to calculate the respective normalised variance, $\sigma^2_{\rm mod}$. The $\sigma^2_{\rm mod}$ values, taken as a function of energy, constitute the model variance-spectrum.

5.4.5.1 Model 1

The five Model 1 variance-spectra are shown in Figure 5.7. Introducing variability in the simplest manner by changing only the power-law normalisation produces a $\sigma^2_{\rm mod}$-spectrum that is humped. There is a decline in the Model 1(a) $\sigma^2_{\rm mod}$-spectrum above $\sim$ 3 keV, which is due to the presence of the constant distant and blurred reflection. As a result, a broad humped profile shape is produced. Changing the ionisation state of the warm absorber (Model 1(b)) in response to the continuum variations produces a spectrum that is soft. As the warm absorption affects the energy spectrum mostly below 2 keV, changing the ionisation state enhances the soft X-ray variability above the hard X-ray variability. Considering variable reflection (Model 1(c)), a third profile shape is found as the $\sigma^2_{\rm mod}$-spectrum is now flat. Varying the reflection strength increases the variability amplitude outside the 1 – 4 keV energy band. Therefore, variable reflection tends to flatten the $\sigma^2_{\rm mod}$-spectrum relative to the variance-spectrum of Model 1(a). The slight decrease around 6 – 7 keV is due to the non-variable distant reflection.

Models 1(d) and 1(e) involve spectral variability arising solely in the PL component as the slope changes along with the PLN. The $\sigma^2_{\rm mod}$-spectra are humped as with Model 1(a), but are less symmetric around the peaks. For example, the peak is at a lower energy for Model 1(d) compared to Model 1(e). Furthermore, the humped shape declines more strongly on the hard X-ray side for Model 1(d) compared to Model 1(e), where the decline is stronger towards the soft X-ray side.

5.4.5.2 Model 2

The wind-based Model 2 $\sigma^2_{\rm mod}$-spectra are shown in Figure 5.8. They do not show the same properties as their Model 1 counterparts. Changing only the PLN in Model 2 (Model 2(a)) produces a $\sigma^2_{\rm mod}$-spectrum that is almost flat in the 0.3 – 10 keV band, as neither the shape of the continuum nor any wind property is variable. Similarly to Model 1(b), changing only the ionisation state of the warm absorber in Model 2 produces a $\sigma^2_{\rm mod}$-spectrum that is soft and dominated by the soft X-ray variability below 2 keV.

The only Model 2 $\sigma^2_{\rm mod}$-spectrum that is humped is Model 2(c). It is more symmetric than the Model 1(a) $\sigma^2_{\rm mod}$-spectrum and unlike all of the humped spectra

.

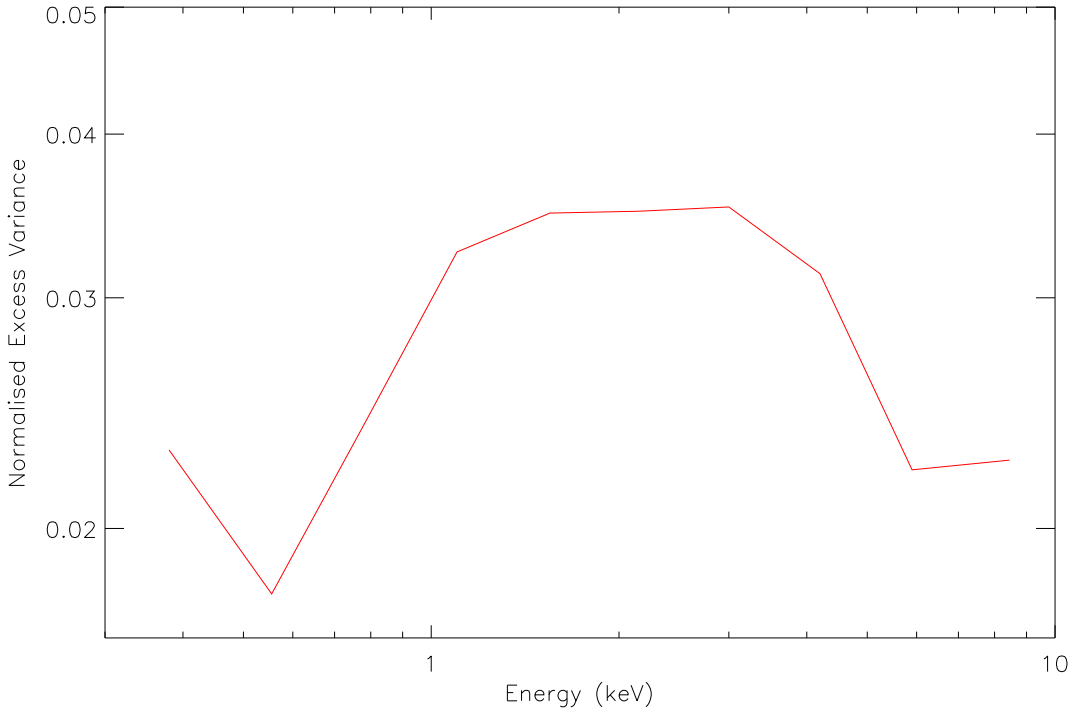

Model 1(a)

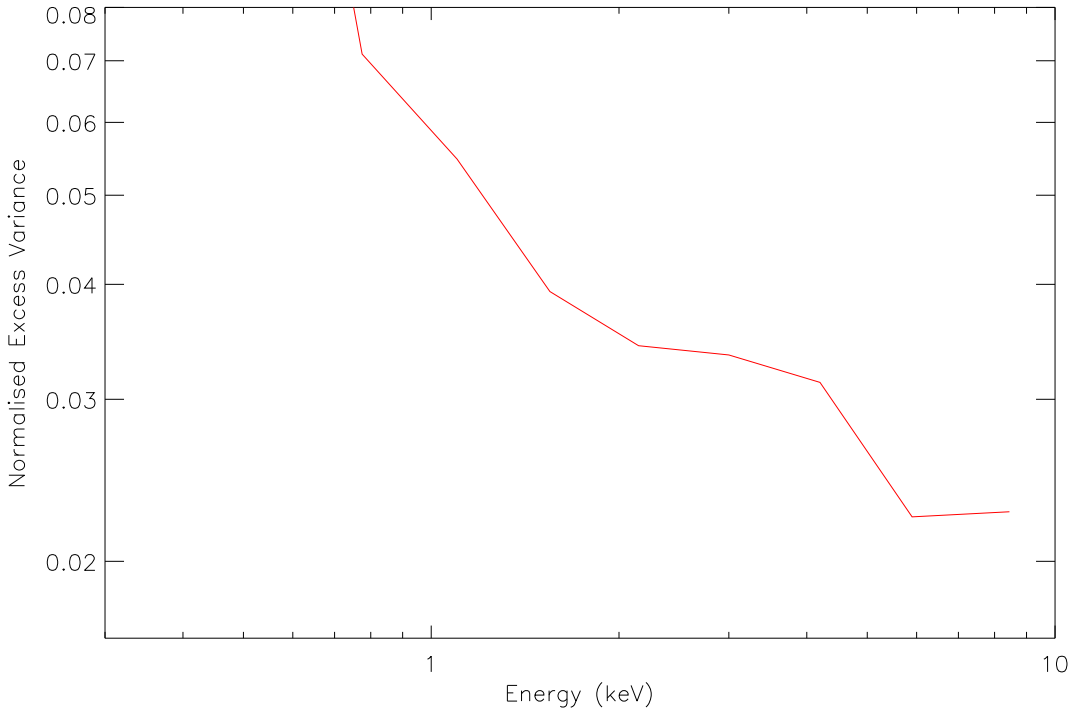

Model 1(b)

.

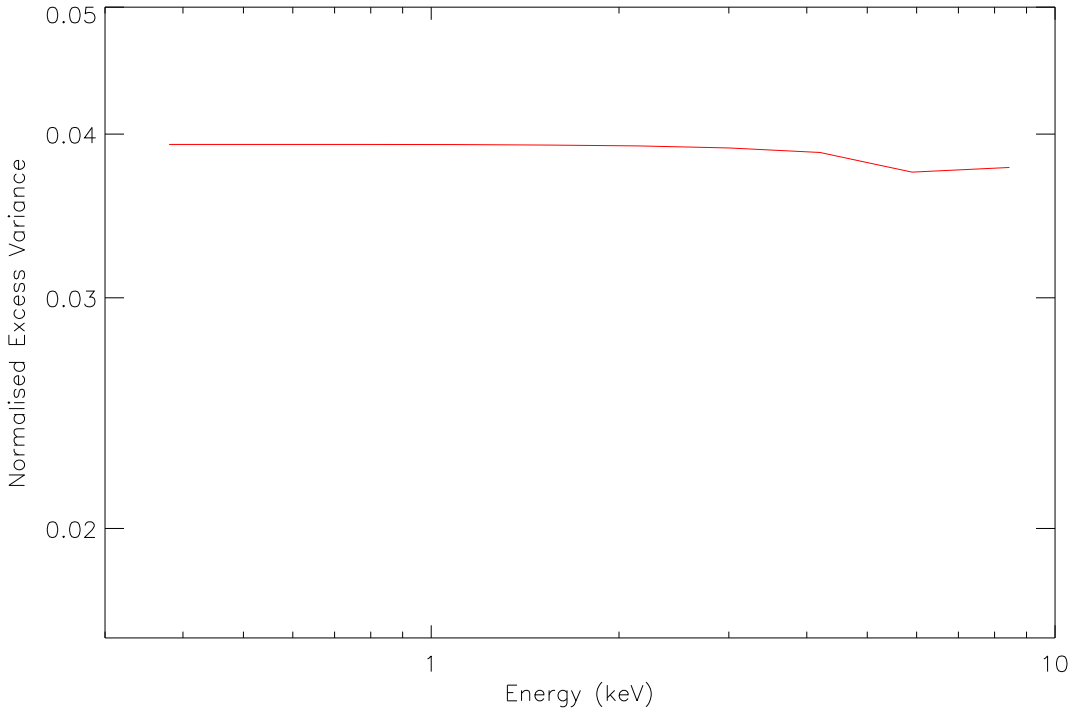

Model 1(c)

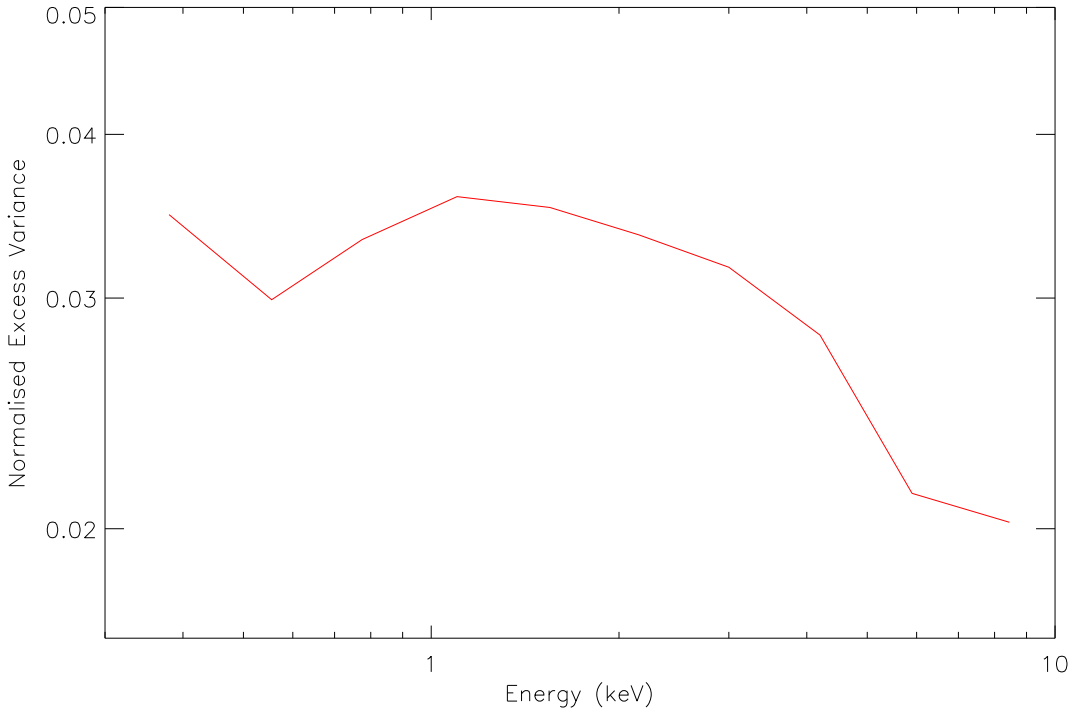

Model 1(d)

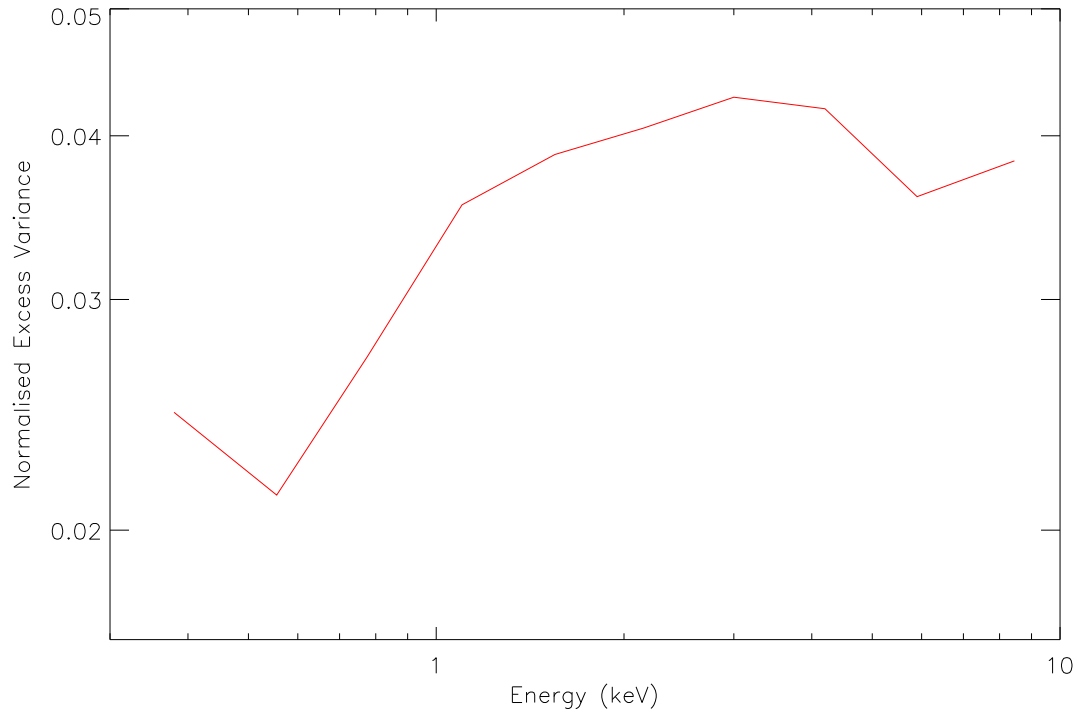

Figure 5.7: The $\sigma^2_{\rm mod}$-spectra of Models 1(a), (b), (c), (d) and (e).

produced with Model 1, there is no upturn below 1 keV as the X-ray lines from reflection are not included in the model. Unlike Models 1(d) and 1(e), changing only the slope and flux of the power-law component does not produce a peak in the $\sigma^2_{\rm mod}$-spectrum. In Model 2(d), as the slope steepens when the X-ray flux brightens, the $\sigma^2_{\rm mod}$ variance-spectrum exhibits more variability in the soft part of the X-ray spectrum. The opposite effect is seen in Model 2(e), with a hard $\sigma^2_{\rm mod}$-spectrum produced as the spectral slope hardens when the X-ray flux brightens. This is the only $\sigma^2_{\rm mod}$-spectrum that produces a hard profile shape.

5.5 Fit to the mean humped variance-spectrum

The classifications of the profile shapes of the 10 $\sigma^2_{\rm mod}$-spectra are given in Table 5.6. All four types of profile shape that were found in the individual variance-spectra of the sample can be produced in our set of $\sigma^2_{\rm mod}$-spectra. It would be very useful to fit each variance-spectrum in Figure 5.3 with the appropriate $\sigma^2_{\rm mod}$-spectrum to determine if a good fit can be obtained and the size of variations required. However, this is computationally intensive and beyond the scope of the Chapter. Without

.

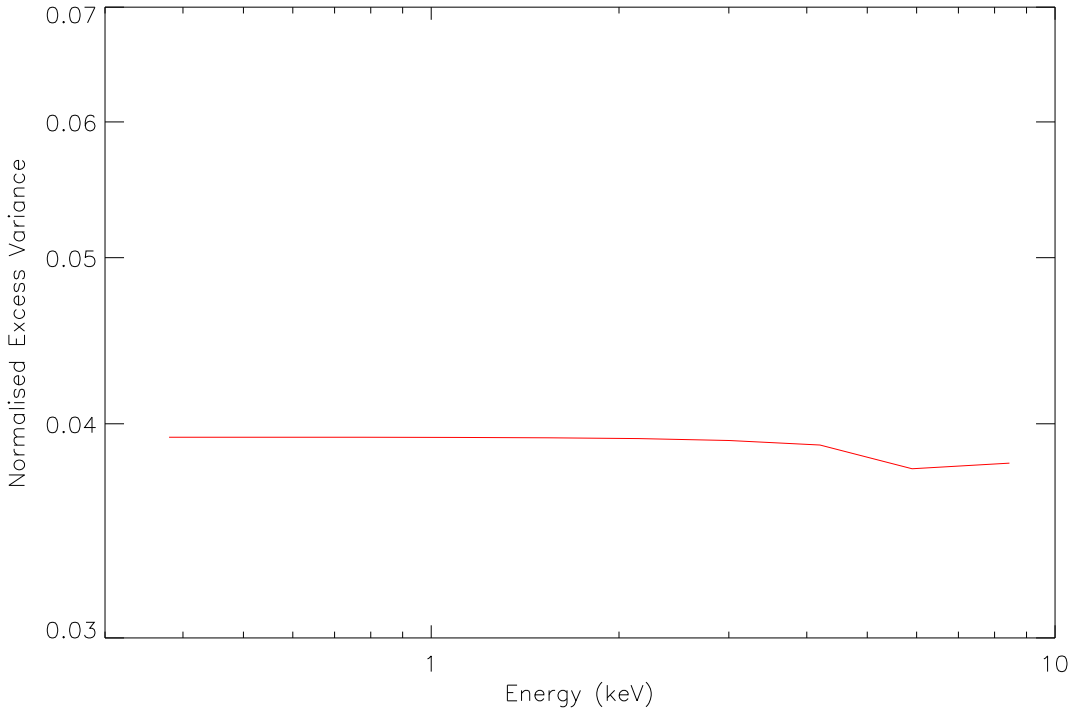

Model 2(a)

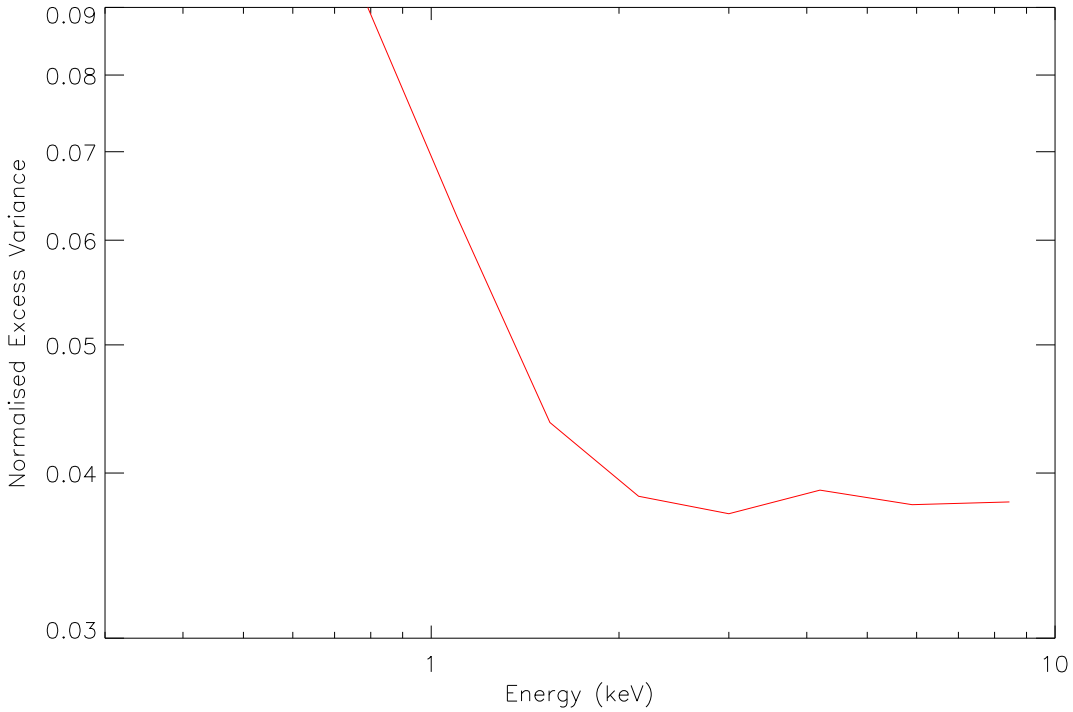

Model 2(b)

.

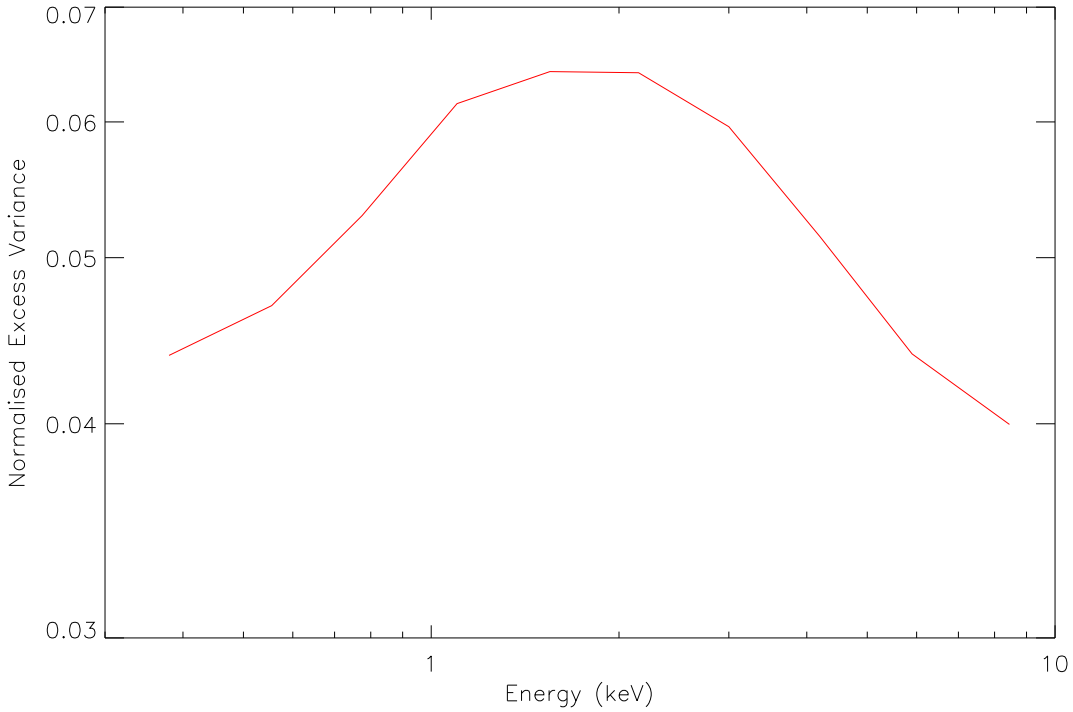

Model 2(c)

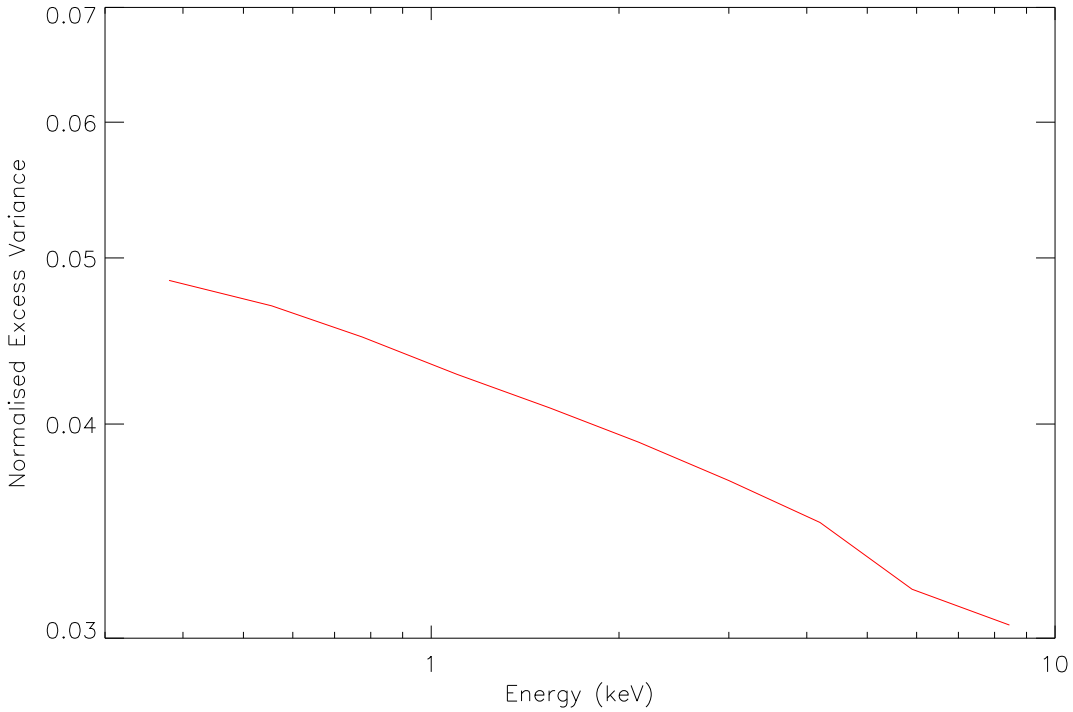

Model 2(d)

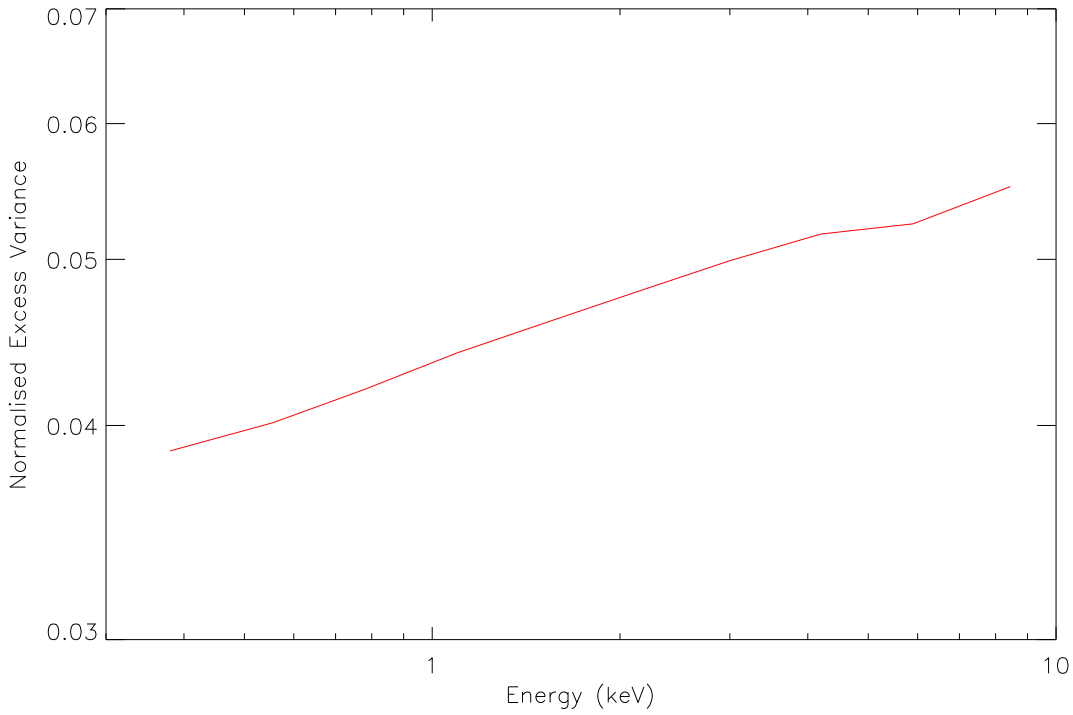

Figure 5.8: The $\sigma^2_{\rm mod}$-spectra of Models 2(a), (b), (c), (d) and (e).

fitting, it is still possible to conclude that different components are likely to be variable in different observations i.e. the blurred disc reflection may be variable in one observation to produce a flat $\sigma^2_{\rm nvar}$-spectrum, but may be constant in another observation to produce a humped $\sigma^2_{\rm nvar}$-spectrum.

In this section, we take the mean of the $M_{\bullet}\sigma^2_{\rm nvar}$-spectra that are humped as this is the largest group in the sample and because both disc reflection and wind absorption models have been used to explain humped profiles in previous works. The $\sigma^2_{\rm nvar}$-spectra are multiplied by the black hole mass because of the anti-correlation between $\sigma^2_{\rm nvar}$ and $M_{\bullet}$ that is discussed in Section 5.3.1. The aim is to determine if the $\sigma^2_{\rm mod}$-spectra can explain both the amplitude and shape of the mean humped $M_{\bullet}\sigma^2_{\rm nvar}$-spectrum ($\overline{M_{\bullet}\sigma^2_{\rm nvar}}$-spectrum). Only the four models that produce a humped profile are tested: Models 1(a), 1(d), 1(e) and 2(c).

For the 24 humped variance-spectra, the straight mean of the $M_{\bullet}\sigma^2_{\rm nvar}$ values is calculated in each energy band to form the $\overline{M_{\bullet}\sigma^2_{\rm nvar}}$-spectrum and the 1σ error bar is set to the standard error on the mean. Fitting to the $\overline{M_{\bullet}\sigma^2_{\rm nvar}}$-spectra requires either the $\sigma^2_{\rm mod}$-spectra to be multiplied by the mean black hole mass of the humped group or for the $\overline{M_{\bullet}\sigma^2_{\rm nvar}}$-spectra to be divided by the mean black hole mass. We do the

Table 5.6: Classifications of the $\sigma^2_{\rm mod}$-spectra.

Model	Profile shape
1(a)	Humped
1(b)	Soft
1(c)	Flat
1(d)	Humped
1(e)	Humped
2(a)	Flat
2(b)	Soft
2(c)	Humped
2(d)	Soft
2(e)	Hard

latter and refer to this spectrum as the "$\overline{\sigma^2_{\rm nvar}}$-spectrum", with units of normalised excess variance. By fitting the $\sigma^2_{\rm mod}$-spectra to the $\overline{\sigma^2_{\rm nvar}}$-spectrum, we are able to test whether each model can reproduce both the amplitude and shape of the mean humped variability-spectrum, when we vary the model parameters within a reasonable range of values.

The amplitude of each $\sigma^2_{\rm mod}$-spectrum depends on $A_{\rm PLN}$. The ratio of (maximum - minimum count rate)/(minimum count rate) for the 24 light curve segments in the humped group ranges from 0.09 – 2.0. For that reason, we tested $A_{\rm PLN}$ variations across the same range in increments of 0.01 when fitting to the $\overline{\sigma^2_{\rm nvar}}$-spectrum. In Models 1(d) and 1(e), Γ also varies and for each $A_{\rm PLN}$, we tested 100 values of $\Delta\Gamma$ between $\pm0.01 - \pm0.10$. The ionisation state of the wind changes in Model 2(c), with the factor change in $\xi_{\rm wind}$ following $A_{\rm PLN}$. The variable parameters of each model and the ranges of variation that we test are given in Columns 2 and 3 of Table 5.7.

The quality of each model is determined by fitting the $\sigma^2_{\rm mod}$-spectrum to the observed $\overline{\sigma^2_{\rm nvar}}$-spectrum with a standard χ^2 test at a confidence level of 99%. The degrees of freedom (d.o.f.) are 9 for Models 1(a) and 2(c) and 8 for Models 1(d) and 1(e), where Γ is a free parameter in addition to the PLN. The best-fit χ^2/d.o.f. for each model are listed in Column (4) of Table 5.7.

5.5.1 Results

The fits of the Model 1(a), 1(d), 1(e) and 2(c) $\sigma^2_{\rm mod}$-spectra to the $\overline{\sigma^2_{\rm nvar}}$-spectrum are shown in Figure 5.9. The simplest of the four models, Model 1(a), which introduces

Table 5.7: The variable parameters of the models we test and their ranges of variation. Column (1): model. Column (2): the variable parameters of the model. Column (3): the range of variation for the parameter. Column (4): The best-fit χ^2/d.o.f. of the fit of the model to the $\overline{\sigma^2_{\rm nvar}}$-spectrum. Fits that are acceptable at a confidence level of 99% are shown in bold.

Model (1)	Variable parameter (2)	Range of variation (3)	χ^2/d.o.f. (4)
1(a)	PLN	$A_{\rm PLN} = 0.09 - 2.0$	53/9
1(d)	PLN	$A_{\rm PLN} = 0.09 - 2.0$	**11/8**
	Γ	$\Delta\Gamma = +0.01$ to $+0.1$	
1(e)	PLN	$A_{\rm PLN} = 0.09 - 2.0$	204/8
	Γ	$\Delta\Gamma = -0.01$ to -0.1	
2(c)	PLN	$A_{\rm PLN} = 0.09 - 2.0$	30/9
	$\xi_{\rm wind}$	follows $A_{\rm PLN}$	

variability by changing only the power-law normalisation does not fit the $\overline{\sigma^2_{\rm nvar}}$-spectrum well. The best-fit χ^2/d.o.f. is 53/9 for a factor change of $A_{\rm PLN} = 1.25$. The reason for the poor fit is that the $\sigma^2_{\rm mod}$-spectrum is broader and peaks at a higher energy than the $\overline{\sigma^2_{\rm nvar}}$-spectrum. Furthermore, the variability below 2 keV is underpredicted.

Model 1(d), where both the normalisation and slope of the power-law increase together, gives a statistically acceptable fit to the data. The best-fit χ^2/d.o.f. of 11/8 is achieved for $A_{\rm PLN} = 1.38$ and $\Delta\Gamma = +0.072$. The humped shape of the $\sigma^2_{\rm mod}$-spectrum in this case is more peaked than for Model 1(a), and the strong, monotonic decrease of the variability at higher energies is fit well. However, a drawback of Model 1(d) is that it predicts an upturn in the variability amplitude below 1 keV, which is not observed in the $\overline{\sigma^2_{\rm nvar}}$-spectrum. The upturn is present as the blurred disc reflection component is strongest around 0.5 keV and is not variable. As a good fit is achieved with Model 1(d), it is no surprise that a poor fit of χ^2/d.o.f. = 204/8 is obtained with Model 1(e), where the slope of the power-law decreases as the PLN increases.

The only Model 2 variance-spectrum that produces a humped profile is Model 2(c). This gives a best-fit of χ^2/d.o.f. = 30/9, obtained for a wind with an ionisation state that responds fully to PLN variations of amplitude $A_{\rm PLN} = 0.81$. This corresponds to a minimum and maximum $\xi_{\rm wind}$ of 1350 erg cm s^{-1} and 2500 erg cm s^{-1} respectively. This model is not acceptable at a confidence level of 99%. Compared to Model 1(d), Model 2(c) does not have an upturn in variability below 1 keV,

.

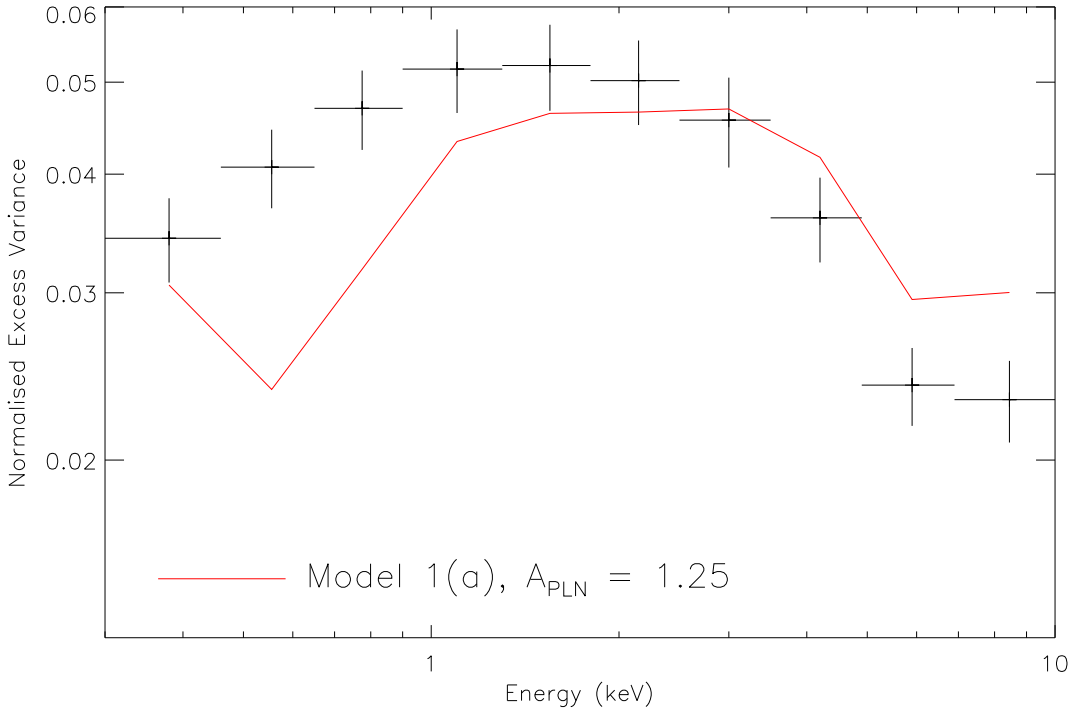
0.06
0.05
0.04
0.03
0.02
Normalised Excess Variance
Model 1(a), A_{PLN} = 1.25
1
10
Energy (keV)

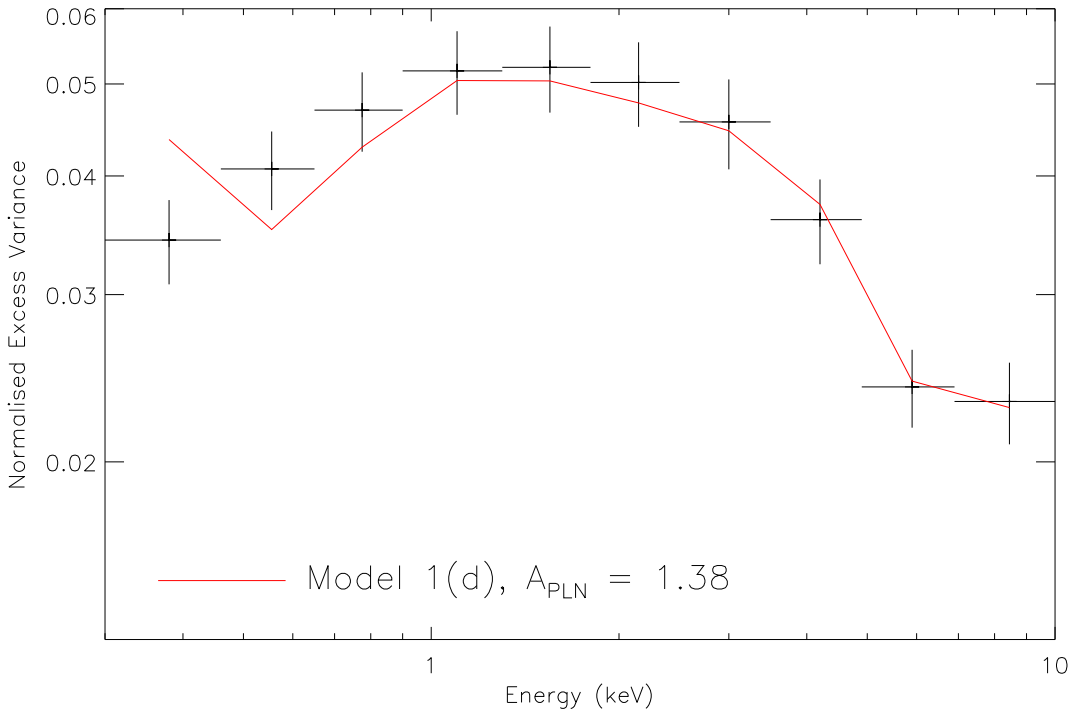
0.06
0.05
0.04
0.03
0.02
Normalised Excess Variance
Model 1(d), A_{PLN} = 1.38
1
10
Energy (keV)

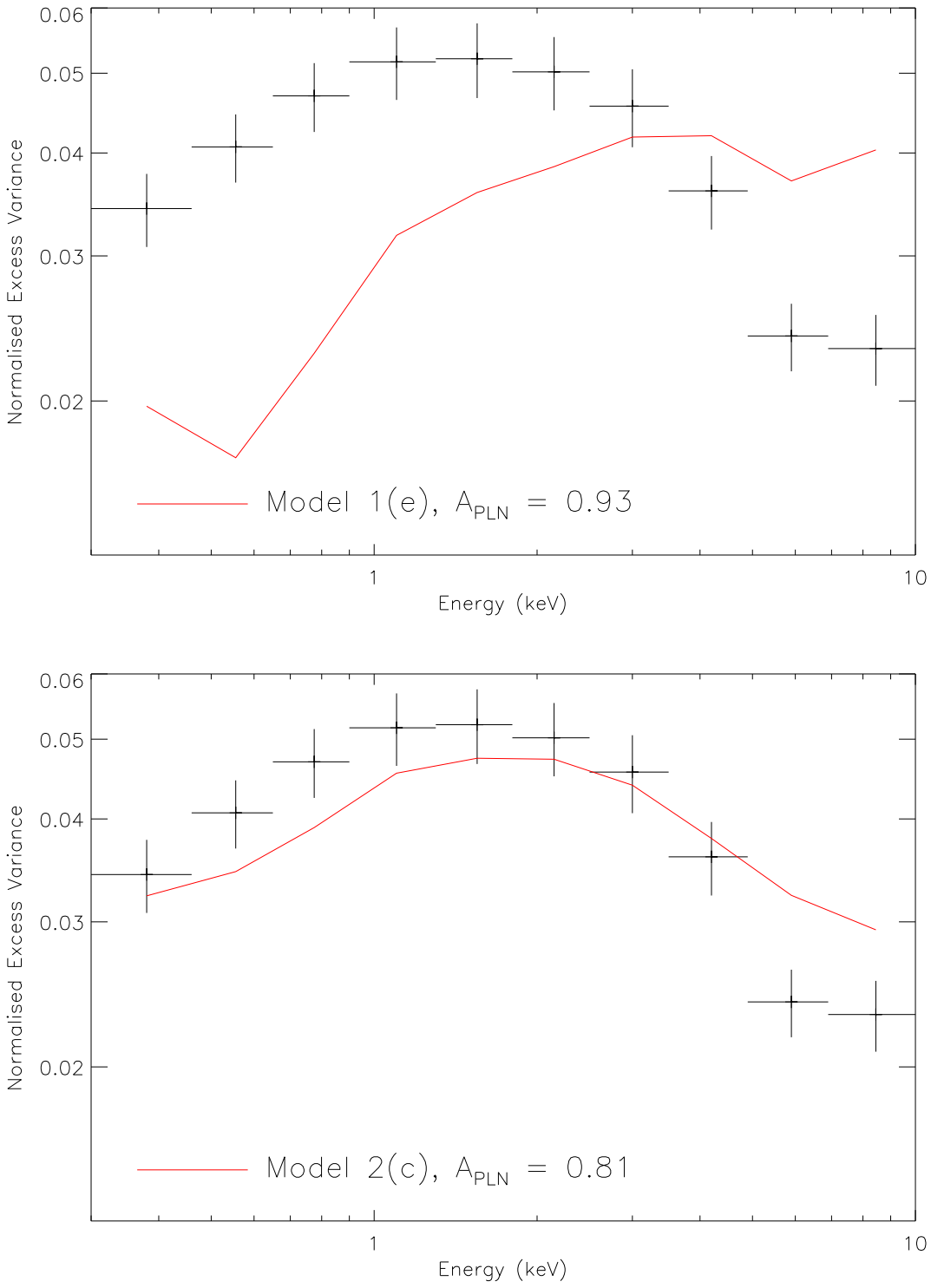

Figure 5.9: Fits to the $\overline{\sigma^2_{\rm nvar}}$-spectrum (black) of the Model 1(a), 1(d), 1(e) and 2(c) $\sigma^2_{\rm mod}$-spectra (continuous red line). The best-fit $A_{\rm PLN}$ variability factors of the PL normalisation are labelled in the panel.

although the $\sigma^2_{\rm mod}$-spectrum is not as strongly peaked as the $\overline{\sigma^2_{\rm nvar}}$-spectrum, with excess variability predicted above 4 keV.

It is possible for the individual humped $M_{\bullet}\sigma^2_{\rm nvar}$-spectra to differ from the mean $\overline{\sigma^2_{\rm nvar}}$-spectrum so that they would give a good fit with the Model 2(c) variance-spectrum. The strongest humped spectra, such as those of NGC 4051, MCG-6-30-15(1) and MCG-6-30-15(2) have steeper declines at energies above the hump than below, in agreement with the $\overline{\sigma^2_{\rm nvar}}$-spectrum. In these cases, Model 2(c) would still be unable to produce a good fit, although it would be beneficial to fit each variance-spectrum separately.

5.6 Discussion

The aim of this Chapter was to learn about the broadband behaviour of the X-ray spectral variability by investigating the energy-dependent normalised variance-spectra of a sample of 17 Seyfert galaxies on time-scales of $\sim$ 30 – 40 ks. The $\sigma^2_{\rm nvar}$-spectra were found to be diverse in both the shape of their profiles and their amplitudes. This is true even when considering the $\sigma^2_{\rm nvar}$-spectra of the same object. After normalising the $\sigma^2_{\rm nvar}$-spectra by $M_{\bullet}$, we found that the scatter of the $M_{\bullet}\sigma^2_{\rm nvar}$-spectra was substantially less, which agrees with the known anti-correlation between the normalised excess variance and black hole mass on time-scales of 30 – 40 ks.

The largest group of variance-spectra were the $\sim$ 50% that possessed a humped shape, while others had flat, soft and hard profiles. The variety of profile shapes cannot arise from red-noise effects that are associated with AGN variability. Instead, they show that there are intrinsic differences in the spectral variability between both different objects and between multiple observations of the same objects. This agrees with the findings of Chapter 4, which showed that there is no single type of iron line variability behaviour across the sample.

The second aim of the Chapter was to investigate the possible spectral variability that can arise from two well-known models: blurred reflection from a relativistic disc and velocity-smeared, ionised absorption in a wind. We found that different modes of spectral variability in each of these models can produce the range of profile shapes that are found in the individual $\sigma^2_{\rm nvar}$-spectra. If these models do explain the spectral variability seen in the sample, this implies that some model components are variable in some observations, but constant in others. The mean humped variance-spectrum was then fit by the four models that produce a humped profile, as this shape is found to be common both in this sample and in other works. Our final result is that the mean humped spectral variability in our sample, on time-scales shorter

than 40 ks, can be explained if the power-law X-ray continuum in these objects varies both in flux *and* slope, while the blurred and distant reflection components remain constant in flux, as well as the properties of the warm absorbing material that is present in most AGN. A good fit is not achieved if there are no changes in the spectral slope or if variability arises in a velocity-smeared wind instead of the blurred disc reflection. The implications of this result on our current views of how the X-ray source operates in AGN are discussed below.

5.6.1 The warm absorbing material

It is possible that warm absorbers are present in all AGNs. However, as they are only visible when they cross our line of sight, warm absorbers have only been found in around 50% of Seyfert galaxies (Crenshaw et al., 2003). It is possible for both spectral and flux variability to arise from changes in the ionisation state, column density or covering fraction of the warm absorber. In this Chapter, we studied the spectral variability induced by the warm absorbing material by coupling the ionisation state of the warm absorber with the continuum flux. This results in a soft variance-spectrum, which is seen in seven $\sigma^2_{\rm nvar}$-spectra in the sample. On the other hand, our results imply that in the remaining $\sigma^2_{\rm nvar}$-spectra, on time-scales shorter than 40 ks, the ionisation state of the absorber must remain relatively constant, despite changes in the power-law continuum on the same time-scales.

Non-variable warm absorption over similar time-scales has been seen in Seyfert 1s such as in *XMM-Newton* observations of NGC 4051 (Krongold et al., 2007) and NGC 5548 (Krongold et al., 2010). It may be the case that the warm absorber is not variable on time-scales of 40 ks and less if the electron density, n_e, of the warm absorber is low. In time-evolving, non-equilibrium photoionisation models (Nicastro et al., 1999), the response of the ionisation state of the gas to sudden changes in the ionising continuum is smoothed and delayed at low gas densities. The recombination time can be much longer (up to orders of magnitude) than the photoionisation time-scale. Hence, a photoionised absorber subject to constant and fast variations of the ionising continuum (like in the sources we study here) is likely to remain overionised with respect to the equilibrium ionisation state. Furthermore, if the warm absorbers are distant, as considered for NGC 5548 (Krongold et al., 2010), the extended travel time for the continuum X-ray photons would not have any effect on the spectral variability on short time-scales.

5.6.2 Blurred disc reflection

As discussed throughout the thesis, the standard model of accretion discs in AGN predicts that the blurred reflection continuum component in the X-ray spectra of AGN should be variable and follow changes in the power-law continuum. Our results have shown that variable reflection leads to a flat variance-spectrum, which is seen in 18 cases including Ark 120, Mrk 110, NGC 4593, HE 1143-1800 and Ark 564, where evidence for heavily blurred disc reflection was found in Chapter 3. For variance-spectra that are not flat, our results indicate that the blurred reflection is far less variable than the PL continuum, which is clearly variable on the same time-scale of ~ 40 ks. If the X-ray source is located above the disc, close to the central black hole, and illuminates the inner parts of the disc, we would expect that the reflected component should, to some extent, respond to the variations in the PL continuum. However, it is also natural to expect that the response of the disc should be smeared out on short time-scales, as some parts of the disc reflect the continuum before other areas do (see e.g. Kazanas & Nayakshin, 2001). This effect can lead to the observation of slowly varying reflection on certain time-scales, although individual parts of the disc may respond to the continuum variations.

N07 found that most of the blurred reflection emission in the objects we studied should come, on average, from a characteristic radius $\sim 7 - 8$ Schwarzchild radii ($R_{\rm s}$). Gilfanov et al. (2000) estimate that, at a distance of $\sim 10R_{\rm s}$, the reflected continuum should not show significant variations on time-scales shorter than ~ 0.01s for a point-like X-ray source located at a height of $10R_{\rm s}$ above a central 10 $M_{\odot}$ black hole (see their Figure 4). For a $\sim 2.4 \times 10^7$ $M_{\odot}$ black hole (i.e. the average black hole mass for the sources in our sample), the same geometry implies a time-scale of ~ 25 ks. In other words, we would not typically expect to observe variability of the blurred reflection in response to the continuum during our 30 – 40 ks segments. Alternatively, the absence of reflection component variations on short time-scales is consistent with the predictions of the gravitational light bending model of Miniutti & Fabian (2004). As discussed in the previous chapters, according to this model, variations in the continuum flux result from changes in the position of the X-ray source with respect to the central black hole. Due to strong general relativistic effects, the X-ray flux which illuminates the disc may remain relatively constant even when the observed continuum flux at infinity varies, and as a result the reflection emission would not be as variable as the continuum. This result is also consistent with the detection of non-variable iron lines in eight observations of the N07 sample (see Chapter 4).

5.6.3 A PL continuum with variable flux *and* spectral slope

Model 1(d) gives the best fit to the mean variance-spectra of those with humped profiles. This implies that, on time-scales shorter than 40 ks, the main drivers of both the flux *and* spectral variability we observe in this group of $\sigma^2_{\rm nvar}$-spectra are the flux *and* intrinsic slope variations of the X-ray continuum. This is then combined with the presence of a constant reflection component (both from the distant torus and the inner disc) and a warm absorber, whose ionisation state remains constant as well.

We found that Model 1(d) fits the data best when Γ and PLN vary by $\Delta\Gamma \sim 0.072$ and $A_{\rm PLN} = 1.38$ respectively, around their mean values. This corresponds to maximum-to-minimum variations of size ~ 2.4, which is entirely consistent with the observed variations in the 40 ks light curve segments of most objects in the sample. The $\Delta\Gamma$ and $A_{\rm PLN}$ values mentioned above result in the following linear relationship between Γ and the PLN: ‘

$$\Delta\Gamma = 0.09 \times \left(\frac{\rm PLN_{max} - PLN_{min}}{\rm PLN_{mean}} \right). \tag{5.5}$$

Previous work has suggested that the observed spectral variability in AGN, especially MCG-6-30-15, can be explained by a combination of a variable power-law that varies in normalisation only, and a non-variable hard reflection component (e.g. Taylor et al., 2003; Miniutti & Fabian, 2004). Similarly, complex variations in the warm absorber can also explain the spectral variations observed in a few objects (Turner et al., 2007; Miller et al., 2008). Our results, which are based on the analysis of the light curves of many objects, indicate that, even on time-scales as short as 40 ks, *intrinsic* $\Delta\Gamma$ variations are almost certainly necessary to explain the X-ray AGN spectral variability in 50% of our sample.

A correlation between the observed power-law slope and the PLN or 2 – 10 keV flux has commonly been observed (e.g. Turner, 1987; Turner & Pounds, 1989; Matsuoka et al., 1990). Intrinsic changes in the power-law slope are expected within the context of thermal Comptonisation models (Haardt & Maraschi, 1993; Haardt et al., 1997). In these models, the two parameters that determine the spectral shape are the temperature and optical depth of the scattering coronal electrons. For a fixed optical depth, a decrease in the electron temperature will lead to a steeper power-law slope. However, at the same time, the 2 – 10 keV count rate should also decrease, which suggests a spectral hardening as the flux increases, opposite to what we observe. The same scenario results if the optical depth is increased at a fixed electron temperature. Therefore, varying only a single coronal parameter does not

produce the observed spectral softening with increasing flux. However, it is possible for simultaneous variations in both parameters to lead to a positive $\Gamma - F_{2-10}$ correlation (see Figure 7 of Haardt et al., 1997). Furthermore, a correlation between the spectral slope and 2 – 10 keV flux will result if the intrinsic driver of the variability is the seed photons. This is because an enhancement in the disc emission cools the coronal electrons and leads to a softer power-law continuum.

5.6.4 Smeared absorption

As mentioned in Section 5.4.2, if there is a dense, ionised wind which absorbs the continuum PL component, it must have a large velocity dispersion. In fact, the required $\sigma^2_{\rm vel}$ is so large, that it may be unrealistic (Schurch & Warwick, 2002; Schurch et al., 2009). We investigated the spectral variability that results if the ionisation state of the wind responds to the continuum flux changes. While a humped variability profile is produced, the shape of the observed variance-spectrum is not satisfactorily explained by smeared absorption above 4 keV. This is primarily because the predicted variance-spectrum is symmetric around the 1 – 2 keV band, whereas the humped variance spectra tend to show steeper declines at higher energies. We therefore conclude that the presence of such a wind is highly unlikely in the Seyfert galaxies with a humped variance-spectrum, although a more definite conclusion could be reached if each variance-spectrum was fitted separately. Interestingly, flat, soft and hard variance-spectra are produced by the wind model if the spectral slope is invariant, steepens with flux and hardens with flux respectively. However, in these cases, it is difficult to explain why the expected variability in the ionisation state of the wind does not occur.

5.6.5 Comparison with past results

The dependence of the average spectral slope of different AGN on their accretion rate has already been suggested/shown in the past (e.g. Porquet et al., 2004; Bian, 2005; Shemmer et al., 2006, 2008; Saez et al., 2008; Papadakis et al., 2009). If this is true, then one would expect that intrinsic spectral slope variations would also appear in a single object as its accretion rate varies, on all time-scales. Recently, Sobolewska & Papadakis (2009) studied the long-term X-ray spectral variability of 10 AGN, using many spectra for each source in their sample, taken by RXTE over a period of up to 10 years in some cases. They found that the apparent spectral variability of the sources could be explained best if the reflection component remains roughly constant (even on these long time-scales) and the PL continuum exhibits a

positive $\Gamma-$source flux correlation.

Sobolewska & Papadakis (2009) found that their data could be explained if $\Gamma_{\rm intrinsic} \propto {\rm PLN}^{0.08}$ (see their Section 4.2.4). According to our results, the average humped AGN variance-spectrum (on time-scales smaller than 40 ks) can be explained, both in shape and amplitude, if $\Delta\Gamma$ follows Equation 5.5. For the same choice of PLN values (i.e. ${\rm PLN}_{\rm mean} = 26$ and PLN varies from 15.4 up to 36.6), the Sobolewska & Papadakis (2009) relation is well approximated with a linear relation of the form: $\Delta\Gamma = 4 \times 10^{-3} \Delta{\rm PLN}$, which implies spectral slope changes of ~ 0.09. Although this spectral slope variability is slightly larger than the value of $\Delta\Gamma \sim 0.07$ that we found, their results are in good agreement with ours. It is possible then that the *intrinsic* spectral slope in AGN varies over both short and long time-scales. On short time-scales, these variations are approximately linear (as we show in this Chapter), while on longer time-scales, perhaps a power-law relation like the one of Sobolewska & Papadakis (2009) holds.

5.6.6 Practical implications of our results

Equation 5.5 can be used in practice when fitting the energy spectra of variable sources. Light curves of AGN covering several orbits can exhibit minimum-to-maximum count rate variations of the order of 2 or more. In these cases, our results suggest that the spectral slope in some cases may change by at least $\Delta\Gamma = 0.07$ from its minimal to maximal value. Therefore, when splitting these light curves into segments and fitting their energy spectra separately, it is wise to allow spectral slope variations, as determined by Equation 5.5. Instead, if the slope is fixed, differences in the shape of the spectra may be falsely interpreted as being due to variations in other model parameters. Therefore, we recommend that accounting for the contribution of the continuum changes to the spectral variability should be made before the variability of more complex models e.g. reflection and absorption, are investigated.

5.7 Conclusions

In this Chapter, we have studied the broadband X-ray variability between 0.3 – 10 keV and over time-scales of 30 – 40 ks in the N07 sample of Seyfert galaxies. 17/26 objects have *XMM-Newton* light curves with sufficient exposure and variability to enable at least a single normalised excess variance-spectrum to be calculated. The key results of analysing the sample of 51 variance-spectra are:

- The normalised variance-spectra of the objects in the sample exhibit differences in both amplitude and shape. The largest group of profiles are those that are humped (peaking between 0.7 – 2 keV), followed by the variance-spectra that are flat, soft and hard. Importantly, such diversity is also seen in the multiple variance-spectra of individual AGN, showing that there are intrinsic differences in the shapes and amplitudes, both from object-to-object and amongst multiple observations of the same object.

- The well-known anti-correlation between the black hole mass and normalised excess variance of AGN can account for part of the scatter in the amplitudes of the variance-spectra. However, even after normalising the variance by the black hole mass, there remains considerable scatter in the variability amplitude across all energy bands.

- Flat, humped, soft and hard profiles of variance-spectra can arise in the relativistically blurred disc reflection and relativistically smeared wind models of the X-ray spectrum in AGN. If these models explain the observed range of profile shapes in the variance-spectra, the spectral variability does not arise in the same way for each observation i.e. the blurred disc reflection may be variable for some observations and constant in others.

- The humped profile was investigated further by examining if the shape and amplitude of the mean humped variance-spectrum can be explained by realistic variations of model parameters in both the reflection and wind scenarios. In addition, we included in both models, non-relativistic reflection from distant material, and a more conventional warm absorber without significant velocity smearing.

- The only model that can explain the observed variations of the mean humped variance-spectrum is the reflection model. This requires the power-law continuum to linearly steepen with increasing X-ray flux while the warm absorber, distant and blurred reflection remain constant. A drawback to this model is the prediction of an upturn in variability below 1 keV, which is not seen in the mean humped variance-spectrum. The best-fit with the wind absorption model requires the ionisation state of the wind to follow changes in the X-ray continuum, but the model overpredicts the hard X-ray variability.

- We find that the continuum slope needs to vary by $\sim \Delta\Gamma = 0.07$ on timescales of ~ 40 ks in order to produce a good fit to the mean humped variance-spectrum. The relative lack of variability of the accretion disc reflection and

ionisation state of the warm absorber are consistent with the results of other works. In the case of the disc reflection, our results imply a smearing out of the variability due to light travel effects, though alternatively, gravitational light bending effects may be present.

Chapter 6

Summary

In this Chapter, I present a summary of the work in this thesis and make some suggestions as to future directions in which this work may be taken.

6.1 Summary

In this thesis, a study of the X-ray time-averaged and variability spectra of Seyfert galaxies has been presented. The basis of the work are 37 *XMM-Newton* observations of 26 local Seyfert 1s. These AGN allow a view into the central regions with X-rays, which can be used to test the standard paradigm of AGN: the feeding of a cold accretion disc to the central supermassive black hole. A prediction of the standard model of accretion discs is the production of a relativistically broad iron line and reflection spectrum that should also respond to variations in the continuum on short time-scales. The three works in this thesis have attempted to identify problems with this model and also address recent results that have argued for modifications to the standard paradigm.

In **Chapter 3**, we investigated the long-standing problem of why some sources do not exhibit a relativistically broad iron line in their time-averaged spectrum. This includes both objects from the N07 survey that show no evidence for any reflection and those that have a line that is less broad than expected. Estimated to form $\sim 50\%$ of local Seyfert 1s, these objects pose a difficulty for models of AGN because a relativistically broadened iron line should be a natural outcome of accretion onto a supermassive black hole. We have tested if the reflection apparently only appears to be "missing" because the accretion disc is ionised and/or the reflection is heavily smeared. The latter effect can arise if the emissivity profile is steep and the black hole is spinning. Considering the objects with no evidence for blurred reflection, the combination of these two factors accounted for the missing component in 8/11

observations although with Mrk 6 and NGC 5506(1), the improvement is small compared to a model that consists of a cold accretion disc and an emissivity power-law that is no steeper than predicted by the standard model.

Similar results were found for the objects with a non-relativistically broadened iron line. In this case, an additional source of iron line emission, such as BLR-type gas, is necessary. A heavily smeared iron line and reflection spectrum from the accretion disc can be detected in 6/8 cases, regardless of if the disc is ionised or cold. In both sets of observations, a high disc inclination is preferred, which enhances the blending of the line into the continuum because of the stronger Doppler effects. However, we were still able to separate this spectral component from the continuum and found that the relative fractions of the reflection and continuum fluxes is similar to the objects classed by N07 as possessing a "classical" relativistically broadened iron line. The FWHM of the iron line in the non-relativistic line observations is greater than the optical lines that are normally associated with the BLR. This may be due to the iron line emission being dominated by photons arriving from the parts of the BLR closest to the black hole. Strong relativistic effects contribute more to the nature of the blurred disc reflection in these objects, as a low ionisation state is preferred across most observations. In the observations where a steep emissivity profile is required, gravitational light bending or extraction of spin energy from the black hole may be important in enhancing the emission from the inner disc regions.

Chapter 4 focused on the variability of the iron line and X-ray continuum between 2.5 – 10 keV in the N07 sample of Seyfert galaxies. Our tool to accomplish this was the $\sigma_{\rm rms}$-spectrum, because it is model-independent and can complement the analysis of the time-averaged energy spectra in N07 and Chapter 3. The main aim was to define and calculate variability spectra for many objects in a uniform manner so that we could test if the iron line follows variations in the X-ray continuum, as expected in the standard model of accretion in AGN. This prediction could only be confirmed in two cases, with two other $\sigma_{\rm rms}$-spectra showing a red wing that is more variable than the continuum. This hints at relativistic beaming or emission from iron moving with a bulk velocity being important in these observations. The diversity of iron line behaviour continued with three observations showing variability only on the blue side of the line, which may arise from the accretion disc, or may be due to emission or absorption by other hot, photoionised gas close to the nucleus.

The presence of a non-variable iron line in one of the two MCG-6-30-15 observations was confirmed by our work and a similar result was also found in ten other observations that showed no excess variability above the continuum across the red wing of the iron line. This is in contrast to the clear detection of an iron line with

a broad red wing in nearly all of the energy spectra. The non-variable iron lines indicated a decoupling of the continuum and reflection component. This requires the intrinsic emission to be anisotropic, which is consistent with the expectations of gravitational light bending. If the X-ray source is at a low height above the disc, the reflection may be both heavily smeared and non-variable, as found with NGC 5506(1), NGC 4593 and Ark 564. However, any solution must also be able to explain the change in the iron line variability properties seen across the multiple observations of 3 objects.

A key result of the Chapter is that $\sigma_{\rm rms}$-spectra can separate between absorption and reflection models for the broad red wing of the iron line. In the absorption scenario, the variability of the red wing should match that of the continuum. However, in observations such as NGC 3516(2), where absorption has been supported by other works, the non-variability of the red wing argues against absorption. Similarly, NGC 4151(3) is another example where absorption models can give a good fit to the iron line in the energy spectrum, but at the same time cannot support the strong variability across the red wing. In these cases, the reflection model appears to be superior as it can explain both the energy and variance-spectra.

The iron line core at 6.4 keV is expected to arise from the distant torus and should not be variable, which is in agreement with the $\sigma_{\rm rms}$-spectra of the sample. Across the sample, the slopes of the continuum variability profile in the $\sigma_{\rm rms}$-spectra are generally steeper than the slopes of the continuum in the time-averaged spectrum, which indicates that either the warm absorption may be variable, quasi-constant reflection adds to the hard X-ray flux but not the hard rms, or the continuum may soften as the 2.5 – 10 keV flux increases.

In **Chapter 5**, we extended the iron line variability analysis to study the broadband X-ray spectral variability between 0.3 – 10 keV. Along with the iron line and reflection, we were able to study the X-ray mechanisms associated with producing the soft excess, the continuum and the warm absorption. The aim was to compare the broadband spectral variability across the sample, so we studied the variability over time-scales of 30 – 40 ks with normalised variance-spectra. As with the iron line analysis, the normalised variance spectra displayed a range of profiles including those that showed flat, soft, hard and humped shapes. This is in contrast to the majority of variance-spectra in other works that show a humped variance-spectrum, which can either be explained by spectral variability arising in relativistically blurred disc reflection or smeared wind absorption models. Along with the profile shape, there is a large scatter in the amplitudes of the spectra including those from the same observation. Part of the scatter can be explained by the likely anti-correlation

between the normalised variance and the black hole mass of the AGN. However, the remaining scatter in the amplitudes is still substantial and along with the variety of profile shapes, suggest that there are intrinsic differences in the spectral variability of both separate objects and within objects themselves as well.

The second part of the Chapter focused on models of variance-spectra that can arise in the blurred disc reflection or velocity-smeared wind models. Firstly, we created an energy spectrum that was representative of the observations with a humped variance-spectrum and classed the variance-spectra of five models in both the disc and wind scenarios. These included: (i) the power-law continuum varying in flux with a constant shape and all other components being constant, (ii) the blurred disc reflection, (iii) the ionisation state of the warm absorber, and (iv) the ionisation state of the wind responding to the continuum variability, (v) an increase and (vi) a decrease in the slope of the intrinsic continuum, correlated with increases in the 2 – 10 keV flux. A range of profile shapes were exhibited by the model variance-spectra with four humped, three soft, two flat and one hard model variance-spectrum in total. Secondly, we tested if the humped model variance-spectra could explain both the amplitude and the shape of the mean humped variance-spectrum. A good fit was only obtained with the blurred reflection model and variations in the power-law continuum, but not in any other model component. Over the ~ 40 ks time-scale of our light-curves, we found that only a slope variation of $\Delta\Gamma \sim +0.07$ was necessary. The disc reflection and ionisation state of the warm absorber were not required to be variable on these time-scales. Constant reflection was not unexpected on these time-scales while similar non-variability of the warm absorber had been found in observations of Seyfert galaxies. One disadvantage of the model is the prediction of an upturn in variability that is not seen in the mean humped variance-spectrum.

6.2 Further work

The work in this thesis is suitable for many further developments. For example, including the Compton hump above 10 keV with the iron line in spectral fitting can help to constrain model parameters further. Furthermore, models from Chapter 3 that included blurred disc reflection predict a higher ratio of hard (> 10 keV) to softer (< 10 keV) fluxes than the model with no blurred disc reflection. As shown with NGC 2110 and NGC 7469(2), analysing the narrow and non-relativistic-line objects with *Suzaku* would help to confirm or argue against the results of Chapter 3.

The iron line variability analysis could be extended by calculating the variance

spectra of objects that we were unable to include in our sample. This would require longer *XMM-Newton* observations to ensure that statistical fluctuations do not lead to negative variances. Similarly, longer observations would also increase the sample size for the broadband variability analysis as more objects would have at least one light curve of length 30 – 40 ks. Furthermore, it would be interesting to compare the spectral variability over both short and long time-scales. As discussed in Chapter 5, a spectral analysis of very long light curves with *RXTE* uncovered a power-law relationship between the spectral slope and X-ray flux (Sobolewska & Papadakis, 2009) whereas we found a linear correlation at short time-scales. A repetition of our analysis with long time-scale light curves could be used to test the Sobolewska & Papadakis (2009) findings.

Half of the variance-spectra in Chapter 5 had non-humped profile shapes in their normalised variance-spectra. These clearly reveal interesting aspects of spectral variability in AGN that could be investigated further by fitting with the models that produce flat, soft and hard variance-spectra. Similarly, instead of taking the mean of the humped variance spectra, it would also be important to model each humped variance-spectrum separately using the best-fitting model of the corresponding energy spectrum. If spectral softening with flux is required to explain each humped variance-spectrum, this would support the results found using only the mean profile.

Chapter 3 has shown that the relatively modest spectral resolution of the *XMM-Newton* EPIC-pn camera can adequately detected heavily blurred iron lines. Strong smearing was associated with a maximally spinning black hole, and one of the aims of the inter-agency Advanced Telescope for High Energy Astrophysics (*ATHENA*) is to make more precise measurements of the black hole spin. For example, Figure 6.1 shows a simulated time-energy plane for the detection of hot spots of iron Kα emission in the disc (Bookbinder, 2010). The "arc" features are dependent on the mass and spin of the black hole as well as the disc inclination. Therefore, this can provide a constraint on the black hole spin in addition to that from fitting the iron line. Furthermore, *ATHENA* will aim to probe close to the event horizon of SMBH. Unlike *XMM-Newton* and *Suzaku*, which integrate for many orbits to collect sufficient photons to define the disc reflection spectrum, the superior throughput of *ATHENA* allows it to detect the continuum and iron line variability on sub-orbital time-scales.

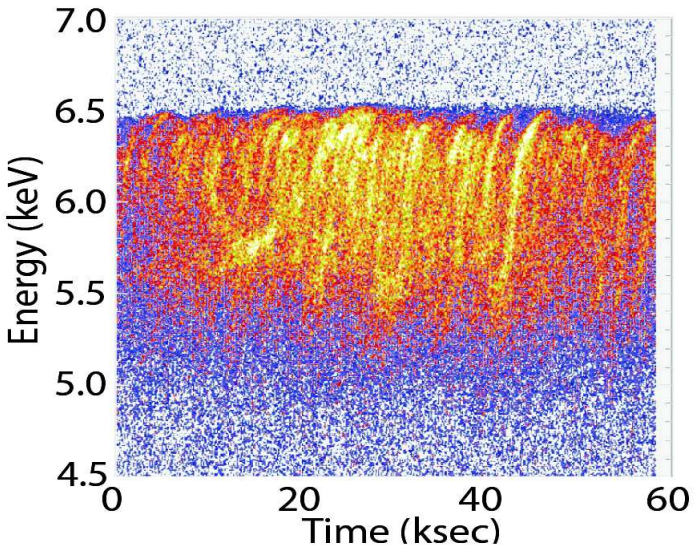

Figure 6.1: How the hot spots of Kα emission will appear as arcs in an *ATHENA* simulation of the time-energy plane. Figure taken from Bookbinder (2010).

APPENDIX A

Blurred ionised disc reflection

The results of fitting the ionised disc model, Model ION of Chapter 3, to the observations with a broad iron line (relativistic and non-relativistic) are presented in Table A.1. The unfolded spectrum (black) and model (red) of all the N07 observations are shown in Figure A.1. Errors are given at a confidence level of 90%.

Considering the sample as a whole, Models ION and N07 give similar goodness-of-fits to the data as the mean difference in their fits is only $\langle \Delta\chi^2 \rangle = -1.3$. This is primarily because on average, the ionisation state of the disc is not high with $\langle \xi_{\rm blur} \rangle = 22$ so that the disc can be assumed to be cold. There is a strong preference for ionised disc reflection in Ark 120, MCG-6-30-15(2), Ark 564 and NGC 7469(2) as the improvements in the fits with Model ION over Model N07 are greater than $\Delta\chi^2 = 10$.

The mean spectral slope of Model ION, $\Gamma = 1.95$, is slightly steeper compared to the mean found with Model N07, $\Gamma = 1.87$, although there is consistency within the error bars. The mean break radius of $r_{\rm br} = 6r_{\rm g}$ shows that on average, the iron line emission originates close to the black hole and should be subject to strong relativistic broadening. Both the disc and distant reflection strengths are similar to those found with Model N07, with $\langle R_{\rm blur} \rangle = 0.48$ implying that the accretion disc covers only half the expected 2π solid angle at the X-ray source.

Table A.1: Fits of Model ION to the N07 observations with a broad iron line (relativistic and non-relativistic). Column(1): name and observation number. Column(2): spectral slope of the power-law continuum. Column(3): reflection fraction of the blurred disc (REFLIONX) component, where $R = 1$ corresponds to a semi-infinite slab seen at an inclination i subtending 2π solid angle at the X-ray source. Column(4): inclination of the slab representing the blurred reflector. Column(5): break radius for the emissivity law. Note that the inner radius is set to $6r_{\rm g}$, assuming the Schwarzchild case, so that the allowed model values of $r_{\rm br} < 6r_{\rm g}$ are statistically indistinguishable from those with $r_{\rm br} = 6r_{\rm g}$. Column(6): reflection fraction of the distant torus (PEXMON) component, where $R = 1$ corresponds to a semi-infinite slab seen at an inclination of 60° and subtending 2π solid angle at the X-ray source. Column(7): ionisation parameter, $\xi_{\rm blur}$, of the blurred reflector. Column (8): change in goodness-of-fit relative to the best-fit of Model N07.

Name	Γ	$R_{\rm blur}$ $(\Omega/2\pi)$	$i_{\rm blur}$ (°)	$r_{\rm br}$ $(r_{\rm g})$	$R_{\rm dist}$ $(\Omega/2\pi)$	$\xi_{\rm blur}$ erg cm s^{-1}	$\Delta\chi^2$
(1)	(2)	(3)	(4)	(5)	(6)	(7)	(8)
NGC 526A	$1.7^{+0.1}_{-0.1}$	$0.5^{+0.2}_{-0.2}$	43^{+42}_{-17}	44^{+357}_{-42}	$0.3^{+0.1}_{-0.1}$	14^{+126}_{-4}	-1.7
Ark 120	$2.1^{+0.0}_{-0.0}$	$1.1^{+0.1}_{-0.1}$	78^{+7}_{-22}	346^{+55}_{-277}	$0.4^{+0.1}_{-0.1}$	32^{+32}_{-11}	-14.6
NGC 2992	$1.8^{+0.1}_{-0.0}$	$0.4^{+0.1}_{-0.2}$	0^{+23}_{-0}	$11^{+9.3}_{-10}$	$0.3^{+0.1}_{-0.1}$	502^{+585}_{-303}	$+4.5$
MCG-5-23-16(1)	$1.8^{+0.1}_{-0.1}$	$0.5^{+0.2}_{-0.3}$	0^{+19}_{-0}	172^{+228}_{-122}	$0.01^{+0.3}_{-0.01}$	57^{+52}_{-47}	-0.3
MCG-5-23-16(2)	$1.8^{+0.1}_{-0.1}$	$0.6^{+0.2}_{-0.2}$	18^{+10}_{-18}	51^{+94}_{-30}	$0.2^{+0.1}_{-0.1}$	10^{+219}_{-0}	-3.6
NGC 3516(1)	$1.8^{+0.1}_{-0.1}$	$1.5^{+0.3}_{-0.3}$	34^{+3}_{-5}	$4.4^{+14}_{-3.2}$	$0.8^{+0.2}_{-0.2}$	25^{+86}_{-15}	-4.2
NGC 3516(2)	$2.1^{+0.1}_{-0.1}$	$5.0^{+5.0}_{-0.7}$	35^{+2}_{-2}	$4.6^{+12}_{-3.4}$	$2.5^{+0.5}_{-0.4}$	20^{+7}_{-7}	-0.4
NGC 3783(2)	$1.7^{+0.0}_{-0.0}$	$0.5^{+0.1}_{-0.1}$	28^{+4}_{-8}	13^{+71}_{-12}	$0.6^{+0.1}_{-0.1}$	45^{+64}_{-35}	-2.4
NGC 4051	$2.1^{+0.1}_{-0.1}$	$1.3^{+0.2}_{-0.2}$	24^{+5}_{-13}	$2.9^{+26}_{-1.6}$	$0.6^{+0.1}_{-0.1}$	22^{+49}_{-12}	$+1.4$
NGC 4151(1)	$1.7^{+0.1}_{-0.1}$	$0.7^{+0.3}_{-0.2}$	17^{+16}_{-17}	361^{+39}_{-360}	$1.3^{+0.2}_{-0.3}$	52^{+74}_{-42}	-1.5

Continues on next page

Table A.1 – continued from previous page

Name	Γ	$R_{\rm blur}$	$i_{\rm blur}$	$r_{\rm br}$	$R_{\rm dist}$	$\xi_{\rm blur}$	$\Delta\chi^2$
NGC 4151(2)	$1.4^{+0.1}_{-0.1}$	$1.1^{+0.2}_{-0.3}$	16^{+74}_{-16}	91^{+309}_{-90}	$1.2^{+0.2}_{-0.2}$	173^{+585}_{-163}	+0.3
NGC 4151(3)	$1.8^{+0.0}_{-0.0}$	$1.0^{+0.1}_{-0.1}$	34^{+1}_{-2}	$2.4^{+11}_{-1.1}$	$0.4^{+0.0}_{-0.0}$	22^{+224}_{-12}	−8.2
Mrk 766(1)	$2.3^{+0.1}_{-0.1}$	$2.0^{+0.3}_{-0.3}$	41^{+4}_{-6}	$4.0^{+24}_{-2.8}$	$0.6^{+0.3}_{-0.2}$	10^{+20}_{-0}	−2.0
Mrk 766(2)	$2.1^{+0.0}_{-0.0}$	$0.4^{+0.0}_{-0.4}$	0^{+35}_{-0}	102^{+298}_{-101}	$0.2^{+0.1}_{-0.1}$	1460^{+1451}_{-783}	+6.8
Mrk 766(3)	$2.0^{+0.0}_{-0.0}$	$0.7^{+0.1}_{-0.1}$	25^{+4}_{-5}	15^{+12}_{-7}	$0.3^{+0.0}_{-0.1}$	496^{+170}_{-238}	+3.7
NGC 4395	$1.5^{+0.1}_{-0.1}$	$1.0^{+0.6}_{-0.5}$	16^{+13}_{-16}	$2.4^{+27}_{-1.2}$	$0.6^{+0.2}_{-0.2}$	156^{+89}_{-146}	−0.9
NGC 4593	$1.8^{+0.0}_{-0.0}$	$0.6^{+0.1}_{-0.1}$	24^{+32}_{-24}	323^{+77}_{-234}	$0.5^{+0.2}_{-0.2}$	75^{+50}_{-34}	−9.5
MCG-6-30-15(1)	$2.4^{+0.1}_{-0.1}$	$2.3^{+0.3}_{-0.3}$	35^{+2}_{-3}	$1.2^{+14}_{-0.0}$	$0.3^{+0.1}_{-0.1}$	21^{+31}_{-7}	−8.2
MCG-6-30-15(2)	$2.4^{+0.0}_{-0.0}$	$0.9^{+0.2}_{-0.1}$	35^{+1}_{-1}	$8.7^{+2.6}_{-7.5}$	$0.2^{+0.1}_{-0.0}$	11^{+6}_{-1}	−11.8
IC 4329A(2)	$1.7^{+0.0}_{-0.0}$	$0.3^{+0.1}_{-0.1}$	35^{+50}_{-12}	253^{+147}_{-191}	$0.3^{+0.1}_{-0.1}$	41^{+35}_{-31}	+3.9
NGC 5506(2)	$1.8^{+0.1}_{-0.1}$	$0.5^{+0.1}_{-0.2}$	41^{+4}_{-4}	$2.6^{+29}_{-1.3}$	$0.1^{+0.1}_{-0.1}$	10^{+480}_{-0}	−4.4
NGC 5548(2)	$1.8^{+0.0}_{-0.0}$	$0.3^{+0.1}_{-0.1}$	25^{+15}_{-15}	238^{+162}_{-237}	$0.2^{+0.1}_{-0.1}$	10^{+55}_{-0}	−6.3
Mrk 509	$1.7^{+0.1}_{-0.1}$	$0.5^{+0.2}_{-0.2}$	33^{+53}_{-33}	36^{+364}_{-35}	$0.3^{+0.1}_{-0.2}$	10^{+6009}_{-0}	−0.5
NGC 7314	$2.0^{+0.0}_{-0.1}$	$0.2^{+0.1}_{-0.1}$	30^{+55}_{-30}	84^{+317}_{-82}	$0.3^{+0.1}_{-0.1}$	996^{+1790}_{-986}	+6.1
Ark 564	$2.6^{+0.0}_{-0.0}$	$0.2^{+4.8}_{-0.2}$	22^{+38}_{-22}	79^{+321}_{-50}	$0.2^{+0.2}_{-0.1}$	982^{+1749}_{-476}	−13.1
NGC 7469(2)	$1.9^{+0.0}_{-0.0}$	$0.5^{+0.1}_{-0.1}$	75^{+10}_{-34}	53^{+58}_{-35}	$0.6^{+0.1}_{-0.1}$	100^{+61}_{-47}	−21.3
Weighted mean	$2.0 \pm 4 \times 10^{-5}$	$0.5 \pm 3 \times 10^{-4}$	33 ± 0.7	6 ± 5	$0.4 \pm 2 \times 10^{-4}$	22 ± 14	−1.3

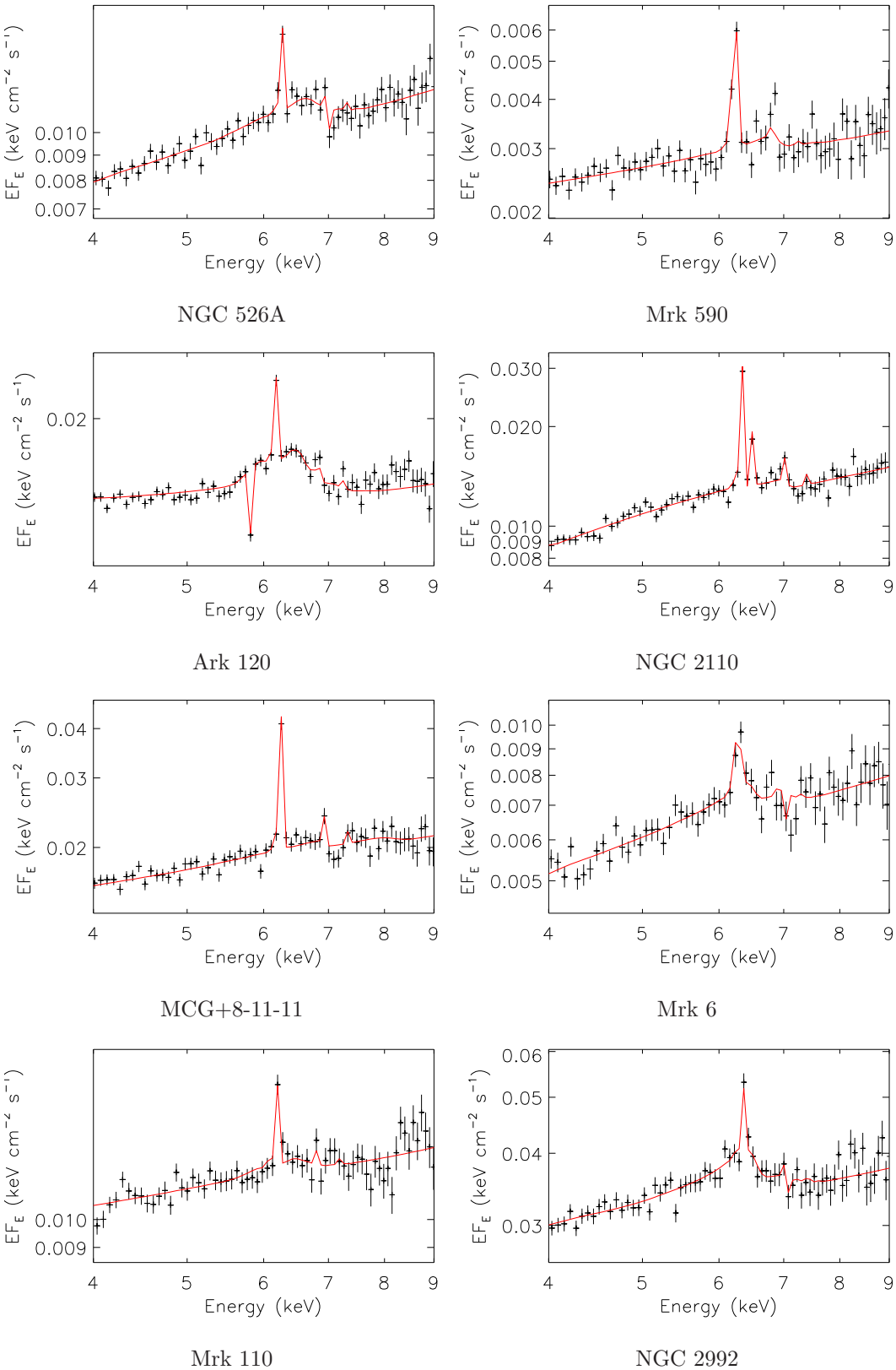

Figure A.1: The unfolded spectra (black error bars) centred around the iron line band (4 – 9 keV) for the entire N07 sample. The solid red line shows the best-fit of Model ION to the data.

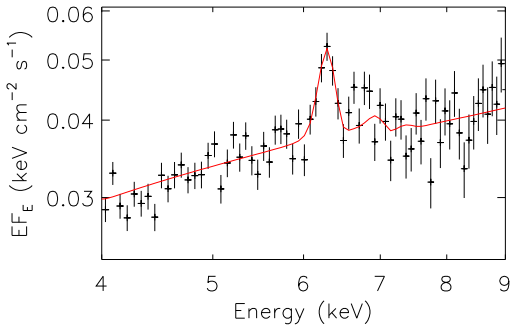

MCG-5-23-16(1)

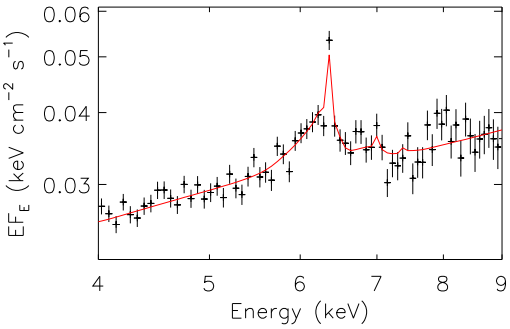

MCG-5-23-16(2)

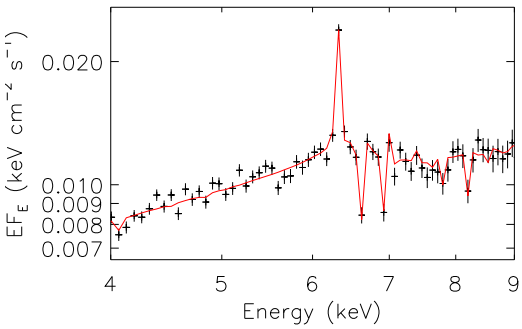

NGC 3516(1)

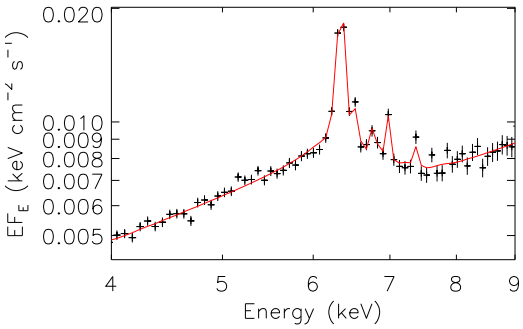

NGC 3516(2)

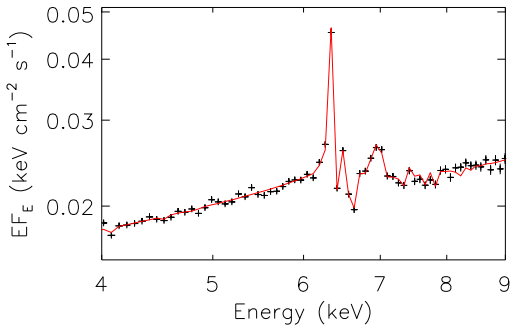

NGC 3783

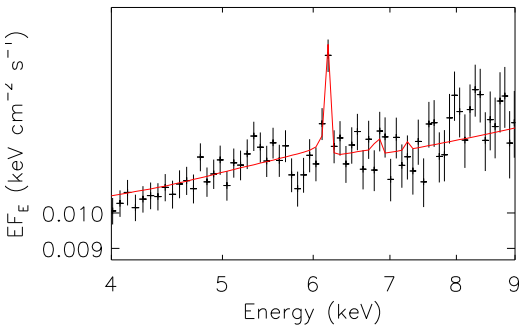

HE 1143-1810

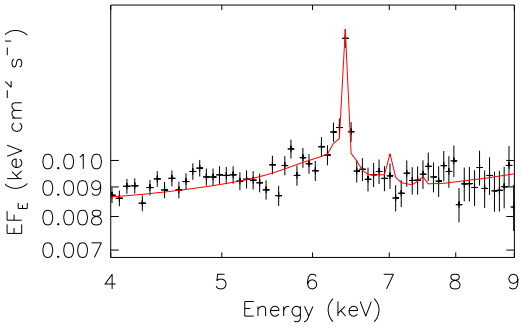

NGC 4051

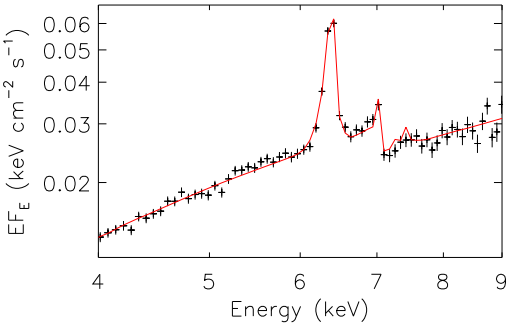

NGC 4151(1)

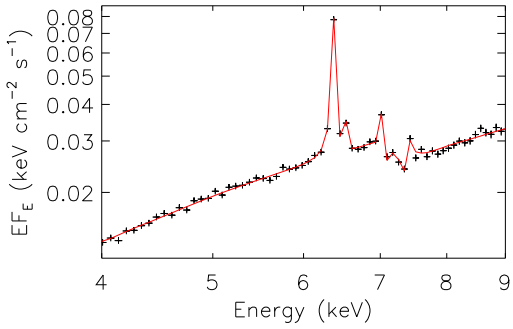

NGC 4151(2)

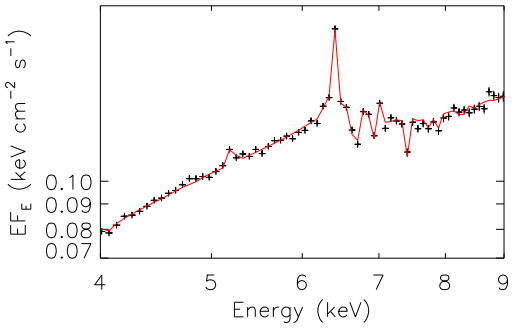

NGC 4151(3)

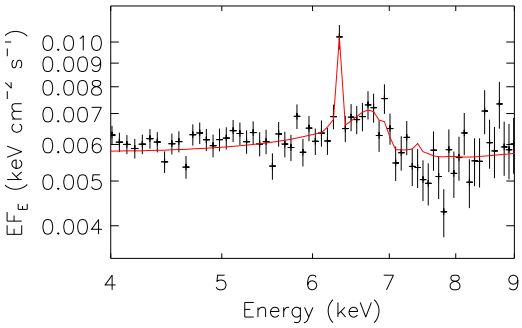

Mrk 766(1)

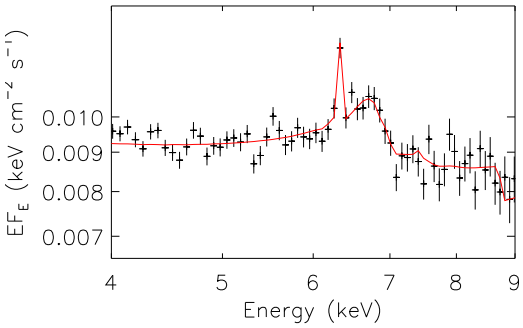

Mrk 766(2)

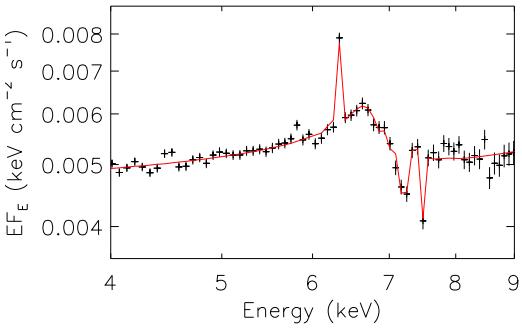

Mrk 766(3)

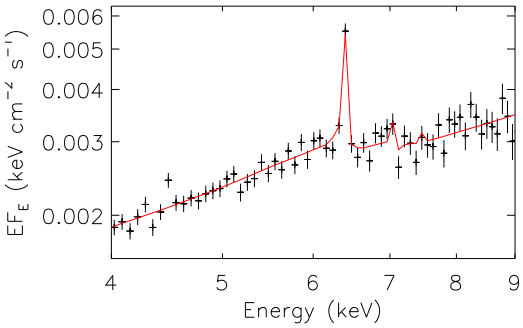

NGC 4395

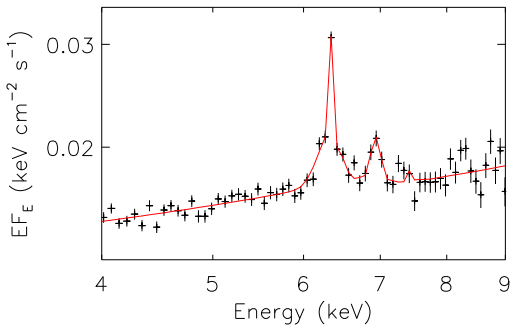

NGC 4593

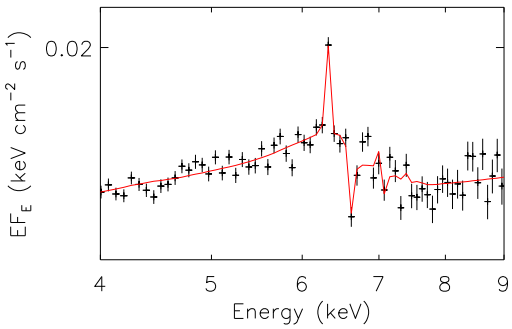

MCG-6-30-15(1)

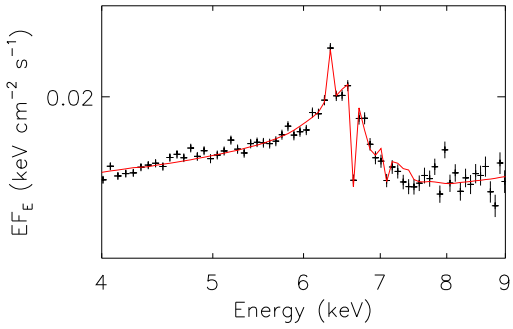

MCG-6-30-15(2)

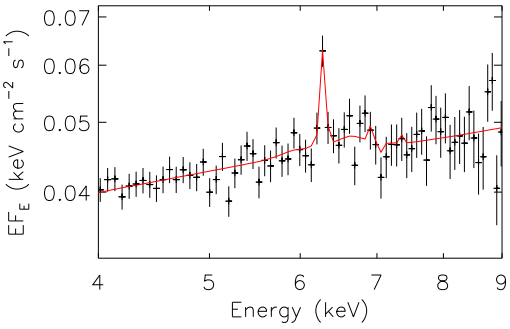

IC 4329A(1)

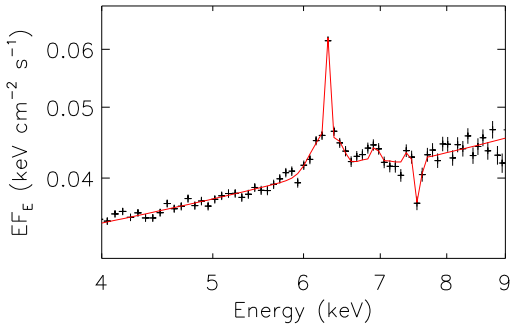

IC 4329A(2)

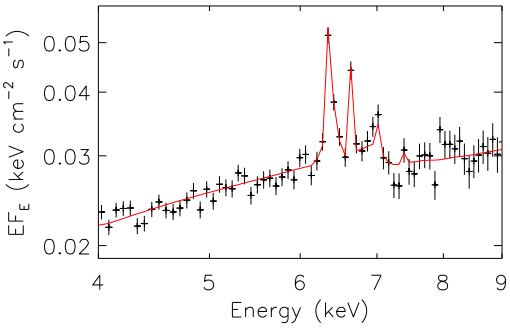

NGC 5506(1)

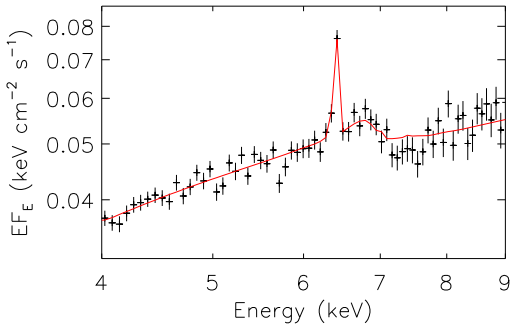

NGC 5506(2)

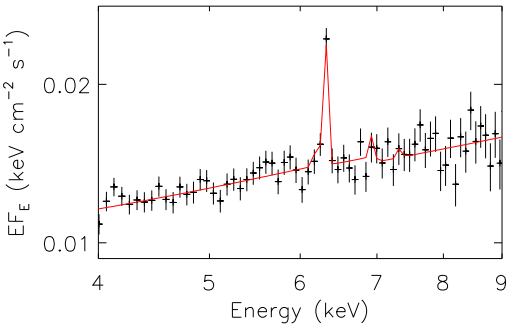

NGC 5548(1)

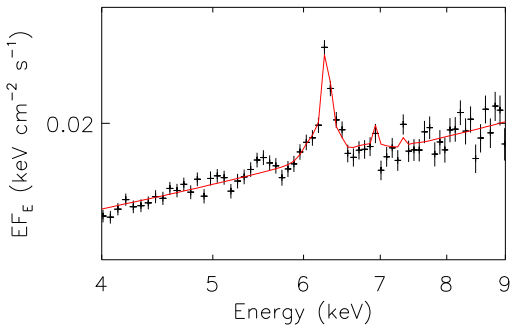

NGC 5548(2)

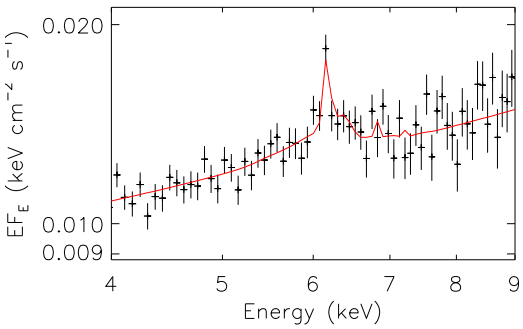

Mrk 509

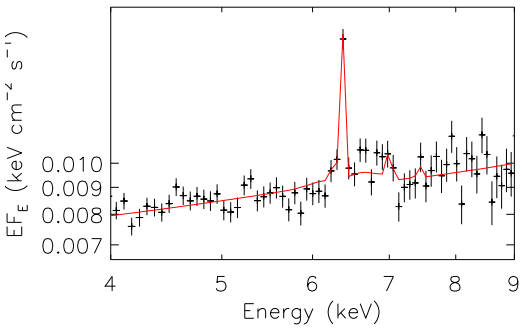

NGC 7213

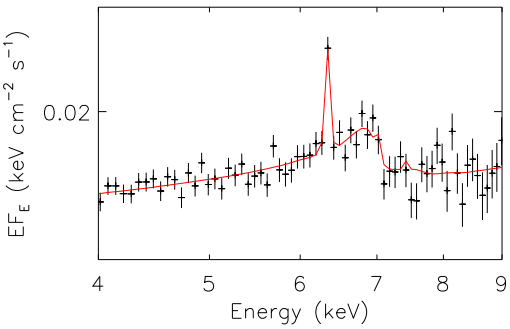

NGC 7314

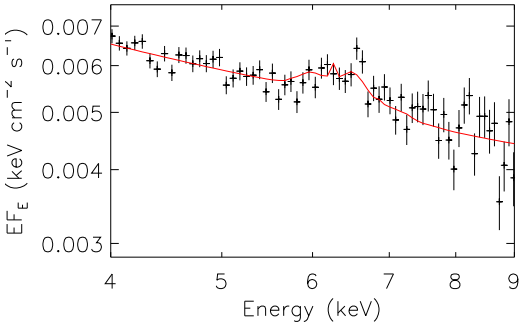

Ark 564

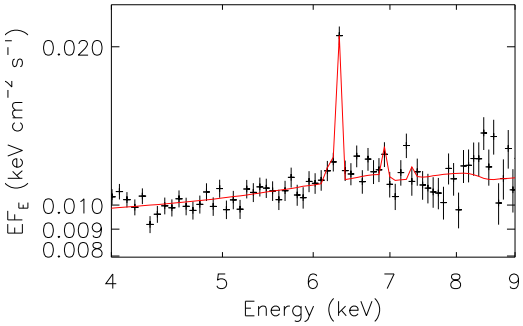

NGC 7469(1)

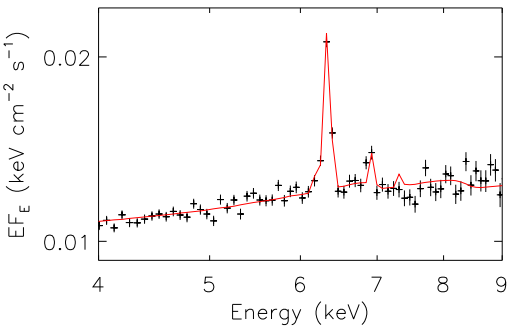

NGC 7469(2)

References

Agol E., Krolik J. H., 2000, ApJ, 528, 161

Antonucci R., 1993, ARA&A, 31, 473

Antonucci R. R. J., Miller J. S., 1985, ApJ, 297, 621

Arnaud K. A., 1996, in Astronomical Society of the Pacific Conference Series, Vol. 101, Astronomical Data Analysis Software and Systems V, G. H. Jacoby & J. Barnes, ed., pp. 17–+

Arnaud K. A., Branduardi-Raymont G., Culhane J. L., Fabian A. C., Hazard C., McGlynn T. A., Shafer R. A., Tennant A. F., Ward M. J., 1985, MNRAS, 217, 105

Balbus S. A., Hawley J. F., 1991, ApJ, 376, 214

Ballantyne D. R., Iwasawa K., Fabian A. C., 2001a, MNRAS, 323, 506

Ballantyne D. R., Ross R. R., Fabian A. C., 2001b, MNRAS, 327, 10

Ballet J., 1999, A&AS, 135, 371

Bardeen J. M., Press W. H., Teukolsky S. A., 1972, ApJ, 178, 347

Barger A. J., Cowie L. L., Mushotzky R. F., Yang Y., Wang W.-H., Steffen A. T., Capak P., 2005, AJ, 129, 578

Barvainis R., 1987, ApJ, 320, 537

Bechtold J., Czerny B., Elvis M., Fabbiano G., Green R. F., 1987, ApJ, 314, 699

Beloborodov A. M., 1999, ApJL, 510, L123

Bentz M. C., Denney K. D., Cackett E. M., Dietrich M., Fogel J. K. J., Ghosh H., Horne K. D., Kuehn C., Minezaki T., Onken C. A., Peterson B. M., Pogge R. W., Pronik V. I., Richstone D. O., Sergeev S. G., Vestergaard M., Walker M. G., Yoshii Y., 2007, ApJ, 662, 205

Bentz M. C., Peterson B. M., Netzer H., Pogge R. W., Vestergaard M., 2009a, ApJ, 697, 160

Bentz M. C., Peterson B. M., Pogge R. W., Vestergaard M., 2009b, ApJL, 694, L166

Bentz M. C., Peterson B. M., Pogge R. W., Vestergaard M., Onken C. A., 2006, ApJ, 644, 133

Bhayani S., Nandra K., 2010, MNRAS, 408, 1020

—, 2011, MNRAS, 416, 629

Bian W., 2005, Chinese Journal of Astronomy and Astrophysics Supplement, 5, 289

Bian W., Zhao Y., 2003, MNRAS, 343, 164

Bianchi S., Corral A., Panessa F., Barcons X., Matt G., Bassani L., Carrera F. J., Jiménez-Bailón E., 2008a, MNRAS, 385, 195

Bianchi S., de Angelis I., Matt G., La Parola V., de Rosa A., Grandi P., Jiménez Bailón E., Piconcelli E., 2010, A&A, 522, A64

Bianchi S., La Franca F., Matt G., Guainazzi M., Jimenez Bailón E., Longinotti A. L., Nicastro F., Pentericci L., 2008b, MNRAS, 389, L52

Blanco P. R., Ward M. J., Wright G. S., 1990, MNRAS, 242, 4P

Blandford R. D., Znajek R. L., 1977, MNRAS, 179, 433

Boller T., Brandt W. N., Fink H., 1996, A&A, 305, 53

Bookbinder J., 2010, ArXiv e-prints

Boroson T. A., 2002, ApJ, 565, 78

Boroson T. A., Green R. F., 1992, ApJS, 80, 109

Botte V., Ciroi S., Rafanelli P., Di Mille F., 2004, AJ, 127, 3168

Brandt W. N., Hasinger G., 2005, ARA&A, 43, 827

Brenneman L. W., Reynolds C. S., 2006, ApJ, 652, 1028

Bridle A. H., Perley R. A., 1984, ARA&A, 22, 319

Brightman M., Nandra K., 2008, MNRAS, 390, 1241

Cid Fernandes R., Gu Q., Melnick J., Terlevich E., Terlevich R., Kunth D., Rodrigues Lacerda R., Joguet B., 2004, MNRAS, 355, 273

Coppi P. S., 1999, in Astronomical Society of the Pacific Conference Series, Vol. 161, High Energy Processes in Accreting Black Holes, J. Poutanen & R. Svensson, ed., pp. 375–403

Cowie L. L., Barger A. J., Bautz M. W., Brandt W. N., Garmire G. P., 2003, ApJL, 584, L57

Crenshaw D. M., Kraemer S. B., George I. M., 2003, ARA&A, 41, 117

Crummy J., Fabian A. C., Gallo L., Ross R. R., 2006, MNRAS, 365, 1067

Czerny B., Elvis M., 1987, ApJ, 321, 305

Czerny B., Nikołajuk M., Różańska A., Dumont A., Loska Z., Zycki P. T., 2003, A&A, 412, 317

Dabrowski Y., Fabian A. C., Iwasawa K., Lasenby A. N., Reynolds C. S., 1997, MNRAS, 288, L11

de La Calle Pérez I., Longinotti A. L., Guainazzi M., Bianchi S., Dovčiak M., Cappi M., Matt G., Miniutti G., Petrucci P. O., Piconcelli E., Ponti G., Porquet D., Santos-Lleó M., 2010, A&A, 524, A50

De Luca A., Caraveo P. A., Mereghetti S., Negroni M., Bignami G. F., 2005, ApJ, 623, 1051

De Luca A., Molendi S., 2004, A&A, 419, 837

de Marco B., Iwasawa K., Cappi M., Dadina M., Tombesi F., Ponti G., Celotti A., Miniutti G., 2009, A&A, 507, 159

Denney K. D., Bentz M. C., Peterson B. M., Pogge R. W., Cackett E. M., Dietrich M., Fogel J. K. J., Ghosh H., Horne K. D., Kuehn C., Minezaki T., Onken C. A., Pronik V. I., Richstone D. O., Sergeev S. G., Vestergaard M., Walker M. G., Yoshii Y., 2006, ApJ, 653, 152

Denney K. D., Watson L. C., Peterson B. M., Pogge R. W., Atlee D. W., Bentz M. C., Bird J. C., Brokofsky D. J., Comins M. L., Dietrich M., Doroshenko V. T., Eastman J. D., Efimov Y. S., Gaskell C. M., Hedrick C. H., Klimanov S. A., Klimek E. S., Kruse A. K., Lamb J. B., Leighly K., Minezaki T., Nazarov S. V., Petersen E. A., Peterson P., Poindexter S., Schlesinger Y., Sakata K. J., Sergeev S. G., Tobin J. J., Unterborn C., Vestergaard M., Watkins A. E., Yoshii Y., 2009, ApJ, 702, 1353

Dewangan G. C., Griffiths R. E., Dasgupta S., Rao A. R., 2007, ApJ, 671, 1284

Dickey J. M., Lockman F. J., 1990, ARA&A, 28, 215

Done C., Madejski G. M., Życki P. T., 2000, ApJ, 536, 213

Dove J. B., Wilms J., Begelman M. C., 1997, ApJ, 487, 747

Eardley D. M., Lightman A. P., 1975, ApJ, 200, 187

Edelson R., Nandra K., 1999, ApJ, 514, 682

Edelson R., Turner T. J., Pounds K., Vaughan S., Markowitz A., Marshall H., Dobbie P., Warwick R., 2002, ApJ, 568, 610

Elvis M., Wilkes B. J., Lockman F. J., 1989, AJ, 97, 777

Evans I. N., Ford H. C., Kinney A. L., Antonucci R. R. J., Armus L., Caganoff S., 1991, ApJL, 369, L27

Fabian A. C., Iwasawa K., Reynolds C. S., Young A. J., 2000, PASP, 112, 1145

Fabian A. C., Miniutti G., Gallo L., Boller T., Tanaka Y., Vaughan S., Ross R. R., 2004, MNRAS, 353, 1071

Fabian A. C., Rees M. J., Stella L., White N. E., 1989, MNRAS, 238, 729

Fabian A. C., Vaughan S., 2003, MNRAS, 340, L28

Fabian A. C., Vaughan S., Nandra K., Iwasawa K., Ballantyne D. R., Lee J. C., De Rosa A., Turner A., Young A. J., 2002, MNRAS, 335, L1

Fabian A. C., Zoghbi A., Ross R. R., Uttley P., Gallo L. C., Brandt W. N., Blustin A. J., Boller T., Caballero-Garcia M. D., Larsson J., Miller J. M., Miniutti G., Ponti G., Reis R. C., Reynolds C. S., Tanaka Y., Young A. J., 2009, Nature, 459, 540

Ferland G. J., Netzer H., 1983, ApJ, 264, 105

Galeev A. A., Rosner R., Vaiana G. S., 1979, ApJ, 229, 318

Gallo L. C., Boller T., Tanaka Y., Fabian A. C., Brandt W. N., Welsh W. F., Anabuki N., Haba Y., 2004, MNRAS, 347, 269

Gammie C. F., 1999, ApJL, 522, L57

Garcia-Rissmann A., Vega L. R., Asari N. V., Cid Fernandes R., Schmitt H., González Delgado R. M., Storchi-Bergmann T., 2005, MNRAS, 359, 765

George I. M., Fabian A. C., 1991, MNRAS, 249, 352

Ghisellini G., Haardt F., Matt G., 1994, MNRAS, 267, 743

Ghisellini G., Tavecchio F., 2008, MNRAS, 386, L28

Gierliński M., Done C., 2004, MNRAS, 349, L7

—, 2006, MNRAS, 371, L16

Gilfanov M., Churazov E., Revnivtsev M., 2000, MNRAS, 316, 923

Green A. R., McHardy I. M., Lehto H. J., 1993, MNRAS, 265, 664

Greene J. E., Ho L. C., 2005, ApJ, 627, 721

Guainazzi M., Matt G., Molendi S., Orr A., Fiore F., Grandi P., Matteuzzi A., Mineo T., Perola G. C., Parmar A. N., Piro L., 1999, A&A, 341, L27

Guainazzi M., Nicastro F., Fiore F., Matt G., McHardy I., Orr A., Barr P., Fruscione A., Papadakis I., Parmar A. N., Uttley P., Perola G. C., Piro L., 1998, MNRAS, 301, L1

Gültekin K., Richstone D. O., Gebhardt K., Lauer T. R., Tremaine S., Aller M. C., Bender R., Dressler A., Faber S. M., Filippenko A. V., Green R., Ho L. C., Kormendy J., Magorrian J., Pinkney J., Siopis C., 2009, ApJ, 698, 198

Haardt F., Maraschi L., 1991, ApJL, 380, L51

—, 1993, ApJ, 413, 507

Haardt F., Maraschi L., Ghisellini G., 1994, ApJL, 432, L95

—, 1997, ApJ, 476, 620

Heckman T. M., 1980, A&A, 87, 152

Ho L. C., Filippenko A. V., Sargent W. L. W., 1997, ApJS, 112, 315

Iwasawa K., Fabian A. C., Reynolds C. S., Nandra K., Otani C., Inoue H., Hayashida K., Brandt W. N., Dotani T., Kunieda H., Matsuoka M., Tanaka Y., 1996, MNRAS, 282, 1038

Iwasawa K., Fabian A. C., Young A. J., Inoue H., Matsumoto C., 1999, MNRAS, 306, L19

Iwasawa K., Miniutti G., Fabian A. C., 2004, MNRAS, 355, 1073

Jaffe W., Meisenheimer K., Röttgering H. J. A., Leinert C., Richichi A., Chesneau O., Fraix-Burnet D., Glazenborg-Kluttig A., Granato G., Graser U., Heijligers B., Köhler R., Malbet F., Miley G. K., Paresce F., Pel J., Perrin G., Przygodda F., Schoeller M., Sol H., Waters L. B. F. M., Weigelt G., Woillez J., de Zeeuw P. T., 2004, Nature, 429, 47

Jin C., Done C., Ward M., Gierliński M., Mullaney J., 2009, MNRAS, 398, L16

Kallman T. R., Palmeri P., Bautista M. A., Mendoza C., Krolik J. H., 2004, ApJS, 155, 675

Kauffmann G., Heckman T. M., Tremonti C., Brinchmann J., Charlot S., White S. D. M., Ridgway S. E., Brinkmann J., Fukugita M., Hall P. B., Ivezić Ž., Richards G. T., Schneider D. P., 2003, MNRAS, 346, 1055

Kawaguchi T., 2003, ApJ, 593, 69

Kazanas D., Nayakshin S., 2001, ApJ, 550, 655

Kennefick J. D., Djorgovski S. G., de Carvalho R. R., 1995, AJ, 110, 2553

Khachikian E. Y., Weedman D. W., 1974, ApJ, 192, 581

Komossa S., Meerschweinchen J., 2000, A&A, 354, 411

Kormendy J., Richstone D., 1995, ARA&A, 33, 581

Koski A. T., 1978, ApJ, 223, 56

Krolik J. H., 1999, ApJL, 515, L73

Krolik J. H., Kallman T. R., 1987, ApJL, 320, L5

Krongold Y., Elvis M., Andrade-Velazquez M., Nicastro F., Mathur S., Reeves J. N., Brickhouse N. S., Binette L., Jimenez-Bailon E., Grupe D., Liu Y., McHardy I. M., Minezaki T., Yoshii Y., Wilkes B., 2010, ApJ, 710, 360

Krongold Y., Nicastro F., Elvis M., Brickhouse N., Binette L., Mathur S., Jiménez-Bailón E., 2007, ApJ, 659, 1022

Kushino A., Ishisaki Y., Morita U., Yamasaki N. Y., Ishida M., Ohashi T., Ueda Y., 2002, PASJ, 54, 327

Laming J. M., Titarchuk L., 2004, ApJL, 615, L121

Laor A., 1991, ApJ, 376, 90

Larsson J., Fabian A. C., Miniutti G., Ross R. R., 2007, MNRAS, 376, 348

Larsson J., Miniutti G., Fabian A. C., Miller J. M., Reynolds C. S., Ponti G., 2008, MNRAS, 384, 1316

Laurent P., Titarchuk L., 2007, ApJ, 656, 1056

Lawrence A., Elvis M., Wilkes B. J., McHardy I., Brandt N., 1997, MNRAS, 285, 879

Lawrence A., Papadakis I., 1993, ApJL, 414, L85

Li L., 2002, ApJ, 567, 463

Liang E. P. T., Price R. H., 1977, ApJ, 218, 247

Liu Y., Elvis M., McHardy I. M., Grupe D., Wilkes B. J., Reeves J., Brickhouse N., Krongold Y., Mathur S., Minezaki T., Nicastro F., Yoshii Y., Zhang S. N., 2010, ApJ, 710, 1228

Lu Y., Yu Q., 2001, MNRAS, 324, 653

Lumb D. H., Warwick R. S., Page M., De Luca A., 2002, A&A, 389, 93

Lutz D., Maiolino R., Moorwood A. F. M., Netzer H., Wagner S. J., Sturm E., Genzel R., 2002, A&A, 396, 439

Lynden-Bell D., 1969, Nature, 223, 690

Maccacaro T., Gioia I. M., Wolter A., Zamorani G., Stocke J. T., 1988, ApJ, 326, 680

Magdziarz P., Zdziarski A. A., 1995, MNRAS, 273, 837

Magorrian J., Tremaine S., Richstone D., Bender R., Bower G., Dressler A., Faber S. M., Gebhardt K., Green R., Grillmair C., Kormendy J., Lauer T., 1998, AJ, 115, 2285

Maiolino R., Rieke G. H., 1995, ApJ, 454, 95

Markowitz A., Edelson R., Vaughan S., Uttley P., George I. M., Griffiths R. E., Kaspi S., Lawrence A., McHardy I., Nandra K., Pounds K., Reeves J., Schurch N., Warwick R., 2003, ApJ, 593, 96

Markowitz A., Papadakis I., Arévalo P., Turner T. J., Miller L., Reeves J. N., 2007, ApJ, 656, 116

Markowitz A., Reeves J. N., George I. M., Braito V., Smith R., Vaughan S., Arévalo P., Tombesi F., 2009, ApJ, 691, 922

Mathur S., 2000, MNRAS, 314, L17

Matsuoka M., Piro L., Yamauchi M., Murakami T., 1990, ApJ, 361, 440

Matt G., Fabian A. C., Reynolds C. S., 1997, MNRAS, 289, 175

Matt G., Fabian A. C., Ross R. R., 1993, MNRAS, 264, 839

—, 1996, MNRAS, 278, 1111

Matt G., Perola G. C., Piro L., 1991, A&A, 247, 25

McHardy I. M., Papadakis I. E., Uttley P., 1999, Nuclear Physics B Proceedings Supplements, 69, 509

McHardy I. M., Papadakis I. E., Uttley P., Page M. J., Mason K. O., 2004, MNRAS, 348, 783

Middleton M., Done C., Gierliński M., 2007, MNRAS, 381, 1426

Middleton M., Done C., Ward M., Gierliński M., Schurch N., 2009, MNRAS, 394, 250

Miller J. M., 2007, ARA&A, 45, 441

Miller J. M., Raymond J., Fabian A. C., Homan J., Nowak M. A., Wijnands R., van der Klis M., Belloni T., Tomsick J. A., Smith D. M., Charles P. A., Lewin W. H. G., 2004, ApJ, 601, 450

Miller J. S., Goodrich R. W., 1990, ApJ, 355, 456

Miller J. S., Goodrich R. W., Mathews W. G., 1991, ApJ, 378, 47

Miller L., Turner T. J., Reeves J. N., 2008, A&A, 483, 437

Miller L., Turner T. J., Reeves J. N., George I. M., Porquet D., Nandra K., Dovciak M., 2006, A&A, 453, L13

Miniutti G., Fabian A. C., 2004, MNRAS, 349, 1435

Miniutti G., Fabian A. C., Anabuki N., Crummy J., Fukazawa Y., Gallo L., Haba Y., Hayashida K., Holt S., Kunieda H., Larsson J., Markowitz A., Matsumoto C., Ohno M., Reeves J. N., Takahashi T., Tanaka Y., Terashima Y., Torii K., Ueda Y., Ushio M., Watanabe S., Yamauchi M., Yaqoob T., 2007, PASJ, 59, 315

Misra R., Kembhavi A. K., 1998, ApJ, 499, 205

Misra R., Sutaria F. K., 1999, ApJ, 517, 661

Mortlock D. J., Warren S. J., Venemans B. P., Patel M., Hewett P. C., McMahon R. G., Simpson C., Theuns T., Gonzáles-Solares E. A., Adamson A., Dye S., Hambly N. C., Hirst P., Irwin M. J., Kuiper E., Lawrence A., Röttgering H. J. A., 2011, Nature, 474, 616

Mushotzky R. F., Cowie L. L., Barger A. J., Arnaud K. A., 2000, Nature, 404, 459

Mushotzky R. F., Done C., Pounds K. A., 1993, ARA&A, 31, 717

Nandra K., George I. M., Mushotzky R. F., Turner T. J., Yaqoob T., 1997a, ApJ, 476, 70

—, 1997b, ApJ, 477, 602

Nandra K., O'Neill P. M., George I. M., Reeves J. N., 2007, MNRAS, 382, 194

Nandra K., Papadakis I. E., 2001, ApJ, 554, 710

Nandra K., Pounds K. A., 1994, MNRAS, 268, 405

Nandra K., Pounds K. A., Stewart G. C., Fabian A. C., Rees M. J., 1989, MNRAS, 236, 39P

Nardini E., Fabian A. C., Reis R. C., Walton D. J., 2011, MNRAS, 410, 1251

Nayakshin S., Kazanas D., 2001, ApJL, 553, L141

Nayakshin S., Rappaport S., Melia F., 2000, ApJ, 535, 798

Nicastro F., Fiore F., Perola G. C., Elvis M., 1999, ApJ, 512, 184

Novikov I. D., Thorne K. S., 1973, in Black Holes (Les Astres Occlus), A. Giannaras, ed., pp. 343–450

Oliva E., Origlia L., Maiolino R., Moorwood A. F. M., 1999, A&A, 350, 9

O'Neill P. M., Nandra K., Cappi M., Longinotti A. L., Sim S. A., 2007, MNRAS, 381, L94

O'Neill P. M., Nandra K., Papadakis I. E., Turner T. J., 2005, MNRAS, 358, 1405

Onken C. A., Peterson B. M., Dietrich M., Robinson A., Salamanca I. M., 2003, ApJ, 585, 121

Osterbrock D. E., 1978, Physics Scripta, 17, 137

—, 1981, ApJ, 249, 462

Osterbrock D. E., Pogge R. W., 1985, ApJ, 297, 166

Ostriker J. P., Weaver R., Yahil A., McCray R., 1976, ApJL, 208, L61

Page D. N., Thorne K. S., 1974, ApJ, 191, 499

Papadakis I. E., 2004, MNRAS, 348, 207

Papadakis I. E., Lawrence A., 1995, MNRAS, 272, 161

Papadakis I. E., Sobolewska M., Arevalo P., Markowitz A., McHardy I. M., Miller L., Reeves J. N., Turner T. J., 2009, A&A, 494, 905

Pappa A., Georgantopoulos I., Stewart G. C., Zezas A. L., 2001, MNRAS, 326, 995

Parmar A. N., Heger D., Metcalfe L., Muñoz R., Schartel N., 2008, Astronomische Nachrichten, 329, 114

Patrick A. R., Reeves J. N., Porquet D., Markowitz A. G., Lobban A. P., Terashima Y., 2010, ArXiv e-prints

Peterson B. M., Bentz M. C., Desroches L., Filippenko A. V., Ho L. C., Kaspi S., Laor A., Maoz D., Moran E. C., Pogge R. W., Quillen A. C., 2005, ApJ, 632, 799

Peterson B. M., Ferrarese L., Gilbert K. M., Kaspi S., Malkan M. A., Maoz D., Merritt D., Netzer H., Onken C. A., Pogge R. W., Vestergaard M., Wandel A., 2004, ApJ, 613, 682

Pogge R. W., 1989, ApJ, 345, 730

Ponti G., Cappi M., Dadina M., Malaguti G., 2004, A&A, 417, 451

Ponti G., Gallo L. C., Fabian A. C., Miniutti G., Zoghbi A., Uttley P., Ross R. R., Vasudevan R. V., Tanaka Y., Brandt W. N., 2010, MNRAS, 406, 2591

Ponti G., Miniutti G., Cappi M., Maraschi L., Fabian A. C., Iwasawa K., 2006, MNRAS, 368, 903

Porquet D., Reeves J. N., O'Brien P., Brinkmann W., 2004, A&A, 422, 85

Pounds K. A., Done C., Osborne J. P., 1995, MNRAS, 277, L5

Pounds K. A., Nandra K., Stewart G. C., George I. M., Fabian A. C., 1990, Nature, 344, 132

Pounds K. A., Reeves J. N., Page K. L., Edelson R., Matt G., Perola G. C., 2003a, MNRAS, 341, 953

Pounds K. A., Reeves J. N., Page K. L., Wynn G. A., O'Brien P. T., 2003b, MNRAS, 342, 1147

Pozdniakov L. A., Sobol I. M., Sunyaev R. A., 1979, A&A, 75, 214

Protassov R., van Dyk D. A., Connors A., Kashyap V. L., Siemiginowska A., 2002, ApJ, 571, 545

Rees M. J., 1984, ARA&A, 22, 471

Reeves J. N., Awaki H., Dewangan G. C., Fabian A. C., Fukazawa Y., Gallo L., Griffiths R., Inoue H., Kunieda H., Markowitz A., Miniutti G., Mizuno T., Mushotzky R., Okajima T., Ptak A., Takahashi T., Terashima Y., Ushio M., Watanabe S., Yamasaki T., Yamauchi M., Yaqoob T., 2007, PASJ, 59, 301

Reeves J. N., Fabian A. C., Kataoka J., Kunieda H., Markowitz A., Miniutti G., Okajima T., Serlemitsos P., Takahashi T., Terashima Y., Yaqoob T., 2006, Astronomische Nachrichten, 327, 1079

Reeves J. N., Nandra K., George I. M., Pounds K. A., Turner T. J., Yaqoob T., 2004, ApJ, 602, 648

Reynolds C. S., Begelman M. C., 1997, ApJ, 488, 109

Reynolds C. S., Nowak M. A., 2003, Physics Reports, 377, 389

Reynolds C. S., Wilms J., Begelman M. C., Staubert R., Kendziorra E., 2004, MNRAS, 349, 1153

Riffert H., Herold H., 1995, ApJ, 450, 508

Risaliti G., Elvis M., Fabbiano G., Baldi A., Zezas A., 2005, ApJL, 623, L93

Rodríguez-Ardila A., Pastoriza M. G., Donzelli C. J., 2000, ApJS, 126, 63

Ross R. R., Fabian A. C., 1993, MNRAS, 261, 74

—, 2005, MNRAS, 358, 211

Ross R. R., Fabian A. C., Young A. J., 1999, MNRAS, 306, 461

Rowan-Robinson M., 1977, ApJ, 213, 635

Ruszkowski M., Fabian A. C., Ross R. R., Iwasawa K., 2000, MNRAS, 317, L11

Saez C., Chartas G., Brandt W. N., Lehmer B. D., Bauer F. E., Dai X., Garmire G. P., 2008, AJ, 135, 1505

Schmidt M., 1963, ApJ, 137, 758

Schmidt M., Schneider D. P., Gunn J. E., 1995, AJ, 110, 68

Schurch N. J., Done C., 2007, MNRAS, 381, 1413

Schurch N. J., Done C., Proga D., 2009, ApJ, 694, 1

Schurch N. J., Warwick R. S., 2002, MNRAS, 334, 811

Schurch N. J., Warwick R. S., Griffiths R. E., Sembay S., 2003, MNRAS, 345, 423

Seyfert C. K., 1943, ApJ, 97, 28

Shakura N. I., Sunyaev R. A., 1973, A&A, 24, 337

Shaver P. A., Wall J. V., Kellermann K. I., Jackson C. A., Hawkins M. R. S., 1996, Nature, 384, 439

Shemmer O., Brandt W. N., Netzer H., Maiolino R., Kaspi S., 2006, ApJL, 646, L29

—, 2008, ApJ, 682, 81

Shih D. C., Iwasawa K., Fabian A. C., 2002, MNRAS, 333, 687

Sobolewska M. A., Done C., 2007, MNRAS, 374, 150

Sobolewska M. A., Papadakis I. E., 2009, MNRAS, 399, 1597

Stanford S. A., Romer A. K., Sabirli K., Davidson M., Hilton M., Viana P. T. P., Collins C. A., Kay S. T., Liddle A. R., Mann R. G., Miller C. J., Nichol R. C., West M. J., Conselice C. J., Spinrad H., Stern D., Bundy K., 2006, ApJL, 646, L13

Stark A. A., Gammie C. F., Wilson R. W., Bally J., Linke R. A., Heiles C., Hurwitz M., 1992, ApJS, 79, 77

Stasińska G., 1984, A&A, 135, 341

Steffen A. T., Barger A. J., Cowie L. L., Mushotzky R. F., Yang Y., 2003, ApJL, 596, L23

Stern B. E., Poutanen J., Svensson R., Sikora M., Begelman M. C., 1995, ApJL, 449, L13

Sunyaev R. A., Titarchuk L. G., 1980, A&A, 86, 121

Sunyaev R. A., Truemper J., 1979, Nature, 279, 506

Tanaka Y., Nandra K., Fabian A. C., Inoue H., Otani C., Dotani T., Hayashida K., Iwasawa K., Kii T., Kunieda H., Makino F., Matsuoka M., 1995, Nature, 375, 659

Taylor R. D., Uttley P., McHardy I. M., 2003, MNRAS, 342, L31

Thorne K. S., 1974, ApJ, 191, 507

Thorne K. S., Price R. H., 1975, ApJL, 195, L101

Titarchuk L., Kazanas D., Becker P. A., 2003, ApJ, 598, 411

Tozzi P., Norman C., 2001, ApJ, 546, 63

Tran H. D., Miller J. S., Kay L. E., 1992, ApJ, 397, 452

Turner A. K., Fabian A. C., Lee J. C., Vaughan S., 2004a, MNRAS, 353, 319

Turner T. J., 1987, MNRAS, 226, 9P

Turner T. J., George I. M., Nandra K., Mushotzky R. F., 1998, ApJ, 493, 91

Turner T. J., George I. M., Nandra K., Turcan D., 1999, ApJ, 524, 667

Turner T. J., Kraemer S. B., George I. M., Reeves J. N., Bottorff M. C., 2005, ApJ, 618, 155

Turner T. J., Kraemer S. B., Reeves J. N., 2004b, ApJ, 603, 62

Turner T. J., Miller L., Reeves J. N., Kraemer S. B., 2007, A&A, 475, 121

Turner T. J., Mushotzky R. F., Yaqoob T., George I. M., Snowden S. L., Netzer H., Kraemer S. B., Nandra K., Chelouche D., 2002, ApJL, 574, L123

Turner T. J., Pounds K. A., 1989, MNRAS, 240, 833

Ueda Y., Akiyama M., Ohta K., Miyaji T., 2003, ApJ, 598, 886

Urry C. M., Padovani P., 1995, PASP, 107, 803

Vaughan S., Edelson R., Warwick R. S., Uttley P., 2003, MNRAS, 345, 1271

Vaughan S., Fabian A. C., 2004, MNRAS, 348, 1415

Vaughan S., Fabian A. C., Ballantyne D. R., De Rosa A., Piro L., Matt G., 2004, MNRAS, 351, 193

Vaughan S., Uttley P., 2008, MNRAS, 390, 421

Véron-Cetty M., Véron P., 2001, A&A, 374, 92

Wang J., Mao Y. F., Wei J. Y., 2009, AJ, 137, 3388

Warren S. J., Hewett P. C., Osmer P. S., 1994, ApJ, 421, 412

Weaver K. A., Nousek J., Yaqoob T., Mushotzky R. F., Makino F., Otani C., 1996, ApJ, 458, 160

Weaver K. A., Reynolds C. S., 1998, ApJL, 503, L39

Weedman D. W., 1976, ApJ, 208, 30

Wilms J., Reynolds C. S., Begelman M. C., Reeves J., Molendi S., Staubert R., Kendziorra E., 2001, MNRAS, 328, L27

Wilson A. S., Tsvetanov Z. I., 1994, AJ, 107, 1227

Woo J., Treu T., Barth A. J., Wright S. A., Walsh J. L., Bentz M. C., Martini P., Bennert V. N., Canalizo G., Filippenko A. V., Gates E., Greene J., Li W., Malkan M. A., Stern D., Minezaki T., 2010, ApJ, 716, 269

Worsley M. A., Fabian A. C., Bauer F. E., Alexander D. M., Hasinger G., Mateos S., Brunner H., Brandt W. N., Schneider D. P., 2005, MNRAS, 357, 1281

Wu X., Chen Z., Jia Z., Zuo W., Zhao Y., Luo A., Bai Z., Chen J., Zhang H., Yan H., Ren J., Sun S., Wu H., Zhang Y., Li Y., Lu Q., Wang Y., Ni J., Wang H., Kong X., Shen S., 2010, Research in Astronomy and Astrophysics, 10, 737

Yaqoob T., George I. M., Kallman T. R., Padmanabhan U., Weaver K. A., Turner T. J., 2003, ApJ, 596, 85

Yaqoob T., Reeves J. N., Markowitz A., Serlemitsos P. J., Padmanabhan U., 2005, ApJ, 627, 156

Young A. J., Ross R. R., Fabian A. C., 1998, MNRAS, 300, L11

Zdziarski A. A., Fabian A. C., Nandra K., Celotti A., Rees M. J., Done C., Coppi P. S., Madejski G. M., 1994, MNRAS, 269, L55

Zdziarski A. A., Lubinski P., Smith D. A., 1999, MNRAS, 303, L11

Zoghbi A., Fabian A. C., Uttley P., Miniutti G., Gallo L. C., Reynolds C. S., Miller J. M., Ponti G., 2010, MNRAS, 401, 2419

Zycki P. T., Czerny B., 1994, MNRAS, 266, 653